



UNIVERSITÀ  
DEGLI STUDI  
FIRENZE

DOTTORATO DI RICERCA IN  
Fisica e Astronomia  
CICLO XXIX

COORDINATORE Prof. Massimo Gurioli

# **Measurements of the Higgs boson decay to $W^+W^-$ with the CMS detector**

Settore Scientifico Disciplinare FIS/04

**Dottorando**

Dott. Lorenzo Viliani

**Tutore**

Prof. Vitaliano Ciulli

---

**Coordinatore**

Prof. Massimo Gurioli

---

Anni 2013/2016



# Contents

<b>Introduction</b>	<b>1</b>
<b>1 Physics at the LHC</b>	<b>3</b>
1.1 The Standard Model of particle physics . . . . .	3
1.1.1 The electroweak interaction . . . . .	4
1.1.2 The strong interaction . . . . .	7
1.2 Beyond the Standard Model . . . . .	8
1.3 Proton-proton interactions . . . . .	9
1.3.1 Hadron collider kinematics . . . . .	10
1.4 Higgs boson phenomenology . . . . .	11
1.4.1 Higgs boson production mechanisms and decay channels . . . . .	11
1.4.2 The $H \rightarrow WW$ decay channel . . . . .	13
1.4.3 Higgs boson kinematics . . . . .	15
1.4.4 Event generators for Higgs boson production . . . . .	16
1.5 Experimental Higgs boson highlights . . . . .	19
<b>2 LHC and the CMS experiment</b>	<b>23</b>
2.1 The Large Hadron Collider . . . . .	23
2.2 The <i>Compact Muon Solenoid</i> experiment . . . . .	27
2.2.1 The solenoid . . . . .	29
2.2.2 The tracker . . . . .	30
2.2.3 The electromagnetic calorimeter (ECAL) . . . . .	35
2.2.4 The hadron calorimeter (HCAL) . . . . .	37
2.2.5 The muon system . . . . .	38
2.3 The CMS trigger system . . . . .	40
2.3.1 The Level-1 trigger . . . . .	41
2.3.2 The high level trigger (HLT) . . . . .	43
<b>3 Reconstruction and identification of physics objects</b>	<b>45</b>
3.1 The Particle Flow technique . . . . .	45
3.2 Leptons reconstruction and identification . . . . .	47
3.2.1 Muon reconstruction and identification . . . . .	47
3.2.2 Muon isolation . . . . .	49

3.2.3	Muon momentum scale and resolution . . . . .	49
3.2.4	Electron reconstruction and identification . . . . .	50
3.2.5	Electron isolation . . . . .	51
3.2.6	Electron momentum scale and resolution . . . . .	52
3.2.7	Lepton identification and isolation efficiency . . . . .	52
3.2.8	Lepton trigger efficiency . . . . .	54
3.3	Jets reconstruction and identification . . . . .	55
3.3.1	Jet reconstruction in CMS . . . . .	55
3.3.2	Jet energy correction . . . . .	57
3.3.3	Jet identification . . . . .	61
3.4	Jet b tagging . . . . .	62
3.5	Missing transverse energy . . . . .	63
3.5.1	$E_T^{\text{miss}}$ scale and resolution measurement . . . . .	65
<b>4</b>	<b>Measurement of the Higgs boson transverse momentum spectrum at 8 TeV using <math>H \rightarrow WW \rightarrow 2\ell 2\nu</math> decays</b>	<b>67</b>
4.1	Data sets and triggers . . . . .	68
4.2	Monte Carlo samples . . . . .	68
4.3	Analysis Strategy . . . . .	71
4.3.1	Event reconstruction and selections . . . . .	71
4.3.2	Simulation efficiencies and scale factors . . . . .	74
4.3.3	Fiducial phase space . . . . .	78
4.3.4	Binning of the $p_T^H$ distribution . . . . .	79
4.4	Background estimation . . . . .	81
4.4.1	Top quark background . . . . .	81
4.4.2	$WW$ background . . . . .	82
4.4.3	$W+jets$ background . . . . .	84
4.4.4	$Z/\gamma^* \rightarrow \tau^+\tau^-$ background . . . . .	86
4.4.5	Diboson backgrounds . . . . .	87
4.5	Systematic uncertainties . . . . .	88
4.5.1	Uncertainties on background predictions . . . . .	88
4.5.2	Experimental uncertainties . . . . .	90
4.5.3	Theoretical uncertainties . . . . .	91
4.5.4	Statistics uncertainty of the simulated samples . . . . .	92
4.5.5	Treatment of systematic uncertainties in the analysis . . . . .	92
4.6	Signal extraction . . . . .	93
4.6.1	Fitting procedure . . . . .	93
4.6.2	Signal and background yields . . . . .	96
4.7	Unfolding . . . . .	100
4.7.1	Treatment of systematic uncertainties in the unfolding . . . . .	103
4.8	Results . . . . .	106
<b>5</b>	<b>Measurement of Higgs boson production using <math>H \rightarrow WW</math> decays</b>	

<b>with first 13 TeV data</b>	<b>109</b>
5.1 Data and simulated samples . . . . .	109
5.2 Analysis strategy . . . . .	112
5.2.1 Event reconstruction . . . . .	112
5.2.2 B tagging performance . . . . .	113
5.2.3 Event selection and background rejection . . . . .	117
5.2.4 Signal extraction . . . . .	119
5.3 Background estimation . . . . .	119
5.3.1 WW background . . . . .	123
5.3.2 Top quark background . . . . .	123
5.3.3 W+jets background . . . . .	124
5.3.4 $Z/\gamma^* \rightarrow \tau^+\tau^-$ background . . . . .	125
5.3.5 Other backgrounds . . . . .	126
5.4 Systematic uncertainties . . . . .	127
5.5 Results . . . . .	129
<b>6 Search for high mass resonances decaying to a W boson pair with first 13 TeV data</b>	<b>133</b>
6.1 Data and simulated samples . . . . .	133
6.2 Analysis strategy . . . . .	135
6.3 Background estimation . . . . .	138
6.4 Systematic uncertainties . . . . .	139
6.5 Signal extraction and limit setting . . . . .	141
6.6 Results . . . . .	144
<b>Summary</b>	<b>151</b>
<b>A Fiducial region definition and optimization</b>	<b>153</b>
<b>Bibliography</b>	<b>157</b>



# Introduction

The Higgs mechanism is an essential element of the Standard Model (SM), explaining the origin of mass and playing a key role in the physics of electroweak symmetry breaking. A suitable Higgs boson candidate, predicted by the Higgs mechanism, was found with a mass of 125 GeV by the ATLAS and CMS experiments in the first run of the CERN Large Hadron Collider (LHC).

After the discovery, the accurate measurement of the Higgs boson properties has become one of the main goals of the LHC. The Higgs sector could in fact be more entangled with respect to what discovered so far and Beyond the Standard Model (BSM) effects could emerge from an accurate measurement of the couplings with fermions and bosons, i.e. from the knowledge of the Higgs boson production processes and decays. The  $H \rightarrow W^+W^-$  channel is one of the most sensitive to these effects and the high branching fraction allows the statistics needed for a precision measurement to be easily collected.

Measurements of the production cross section of the Higgs boson times branching fraction of decay in a restricted part of the phase space (fiducial phase space) and its kinematic properties thus represent an important test for possible deviations from the SM predictions. In particular, it has been shown that the Higgs boson transverse momentum spectrum can be significantly affected by the presence of physics phenomena not predicted by the SM. In addition, these measurements facilitate tests of the theoretical calculations in the SM Higgs sector.

A complementary strategy to seek hints of BSM physics is to perform direct searches for additional Higgs bosons in the full mass range accessible to current and future experiments. There are indeed several models that predict a more rich Higgs sector, requiring the existence of new particles that could show up in direct searches at energies achievable at LHC.

The purpose of this thesis is then twofold, reporting firstly a precision measurement of the Higgs boson transverse momentum spectrum using proton-proton collision data collected at a centre-of-mass energy of 8 TeV and thereafter focusing on the first data collected by the CMS experiment at the unprecedented centre-of-mass energy of 13 TeV. These latter data will be used both to perform a preliminary re-discovery of the Higgs boson at the new collision energy, and to directly search for new resonances with masses up to 1 TeV. All the analyses discussed in this thesis are performed looking at the Higgs boson (or the new resonance) decays to a W boson pair.

The transverse momentum spectrum and the inclusive cross section times branch-

ing fraction measurements reported here, represent the first measurements at the LHC for the Higgs boson production using  $H \rightarrow W^+W^- \rightarrow e^\pm\mu^\mp\nu\bar{\nu}$  decays. The Higgs boson transverse momentum is reconstructed using the lepton pair transverse momentum and missing transverse momentum. The differential cross section times branching fraction is measured as a function of the Higgs boson transverse momentum in a fiducial phase space defined to match the experimental acceptance in terms of lepton kinematics and event topology. The measurements are corrected for detector effects and compared to theoretical calculations based on the SM, to which they agree within experimental uncertainties.

The first data collected during 2015, corresponding to an integrated luminosity of  $2.3\text{ fb}^{-1}$ , are used to perform a re-discovery analysis of the Higgs boson in the  $H \rightarrow W^+W^- \rightarrow e^\pm\mu^\mp\nu\bar{\nu}$  decay channel. Since the amount of analysed data is small, this preliminary result does not provide a significant signal evidence, as expected given the Higgs boson production cross section predicted by the SM. Nevertheless, this analysis is useful to pave the way for similar analyses that are now studying the same channel with an enlarged data set.

Furthermore, the same data are used to search for new resonances decaying to  $W^+W^- \rightarrow e^\pm\mu^\mp\nu\bar{\nu}$  in the mass range between 200 GeV and 1 TeV. No significant excess with respect to the SM background expectation is observed, and exclusion limits on the production cross section times branching fraction of the new resonance are reported over the whole analysed mass spectrum, studying also different hypotheses of the resonance decay width.

# Chapter 1

## Physics at the LHC

In this chapter the Standard Model (SM) of particle physics is briefly described, in particular the main characteristics of the electroweak and strong interactions are discussed, as well as the mechanism of the electroweak symmetry breaking. Afterwards, few models that provide a simple extension of the SM Higgs sector are briefly described. In addition, the phenomenology of Higgs boson production at LHC is described, focusing on its kinematic properties and, in particular, on the  $H \rightarrow WW$  decay channel. An overview of the main features of the Monte Carlo (MC) simulation techniques for the Higgs boson production are also given, as well as a brief report of the Higgs boson highlights from the experiments.

Unless otherwise stated, natural units  $\hbar = c = 1$  are used throughout this work.

### 1.1 The Standard Model of particle physics

The Standard Model of Particle Physics is the theory that describes all fundamental constituents of matter and their interactions [1]. It is a renormalisable quantum field theory based on a  $SU(3)_c \otimes SU(2)_L \otimes U(1)_Y$  local gauge symmetry, and is capable to provide a quantitative description of three of the four interactions in nature: electromagnetism, weak interaction and strong nuclear force.

According to the SM, the ordinary matter is made up of spin-1/2 particles, denoted as fermions. The fermions are subdivided into two classifications of elementary particles: leptons and quarks. Both classes consist of six particles, grouped into three doublets, called generations. Additional three doublets for each class are composed of leptons and quarks antiparticles. A charged particle with electric charge  $Q = -1$ , either the electron  $e$ , the muon  $\mu$  or the tauon  $\tau$ , and a neutral particle, the corresponding neutrino, compose the following lepton generations, ordered according to an increasing mass hierarchy:

$$\begin{pmatrix} e^- \\ \nu_e \end{pmatrix}, \quad \begin{pmatrix} \mu^- \\ \nu_\mu \end{pmatrix}, \quad \begin{pmatrix} \tau^- \\ \nu_\tau \end{pmatrix} \quad . \quad (1.1)$$

Charged leptons can interact via the electromagnetic and weak force, while neutrinos, that are assumed to be massless, can interact only through the weak interaction.

Similarly, the quarks are organized in pairs composed of a particle with  $Q = +2/3$ , *up* (u), *charm* (c) and *top* (t) quarks, and another particle with  $Q = -1/3$ , *down* (d), *strange* (s) and *bottom* (b) quarks:

$$\begin{pmatrix} u \\ d \end{pmatrix}, \quad \begin{pmatrix} c \\ s \end{pmatrix}, \quad \begin{pmatrix} t \\ b \end{pmatrix} \quad . \quad (1.2)$$

As well as leptons, quarks can interact via the electromagnetic and weak force, but also through the strong interaction, responsible of their confinement within hadrons. In fact, free quarks are not observed in nature, but they bind together forming two categories of hadrons: mesons, bound states of a quark q and an anti-quark  $\bar{q}$ , and baryons, bound states of three quarks.

In the SM the interaction between elementary particles occurs through the exchange of spin-1 particles, known as bosons, which identify the fundamental forces. The photon  $\gamma$  is the mediator of the electromagnetic interaction, the  $W^\pm$  and Z bosons are the mediators of the weak interaction, while the strong force is mediated by eight gluons g. Electromagnetic and weak interactions are actually the manifestations of the same fundamental interaction, the electroweak force.

### 1.1.1 The electroweak interaction

The theory of electroweak interaction was formulated in the 1960s by S. L. Glashow, A. Salam and S. Weinberg [2, 3] as an  $SU(2) \otimes U(1)$  local gauge theory. The Lagrangian density governing the electroweak interaction is therefore invariant under gauge transformations of the  $SU(2)_L \otimes U(1)_Y$  symmetry group. The  $SU(2)_L$  group refers to the weak isospin charge  $I$ , while  $U(1)_Y$  to the weak hypercharge  $Y$ , which are connected to the charge Q by the following equation:

$$Y = 2(Q - I_3) \quad , \quad (1.3)$$

where  $I_3$  represents the third component of the weak isospin.

According to the Noether theorem, the  $SU(2)_L$  invariance of the theory leads to the existence of three conserved currents,  $J_\mu^\pm$  and  $J_\mu^3$ , which constitute an isospin triplet of weak currents. The two currents  $J_\mu^\pm$  represent the weak charged current interactions, which describe the interaction between fermions that are mediated by the charged  $W^\pm$  bosons. These currents only involve left-handed particles or right-handed anti-particles, in accordance with the fact that the parity symmetry is maximally violated for weak charged current interactions, as confirmed by the experiments of Madame Wu [4] and Garwin-Lederman-Weinrich [5] in 1957. In the case of leptons, charged currents can only connect two particles within the same generation, for example the electron and the electron neutrino, while for the quarks a mixing of different generations may occur, according to the Cabibbo-Kobayashi-Maskawa matrix (CKM).

Another possible interaction in the weak sector is known as neutral current interaction and is mediated by the neutral Z boson. In the vertex of this interaction the identity of the interacting lepton does not change, resembling in this matter the electromagnetic current. Concerning the quark sector, the weak neutral currents involving different quark flavours, i.e. *flavour changing neutral currents*, are strictly suppressed at tree level by the Glashow-Iliopoulos-Maiani mechanism (GIM) [6].

Nevertheless, the other component of the weak isospin triplet of currents  $J_\mu^3$ , cannot be identified with the weak neutral current, because the latter involves both left- and right-handed components. The electromagnetic current cannot be represented by  $J_\mu^3$  as well, for the aforementioned reason and because it cannot be coupled with the uncharged neutrino. In order to save the SU(2) symmetry, the existence of the U(1)<sub>Y</sub> symmetry is required, and a new conserved current,  $j_\mu^Y$ , arises. The  $j_\mu^Y$  current is unchanged under SU(2)<sub>L</sub> transformations (is an isospin singlet) and is incorporated, together with  $J_\mu^3$ , in the definition of the electromagnetic current, giving rise to the electroweak unification.

Local gauge symmetries naturally lead to the presence of gauge bosons, the exchange particles mediators of the fundamental interactions. The symmetry requires these gauge bosons to be massless, which is unproblematic for photons and gluons, but in drastic contrast to the known masses of the Z and W<sup>±</sup> bosons, which are  $m_Z = 91.1876 \pm 0.0021$  GeV and  $m_W = 80.385 \pm 0.015$  GeV, respectively. Moreover, the maximally parity violating structure of the weak charged currents also breaks local gauge invariance for all massive fermions, due to their coupling to the W boson. This leads to the apparent antagonism that, while the SU(2)<sub>L</sub>  $\otimes$  U(1)<sub>Y</sub> gauge symmetry does describe the coupling structure of the electroweak force, at the same time it seems to contradict the fact that the W and Z bosons, and all fermions have a non-vanishing mass.

The proposed solution to this problem is the mechanism of *spontaneous symmetry breaking*, where the gauge symmetry is still intrinsic to the Lagrangian density of the theory, but not manifest in its energy ground state, which in this case is the quantum vacuum. The spontaneous symmetry breaking of the SU(2)<sub>L</sub>  $\otimes$  U(1)<sub>Y</sub> symmetry group requires the introduction of a self-interacting complex scalar field [7], which is an isospin doublet:

$$\phi = \begin{pmatrix} \phi^+ \\ \phi^0 \end{pmatrix} = \begin{pmatrix} (\phi_1 + i\phi_2)/\sqrt{2} \\ (\phi_3 + i\phi_4)/\sqrt{2} \end{pmatrix} . \quad (1.4)$$

The simplest lagrangian involving this field has the form:

$$\begin{aligned} \mathcal{L}_H &= \mathcal{D}_\mu \phi^\dagger \mathcal{D}^\mu \phi - V(\phi) , \\ V(\phi) &= -\mu^2 \phi^\dagger \phi + \lambda (\phi^\dagger \phi)^2 \end{aligned} \quad (1.5)$$

Here  $\mathcal{D}_\mu$  represents the covariant derivative, which is defined as:

$$\mathcal{D}_\mu = \partial_\mu + ig \vec{A}_\mu \cdot \frac{\vec{\tau}}{2} - \frac{1}{2} ig' Y B_\mu , \quad (1.6)$$

where  $\vec{A}_\mu$  is a vector of three gauge fields satisfying the local SU(2) symmetry, and  $B_\mu$  is the gauge field assuring the U(1) symmetry. The parameters  $g$  and  $g'$  represent the coupling constants for the gauge fields.

The term  $V(\phi)$  in Eq.(1.5) is a potential term that depends on two parameters,  $\mu$  and  $\lambda$ , with  $\lambda > 0$  in order to have vacuum stability. If the  $\mu$  parameter is chosen so that  $\mu^2 < 0$ , the symmetry of  $V(\phi)$  may be broken, since its minimum value is degenerate:

$$\phi^\dagger \phi = -\frac{\mu^2}{2\lambda} = \frac{v^2}{2} \quad , \quad (1.7)$$

where  $v$  corresponds to the *vacuum expectation value* (VEV). Perturbation theory requires an expansion of  $\phi$  around its energy ground state. The ground state is chosen in such a way it breaks the  $SU(2)_L \otimes U(1)_Y$  symmetry group but preserves the invariance under  $U(1)_{\text{em}}$  transformations, i.e. it has a null electric charge. This latter requirement guarantees the presence of a neutral massless gauge boson, the photon. Therefore, the ground state can be written without any loss of generality as:

$$\tilde{\phi} = \frac{1}{\sqrt{2}} \begin{pmatrix} 0 \\ v \end{pmatrix} \quad . \quad (1.8)$$

The field  $\phi$  can be expanded at first order around the ground state obtaining:

$$\phi = \frac{1}{\sqrt{2}} \begin{pmatrix} 0 \\ v + h \end{pmatrix} \quad . \quad (1.9)$$

Introducing this field in the Higgs Lagrangian in Eq. (1.5), the bosonic fields acquire a mass given by:

$$m_W = \frac{v}{2} g \quad m_Z = \frac{v}{2} \sqrt{g^2 + g'^2} \quad . \quad (1.10)$$

Furthermore, given the self-interaction terms of the  $h$  field, a new physical state (the Higgs boson) also arises, with a mass:

$$m_H = v\sqrt{2\lambda} \quad . \quad (1.11)$$

whose value is not predicted by the theory, since  $\lambda$  is unknown<sup>1</sup>.

The mass of fermions is achieved without breaking the gauge symmetry of the Lagrangian by introducing a coupling term, known as Yukawa coupling, between the fermion doublets and the Higgs field.

In addition to the mass of the particles, the model also predicts the couplings  $f$  of the Higgs boson to fermions and heavy gauge bosons, despite their numerical values

---

<sup>1</sup>On the other hand, the value of  $v$  can be obtained using the relation between  $m_W$  and the Fermi constant  $G_F$ , which leads to  $v = 1/\sqrt{\sqrt{2}G_F} = 246.22 \text{ GeV}$ , setting the scale of the electroweak symmetry breaking.

need to be determined by experiments:

$$\begin{aligned}
 f_{H \rightarrow ff} &\propto \frac{m_f}{v}, \quad \text{fermions} \\
 f_{H \rightarrow VV} &\propto \frac{2m_V^2}{v}, \quad \text{heavy bosons trilinear} \\
 f_{HH \rightarrow VV} &\propto \frac{2m_V^2}{v^2}, \quad \text{heavy bosons quartic} \\
 f_{H \rightarrow HH} &\propto \frac{3m_H^2}{v}, \quad \text{Higgs boson trilinear} \\
 f_{HH \rightarrow HH} &\propto \frac{3m_H^2}{v^2}, \quad \text{Higgs boson quartic} .
 \end{aligned} \tag{1.12}$$

During the past decades the predictions of the SM have been confirmed by experimental results with outstanding precision, and in 2012 the discovery of a new boson with a mass of about 125 GeV, consistent with the predicted Higgs boson, was announced by the ATLAS and CMS experiments at LHC.

### 1.1.2 The strong interaction

Quantum Chromo-Dynamics (QCD) is the theory that describes the strong interactions [8]. It is an unbroken gauge non-abelian theory based on the group  $SU(3)$  of colour ( $SU(3)_c$ ). The mediators of the interaction are eight massless gluons and the elementary particles of matter are colour triplets of quarks, with different flavours. In fact, as shown in (1.2), six types (flavours) of quark exist and each quark possesses a colour charge that can assume three values, namely red, green and blue.

The physical vertices in QCD include the gluon-quark-antiquark vertex, analogous to the Quantum Electro-Dynamics (QED) photon-fermion-antifermion coupling, but also the three-gluon and four-gluon vertices, i.e. gluon themselves carry colour charge, which have no analogue in an abelian theory like QED. Quark and gluons are the only particles that interact through the strong interaction.

The non-abelian nature of the theory leads to two important characteristics:

- *colour confinement*: the QCD coupling constant  $\alpha_s = g_s^2/4\pi$  is a function of the scale of the interaction  $Q$ . At low energy (corresponding to large distances of the order of 1 fm) the  $\alpha_s$  value is large and a perturbative approach is not applicable. When a quark-antiquark pair begins to separate, the colour field generated by the exchanged gluons increases its intensity and, at some point, the creation of a new quark-antiquark pair from the vacuum becomes more energetically favourable than increasing further the interaction strength. This explains why free quarks are not observed and the final state particles are made of colourless quark bound states (hadrons). This is also the cause of the hadronization process which causes the formation of jets.
- *asymptotic freedom*: the coupling constant decreases at large scales  $Q$  approaching to zero, meaning that quarks can be asymptotically considered as free parti-

cles. The small value of the coupling constant at large scales justifies the usage of a perturbative approach to describe hard processes.

## 1.2 Beyond the Standard Model

The discovery of the new boson in accordance with the Higgs boson predicted by the SM has been a major breakthrough in the contemporary particle physics. The Higgs boson mass is a free parameter in the SM and its measurement fixes all the other parameters related to the Higgs field, such as the coupling strengths with bosons and fermions. The current quest is to establish whether the properties of the discovered boson are consistent with the SM predictions, or it is only a component of a more entangled Higgs sector. Moreover, there are still several aspects that are not explained by the SM, such as the hierarchy problem, the nature of dark matter and others [9].

Several theoretical models have been proposed to explain the deficiencies of the SM. One of the simplest extension of the SM Higgs sector requires the existence of an additional singlet scalar field,  $S$ , which is neutral under all quantum numbers of the SM gauge group [10]. In general the singlet field mixes with the SM Higgs boson,  $H$ , allowing it to couple to the same states as the SM Higgs boson itself. If the mass of the scalar singlet was more than twice that of the SM Higgs boson, the  $S$  branching ratios would be reduced with respect to the  $H$  ones, because of the opening of the new  $S \rightarrow HH$  decay channel.

The mixing of the two states  $S$  and  $H$  would manifest as a suppression of the production cross section of both states and a suppression of the heavy mass Higgs boson decay modes to SM particles, if the  $S \rightarrow HH$  decay is kinematically accessible. In particular, identifying as  $H$  the observed Higgs boson with  $m_H = 125\text{ GeV}$ , and supposing that the new scalar singlet  $S$  is heavier than  $H$ , one can introduce the scale factors of the low and high mass state couplings,  $\mathcal{C}$  and  $\mathcal{C}'$ , respectively. These factors are related by the unitarity condition  $\mathcal{C}^2 + \mathcal{C}'^2 = 1$ . The singlet cross section and width are consequently modified by the factors  $\mu'$  and  $\Gamma'$ , respectively:

$$\begin{aligned}\mu' &= \mathcal{C}'^2 \cdot (1 - \mathcal{B}_{\text{new}}) \quad , \\ \Gamma' &= \Gamma_{\text{SM}} \cdot \frac{\mathcal{C}'^2}{1 - \mathcal{B}_{\text{new}}} \quad ,\end{aligned}\tag{1.13}$$

where  $\mathcal{B}_{\text{new}}$  is the singlet branching fraction to non-SM-like decay modes.

Other models, such as the *two-Higgs-doublet model* (2HDM) [11], extend the minimal Higgs content requiring the introduction of a second Higgs doublet. The generalization of the SM Lagrangian with two complex scalar fields, which are  $SU(2)_L$  doublets, eventually gives rise to five physical Higgs bosons: a charged pair ( $H^\pm$ ); two neutral  $CP$ -even scalars ( $H$  and  $h$ , where  $m_H > m_h$  by convention); and a neutral  $CP$ -odd scalar ( $A$ ) [12]. The parameter space of these 2HDM models can accommodate a wide range of variations in the production and decay modes of the SM-like Higgs boson. Nevertheless, tight constraints on flavour-changing neutral currents dis-

favour 2HDM with tree-level flavour violation. Similarly, limits on additional sources of  $CP$  violation favour 2HDM with a  $CP$ -conserving potential. These assumptions significantly reduce the parameter space of 2HDM models. Moreover, if the h boson is identified with the observed 125 GeV boson, the experimental measurements further constraint the possible production and decay modes of the other predicted particles. Examples of possible decay channels in this framework are the following: the heavy  $CP$ -even Higgs may decay to two light  $CP$ -even Higgs,  $H \rightarrow hh$ ; the  $CP$ -odd pseudoscalar Higgs may decay to a light  $CP$ -even Higgs and a Z boson,  $A \rightarrow Zh$ ; the charged Higgs bosons may decay to a SM-like Higgs and a  $W^\pm$  boson,  $H^\pm \rightarrow W^\pm h$ .

In order to search for new particles that could be ascribable to the simple models depicted above, or even to more complicated theories, it is of utmost importance to provide precise measurements of the Higgs boson couplings and kinematics, as well as its spin and parity properties. A complementary strategy is to perform direct searches for additional Higgs bosons in the full mass range accessible to current and future experiments.

### 1.3 Proton-proton interactions

The fundamental difference between hadron and lepton collisions is the fact that hadrons, differently from leptons, are not elementary particles but have an internal structure that can be described in terms of the QCD-improved parton model. The basic idea of this model is to represent the inelastic scattering as a quasi-free scattering of point-like constituents within the proton, the partons [13]. Hadrons, along with the valence quarks that contribute to their quantum numbers ( $uud$  for protons), contain virtual quark-antiquark pairs known as sea quarks. Sea quarks arise from gluon splitting; a pair of quarks can in turn annihilate producing a gluon. In addition, gluons are present in the sea also owing to the three-gluon and four-gluon vertices.

In proton-proton collisions the interaction generally involves a pair of partons and any of the partons in the sea can interact with a given likelihood, making possible several types of interaction, such as  $qq$ ,  $qq'$ ,  $q\bar{q}$ ,  $q\bar{q}'$ ,  $gq$ ,  $g\bar{q}$  or  $gg$ .

At a hadron collider the partons entering the hard scattering carry an event-by-event variable fraction  $x$  of the proton four-momentum, also known as Bjorken's scaling variable. Therefore the centre-of-mass energy of the hard scattering is given by  $\sqrt{\hat{s}} = \sqrt{x_1 x_2 s}$ , where  $\sqrt{s}$  is the centre-of-mass energy of the incoming protons, and  $x_1, x_2$  are the four-momentum fractions carried by the two interacting partons<sup>2</sup>. Since generally  $x_1$  and  $x_2$  have different values, the centre-of-mass frame of the interaction is boosted along the beam direction. While this represents an experimental struggle, on the other hand it allows to explore a wider range of energies with respect to an electron-positron collider.

In order to evaluate cross sections in hadron collisions, the calculation can be

---

<sup>2</sup>Considering  $\sqrt{s} = 14$  TeV and  $x_1, x_2 \approx 0.15\text{--}0.20$ , the partonic centre-of-mass energy is of the order of 1–2 TeV.

factorized into long-distance and short-distance components according to the QCD factorization theorem [14]. Therefore, a typical cross section calculation for an inclusive process  $pp \rightarrow X$  consists of a term that describes the partonic hard scattering, which can be calculated using perturbative QCD, and factors that describe the incoming flux of partons, the *parton distribution functions* (PDF)  $f_i$ , as shown in the following equation [15]:

$$\sigma(pp \rightarrow X) = \sum_{i,j} \int dx_1 dx_2 f_i(x_1, \mu_F^2) f_j(x_2, \mu_F^2) \hat{\sigma}_{ij \rightarrow X}(x_1 x_2 s, \mu_R^2, \mu_F^2) . \quad (1.14)$$

In this expression the sum runs over all the initial-state partons with longitudinal momentum fractions  $x_1$  and  $x_2$ , where the subscripts 1 and 2 refers to the two incoming protons. The factorization scale  $\mu_F$  is an arbitrary parameter that represents the scale at which the separation between the hard perturbative interaction and the long distance, non-perturbative, evolution of the produced partons occurs. The  $\hat{\sigma}_{ij \rightarrow X}$  term corresponds to the partonic cross section evaluated at the scales  $\mu_F$  and  $\mu_R$ , where  $\mu_R$  is the renormalization scale, an additional scale introduced in perturbative QCD to treat the ultraviolet divergences. The PDF  $f_{i,j}$  represents the probability density for a parton  $i, j$  to be found within the incoming proton and to carry a fraction  $x_{1,2}$  of its momentum. The PDFs are obtained performing global fits to data at different scales  $Q^2$  and their evolution with scale is governed by the DGLAP equation [16]. The global PDFs fits are provided by three main collaborations: CTEQ [17], MSTW 2008 [18] and NNPDF [19].

### 1.3.1 Hadron collider kinematics

As described before, at hadron colliders the centre-of-mass energy of the parton hard scattering is generally boosted along the beam direction. It is therefore useful to describe the final state in terms of variables that are invariant under Lorentz transformations along that direction. A convenient set of kinematic variables is the transverse momentum  $p_T$ , the rapidity  $y$  and the azimuthal angle  $\phi$ . In term of these variables, the four-momentum of a particle of mass  $m$  can be written as:

$$p^\mu = (E, p_x, p_y, p_z) = (m_T \cosh y, p_T \sin \phi, p_T \cos \phi, m_T \sinh y) , \quad (1.15)$$

where  $p_x$ ,  $p_y$  and  $p_z$  are the components of the momentum  $\vec{p}$  ( $p_z$  is directed along the beam direction) and the transverse mass is defined as  $m_T = \sqrt{p_T^2 + m^2}$ . The rapidity  $y$  is defined by the following formula:

$$y = \frac{1}{2} \ln \left( \frac{E + p_z}{E - p_z} \right) . \quad (1.16)$$

The rapidity is not invariant under boosts along the beam direction but it transforms according to the law:

$$y \longrightarrow y + \frac{1}{2} \ln \left( \frac{1 + \beta}{1 - \beta} \right) , \quad (1.17)$$

where  $\beta$  is the boost velocity. According to this definition the rapidity differences  $\Delta y$  are Lorentz invariant. Experimentally it is more convenient to use the pseudorapidity  $\eta$ , defined as:

$$\eta = -\ln \tan \frac{\theta}{2} , \quad (1.18)$$

where  $\theta$  is the polar angle between the particle momentum and the beam direction ( $\cos \theta = p_z / |\vec{p}|$ ). For ultra-relativistic particles the pseudorapidity coincides with the rapidity.

## 1.4 Higgs boson phenomenology

In this section the Higgs boson production modes and decay channels are described, spending some time on the description of the  $H \rightarrow WW$  channel, which is the channel investigated in this work. Afterwards, a description of the effects due to higher order QCD corrections on Higgs boson kinematic variables is shown. Finally, a brief review of the Monte Carlo (MC) generators used for the simulation of Higgs boson processes is given.

### 1.4.1 Higgs boson production mechanisms and decay channels

The main processes contributing to the Higgs boson production at hadron colliders are represented by the Feynman diagrams shown in Fig. 1.1.

In order of decreasing cross section, the Higgs boson production modes are:

- *Gluon fusion* (ggH): this is the main Higgs boson production mode at LHC over the whole mass spectrum. The process involves the fusion of two incoming gluons that give rise to the Higgs boson through a heavy quark loop, whose main contribution comes from the top quark, as shown in Fig. 1.1(a).
- *Vector Boson Fusion* (VBF): each of the two interacting quarks emit a W or Z boson which, in turn, interact to produce the Higgs boson, as shown in Fig. 1.1(b). Quarks deriving from the incoming partons after the emission of vector bosons proceed in the forward direction and represent the peculiar signature of this production mode, i.e. two high energy forward jets separated by a large pseudorapidity gap. This process has a cross section which is one order of magnitude lower than ggH for a large range of  $m_H$  values and it becomes comparable to ggH only for masses of the order of 1 TeV.
- *Vector boson associated production* (VH): also known as *Higgsstrahlung*, this process is characterized by the emission of a Higgs boson from a  $W^\pm$  or Z boson produced by two incoming quarks, as depicted in Fig. 1.1(c). The VH cross section is several orders of magnitude lower than the ggH and VBF cross sections.

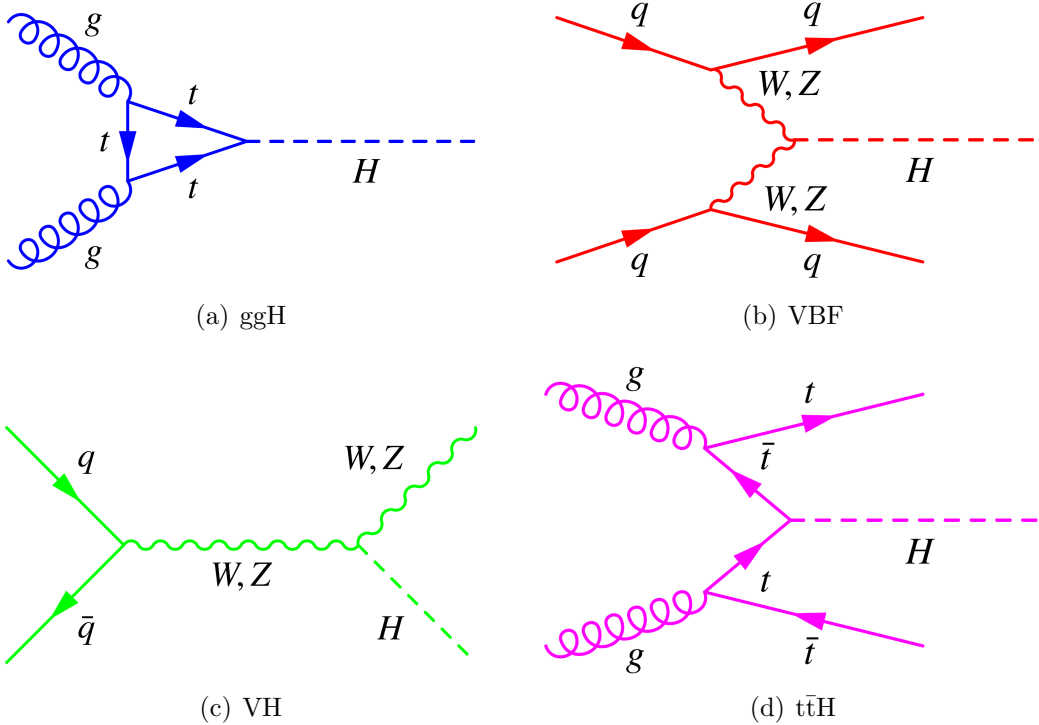


**Figure 1.1:** Main Higgs boson production processes at LHC.

- *Top quark associated production ( $t\bar{t}H$ ):* a pair of top quarks, originated from the splitting of two incoming gluons, interacts to give rise to a Higgs boson, as illustrated in Fig. 1.1(d).

Another production mechanism analogous to the  $t\bar{t}H$  process and with a similar cross section is the b quark associated production.

The SM Higgs boson production cross section for the various production modes depends on the Higgs boson mass and on the centre-of-mass energy, as shown in Fig. 1.2. In general, the production cross section of all processes decreases with increasing the Higgs boson mass, while the raise of the centre-of-mass energy reflects in an increase of the cross section over the whole mass range.

The Higgs boson can decay to a variety of final states that can be divided in bosonic channels, like  $\gamma\gamma$ ,  $ZZ$  or  $W^+W^-$ , and fermionic channels, like  $\tau\tau$ ,  $bb\bar{b}$ , etc. Its branching ratio depends on the Higgs boson mass, as illustrated in Fig. 1.3, where different decay channels are compared over the whole mass spectrum. At  $m_H = 125$  GeV the decay channel with the largest branching ratio is  $bb\bar{b}$ , followed by  $WW$ ,  $\tau\tau$ ,  $ZZ$  and others. Although being the channel with the largest branching ratio, analyses looking at the  $H \rightarrow bb\bar{b}$  decays are in practical cases limited by the overwhelming background contribution, which makes it possible only if the Higgs boson is produced via VBF, VH or  $t\bar{t}H$ , where additional jets or leptons can be used to tag the events.

The branching ratio to the  $WW$  and  $ZZ$  decay channels are instead dominant

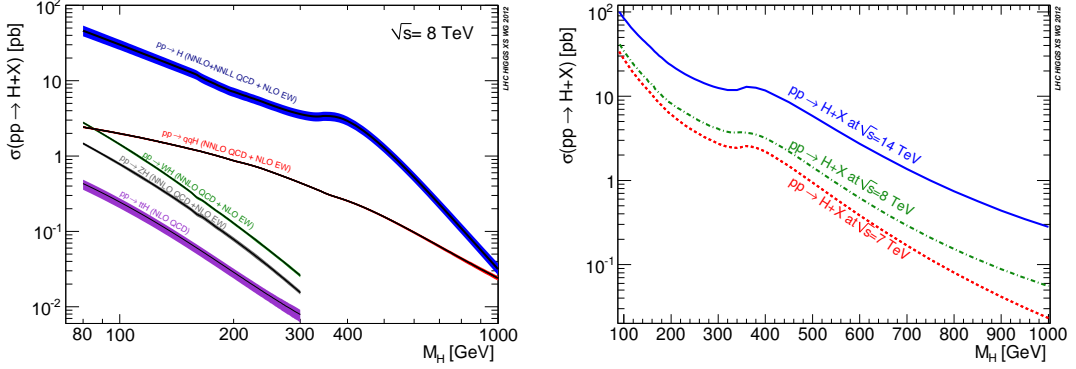


**Figure 1.2:** Higgs boson cross section as a function of  $m_H$  for the various production mechanisms (left) and for different centre-of-mass energies (right).

when increasing the Higgs boson mass, because the decays to real vector boson pairs become energetically allowed. In particular, the  $H \rightarrow W^+W^-$  decay channel, which is described in Sec. 1.4.2, is the second channel in terms of signal yield at  $m_H = 125$  GeV and the first one for higher mass values. Moreover, these channels are characterized by a much cleaner signature if the leptonic decays of one or both vector bosons are sought.

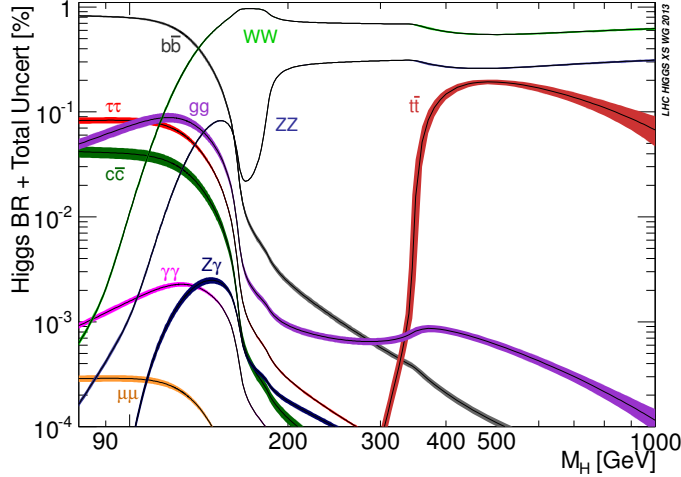


**Figure 1.3:** Higgs boson branching ratio for all the decay channels as a function of  $m_H$ .

### 1.4.2 The $H \rightarrow WW$ decay channel

As stated in the previous section, the  $H \rightarrow WW$  decay channel is one of the channels with the largest branching ratio across the full Higgs boson mass range. For Higgs boson masses below two times the W boson mass,  $m_H < 2m_W$ , the decay to two real

$W$  bosons is energetically forbidden, therefore one of the two is produced *off-shell*. The  $W$  boson can in turn decay to hadrons, with a branching ratio of 67.41%, or to leptons ( $W \rightarrow \ell\nu$ ) with a branching ratio of 10.86%. The fully hadronic decay  $H \rightarrow W^+W^- \rightarrow 4q$  is thus the most probable decay mode, but the presence of four jets in the final state makes it hard to separate the signal from the overwhelming background contribution. The semi-leptonic final state, where one  $W$  boson decays to leptons and the other to hadrons, still has a large branching ratio and the presence of one electron or muon can be exploited to tag the events. Nevertheless the background contribution is, even in this case, very large.

The analyses presented in this work are focused on the fully leptonic final state ( $H \rightarrow WW \rightarrow 2\ell 2\nu$ ) which, despite the lower branching ratio with respect to the other decay modes, is characterized by a clean signature and affected by much less background contribution. The signature of this final state is characterized by two leptons with opposite charge and a moderate amount of missing transverse energy, due to the presence of two neutrinos in the final state. In general the two leptons are characterized by high  $p_T$  values and, in case one of the  $W$  boson is off-shell (as for the SM Higgs boson case), the corresponding lepton has on average a smaller  $p_T$  with respect to the one arising from the on-shell  $W$  boson.

The final state with two same flavour leptons is not taken into account in the analyses discussed in this work, since it provides a smaller signal significance with respect to the different flavour case due to the presence of the huge contamination from Drell-Yan background processes.

Because of the presence of missing transverse energy in the final state, is not possible to reconstruct the full Higgs boson mass in this channel, and other methods must be used to distinguish between signal and background contributions.

The most important background processes contributing to this final state are non-resonant  $q\bar{q} \rightarrow W^+W^-$  and  $t\bar{t}$  production, whose Feynman diagrams are illustrated in Fig. 1.4. The first one is characterized by a final state identical to the signal, while the latter has two additional  $b$  quarks arising from the top quark decay. Despite the same final state, the lepton kinematics for signal and  $q\bar{q} \rightarrow W^+W^-$  processes is rather different. For the signal process, the  $W$  boson originates from a spin-0 particle decay and their spins must therefore be antiparallel, implying that the charged leptons produced in their decays appear preferentially in the same hemisphere [20]. In contrast, there is no preferential spin direction in the background case. For this reason the azimuthal angle difference between the two leptons is on average smaller for signal than for background, resulting in a smaller dilepton invariant mass in the former case.

Other sub-dominant backgrounds arise from single top quark ( $tW$ , s-channel or t-channel), Drell-Yan,  $W+jets$ , di-boson and tri-boson processes.

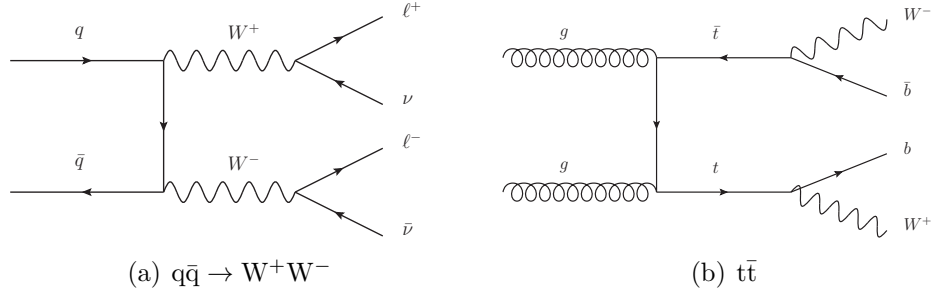


**Figure 1.4:** Feynman diagrams corresponding to the  $q\bar{q} \rightarrow W^+W^-$  (left) and  $t\bar{t}$  (right) processes. The  $t\bar{t}$  diagram represents just one of the possible ways to produce a pair of top quarks at hadron colliders.

### 1.4.3 Higgs boson kinematics

The Higgs boson production at hadron colliders is kinematically characterized by its transverse momentum,  $p_T^H$ , and pseudorapidity,  $\eta$ . The  $\eta$  distribution is essentially driven by the PDF of the partons in the colliding hadrons and it is only mildly sensitive to radiative corrections. The  $p_T^H$  distribution is instead sensitive to QCD radiative corrections. Considering the ggH production mode, at LO in perturbation theory,  $\mathcal{O}(\alpha_s^2)$ , the Higgs boson is always produced with  $p_T^H$  equal to zero. Indeed in order to have  $p_T$  different from zero, the Higgs boson has to recoil at least against one parton. Higher order corrections to the ggH process are numerically large and are known at NLO including full top quark mass dependence [21, 22], and at NNLO using the so-called large- $m_t$  approximation [23–25], in which the top quark mass is assumed to be very large and the fermionic loop is replaced by an effective vertex of interaction. Starting from the NLO, the Higgs boson can be produced recoiling against other final state partons, resulting in finite  $p_T^H$  values. For this reason the LO process for Higgs production at  $p_T \neq 0$  is at  $\mathcal{O}(\alpha_s^3)$ , and the counting of perturbative orders differs between inclusive Higgs boson production and  $p_T^H$  distribution. Also, NNLO QCD corrections in the  $p_T^H$  observable have recently been shown [26].

When  $p_T^H \sim m_H$  the QCD radiative corrections to  $p_T^H$  differential cross section are theoretically evaluated using fixed-order calculations. When  $p_T^H \ll m_H$  the perturbative expansion does not converge due to the presence of large logarithmic terms of the form  $\alpha_s^n \ln^{2n} m_H^2/p_T^2$ , leading to a divergence of  $d\sigma/dp_T$  in the limit of  $p_T \rightarrow 0$ . For computing the  $p_T^H$  spectrum in this region, soft-gluon resummation techniques are used [27, 28], and matched to the fixed-order calculation in the  $p_T^H \sim m_H$  region. For the  $p_T^H$  differential cross section the large- $m_t$  calculation is a crude approximation, since it is known that the top quark mass has a non-negligible effect on the shape of the spectrum. Moreover the inclusion of the bottom quark contribution in the fermionic loop can significantly modify the  $p_T^H$  shape [29], as shown in Fig. 1.5. Hence, a precise experimental measurement of the  $p_T^H$  spectrum is important to test the existing SM calculations.

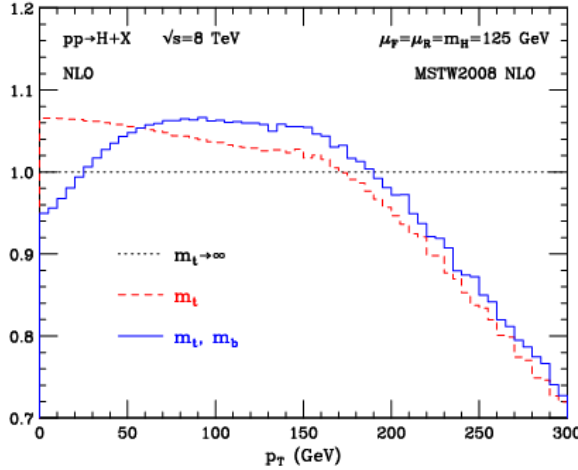


**Figure 1.5:** Distribution of  $p_T^H$  computed at NLO ( $\alpha_s^4$ ) and divided by the calculation obtained in the large- $m_t$  approximation. The red dashed line corresponds to the calculation including the top quark mass while the blue line refers to the calculation including also the bottom quark effects.

Possible extensions of the SM predict a modification of the Higgs boson couplings to gluons and top quarks. Many of these models actually predict the existence of new states that interact with the SM Higgs boson but are beyond the direct production reach at the actual LHC energies. The effect of these new states could however show up as a deviation of the Higgs boson couplings with respect to the SM expectation. The modification of the couplings, as shown in Refs. [30, 31], can change the kinematics of the Higgs boson production and the effect can be particularly sizeable in the tail of the  $p_T^H$  distribution. Other models, such as Composite Higgs [32], predict the existence of top-partners, which are heavy resonances with the same quantum numbers as the top quark, that can interact with the Higgs boson in the ggH fermionic loop, changing the  $p_T^H$  shape with respect to what the SM predicts [33]. The measurement of the  $p_T^H$  spectrum is thus a useful tool for indirect searches of new particles predicted by theories beyond the SM.

#### 1.4.4 Event generators for Higgs boson production

The structure of events produced at high energy colliders is extremely complex, and complex numeric simulations are necessary to effectively simulate realistic events. Monte Carlo (MC) event generators are programs that subdivide the problem of producing realistic events into a sequence of tasks that can be handled separately with the help of both analytic and numeric computations.

The production of hadron-hadron collision events is the result of the following chain of calculations:

- the first step consists in the calculation of cross section for the selected process, considering partons extracted from the incoming hadrons as free particles;

- the event production starts with two colliding hadrons with given momenta. One parton out of each hadron is selected to enter the scattering process of interest. This step is often referred to as *hard scattering* generation. Final state partons and leptons are produced according to the calculated differential cross sections;
- resonances produced in the hard event are decayed;
- when two partons take part in the hard event, accelerated colour charges are present, thus bremsstrahlung can occur. This effect is called initial state radiation (ISR) and is simulated with the so called *Initial State Parton Showers* algorithm, using the knowledge of the PDFs;
- also the final state partons can produce further radiation, called final state radiation (FSR), which is simulated by the *Final State Parton Showers* algorithms;
- in addition to the partons taking part in the hard interaction, several other parton pairs can interact during a hadron-hadron collision, giving rise to interactions with smaller transferred momentum. These *multiple parton interactions* (MPI) contribute to the so called *underlying event* (UE). Such interactions need to be well simulated to produce realistic events;
- leftovers of the interacting hadrons need to be simulated to balance the colour charge and four-momentum conservation. The beam remnant handling is thus another step in the event generation;
- the partons produced in the final state after the hard scattering are not observed as free particles but are subjected to the hadronization process, that cannot be described with perturbative QCD and is simulated using empirical models;
- finally, the event generator takes care of decaying  $\tau$  leptons and B hadrons. Particles with very short lifetime are generally decayed by the generator itself, while those with longer lifetimes are left undecayed.

The calculation of the hard process cross section is performed using the Matrix Element (ME) method, which is available for a variety of processes and consists on the exact matrix element calculation of the Feynman diagram of the process of interest. This approach is performed using perturbative QCD calculations and provide an analytically exact solution. Tree-level cross sections can be calculated including up to several partons in the final state. Loop calculations are instead more complex and are available only for a limited set of processes.

The ME method presents two complications: the first one arises from the presence in the calculation of partons with low transverse momentum (*soft divergence*) and the second to situations in which the emitted parton is collinear to the radiating parton (*collinear divergence*). Both these cases lead to divergences that spoil the perturbative

calculation. The virtual corrections would cancel these divergences but, since at tree-level they are not included, the phase space has to be carefully tailored to avoid the problematic regions. This means that the matrix element cross section calculations are performed away from soft and collinear divergences. Therefore, in order to produce realistic events, the phase space regions omitted in the ME calculation need to be handled using a different method, the Parton Shower calculation.

Parton Shower (PS) algorithms offer an alternative way both to handle the complexity of several successive branchings and to remove soft and collinear divergences. The parton showers are described by the algorithm as a sequence of elementary events  $a \rightarrow bc$ , where each event can happen with a certain probability driven by the structure of perturbative QCD. The introduction of a threshold value and the application of an angular sorting procedure in the emission of partons allows to eliminate soft and collinear divergences typical of the ME method. The parton cascade is evolved down to a certain virtuality, of the order of 1 GeV. After that, non perturbative effects take place and the hadronization is applied. Since the parton shower machinery relies on a collinear approximation of the matrix element, it is supposed to perform well in the description of the evolution of jets, but not to provide a precise description of configurations with well separated partons.

The two aforementioned techniques are therefore complementary and their combined application in the intermediate cases allows to exploit the characteristics of the two algorithms in the respective limits of validity. Several prescriptions exist to combine together the ME and PS calculations avoiding double-counting or holes in the phase space [34].

In this work the POWHEG [35–39] and MADGRAPH (and its evolution MADGRAPH5\_AMC@NLO) generators [40] are mostly used for the ME calculation, interfaced to PYTHIA [41, 42] for the PS and hadronization.

POWHEG is a ME event generator that performs calculations with NLO QCD accuracy and provides an easy prescription for the interface to PS programs. It can be used to generate events corresponding to a large number of predefined processes. It is used for the simulation of the majority of the processes involving Higgs boson production, as ggH and VBF. The JHUGEN [43] generator, which is capable to take into account all spin correlations, is usually employed together with POWHEG to simulate the Higgs boson decay to whatever final state is desired. In the analyses described in Chapter 4 two versions of this generator are used for simulating events produced via the ggH mechanism: POWHEG V1 and the more recent POWHEG V2, which takes into account the finite mass of the bottom and top quarks in the ggH loop.

MADGRAPH5\_AMC@NLO is a software that allows to generate amplitudes and events for any user defined process (with up to 9 external particles) with LO or NLO QCD accuracy.

PYTHIA is a general purpose generator. It contains a large subprocess library covering SM and BSM physics. It can be used standalone as a ME generator to perform cross section calculation and generate events at LO QCD accuracy, or interfaced to

a ME generator like POWHEG or MADGRAPH5\_AMC@NLO as a PS and for the simulation of the hadronization process.

## 1.5 Experimental Higgs boson highlights

The discovery of the new boson has been followed by a comprehensive set of measurements aimed at establishing the properties of the particle. Latest results reported by both the ATLAS and CMS experiments are consistent with the SM expectations for the Higgs boson. The properties that have been measured are, mainly:

- the signal strength modifier  $\mu = \sigma/\sigma_{\text{SM}}$ , where  $\sigma$  is the observed production cross section and  $\sigma_{\text{SM}}$  is the value predicted by the SM for a given mass hypothesis;
- the couplings to bosons and fermions;
- the spin and parity;
- the total decay width of the resonance.

Moreover, the combination of the results of the two experiments has recently been performed concerning the mass of the new boson, which is found to be  $m_H = 125.09 \pm 0.21 \text{ (stat.)} \pm 0.11 \text{ (syst.)} \text{ GeV}$  [44].

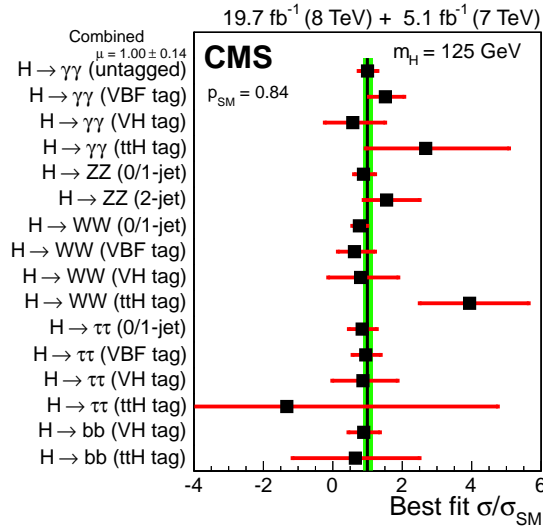


**Figure 1.6:** Values of the best-fit  $\mu$  for the overall combined analysis (solid vertical line) and separate combinations grouped by production mode tag and decay channel. The vertical band represents the total uncertainty on the combination while the horizontal red bars correspond to uncertainties on the individual channels.

The CMS experiment has investigated the Higgs boson decays to ZZ, WW,  $\gamma\gamma$ ,  $\tau\tau$  and  $b\bar{b}$  using 2011 and 2012 data, and is now looking at the same channels using

new data collected at a centre-of-mass energy of 13 TeV. The 8 TeV CMS results of all the channels have been combined and the best-fit signal strength corresponding to the measured mass is found to be  $\mu = 1.00 \pm 0.09 \text{ (stat.)}^{+0.08}_{-0.07} \text{ (theo.)} \pm 0.07 \text{ (syst.)}$  [45], in good agreement with the SM expectation  $\mu = 1$ . The signal strengths modifiers obtained in different sub-combinations of channels for  $m_H = 125 \text{ GeV}$  are shown in Fig. 1.6, grouped by production mode tag and decay channel.

The combination of all measurements in all decay channels is used to extract ratios between the observed coupling strengths and those predicted by the SM. The formalism used to test for deviations from the SM expectations has been established by the LHC Higgs Cross Section Working Group in Ref. [46]. This formalism makes some assumptions, in particular that the observed state has  $J^P = 0^+$  and that the narrow width approximation holds, leading to a factorization of the coupling strengths for production and decay modes. As an example, Higgs boson events produced via ggH and decaying to WW, i.e.  $gg \rightarrow H \rightarrow WW$ , can be used to measure the Higgs boson coupling to W bosons and fermions (mainly top quarks that are present in the gluon fusion loop). The combination of ATLAS and CMS results using data collected at 7 and 8 TeV is used to test the Higgs boson coupling to fermions  $k_F$  and bosons  $k_V$  [47]. The contours at 68% CL in the  $(k_F^f, k_V^f)$  plane (where the  $f$  refers to the generic decay channel  $H \rightarrow f$ ) for the combination of ATLAS and CMS results and for the individual channels are shown in Fig. 1.7.

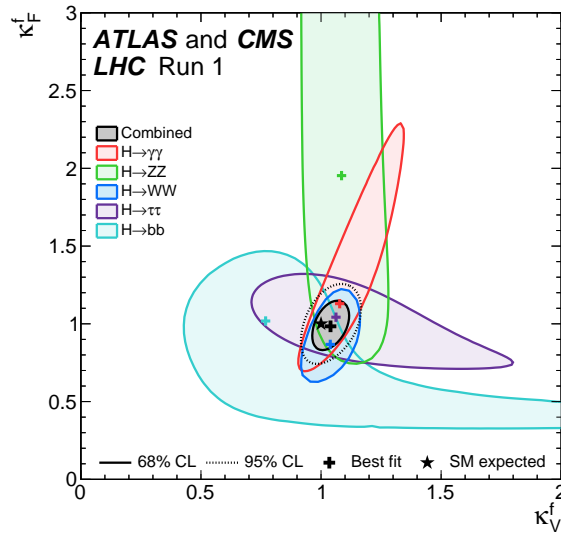


**Figure 1.7:** Contours at 68% CL in the  $(k_F^f, k_V^f)$  plane for the combination of ATLAS and CMS results and for the individual channels.

The combined result is in agreement with the SM expectation and the final confidence interval is driven by the  $H \rightarrow WW$  channel, which provides the most precise determination of  $k_F^f$  and  $k_V^f$  because it is the only channel that provides significant constraints on both parameters through the measurements of the ggH and VBF pro-

duction processes.

About the spin and parity properties, the results of the  $H \rightarrow \gamma\gamma$ ,  $H \rightarrow ZZ \rightarrow 4\ell$  and  $H \rightarrow WW \rightarrow 2\ell 2\nu$  channels confirmed the hypothesis of a scalar boson ( $J^P = 0^+$ ), excluding the other hypotheses with a confidence level of 99% or higher.

The Higgs boson total decay width ( $\Gamma_H$ ) is predicted by the SM as a function of its mass, as shown in Fig. 1.8. At  $m_H = 125$  GeV the Higgs boson is predicted to be a narrow resonance, with a total decay width of the order of 4.1 MeV. Direct measurements of the decay width have been performed in the  $H \rightarrow ZZ \rightarrow 4\ell$  and  $H \rightarrow \gamma\gamma$  channels, but the results are limited by the experimental resolution, which is about three orders of magnitude larger than the expected value, thus not allowing to provide significant constraints. The sizeable off-shell production of the Higgs boson can also be used to constrain its natural width. In fact, a measurement of the relative off-shell and on-shell production provides direct information on  $\Gamma_H$  [48], under the assumption that the Higgs boson off- and on-shell production mechanisms are the same as in the SM and the ratio of couplings governing the two remains unchanged with respect to the SM predictions. Using this technique and combining the CMS results of the  $H \rightarrow ZZ \rightarrow 4\ell$  and  $H \rightarrow WW \rightarrow 2\ell 2\nu$  channels, the upper limit at 95% CL on the Higgs boson total decay width is found to be  $\Gamma_H^{\text{obs}} < 13$  MeV [49], which represents a far better constraint with respect to direct measurements.

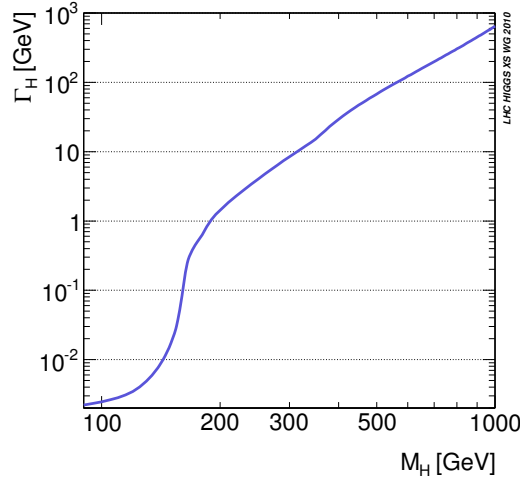


**Figure 1.8:** Total decay width of the SM Higgs boson as a function of  $m_H$ .

Differential cross section measurements have also been performed by both experiments in the bosonic channels,  $\gamma\gamma$ ,  $ZZ$  and  $W^+W^-$  (the latter is presented in Chapter 4 of this work), showing agreement with the SM-based theoretical predictions.



# Chapter 2

## LHC and the CMS experiment

In this chapter, the main characteristics of the Large Hadron Collider (LHC) particle accelerator and Compact Muon Solenoid (CMS) experiment are described.

### 2.1 The Large Hadron Collider

The LHC [50–53] at CERN, officially inaugurated on 21<sup>st</sup> October 2008, is the largest and most powerful hadron collider ever built. Installed in the underground tunnel which hosted the Large Electron Positron Collider (LEP) [54–56], the leptonic accelerator in operation until 2<sup>nd</sup> November 2000, the LHC accelerator has a circular shape with a length of about 27 km and is located underground at a depth varying between 50 m to 175 m, straddling the Franco-Swiss border near Geneva. It is designed to collide two 7 TeV counter-circulating beams of protons resulting in a centre-of-mass energy of 14 TeV, or two beams of heavy ions, in particular lead nuclei at an energy of 2.76 TeV/nucleon in the centre-of-mass frame.

The transition from a leptonic collider to a hadronic collider entailed the following advantages: first, it was possible to build a machine that having the same size of the previous one (and therefore accommodated in the same LEP tunnel, substantially reducing the cost and time of construction), could reach a higher energy in the centre-of-mass frame. This is due to the much lower amount of energy loss through synchrotron radiation emitted by the accelerated particles, that is proportional to the fourth power of the ratio  $E/m$  between their energy and their mass. Secondly, the composite structure of protons compared to the elementary structure of electrons allows LHC to be able to access a wider energy spectrum, despite the production of many low energies particles in a complex environment. This is a particularly important feature for a machine dedicated to the discovery of “new” physics.

In Fig. 2.1 a schematic description of the accelerator complex installed at CERN is shown. The acceleration is performed in several stages [53]. The protons source is a *Duoplasmatron*: the protons are obtained by removing electrons from a source of hydrogen gas and then sent to the LINAC2, a 36 m long linear accelerator which generates a pulsed beam with an energy of 50 MeV using Radio Frequency Quadrupoles

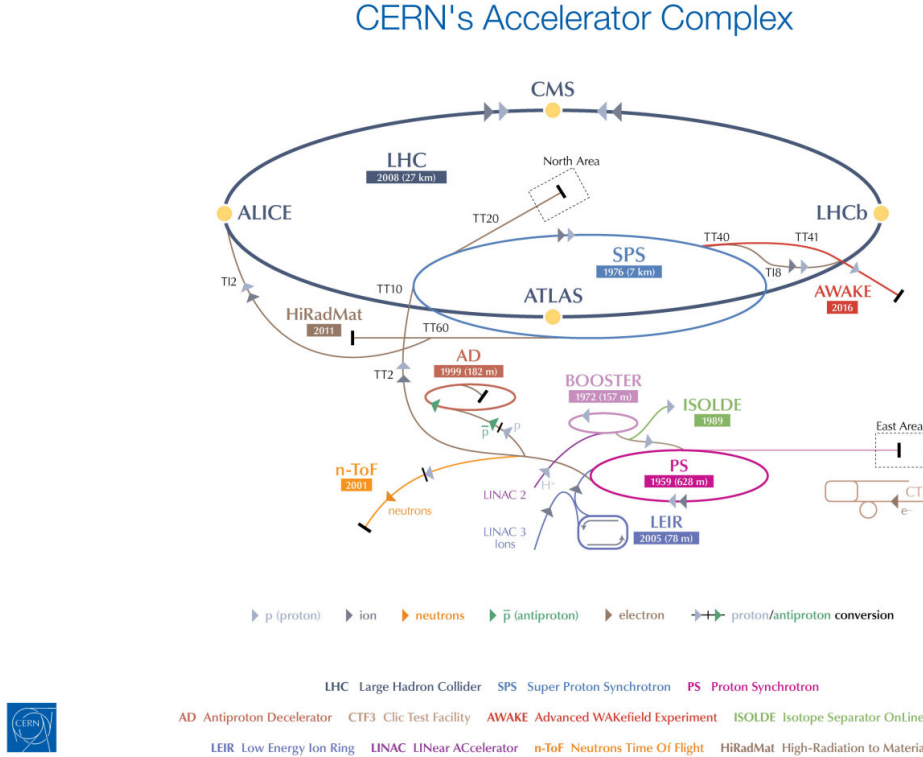


**Figure 2.1:** Schematic description of the accelerator complex installed at CERN.

(RFQ) and focusing quadrupole magnets. The beam is subsequently sent to the Proton Synchrotron Booster (PSB), a circular accelerator consisting of four superimposed synchrotron rings with a circumference of about 160 m, which increases the proton energy up to 1.4 GeV. Then, protons are injected into the Proton Synchrotron (PS), a single synchrotron ring with a circumference of about 600 m where the energy is increased to 25 GeV. The sequential combination of these two synchrotrons also allows to create a series of protons bunches interspersed by 25 ns as required for the correct operation of LHC. The final proton injection stage is the Super Proton Synchrotron (SPS), a synchrotron with a circumference of approximately 7 km where protons reach an energy of 450 GeV. Subsequently, protons are extracted and injected into the LHC ring via two transmission lines, to generate two beams running in opposite directions in two parallel pipes which are accelerated up to the energy of interest. In the two pipes an ultrahigh vacuum condition is maintained (about  $10^{-10}$  Torr) to avoid the spurious proton interactions with the gas remnants. At full intensity, each proton beam consists of 2808 bunches and each bunch contains around  $10^{11}$  protons. The beams are squeezed and collide for a length of about 130 m at four interaction points where the four main experiments (ALICE, ATLAS, CMS and LHCb) are placed:

- CMS (Compact Muon Solenoid) [57] and ATLAS (A Toroidal LHC Appar-

tuS) [58] are two general-purpose detectors designed to investigate the largest possible spectrum of physics. In particular, they have been devoted to the detection of particles produced by a Higgs boson decay and to look for any possible evidence of new physics. The use of two detectors chasing the same objectives but designed independently is crucial for a cross-check of any possible new discovery;

- LHCb (LHC beauty) [59] is an experiment primarily designed to study CP (combined Charge conjugation and Parity symmetry) violation in electroweak interactions and to study asymmetries between matter and antimatter through the analysis of rare decays of hadrons containing b quarks. The detector is also able to perform measurements in the forward region, at small polar angles with respect to the beam line;
- ALICE (A Large Ion Collider Experiment) [60] is an experiment studying heavy ions collisions, through the production of a new state of matter called quark-gluon plasma.

Two other smaller experiments are located along the circumference of the LHC accelerator, TOTEM and LHCf, which focus on particles emitted in the forward direction. TOTEM (TOTal Elastic and diffractive cross section Measurement) [61] measures the proton-proton interaction cross section and accurately monitors the luminosity of the LHC using detectors positioned at each side of the CMS interaction point. LHCf (LHC forward) [62] is made up of two detectors which sit along the LHC beamline, at a distance of 140 m from each side of the ATLAS collision point. It makes use of neutral particles thrown in the forward direction by LHC collisions as a source to simulate the interaction of very high energy cosmic rays (between  $10^{17}$  TeV and  $10^{20}$  TeV) with the atmosphere in laboratory conditions.

A series of about 1200 magnetic dipoles bend the beams along the accelerator ring. They are located along the “arc” structures of the circumference. The ring, in fact, can be subdivided into octants, with eight curve regions (the “arcs”) separated by rectilinear regions. In these straight regions, instead, almost 400 focusing and defocusing quadrupoles are located, which maintain the beam stable along the orbit, and some other small multipolar magnets (sextupoles and octupoles) are used to make additional minor corrections to the beam direction. A radio frequency acceleration system, consisting of 16 superconducting radio-frequency resonant cavities, is used to increase the proton energy by 0.5 MeV with each beam revolution. The 7 TeV per-beam-energy limit on the LHC is not determined by the electric field generated by the radiofrequency cavity but by the magnetic field necessary to maintain the protons in orbit, given the current technology for the superconducting magnets, which is about 5.4 T on average.

One of the most important parameters of an accelerator is the instantaneous luminosity  $\mathcal{L}$ , which provides a measure of the rate of events one can expect given the process cross section. In fact, for a given physics process with cross section  $\sigma$ , produc-

ing  $N$  events for unit of time, the instantaneous luminosity is defined by the following equation:

$$N = \sigma \mathcal{L} \quad . \quad (2.1)$$

The LHC design luminosity is  $\mathcal{L} = 10^{34} \text{cm}^{-2}\text{s}^{-1}$ , leading to around 1 billion proton interactions per second.

The instantaneous luminosity is a parameter which depends on the construction characteristics of the accelerator, and can be expressed by the following approximated formula:

$$\mathcal{L} = f \frac{n_1 n_2}{4\pi \sigma_x \sigma_y} \quad , \quad (2.2)$$

where  $n_1$  and  $n_2$  are the number of particles contained in the two bunches colliding at a frequency  $f$ , and  $\sigma_x$  and  $\sigma_y$  are the beam sizes in the transverse plane. At LHC, the bunches collide with  $f = 40 \text{ MHz}$  and the transverse size of the beam can be squeezed down to around  $15 \mu\text{m}$ . The integrated luminosity  $L$  is defined as the time integral of the instantaneous luminosity:

$$L = \int \mathcal{L} dt \quad . \quad (2.3)$$

The main parameters of the LHC machine are listed in Table 2.1.

The LHC started to be operative in September 2008 but, due to a faulty interconnection between two magnets which caused a helium leakage in the tunnel, the operation was stopped and restarted in March 2010. During 2010 and 2011 LHC ran successfully and provided proton-proton collisions at a centre-of-mass energy of  $7 \text{ TeV}$ , delivering a total integrated luminosity of about  $6.1 \text{ fb}^{-1}$ . The encouraging results in the Higgs boson search provided by the ATLAS and CMS Collaborations led to the decision of extending the data taking period to the end of 2012, and to increase the centre-of-mass energy up to  $8 \text{ TeV}$ . During 2012, LHC delivered to the experiments an integrated luminosity of  $23.3 \text{ fb}^{-1}$ . After the first long shutdown (LS1), a two years period started in the early 2013 where the LHC operation stopped for maintenance and upgrade, the LHC started again delivering proton-proton collisions on 3<sup>rd</sup> June 2015, at the new record centre-of-mass energy of  $13 \text{ TeV}$ . During the 2015 the LHC delivered an integrated luminosity of  $4.2 \text{ fb}^{-1}$ . Nowadays, LHC is still colliding bunches of protons at  $\sqrt{s} = 13 \text{ TeV}$ , reaching unprecedented instantaneous luminosities and delivering a total integrated luminosity of  $41.1 \text{ fb}^{-1}$ . The cumulative delivered luminosity versus time for the different LHC data taking periods is shown in Fig. 2.2.

As the instantaneous luminosity increases, the probability of multiple proton-proton interactions to occur in a single bunch crossing grows higher as well. In this instance, the main goal is the identification and reconstruction of a single primary collision where the physics event of interest occurs among the background of the additional proton-proton interactions. Such backgrounds are due to processes occurring with very high probability, like the production of low- $p_T$  jets. These additional collisions are known as pile-up. During the LHC current run the average number of

**Table 2.1:** LHC technical parameters for proton-proton collisions.

Parameter	Value
Maximum dipole magnetic field	8.33 T
Dipole operating temperature	1.9 K
Beam energy at injection	450 GeV
Beam energy at collision (nominal)	7 TeV
Beam energy at collision (2012)	4 TeV
Beam energy at collision (2015–2016)	6.5 TeV
Maximum instantaneous luminosity (nominal)	$10^{34} \text{ cm}^{-2}\text{s}^{-1}$
Maximum instantaneous luminosity (2012)	$7.7 \cdot 10^{33} \text{ cm}^{-2}\text{s}^{-1}$
Maximum instantaneous luminosity (2015–2016)	$1.2 \cdot 10^{34} \text{ cm}^{-2}\text{s}^{-1}$
Number of bunches per proton beam (nominal)	2808
Number of bunches per proton beam (2012)	1380
Number of bunches per proton beam (2015–2016)	2220
Maximum number of protons per bunch	$1.69 \cdot 10^{11}$
Bunch collision frequency (nominal)	40 MHz
Bunch collision frequency (2012)	20 MHz
Bunch collision frequency (2015–2016)	40 MHz
Energy loss per turn at 14 TeV	7 keV

pile-up events is 23, with some events exhibiting over 45 pile-up collisions. Two different types of pile-up may be identified: the *in-time* pile-up, in which the additional collisions occur in the same bunch-crossing as the collision of interest and *out-of-time* pile-up, in which the additional proton-proton collisions occur in the bunch-crossings just before or after the one containing the collision of interest.

## 2.2 The *Compact Muon Solenoid* experiment

The CMS apparatus is a general purpose detector situated in one of the four LHC interaction points<sup>1</sup>. The detector is designed to investigate a wide range of physics, from the search of the Higgs boson, to SM measurements and BSM physics searches. To achieve this goal, the detector is able to identify and reconstruct all the physics objects that may be produced in the proton-proton collisions: electrons, muons, photons and jets. The main feature of the CMS detector is a superconducting solenoidal

---

<sup>1</sup>The CMS detector is placed in a cavern 100 m underground in the area called Point 5, near the village of Cessy, in France.

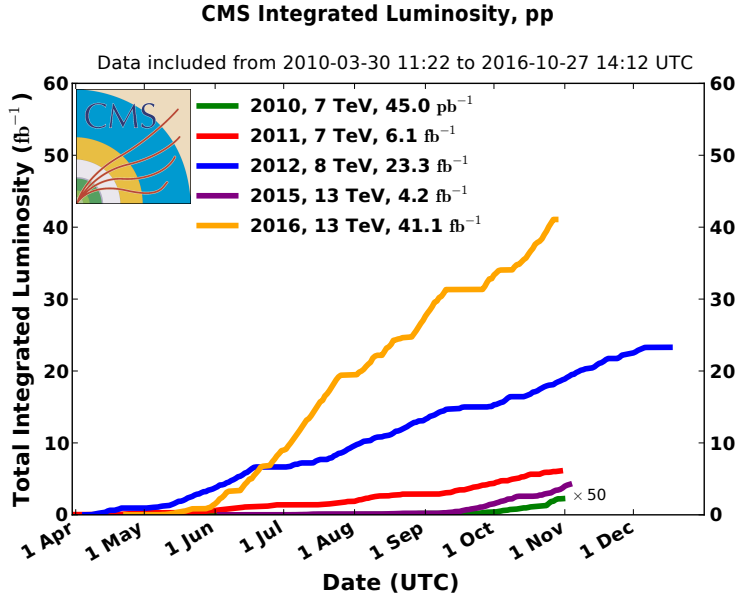


**Figure 2.2:** Cumulative luminosity versus day delivered to CMS during proton-proton collisions.

magnet which is capable to produce a 3.8 T magnetic field. Such a strong magnetic field is the key aspect which permits to have a compact design of the detector. The detector has a cylindrical structure, typical of general purpose detectors, which consists of several cylindrical detecting layers, coaxial with the beam direction (*barrel* region), closed at both ends with detecting disks (*endcap* region), in such a way to ensure the hermetic closure of the apparatus.

The coordinate system used by CMS is a right-handed Cartesian system, with the origin at the centre of the detector, in the nominal beam collision point. The  $x$  axis is chosen to point radially towards the centre of the LHC circumference and the  $y$  axis is directed upwards along the vertical. The  $z$  axis is oriented along the beam direction, according to the anticlockwise direction of the LHC ring if seen from above. The CMS cylindrical symmetry and the Lorentz invariant description of the proton-proton collisions, suggest the use of a pseudo-angular reference frame, described by the triplet of coordinates  $(r, \phi, \eta)$ , where  $r$  is the distance from the  $z$  axis,  $\phi$  is the azimuthal angle, measured starting from the  $x$  axis positive direction, and  $\eta$  is the pseudorapidity, defined in Sec. 1.3.1.

The schematic view of the CMS detector, which has a length of 21.5 m, a diameter of 15 m and a weight of about 14000 tons, is shown in Fig. 2.3. From the inner region to the outer one, the various CMS sub-detectors are:

- **Silicon tracker:** it occupies the region  $r < 1.2$  m and  $|\eta| < 2.5$ . It is composed of an inner silicon pixel vertex detector and a surrounding silicon microstrip detector, with a total active area of about  $215\text{ m}^2$ . It is used to reconstruct charged particle tracks and vertices;

- **Electromagnetic calorimeter (ECAL)**: placed in the region  $1.2 \text{ m} < r < 1.8 \text{ m}$  and  $|\eta| < 3$ , it consists of many scintillating crystals of lead tungstate ( $\text{PbWO}_4$ ). It is used for the measurement of the trajectory and the energy released by electrons and photons;
- **Hadronic calorimeter (HCAL)**: it is placed in the region  $1.8 \text{ m} < r < 2.9 \text{ m}$  and  $|\eta| < 5$ . It is made up of brass layers alternated with plastic scintillators and it is used to measure the direction and energy deposited by the hadrons produced in the interactions;
- **Superconducting solenoidal magnet**: it occupies the region  $2.9 \text{ m} < r < 3.8 \text{ m}$  and  $|\eta| < 1.5$  and generates an internal uniform magnetic field with an intensity of  $3.8 \text{ T}$ , pointing along the direction of the beams. The magnetic field is necessary to bend the trajectories of charged particles, in order to allow the measurement of their momentum through the curvature observed in the tracking system. The magnetic field lines are closed by an external  $21 \text{ m}$  long iron yoke, that has a diameter of  $14 \text{ m}$ . Outside the return yoke, a residual  $1.8 \text{ T}$  magnetic field is present, pointing at the opposite direction with respect to the internal field;
- **Muon system**: the outermost system, which is placed in the region  $4 \text{ m} < r < 7.4 \text{ m}$  and  $|\eta| < 2.4$ , has the purpose of reconstructing the tracks of muons passing through it. It consists of Drift Tubes (DT) in the barrel region and Cathode Strip Chambers (CSC) in the endcaps. A complementary system of Resistive Plate Chambers (RPC) is used both in the barrel and endcaps. The muon chambers are housed inside the iron structure of the return yoke.

In Fig. 2.4 the response of the various CMS sub-detectors to the passage of different types of particles is sketched. In the following sections a brief description of each sub-detector is given.

### 2.2.1 The solenoid

The CMS magnet [63], which contains the tracker, the electromagnetic and the hadronic calorimeters, is the biggest superconducting solenoid ever built. The solenoid can generate a magnetic field of  $3.8 \text{ T}$  in the internal bore, which has a diameter of  $6 \text{ m}$  and a length of  $12.5 \text{ m}$ . The energy stored in the magnet is about  $2.7 \text{ GJ}$  at full current. The superconductor is made of four Niobium-Titanium layers and it is cooled down to about  $4 \text{ K}$  through a liquid Helium cooling plant. In case of a quench, when the magnet loses its superconducting property, the energy is dumped to resistors within  $200 \text{ ms}$ . The magnet return yoke of the barrel is composed of three sections along the  $z$  axis; each one is split into 4 layers (holding the muon chambers in the gaps). Most of the iron volume is saturated or nearly saturated, and the field in the yoke is about half ( $1.8 \text{ T}$ ) of the field in the central volume.

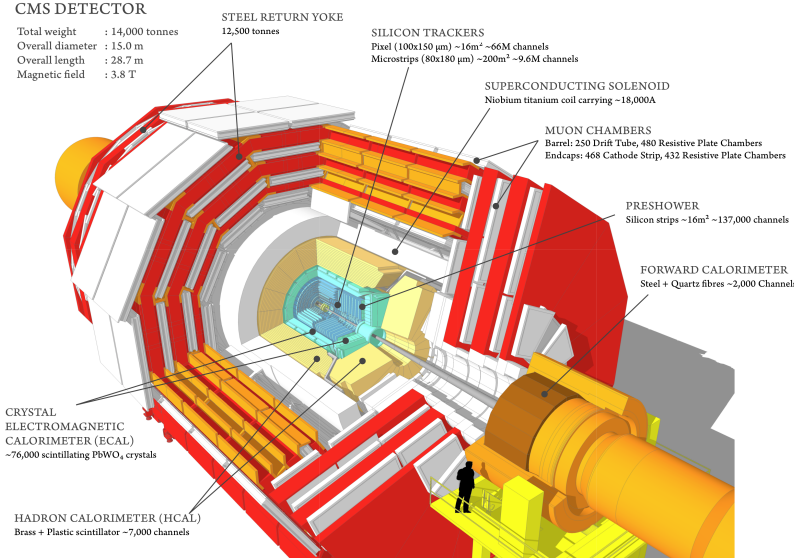


**Figure 2.3:** Schematic view of the CMS detector showing its sub-detectors.

### 2.2.2 The tracker

The silicon tracker is the detector closest to the beam collision point. Its goal is the high resolution reconstruction of the trajectories of charged particles originating from the interaction point and the identification of the position of secondary vertices produced by particles with a short mean life time (in particular hadrons containing the b quark, that decay after few hundred of  $\mu\text{m}$ ). The events produced in the proton-proton collisions can be very complex and track reconstruction is an involved pattern recognition problem. Indeed, at the nominal instantaneous luminosity of operation, an average of about 20 pile-up events overlapping to the event of interest are expected, leading to about 1000 tracks to be reconstructed every 25 ns. In order to make the pattern recognition easier, two requirements are fundamental:

- a low occupancy detector;
- a large redundancy of the measured points (*hits*) per track.

The first requirement is achieved building a detector with high granularity<sup>2</sup>. The redundancy of the hits is instead achieved having several detecting layers, and is necessary to reduce the ambiguity on the assignment of the hits to a given track. Nevertheless, the amount of tracker material has to be as low as possible, in order to avoid compromising the measurement of the particle trajectory. An excessive amount of material would indeed deteriorate the measurement, mainly because of the increased probability of particle multiple scattering. The outer detectors such as ECAL would

<sup>2</sup>The granularity of a detector is defined as the angular range ( $\Delta\eta \times \Delta\phi$ ) that each individual element is able to resolve.

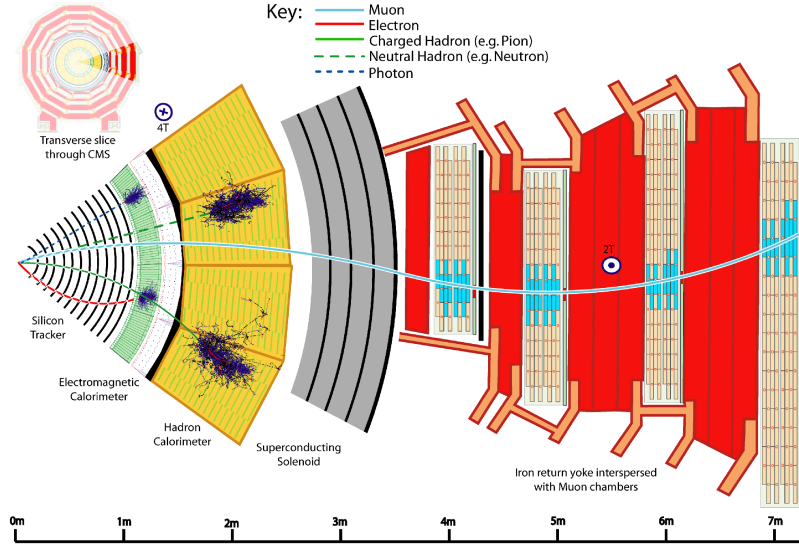


**Figure 2.4:** Schematic view of a slice of the CMS detector, showing the sub-detectors response to the passage of different types of particles.

be influenced by the material as well, for example because of the increased probability for a photon to convert to an electron-positron pair in the tracker material. For this reasons, the tracker layers are limited in number and thickness.

The tracker comprises a large silicon strip detector with a small silicon pixel detector inside it. In the central  $\eta$  region, the pixel tracker consists of three co-axial barrel layers at radii between 4.4 cm and 10.2 cm and the strip tracker consists of ten co-axial barrel layers extending outwards to a radius of 110 cm. Both sub-detectors are completed by endcaps on either side of the barrel, each consisting of two disks in the pixel tracker, and three small plus nine large disks in the strip tracker. The endcaps extend the acceptance of the tracker up to  $|\eta| < 2.5$ . A three-dimensional schematic view of the tracker is shown in Fig. 2.5, while in Fig. 2.6 a pictorial representation of a slice of the tracker is displayed, showing the various layers of the sub-detectors.

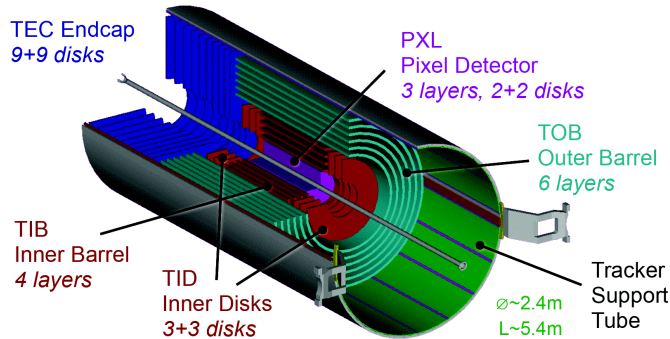


**Figure 2.5:** Three-dimensional schematic view of the CMS silicon tracker.

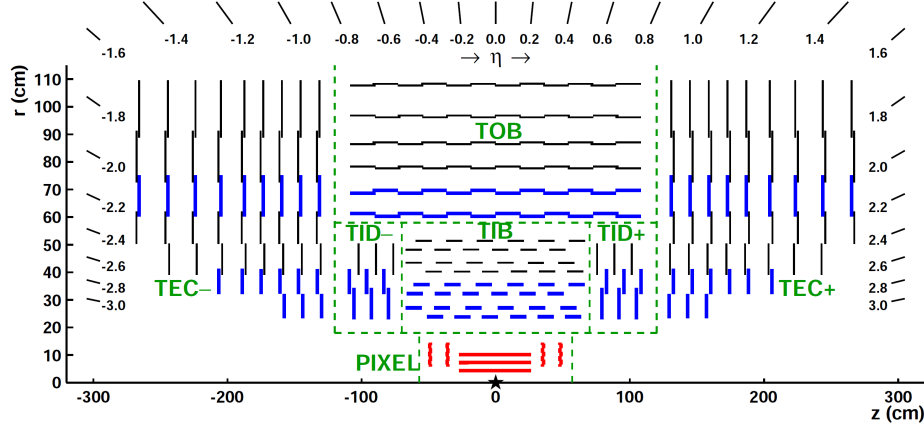


**Figure 2.6:** Pictorial view of a tracker slice in the  $r$ - $z$  plane. Pixel modules are shown in red, single-sided strip modules are depicted as black thin lines and strip stereo modules are shown as blue thick lines.

The whole tracker has a cylindrical shape with a length of 5.8 m and a diameter of 2.5 m, with the axis aligned to the beams direction. The average number of hits per track is 12-14, allowing high reconstruction efficiency and low rate of fake tracks.

The material budget of the tracker as obtained from a simulation of the detector is shown in Fig. 2.7, reported both in units of radiation length  $t/X_0$  and in units of nuclear interaction length  $t/\lambda_I$ , as a function of  $\eta$ . The region  $1 < |\eta| < 2$  exhibits a larger material budget due to the presence of cables and services.

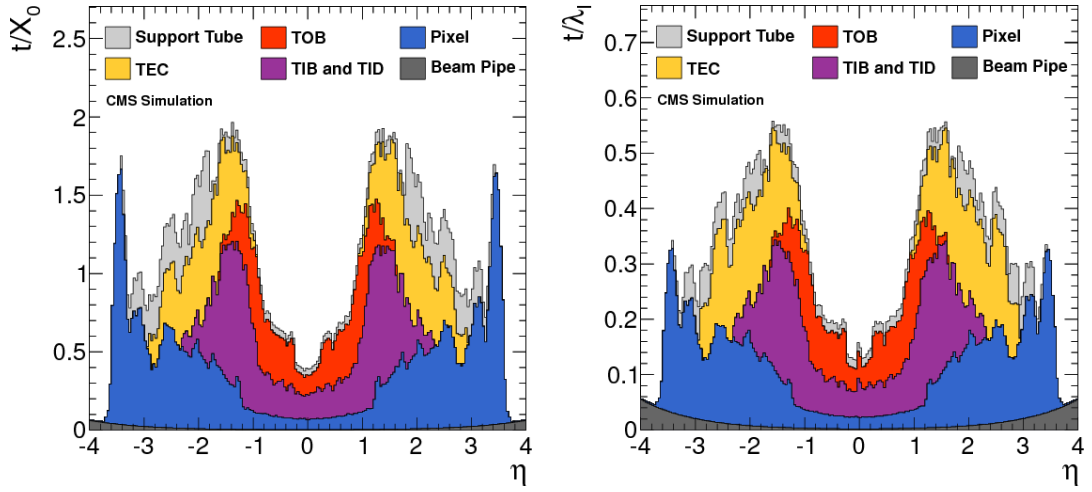


**Figure 2.7:** Total thickness  $t$  of the tracker material expressed in units of  $X_0$  (left) and  $\lambda_I$  (right), as a function of  $\eta$ . The contribution to the total material budget of each part of the detector is shown.

### The pixel detector

The pixel detector, shown in Fig. 2.8, is mainly used as starting point in the CMS track reconstruction and is of fundamental importance for the reconstruction of primary and secondary vertices. The pixel detector is placed in the closest position to the collision

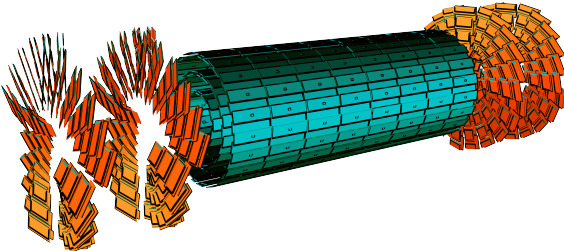


**Figure 2.8:** Schematic view of the CMS pixel detector.

point, where the amount of radiation is larger. It is placed in the region  $|\eta| < 2.5$  and consists of three cylindrical layers 53 cm long in the barrel region, located at  $r = 4.4, 7.3$  and  $10.2$  cm, and two pairs of endcap disks with radii between 6 and 15 cm at  $z = \pm 34.5$  and  $\pm 46.5$  cm, covering a total area of about  $1\text{ m}^2$ . The detector is composed of many modules, for a total of 768 in the barrel and 672 in the endcaps. Each endcap is composed of 24 segments, each one tilted with respect to the adjacent ones and containing 7 modules. Each module consists of several units which contain a highly segmented silicon sensor with a thickness of 250  $\mu\text{m}$ . In order to achieve an optimal vertex position resolution in both the  $(r, \phi)$  and  $z$  coordinates, a design with a rectangular pixel shape with an area of  $150 \times 100\text{ }\mu\text{m}^2$  was adopted, with the 100  $\mu\text{m}$  size oriented along the  $(r, \phi)$  direction in the barrel region, and along the  $z$  direction in the endcap region. The achievable hit reconstruction resolution is about 10–15  $\mu\text{m}$  in the barrel and 15  $\mu\text{m}$  in the endcaps.

### The microstrip detector

In this region of the detector the radiation flow is low enough to allow the use of a less segmented device, such as the silicon microstrip detector. The microstrip tracker is composed of 15148 silicon modules, covering a total area of about  $193\text{ m}^2$  with a total of 9.3 million strips. Two types of modules are installed: single sided modules consist of one sensor stucked onto a carbon fiber support together with the readout electronics, with the silicon strips laying along the  $z$  direction in the barrel and along the  $(r, \phi)$  direction in the endcaps. The other type of module, referred to as stereo-module, consists of two sensors stucked together back to back and tilted of a relative angle of 100 mrad. This combination allows a three-dimensional measurement of the particle interaction point, providing the information along the  $z$  direction. The whole microstrip tracker is 5.4 m long and extends up to  $r = 1.1$  m. As the pixel detector, the microstrip detector consists of a barrel and an endcap region and is divided into

four distinct parts, as shown in Fig. 2.6. The barrel is made up of the following parts:

- TIB (*Tracker Inner Barrel*): it consists of four cylindrical coaxial layers, covering the region up to  $|z| < 65$  cm. In this region the detectors have a thickness of 300  $\mu\text{m}$  and the strips are separated by a variable pitch between 80 and 120  $\mu\text{m}$ . The first two layers are composed of stereo modules while the other layers have single-sided modules. Since the strips are oriented along the  $z$  axis, the position resolution is more precise in the  $(r, \phi)$  direction, about 23–34  $\mu\text{m}$ , with respect to the  $z$  direction, where a resolution of about 230  $\mu\text{m}$  is obtained thanks to the stereo modules.
- TOB (*Tracker Outer Barrel*): it consists of six cylindrical coaxial layers, placed in the region  $55 \text{ cm} < r < 65 \text{ cm}$  and  $|z| < 110 \text{ cm}$ . Stereo modules are mounted on the two inner layers. Since the density of particles passing through this region is lower with respect to the TIB, the pitch between the strips is larger (120–180  $\mu\text{m}$ ) and the strips are longer (190 mm). The spatial resolution varies in the range 25–52  $\mu\text{m}$  in the  $(r, \phi)$  direction, and is about 530  $\mu\text{m}$  in the  $z$  coordinate for the stereo modules.

The endcaps are also made up of two parts:

- TID (*Tracker Inner Disk*): it consists of six disks, three per side, placed orthogonally with respect to the beam axis, between the TIB and the TOB. The modules are positioned in a ring shape, with the strips oriented in the radial direction, and are alternately placed on the internal and external side of the disk. The two innermost rings of the TID are equipped with stereo modules. The thickness of the silicon is 300  $\mu\text{m}$ .
- TEC (*Tracker EndCap*): each one of the two TEC is made of nine disks which extend to the region  $120 \text{ cm} < |z| < 280 \text{ cm}$ . Each disk is divided into 8 slices in each of which a number ranging from 4 to 7 modules are mounted in a ring shape, depending on the position along  $z$ . Also in this case the modules are alternately mounted on the internal and external side of the disk, with the strips radially oriented. On the two innermost rings and on the fifth one the stereo modules are installed to measure the  $z$  coordinate. The thickness of the sensors range between 300 and 500  $\mu\text{m}$  depending on the disk.

The tracker is operated at low temperature in order to reduce those radiation damage induced effects that have a temperature dependence, such as the increase of the leakage current and the long-term increase of the depletion voltage (also called reverse annealing)<sup>3</sup>.

---

<sup>3</sup>The tracker in Run 1 was operated at a temperature of +4°C, but during the Long Shutdown 1 a new cooling dry gas plant has been installed and the tracker is now operating at the lower temperature of -15°C.

The alignment of the tracker modules is very important to obtain a high spatial resolution. Deviations are caused by assembly inaccuracy, deformations due to cooling and stress from the magnetic field. Therefore, three methods are used for the tracker alignment. The geometry was determined during the assembly to an accuracy of 80 to 150  $\mu\text{m}$ . An infrared laser system is used for continuous monitoring of the position of selected tracker modules. The final alignment is done with tracks from well known physics processes, e.g. cosmic muons or muon pairs from the  $J/\Psi$ ,  $\Upsilon$  or  $Z$  decays.

### 2.2.3 The electromagnetic calorimeter (ECAL)

The main function of an electromagnetic calorimeter is to identify electrons and photons and to accurately measure their energy. The CMS electromagnetic calorimeter (ECAL) [64, 65], shown in Fig. 2.9, is a hermetic homogeneous calorimeter with cylindrical geometry, composed of many scintillating crystals of lead tungstate ( $\text{PbWO}_4$ ) with a truncated pyramidal shape. As the other detectors it consists of two parts, the ECAL barrel (EB), which contains 61200 crystals, and two endcaps (EE) containing 7324 crystals each one.

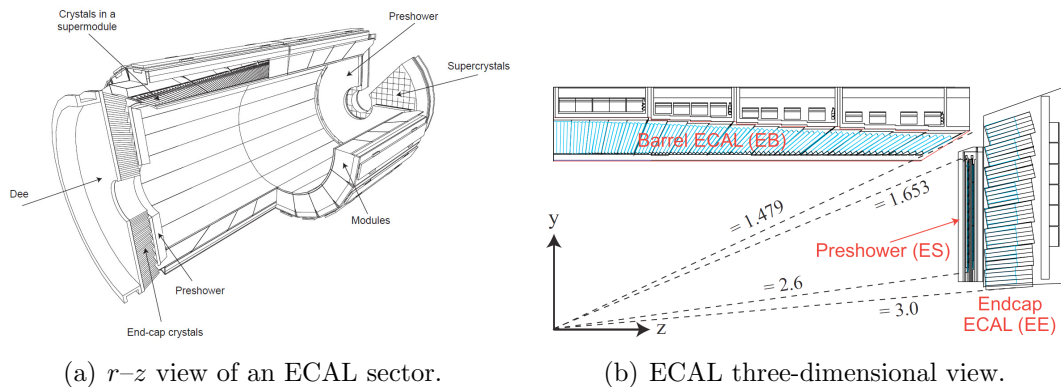


**Figure 2.9:** Schematic representation of the CMS electromagnetic calorimeter.

The characteristics of the  $\text{PbWO}_4$  crystals make them an appropriate choice for operation at LHC. The high density ( $\rho = 8.3 \text{ g/cm}^3$ ), short radiation length ( $X_0 = 0.89 \text{ cm}$ ) and small Molière radius<sup>4</sup> (2.2 cm) allow to build a compact and high granularity calorimeter. Another advantage of this material is the radiation hardness and the fast scintillation decay time ( $\tau = 10 \text{ ns}$ ), that permits to collect about 80% of the produced light within the 25 ns interval between two consecutive bunch crossings. The main drawbacks of this material are the low light yield ( $\sim 10 \text{ photoelectrons/MeV}$ ) and the strong dependence on the operating temperature, that makes it necessary to keep the crystals at a stabilized temperature (18°C).

<sup>4</sup>The Molière radius  $R_M$  characterizes the transverse development of an electromagnetic shower in a calorimeter. On average 90% of the energy deposited by a shower is contained inside a cylinder with radius  $R_M$ .

The crystals are grouped into  $5 \times 5$  matrices called *towers*. The barrel has an inner radius of 129 cm, a length of 630 cm and extends in the region  $|\eta| < 1.479$ . The crystals in the barrel have the following dimensions:  $22 \times 22 \text{ mm}^2$  at the front face,  $26 \times 26 \text{ cm}^2$  at the rear face, and a length of 23 cm, corresponding to  $25.8X_0$ , and are mounted in a quasi-projective geometry, in order to have the long side tilted by  $3^\circ$  with respect to the direction pointing to the interaction point, both in the  $\eta$  and  $\phi$  coordinates. This is done to avoid the empty spaces between adjacent crystals to be aligned with the direction pointing to the interaction point. The granularity of the EB is about  $1^\circ$ . Avalanche photodiodes (APDs) are used as photodetectors connected with the crystals in the barrel region.

Each endcap covers the region  $1.479 < |\eta| < 3$  and is formed by two semicircular aluminium halves called *dees*. Crystals in endcaps have a length of 22 cm, a frontal area equal to  $28.6 \times 28.6 \text{ mm}^2$  and a rear surface of  $30 \times 30 \text{ mm}^2$ . In the endcaps the crystals are arranged in a  $\eta$ - $\phi$  symmetry. The photodetectors used to collect the light produced in the endcap crystals are single stage vacuum phototriodes (VPTs), because this region experiences a rather high particle flux and VPTs are more robust against radiation damages with respect to APDs. A preshower system is installed in front of the ECAL endcaps in order to separate the showers produced by a primary  $\gamma$  from those produced by forward emitted  $\pi^0$ . This detector, which covers the region  $1.653 < |\eta| < 2.6$ , is a sampling calorimeter consisting of two lead disks ( $2X_0$  and  $1X_0$  thick respectively) that initiate the electromagnetic shower from incoming photons or electrons, with silicon strip sensors after each disk, which measure the deposited energy as well as the shower transverse profile.

The energy resolution of a homogeneous calorimeter can be expressed by the sum in quadrature of three terms, as shown in the following formula:

$$\left(\frac{\sigma_E}{E}\right)^2 = \left(\frac{a}{\sqrt{E}}\right)^2 + \left(\frac{b}{E}\right)^2 + c^2 \quad (2.4)$$

The stochastic term  $a$  dominates at low energies: it includes the contribution of statistical fluctuations in the number of generated and collected photoelectrons. This term takes into account the crystal light emission, the light collection efficiency and the photodetector quantum efficiency<sup>5</sup>. The noise term  $b$  includes the contributions of pile-up events and electronic noise, both due to the photodetector and preamplifier. These contributions depend on  $\eta$  and on the LHC operational luminosity. The constant term  $c$ , dominant at high energies, takes into account several contributions. The most relevant are the non-uniformity of the longitudinal light collection, the intercalibration errors and the leakage of energy from the rear side of the crystal. The EB resolution for electrons was measured using test beams to be:

$$\left(\frac{\sigma_E}{E}\right)^2 = \left(\frac{2.8\% \text{ GeV}^{1/2}}{\sqrt{E}}\right)^2 + \left(\frac{12\% \text{ GeV}^{1/2}}{E}\right)^2 + (0.3\%)^2 , \quad (2.5)$$

---

<sup>5</sup>The quantum efficiency is the ratio between the number of collected electron-hole pairs (or photoelectrons) and the number of photons incident on the photodetector.

where  $E$  is the energy measured in GeV.

### 2.2.4 The hadron calorimeter (HCAL)

The hadron calorimeter (HCAL) [66] is used together with ECAL to make a complete calorimetric system for the jet energy and direction measurement. Moreover, thanks to its hermetic structure, it can measure the energy imbalance in the transverse plane,  $E_T^{\text{miss}}$ , a typical signature of non interacting particles such as neutrinos. The HCAL is a sampling calorimeter covering the region  $|\eta| < 5$ . As shown in Fig. 2.10, it is divided in four sub-detectors: HB (*Barrel Hadronic Calorimeter*), located in the barrel region inside the solenoid, extending up to  $|\eta| < 1.4$ ; HE (*Endcap Hadronic Calorimeter*), placed in the endcaps region inside the magnet, covering the region  $1.3 < |\eta| < 3$  and partially overlapping with the HB coverage; HO (*Outer Hadronic Calorimeter*), also known as *tail-catcher*, placed along the inner wall of the magnetic field return yoke, just outside of the magnet; HF (*Forward Hadronic Calorimeter*), a sampling calorimeter consisting of quartz fibers sandwiched between iron absorbers, formed by two units placed in the very forward region ( $3 < |\eta| < 5$ ) outside the magnetic coil. The quartz fibers emit Cherenkov light with the passage of charged particles and this light is detected by radiation resistant photomultipliers. In order to

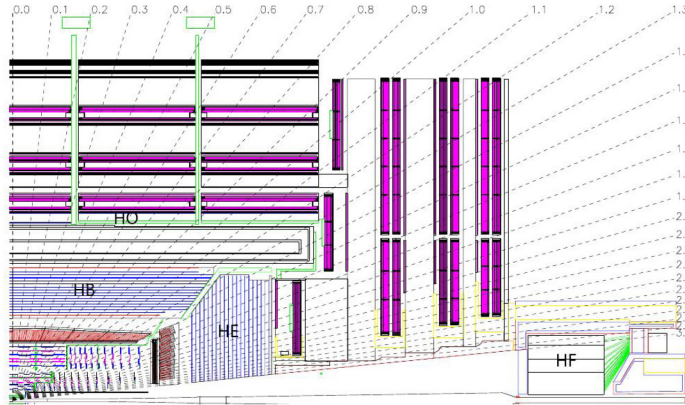


**Figure 2.10:** Longitudinal view of the CMS detector showing the HCAL sub-detectors.

maximize particle containment for a precise missing transverse energy measurement, the amount of absorber material was maximized, reducing therefore the amount of the active material. Since HCAL is mostly placed inside the magnetic coil, a non-magnetic material like brass was chosen as absorber. HB and HE are therefore made with 5 cm brass absorber layers interleaved with 3.7 mm plastic scintillators. The scintillation light is collected by wavelength shifting (WLS) fibres and read out by hybrid photodiodes (HPD). The granularity of the calorimeter is  $\Delta\eta \times \Delta\phi = 0.087 \times 0.087$  for  $|\eta| < 1.6$  and  $\Delta\eta \times \Delta\phi \approx 0.17 \times 0.17$  for  $|\eta| \geq 1.6$ . HO is made of 5 rings installed in the wheel that compose the return yoke and is divided in 12 sectors, each one covering a  $30^\circ$  angle in  $\phi$ . It consists of scintillating layers, with the same

granularity as HB, and the solenoid coil is used as an additional absorber to increase the effective depth of the calorimeter in the barrel region, which is extended up to  $11.8\lambda_I$ , thus improving the energy resolution.

The energy resolution in the different regions of HCAL can be parametrized using a stochastic and a constant term, as follows:

$$\begin{aligned} \left(\frac{\sigma_E}{E}\right)^2 &= \left(\frac{90\% \text{GeV}^{1/2}}{\sqrt{E}}\right)^2 + (4.5\%)^2 && \text{in the barrel/endcap} , \\ \left(\frac{\sigma_E}{E}\right)^2 &= \left(\frac{172\% \text{GeV}^{1/2}}{\sqrt{E}}\right)^2 + (9\%)^2 && \text{in the HF} , \end{aligned} \quad (2.6)$$

where  $E$  is expressed in GeV.

### 2.2.5 The muon system

The CMS muon system [67] is dedicated to the identification and measure of high  $p_T$  muons, in combination with the tracker. The system is placed outside the magnetic coil, embedded in the return yoke, to fully exploit the 1.8 T return flux. As shown in

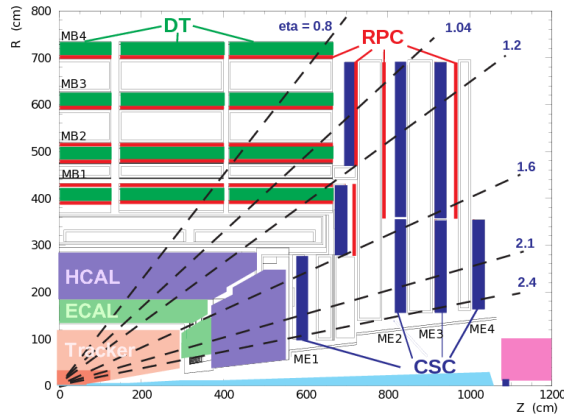


**Figure 2.11:** Schematic view of a quadrant of the CMS muon system.

Fig. 2.11, the system consists of three types of independent gaseous particle detectors:

- *Drift Tubes* (DT) are placed in the barrel region, where the occupancy is relatively low ( $< 10 \text{ Hz/m}^2$ );
- *Cathode Strip Chambers* (CSC) are installed in the endcaps, where the occupancy is higher ( $> 100 \text{ Hz/m}^2$ );
- *Resistive Plate Chambers* (RPC) are placed both in the barrel and endcaps.

The DT system is placed in the region of the barrel with  $|\eta| < 1.2$ , where the magnetic field is sufficiently weak and homogeneous. Along the longitudinal direction, the barrel region is divided in 5 wheels, which are subdivided in 12 sectors covering a  $30^\circ$  azimuthal angle each. The wheels are composed of 4 concentric rings of chambers, called *stations*, interspersed in the layers of the iron return yoke, and each one formed by 12 DT chambers. The basic element of the DT system is a rectangular drift tube cell with a transverse size of  $13 \times 42 \text{ mm}^2$  and a variable length from 2 to 4 m. The chambers are filled with a gas mixture of Ar (85%) and CO<sub>2</sub> (15%) and are grouped in the radial direction to form detection layers. Groups of four layers form a *superlayer*. In each superlayer two chambers have anode wires parallel to the beam axis and two have perpendicular wires, thus providing two measurements of the  $(r, \phi)$  coordinate and two measurements of the  $z$  coordinate of the track hit position. As shown in

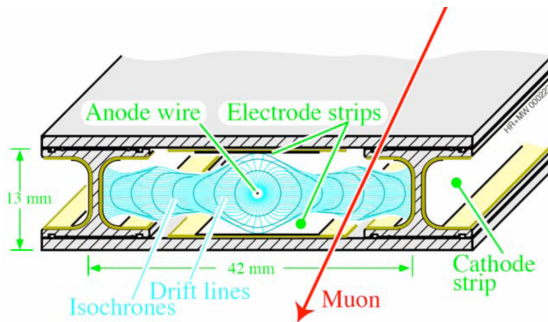


**Figure 2.12:** Schematic representation of a drift tube chamber, showing the drift lines in presence of magnetic field.

Fig. 2.12, each chamber is made of a stainless steel anode wire between two parallel aluminium plates with “I” shaped spacer cathodes, isolated from the aluminium plates with polycarbonate plastic. The hit resolution is about 100  $\mu\text{m}$  in both  $(r, \phi)$  and  $(r, z)$  directions.

In the endcaps, the high and non-uniform magnetic field and the particle rate do not allow to use drift tubes detectors to perform measurements. Therefore, a solution based on the CSC detector has been adopted. CSC are multi-wire proportional chambers with the cathodes segmented into strips oriented radially and transversely with respect to the anode wires (see Fig. 2.13), allowing a simultaneous measurement of two coordinates ( $r$  through wires and  $\phi$  using strips). The CSC chambers are filled with a gas mixture of Ar (40%), CO<sub>2</sub> (50%) and CF<sub>4</sub> (10%) and provide a spatial resolution of about 80–85  $\mu\text{m}$ . The drift path of the charge carriers is shorter with respect to the drift tubes, therefore these detectors can be placed in regions with higher flows of charged particles and less homogeneous magnetic fields. The CSC coverage is  $0.8 < |\eta| < 2.4$ .

RPCs are used both in barrel and endcaps, complementing DT and CSC systems, in order to ensure robustness and redundancy to the muon spectrometer. RPCs are gaseous detectors characterized by a coarse spatial resolution but able to perform

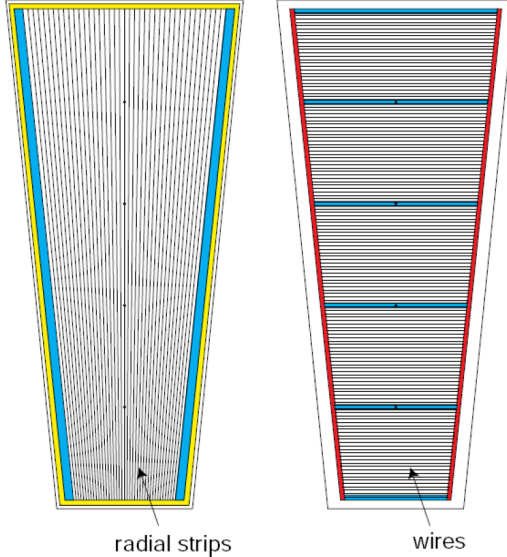


**Figure 2.13:** Schematic representation of CSC cathode (left) and anode (right) panels.

precise time measurements, comparable with the ones provided by scintillators. These chambers are made of 4 bakelite planes, with a bulk resistivity of  $10^{10}$ – $10^{11} \Omega\text{cm}$ . The 2 mm gap between the plates is filled with a mixture of  $\text{C}_2\text{H}_2\text{F}_4$  (94.5%) and Isobutane. The central part of the chamber is equipped with insulated aluminum strips, used to collect the signal generated by crossing particles. In the barrel the strips are rectangularly segmented and run along the beam axis, whereas the endcaps are equipped with trapezoidal shaped strips. The detector operates in avalanche mode, and covers the region  $|\eta| < 2.1$ .

## 2.3 The CMS trigger system

The LHC can provide proton-proton interactions at a crossing frequency of 40 MHz and, for each bunch crossing, several collisions can occur (approximately 20 at the nominal instantaneous luminosity). Since it is impossible to store and process the large amount of data associated with the resulting large number of events, a drastic rate reduction has to be achieved. In fact the speed at which data can be written to mass storage is limited and, moreover, the vast majority of produced events is not interesting for physics analyses, because it involves low transverse momentum interactions (also called *minimum bias events*). The task of reducing this rate is accomplished by the CMS trigger system, which represents the first step of the physics event selection. CMS makes use of a two-stage trigger system, consisting of a *Level-1* trigger (L1) [68] and a *High Level Trigger* (HLT) [69].

Level-1 trigger runs on dedicated processors, and accesses coarse level granularity information from calorimetry and muon system. A L1 Trigger decision has to be taken

for each bunch crossing within  $3.2\ \mu\text{s}$ . Its task is to reduce the data flow from 40 MHz to about 100 kHz.

The High Level Trigger is responsible for reducing the L1 output rate down to a maximum rate of the order of 1 kHz. The HLT code runs on a farm of commercial processors and can access the full granularity information of all the sub-detectors.

The main characteristics of the CMS trigger system are described in the following.

### 2.3.1 The Level-1 trigger

The L1 trigger is responsible for the identification of electrons, muons, photons, jets and missing transverse energy. It is required to have a high and carefully understood efficiency. Its output rate and speed are limited by readout electronics and performance of the data acquisition (DAQ) system [69]. It consists of three main subsystems:

- L1 Calorimeter Trigger;
- L1 Muon Trigger;
- L1 Global Trigger.

The L1 Global Trigger is responsible for combining the output of L1 Calorimeter Trigger and L1 Muon Trigger and for making the decision to either retain the event or discard it. The organization of CMS L1 Trigger is schematically summarized in Fig. 2.14.

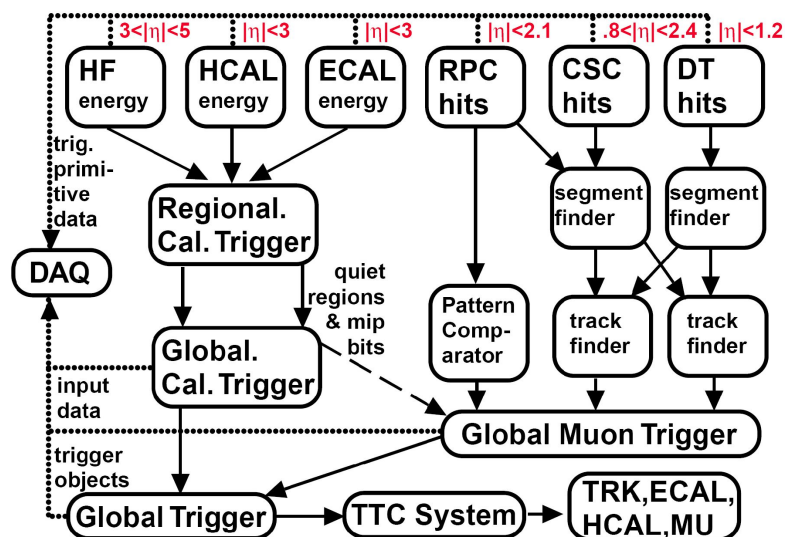


**Figure 2.14:** Schematic representation of the Level-1 trigger components.

## **L1 Calorimeter Trigger**

The input for the L1 Calorimeter Trigger are calorimeter towers, which are clusters of signals collected both from ECAL and HCAL. Towers are calculated by calorimeter high level readout circuits, called Trigger Primitive Generators. The Regional Calorimeter Trigger identifies electron, photon,  $\tau$  and jet candidates together with their transverse energy and sends the information to the Global Calorimeter Trigger. The Global Calorimeter Trigger sorts the candidates according to their transverse energy and sends the first four objects to the L1 Global Trigger.

## **L1 Muon Trigger**

The L1 Muon Trigger is actually a composite system itself: information from RPC, CSC and DT specific triggers are combined in the so called L1 Global Muon Trigger.

The RPC trigger electronics builds Track Segments, gives an estimate of their  $p_T$  and sends these segments to the Global Muon Trigger. It also provides the CSC logic unit with information to solve hit position ambiguities in case of two or more muon tracks crossing the same CSC chamber.

The CSC trigger builds Local Charged Tracks (LCT), that is track segments made out of the cathode strips only, and assign a  $p_T$  value and a quality flag to the LCTs. The best three LCTs in each sector of nine CSC chambers are passed to the CSC Track Finder, that uses the full CSC information to build tracks, assigns them a  $p_T$  and a quality flag and sends them to the Global Muon Trigger.

DTs are equipped with Track Identifier electronics, which is able to find groups of aligned hits in the four chambers of a superlayer. Those Track Segments are sent to the DT Track Correlator that tries to combine segments from two superlayers, measuring the  $\phi$  angle. The best two segments are sent to the DT Track Finder that builds tracks and sends them to the Global Muon Trigger.

The Global Muon Trigger sorts the RPC, CSC and DT muon tracks and tries to combine them. The final set of muons is sorted according to the quality, and the best four tracks are passed to the L1 Global Trigger.

## **L1 Global Trigger**

The L1 Global Trigger is responsible for collecting objects created from the Calorimeter and Muon Triggers and for making a decision whether to retain the event or not. In case the event is accepted, the decision is sent to the Timing Trigger and Control System, that commands the readout of the remaining subsystems.

In order to take the decision, the L1 Global Trigger sorts the ranked objects produced by calorimetry and muon system and checks if at least one of the thresholds in the L1 trigger table is passed.

### 2.3.2 The high level trigger (HLT)

The High Level Trigger is designed to reduce the L1 output rate down to about 1000 events/s, which is the amount that will be written to mass storage. HLT code runs on commercial processors and performs reconstruction using the information from all sub-detectors. Events passing the HLT are stored on local disks or in CMS Tier 0<sup>6</sup>.

Data read from sub-detectors are assembled by a builder unit and then assigned to a switching network that dispatches events to the processor farm. The CMS switching network has a bandwidth of 1 Tbit/s. This simple design ensures maximum flexibility to the system, the only limitation being the total bandwidth and the number of processors. The system can be easily upgraded adding new processors or replacing the existing ones with faster ones as they become available. Since the algorithms have a fully software implementation, improvements to the algorithms can be easily implemented and do not require any hardware intervention.

Event by event, the HLT code is run on a single processor, and the time available to make a decision is about 300 ms. The real time nature of this selection imposes several constraints on the resources an algorithm can use. The reliability of HLT algorithms is of capital importance, because events not selected by the HLT are lost. In order to efficiently process events, the HLT code has to be able to quickly reject not interesting events; computationally expensive algorithms must be run only on good candidates for interesting events. In order to cope with this requirement the HLT code is organized in a virtually layered structure:

- Level 2: uses only complete muon and calorimetry information;
- Level 2.5: uses also the pixel information;
- Level 3: makes use of the full information from all the tracking detectors.

Each step reduces the number of events to be processed in the following step. The most computationally expensive tasks are executed in the Level 3; time consuming algorithms such as track reconstruction are only executed in the region of interest. Besides, since the ultimate precision is not required at HLT level, track reconstruction is performed on a limited set of hits, and is stopped once the required resolution is achieved.

---

<sup>6</sup>The Worldwide LHC Computing Grid (WLCG) is composed of four levels, or “Tiers”, identified with numbers 0, 1, 2 and 3. Each Tier is made up of several computer centres and provides a specific set of services; they process, store and analyse all the data from the Large Hadron Collider (LHC). Tier 0 is the CERN Data Centre. All of the data from the LHC pass through this central hub. Tier 0 distributes the raw data and the reconstructed output to Tier 1’s, and reprocesses data when the LHC is not running.



# Chapter 3

## Reconstruction and identification of physics objects

In CMS the physics object reconstruction and identification is based on standard algorithms developed by the collaboration and used by all physics analyses. In this section, the techniques used for the reconstruction and identification of the physics objects of interest for  $H \rightarrow WW \rightarrow 2\ell 2\nu$  analyses are described.

### 3.1 The Particle Flow technique

The Particle Flow (PF) event reconstruction technique [70] aims at the reconstruction and identification of all the stable particles in the event, i.e. electrons, muons, photons, charged and neutral hadrons, with a thorough combination of the information from all CMS sub-detectors, in order to determine their energy, direction and type. These individual particles are then used, for example, to build jets, to measure the missing transverse energy  $E_T^{\text{miss}}$ , to reconstruct the  $\tau$  from their decay products, to quantify the charged lepton isolation and to tag b-jets.

The CMS detector is well suited for this purpose. Indeed, the presence of a large internal silicon tracker immersed in an intense solenoidal magnetic field allows the reconstruction of charged particles with high efficiency and small fake rate, and provides a high precision measurement of the particle  $p_T$  down to about 150 MeV, for  $|\eta| \leq 2.6$ . The high granularity of the ECAL calorimeter is the additional key element for the feasibility of the PF technique, allowing the reconstruction of photons and electrons with high energy resolution.

The first step of the PF technique consists in the reconstruction of the basic elements from the various sub-detectors, such as charged-particle tracks, calorimeter clusters and muon tracks. These elements, which are provided by the sub-detectors with high efficiency and low fake rate, are then connected together with a link algorithm.

The good performance of the tracking system are achieved by means of an iterative tracking strategy [71], based on the Kalman Filter algorithm [72]. The basic idea of iterative tracking is that initial iterations search for tracks that are easiest to find, e.g.

high  $p_T$  tracks produced near the interaction region. After each iteration, hits associated to reconstructed tracks are removed from the hit collection, thereby reducing the combinatorial complexity and simplifying the subsequent iterations, which aim at finding more complicated set of tracks, e.g. low  $p_T$  or displaced tracks. The *Iteration 0*, where the majority of tracks is reconstructed, is designed to identify prompt tracks with  $p_T > 0.8$  GeV that have three hits in the three layers of the pixel detector. *Iteration 1* is used to recover prompt tracks that have only two pixel hits. *Iteration 2* aims at finding low- $p_T$  prompt tracks while *Iterations 3–5* are intended to find tracks that originate outside the collision point, i.e. tracks produced by a secondary vertex, and to recover undetected tracks in the previous iterations. Each iteration proceeds according to four steps:

- *seeding*: initial track candidates are obtained using 2 or 3 hits in the innermost layers (these proto-tracks are called seeds);
- *pattern recognition*: this step is based on Kalman Filter and searches for hits in the outer layers that could be associated to the initial track candidate, reconstructing the particle trajectory;
- *track fitting*: in this step a fit of the trajectory is performed, using its associated hits and providing an estimate of the track parameters ( $p_T$ ,  $\eta$ ,  $\phi$ , charge, etc.);
- *selection*: finally tracks are selected based on quality requirements.

The high detection efficiency of the calorimeters is based on a specific calorimeter clustering algorithm, which is performed separately in each sub-detector. The algorithm is based on three steps: in the first step, “cluster seeds” are identified as local calorimeter cells with an energy deposit above a given threshold. Then, “topological clusters” are grown from the seeds by gathering cells with at least one side in common with a cell already in the cluster, and with an energy above a given threshold. A topological cluster usually gives rise to many “particle flow clusters” as seeds, which are identified sharing the energy of each cell among the particle flow clusters, thereby allowing the determination of the particle flow cluster energy and position.

These elements are then connected to each other using a link algorithm, which identifies blocks of elements that are topologically compatible. For example, a charged-particle track is linked to a calorimeter particle flow cluster if the extrapolated position from the track to the calorimeter is compatible with the cluster boundaries. From these blocks, PF candidates are identified according to the following order:

- Muons: a *global muon* gives rise to a *PFPF muon* if its combined  $p_T$  measurement is compatible within 3 standard deviation with the one provided by the sole tracker. The corresponding track is removed from the block;
- Electrons: electrons tend to give rise to short tracks, and to lose energy by Bremsstrahlung in the tracker layers on their way to the calorimeter. The

link between a charged-particle track (refitted with the Gaussian-Sum Filter (GSF) [73]) and one or more ECAL clusters identifies a *PF electron*. After the identification, the corresponding tracks and clusters are removed from the block.

- Charged hadrons: the remaining tracks give rise to *PF charged hadrons*. Tracks can be linked to ECAL and HCAL clusters, and the energy is determined taking into account information from calorimeters;
- Photons and neutral hadrons: ECAL clusters not linked with tracks give rise to *PF photons*, while the remaining HCAL clusters are identified as *PF neutral hadrons*.

After the identification of all PF candidates in the event, *PF jets* are clustered as described in Sec. 3.3. The last step is the reconstruction of the *PF  $\vec{p}_T^{\text{miss}}$* , which is described in Sec. 3.5. The missing transverse energy,  $E_T^{\text{miss}}$ , is defined as the modulus of  $\vec{p}_T^{\text{miss}}$ .

## 3.2 Leptons reconstruction and identification

### 3.2.1 Muon reconstruction and identification

Muons produced at the collision point can go through the entire detector with a negligible energy loss, reaching the detector outermost part where the muon chambers are installed (see Sec. 2.2.5). Muons interact through ionization with the layers of the silicon tracker, which is able to reconstruct their tracks (*tracker track*). The muon tracks are also reconstructed using the muon system (*standalone muon track*). Based on these objects, two reconstruction approaches are used [74]: in the first method (outside-in), for each standalone muon track a tracker track is searched for by extrapolating the two tracks to a common surface. If a match is found, the hits associated to the two tracks are fitted together giving rise to a *Global Muon*. The second approach (inside-out) consists in considering all tracker tracks with  $p_T > 0.5 \text{ GeV}$  as potential muon candidates. These tracks are extrapolated to the muon system taking into account the magnetic field, the expected energy losses and the multiple scattering in the detector material. If at least one muon segment (a short track stub made of DT or CSC hits) matches the extrapolated tracks, the corresponding tracker track is identified as a *Tracker Muon*.

The matching with the muon system improves significantly the muon  $p_T$  resolution that can be obtained from the tracker only, especially in the region with  $p_T > 200 \text{ GeV}$ , as shown in Fig. 3.1.

Depending on the physics analysis, different muon definitions can be used by changing the selection on the muon identification variables, hence balancing between the muon identification efficiency and purity. The most widely used definition in physics analyses at CMS is the so-called *Tight muon selection*<sup>1</sup>. This selection requires

---

<sup>1</sup>Small variations with respect to this baseline definition are adopted by the specific analyses.

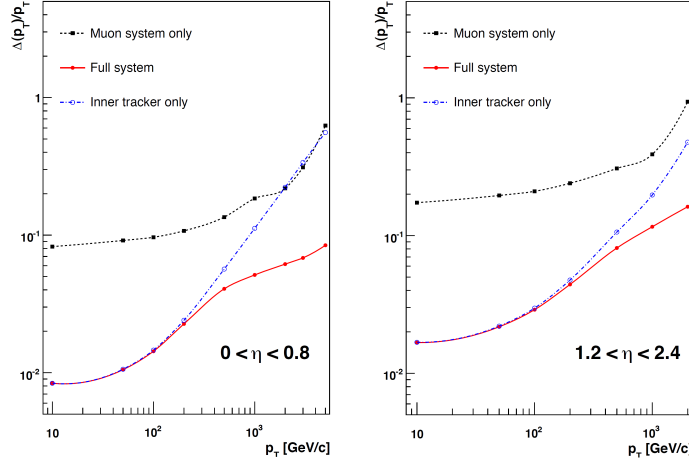


**Figure 3.1:** Muon  $p_T$  resolution as a function of the muon  $p_T$  in the barrel (left) and in the endcap (right) regions. The resolution is provided for the measurement using the tracking system or the muon system only, as well as for the combination of the two methods.

the muon candidate to be reconstructed as a Global Muon and identified by the PF algorithm. The fit of the global track, which is required to include muon segments in at least two muon stations (this implies that the muon is also reconstructed as a Tracker Muon), must have a  $\chi^2/d.o.f.$  less than 10 and use more than 10 inner tracker hits. The transverse impact parameter with respect to the primary vertex is required to be  $|d_{xy}| < 2 \text{ mm}$ , significantly reducing the rate of muons from decays in flight, i.e. non-prompt muons. The requirements defining the Tight Muon identification are summarized in Table 3.1.

**Table 3.1:** Summary of the muon identification variables and the corresponding selections commonly used by physics analyses.

Observable	Cut
Is Global Muon	true
Is PF muon	true
Tracker layers with valid hits	> 5
Number of valid pixel hits	> 0
Number of valid muon hits	> 0
Number of matched muon stations	> 1
$\chi^2/d.o.f.$	< 10
$d_{xy}(PV)$	< 0.2 cm
$d_z(PV)$	< 0.5 cm

Another selection which is optimised for low- $p_T$  muons coming from in flight decays

is called *Soft-Muon selection*. This selection requires the muon to be reconstructed as a Tracker Muon with additional loose cuts on the transverse and longitudinal impact parameters. This selection is commonly used to identify muons coming from B hadron decays.

### 3.2.2 Muon isolation

One of the most powerful requirements to select prompt muons, as the ones produced from W or Z boson decays, and to reject muons produced by decays in flight, is the isolation. Indeed, prompt muons are expected to be isolated in the event, differently to non-prompt muons that are generally produced within jets and characterized by many nearby particles.

Muons commonly used to reconstruct the W or Z boson decays are thus required to pass an isolation requirement, which includes a pile-up mitigation correction called “ $\Delta\beta$  correction”. This correction is needed to obtain a robust isolation definition that is less sensitive to the pile-up contribution. Indeed, simultaneous interactions manifest themselves as a mean energy deposited over all the detector acceptance, which is not due to the particles produced in the primary events, thus spoiling the isolation measurement. The relative isolation variable, usually called *PF relative isolation*, is defined as follows:

$$I_{\Delta\beta}^{rel} = \left[ \sum_{ChH} p_T + \max \left( 0, \sum_{NH} p_T + \sum_{Ph} p_T - 0.5 \sum_{ChHPU} p_T \right) \right] / p_T^{\text{muon}} . \quad (3.1)$$

The sums in Eq. (3.1) are performed in a cone of radius  $\Delta R < 0.4$  around the muon direction. The  $ChH$  subscript refers to charged hadrons,  $NH$  to neutral hadrons,  $Ph$  to photons and  $ChHPU$  to charged hadrons not arising from the primary vertex.

The cut applied on the isolation variable is analysis dependent, but a common value is  $I_{\Delta\beta}^{rel} < 0.15$ .

A different isolation definition is called *Tracker relative isolation*,  $I_{trk}^{rel}$ , which is calculated as the scalar sum of all the  $p_T$  of the tracker tracks reconstructed inside a cone of radius  $\Delta R < 0.3$  centred on the muon track direction.

### 3.2.3 Muon momentum scale and resolution

The measurement of the muon  $p_T$  is sensitive to the alignment of the tracker and the muon chambers, to the material composition and distribution inside the detector and to the knowledge of the magnetic field produced by the solenoid. The imperfect knowledge of the magnetic field and the effect of the material distribution introduce a relative bias in the muon  $p_T$  that is generally independent on the  $p_T$  itself, while the effect of the alignment is known to produce a bias that increases linearly with the  $p_T$ .

Different methods are used to estimate the muon  $p_T$  scale and resolution effects and to determine the corresponding uncertainties, depending on the  $p_T$  range. At low

and intermediate  $p_T$  ( $< 100$  GeV), the di-muon events arising from the  $J/\Psi$  and Z resonance decays are used to correct the  $p_T$  scale and to measure the  $p_T$  resolution. In the high  $p_T$  regime, the muon  $p_T$  scale and resolution are instead measured using cosmic ray muons. One of the methods that is commonly used in the intermediate  $p_T$  range is the *MuScleFit* (Muon momentum Scale calibration Fit), which provides the muon  $p_T$  scale corrections by fitting the Z boson mass peak in data and simulation. These corrections are meant to recover the bias of the Z mass peak with respect to the  $\eta$  and  $\phi$  coordinates of the muon. After applying these corrections, the relative  $p_T$  resolution,  $\sigma(p_T)/p_T$ , is measured as a function of  $\eta$  and  $\phi$  and is found to be on average of the order of 2% in the barrel and up to 6% in the endcaps, for muon  $p_T$  below 100 GeV.

### 3.2.4 Electron reconstruction and identification

The electron reconstruction is based on the combination of tracker and ECAL information. The reconstruction technique starts by measuring the energy deposits in ECAL by electrons, which form a “supercluster”. A supercluster is a group of one or more ECAL clusters associated using an algorithm that takes into account the characteristic shape of the energy deposited by electrons emitting Bremsstrahlung radiation in the tracker material. The supercluster shape is characterized by a narrow width profile in the  $\eta$  coordinate spread over the  $\phi$  direction. The superclusters are matched to tracks, reconstructed in the tracker with the GSF algorithm, in order to obtain an electron candidate. An additional reconstruction method, described in details in Refs. [75, 76], is instead seeded by electron tracks reconstructed in the inner tracker layers.

Several strategies are used in CMS to identify prompt isolated electrons (characteristic of the signal processes of interest), and to separate them from background sources, mainly originating from photon conversions, jets misidentified as electrons, or electrons from semileptonic decays of b and c quarks. In order to achieve a good discrimination, several identification variables are used:

- $\Delta\eta_{\text{trk,SC}}$  and  $\Delta\phi_{\text{trk,SC}}$ : the variables measuring the spatial matching between the track and the supercluster in the  $\eta$  and  $\phi$  coordinates, respectively;
- $\sigma_{i\eta,i\eta}$ : a variable related to the calorimeter shower shape, measuring the width of the ECAL supercluster along the  $\eta$  direction computed for all the crystals in the  $5 \times 5$  block of crystals centred on the highest energy crystal of the seed supercluster;
- $H/E$ : the ratio between the energy deposited in the HCAL tower behind the ECAL seed and the supercluster seed energy;
- $|1/E - 1/p|$ : the difference of the inverse of energy  $E$  measured in ECAL and the inverse of momentum  $p$  measured in the tracker;

- the number of missing hits in the back-propagation of the track to the interaction point;
- $d_{xy}$  and  $d_z$ : the transverse and longitudinal impact parameters with respect to the primary vertex.
- a photon conversion veto ( $\gamma \rightarrow e^+e^-$ ) based on the primary vertex measurement.

Different working points are provided by CMS corresponding to different selections on the previously defined variables. One of the common working points used by several physics analyses, as the  $H \rightarrow WW$  analyses described in Chapters 4, 5 and 6, is the “tight working point”, summarised in Table 3.2.

**Table 3.2:** Electron identification selections corresponding to the tight working point.

Variable	Selection	
	$ \eta_{\text{SC}}  \leq 1.479$	$1.479 <  \eta_{\text{SC}}  \leq 2.5$
$\sigma_{i\eta,i\eta}$	0.01	0.028
$ \Delta\eta_{\text{trk,SC}} $	0.009	0.007
$ \Delta\phi_{\text{trk,SC}} $	0.03	0.09
$H/E$	0.06	0.06
$ 1/E - 1/p $	0.012	0.010
$ d_{xy} $	0.011 cm	0.035 cm
$ d_z $	0.047 cm	0.42 cm
missing inner hits	$\leq 2$	$\leq 1$
conversion veto	yes	yes

### 3.2.5 Electron isolation

Selected electrons are required to pass an isolation requirement that includes a pile-up mitigation correction based on the electron effective catchment area, which is different in different  $\eta$  ranges. The isolation variable is given by the following formula:

$$I_{EA \text{ corrected}}^{\text{rel}} = \left[ \sum_{ChH} p_T + \max \left( 0, \sum_{Ph} p_T + \sum_{NH} p_T - \rho E A \right) \right] / p_T^{\text{electron}} \quad (3.2)$$

where  $ChH$  refers to charged hadrons,  $Ph$  to photons,  $NH$  to neutral hadrons,  $\rho$  is the energy density due to pile-up events,  $E$  is the energy and  $A$  is an effective area. The sums are performed inside a cone of radius  $\Delta R < 0.4$  around the electron direction. The cut applied on this variable for the tight working point is  $I_{EA \text{ corrected}}^{\text{rel}} < 0.04$ .

### 3.2.6 Electron momentum scale and resolution

The electron momentum is estimated using a combination of the tracker and ECAL measurements. Before making the combination of the two measurements, the ECAL energy response is calibrated. Before doing the clustering, the energy response in individual crystals is calibrated and a correction factor is applied to take into account effects as energy leakage or changes in the crystal transparency induced by radiation<sup>2</sup>. Then the supercluster energy is also corrected using an MVA technique, selecting  $Z \rightarrow e^+e^-$  events in data and comparing to simulation. A detailed description of the techniques used to estimate the electron scale and resolution and the associated uncertainties is given in Ref. [76].

### 3.2.7 Lepton identification and isolation efficiency

The efficiency related to the identification and isolation selections applied to muons and electrons are generally estimated both in data and simulation and the simulated events are corrected for the observed differences by means of a scale factor ( $SF$ ), defined as the ratio of the efficiency measured in data and simulation, i.e.  $SF = \varepsilon_{\text{data}}/\varepsilon_{\text{MC}}$ .

The identification and isolation efficiencies are measured using a Tag and Probe technique. The Tag and Probe technique is a method to estimate the efficiency of a selection on data. It can be applied whenever one has two objects in a given event, by using one of the two, the *tag*, to identify the process of interest, and the second, the *probe*, to actually measure the efficiency of the selection being studied. Concerning the electron and muon case, the Tag and Probe method uses a known mass resonance (e.g.  $J/\Psi$ ,  $Z$ ) to select particles of the desired type, and probe the efficiency of a particular selection criterion on these particles. In general the *tag* is an object that passes a set of very tight selection criteria designed to isolate the required particle type. Tags are often referred to as a “golden” electrons or muons and the fake rate for passing tag selection criteria should be very small. A generic set of the desired particle type, the *probe* (with potentially very loose selection criteria), is selected by pairing these objects with tags such that the invariant mass of the combination is consistent with the mass of the resonance. Combinatorial backgrounds may be eliminated through any of a variety of background subtraction methods such as fitting, or sideband subtraction. The definition of the probe objects depend on the specifics of the selection criterion being examined. The simple expression to get the efficiency  $\varepsilon$  as a function of  $p_T$  and  $\eta$  is given below:

$$\varepsilon(p_T, \eta) = \frac{N_{\text{pass}}^{\text{probe}}}{N_{\text{pass}}^{\text{probe}} + N_{\text{fail}}^{\text{probe}}} \quad (3.3)$$

For the estimation of the electron or muon identification efficiency, the tag is chosen to be a well identified and isolated electron or muon, while the probe is chosen as an electron or muon identified with loose selections. The invariant mass of the *tag-probe*

---

<sup>2</sup>The continuous monitoring of the crystals transparency is achieved by a laser-monitoring system.

pair is required to be within a window around the Z boson mass (the effect of changing the Z mass window is included as a systematic uncertainty). After that, the probe is required to pass the identification selections discussed before for electrons and muons, and the efficiency is computed both in data and simulation. A scale factor is then calculated by taking the ratio of the two efficiencies and applied to reweight simulated events.

There are two methods to measure the efficiencies: the counting method consists in simply computing the ratio of probe events that pass the selections and total number of probe events, as shown in Eq. (3.3). This method can be used when the tag requirement selects a very pure set of events, with a small background contribution. The other approach is the fitting method, which is used when the background contamination is not negligible. In this latter case, which represents the commonly used method for estimating the lepton identification and isolation efficiencies, the invariant mass distribution of the tag-probe pair for signal and background is fitted choosing proper functions. The signal plus background fit is performed simultaneously in two categories, corresponding to events in which the probe lepton passes or fails the identification requirements, and separately in bins of  $\eta$  and  $p_T$ .

A similar approach is used to estimate the lepton isolation efficiency, requiring the probe lepton to pass the isolation requirements instead of the identification ones and calculating the corresponding scale factor.

The identification and isolation efficiency and the scale factor are shown in Fig. 3.2 corresponding to the selections described in Sec. 3.2.4, for events of interest for a typical physics analysis of the  $H \rightarrow WW \rightarrow 2\ell 2\nu$  channel (in particular the analyses described in Chapters 5 and 6).

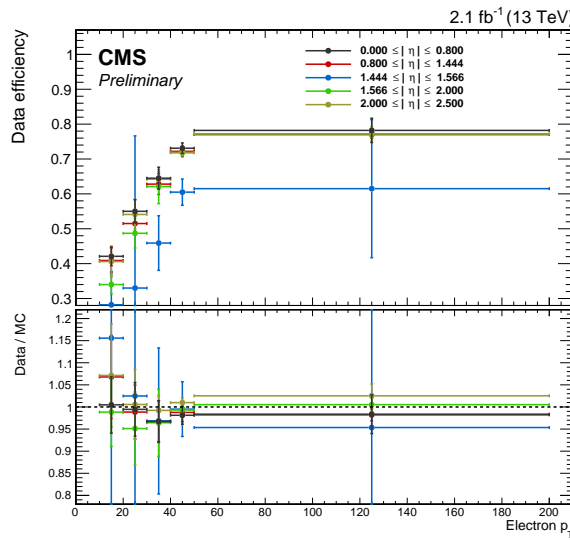


**Figure 3.2:** Typical electron identification and isolation efficiencies in data (top panel) and data/simulation scale factor (bottom panel), as a function of the electron  $p_T$  and for different  $\eta$  bins.

### 3.2.8 Lepton trigger efficiency

Analyses that involves leptons in the final state generally select the interesting events using lepton triggers. For instance, the  $H \rightarrow WW \rightarrow 2\ell 2\nu$  channel is characterized by the presence of two leptons in the final state, thereby both single lepton and double lepton triggers are used. The lepton triggers at the HLT level are characterized by  $p_T$  thresholds, above which the trigger efficiency is very high (plateau region). Nevertheless, the trigger efficiency as a function of the lepton  $p_T$  is not a step function, but is characterized by a steep increase of the efficiency around the  $p_T$  threshold (turn-on region). The simulated samples thus need to be corrected in order to properly take into account the trigger efficiency. This can be achieved in two ways: including the HLT trigger in the event simulation or calculating the trigger efficiency in data and then applying it on top of simulated events. Several analyses, such as those related to the  $H \rightarrow WW \rightarrow 2\ell 2\nu$  channel, opt for the second approach.

The trigger efficiency for single and double lepton triggers is calculated in bins of  $\eta$  and  $p_T$  using a Tag and Probe technique similar to the one described in Sec. 3.2.7, separately for muons and electrons. Since the triggered events arise from a mixture of two different triggers, the combined efficiency has to be computed and applied to simulated samples as an event weight. In the following, the approach used in the  $H \rightarrow WW \rightarrow 2\ell 2\nu$  analyses is described.

The event efficiency  $\varepsilon_{\text{ev}}$  for an event with two leptons to pass the single lepton trigger is given by the following formula:

$$\varepsilon_{\text{ev}} = 1 - (1 - \varepsilon_{S,\ell 1}) \cdot (1 - \varepsilon_{S,\ell 2}) , \quad (3.4)$$

where  $\varepsilon_{S,\ell 1}$  and  $\varepsilon_{S,\ell 2}$  are the efficiencies for the leading and subleading lepton to pass the single lepton trigger. In other words, the dilepton event passes the single lepton trigger if either one of the two leptons passes the single lepton trigger, excluding the cases for which both leptons pass the trigger.

For double lepton triggers the efficiency is calculated separately for each leg of the trigger. In the calculation of the efficiencies, the two trigger legs are considered independent, given that the correlations are very small. The combined efficiency is then used as a kinematics-dependent weight to be applied on top of simulated events. The event efficiency can be written as:

$$\varepsilon_{\text{ev}} = \varepsilon_{D,\ell 1}^{\text{lead}} \cdot \varepsilon_{D,\ell 2}^{\text{trail}} + (1 - \varepsilon_{D,\ell 1}^{\text{lead}} \cdot \varepsilon_{D,\ell 2}^{\text{trail}}) \cdot \varepsilon_{D,\ell 1}^{\text{trail}} \cdot \varepsilon_{D,\ell 2}^{\text{lead}} , \quad (3.5)$$

where  $\varepsilon_{D,\ell 1}^{\text{lead(trail)}}$  is the efficiency of the first lepton to pass the leading (trailing) leg of the double lepton trigger, and  $\varepsilon_{D,\ell 2}^{\text{lead(trail)}}$  is the efficiency of the second lepton to pass the leading (trailing) leg of the double lepton trigger. The final event efficiency applied to reweight the events in simulation is given by the boolean OR of the event efficiencies corresponding to the single and double lepton triggers, which, using Eqs. (3.4) and

(3.5), can be written as:

$$\begin{aligned}\varepsilon_{\text{ev}} = & 1 - (1 - \varepsilon_{S,\ell 1}) \cdot (1 - \varepsilon_{S,\ell 2}) + \\ & + (1 - \varepsilon_{S,\ell 1}) \cdot (1 - \varepsilon_{S,\ell 2}) \cdot \\ & \cdot [\varepsilon_{D,\ell 1}^{\text{lead}} \cdot \varepsilon_{D,\ell 2}^{\text{trail}} + (1 - \varepsilon_{D,\ell 1}^{\text{lead}} \cdot \varepsilon_{D,\ell 2}^{\text{trail}}) \cdot \varepsilon_{D,\ell 1}^{\text{trail}} \cdot \varepsilon_{D,\ell 2}^{\text{lead}}] .\end{aligned}\quad (3.6)$$

### 3.3 Jets reconstruction and identification

Jets are the experimental signature of quarks and gluons produced in high energy physics processes. They arise from the hadronization of partons, which forms collimated sprays of particles, and play a predominant role in hadron colliders like the LHC, where the production cross section is very large. In this section, the jet reconstruction techniques used in CMS are described.

#### 3.3.1 Jet reconstruction in CMS

The majority of physics analyses involving jets in the final state make use of particle flow jets. The PF jets are reconstructed using the technique described in Sec. 3.1, clustering all particles reconstructed with the PF algorithm, without any distinction of type and energy threshold. This method allows a remarkable improvement in the jet momentum and spatial resolutions with respect to the calorimeter jets, which are instead reconstructed using solely the information from the calorimeters, as the use of the tracker information provides a better  $p_T$  resolution for the charged particles constituting the jets<sup>3</sup>.

Jets are defined through sequential, iterative clustering algorithms that combine the four-momenta of input particles until certain conditions are satisfied and jets are formed [77]. Several algorithms are available for jet clustering, characterized by different features. From a theoretical point of view, an ideal jet clustering algorithm should fulfil the following requirements [78]:

- *Infrared safety*: infrared singularities should not appear in the perturbative calculations and the solutions of the algorithm should be insensitive to soft radiation in the event;
- *Collinear safety*: collinear singularities should not appear in the perturbative calculations and jets should be insensitive to collinear radiation in the event;
- *Invariance under boosts*: the solutions of the algorithm should be the same independently of boosts in the longitudinal direction. This is particularly important for hadron colliders, where the centre-of-mass of the individual parton-parton collisions is typically boosted along the beam direction;

---

<sup>3</sup>On average, the typical jet energy fractions carried by charged particles, photons and neutral particles are 65%, 25% and 10%, respectively.

- *Order independence*: the algorithm should find the same jets at parton, particle and detector level;
- *Straightforward implementation*: the algorithm should be straightforward to implement in perturbative calculations.

The ideal algorithm should also follow some experimental attributes. Among them, the performance of the algorithm should be as independent as possible of the detector that provides the data, the algorithm should not amplify the inevitable effects of resolution smearing and angle bias and should not be strongly affected by pile-up and high beam luminosities. Furthermore, the algorithm should be easy to implement, efficient to identify all possible jet candidates and should keep the necessary computing resources at an acceptable level.

Two main classes of jet clustering algorithms may be defined. The first one consists in the “cone” recombination, where jets are reconstructed associating together particles whose trajectories lie within a cone of radius  $\Delta R$  in the  $\eta$ - $\phi$  plane. The second class of algorithms uses the sequential recombination scheme, that iteratively recombine the closest pair of particles according to some distance measure.

The standard algorithms used by CMS are the SISCone, which is a “cone” recombination algorithm, and the  $k_t$ , anti- $k_t$  and *Cambridge Aachen* (CA) algorithms, which instead belong to the sequential recombination class. All the analyses presented in Secs. 4, 5 and 6 make use of the sequential recombination scheme, in particular of the anti- $k_t$  algorithm with  $R = 0.4$ , which is briefly described in the following.

The  $k_t$ , anti- $k_t$  and CA algorithms are infrared and collinear safe algorithms characterized by the introduction of two definitions of distance:  $d_{ij}$ , the distance between the two objects  $i$  and  $j$ , and  $d_{iB}$ , the distance between the object  $i$  and the beam. These distances are defined by the following equations:

$$\begin{aligned} d_{ij} &= \min(k_{ti}^{2p}, k_{tj}^{2p}) \frac{\Delta_{ij}^2}{R^2} \quad , \\ d_{iB} &= k_{ti}^{2p} \quad , \end{aligned} \tag{3.7}$$

where  $\Delta_{ij} = (y_i - y_j)^2 + (\phi_i - \phi_j)^2$  and  $k_{ti}$ ,  $y_i$  and  $\phi_i$  are the transverse momentum, rapidity and azimuthal angle of the particle  $i$ , respectively. In these formulas,  $R$  represents the radial parameter and  $p$  is a parameter that is 1 for  $k_t$ , 0 for CA and  $-1$  for anti- $k_t$  algorithm. The algorithm proceeds as follows:

- the distances  $d_{ij}$  are calculated for all pairs of particles  $i, j$  and the distances  $d_{iB}$  are calculated for each particle  $i$ , according to Eq. (3.7);
- the smallest distance, which could be either of type  $d_{ij}$  or  $d_{iB}$ , is identified;
- if the smallest distance is a  $d_{ij}$ , the particles  $i$  and  $j$  are combined into a single new particle summing their four-momenta and the algorithm restarts from the first step;

- otherwise, if it is a  $d_{iB}$ ,  $i$  is declared to be a final state jet and the algorithm returns to the first step;
- the procedure is repeated until no particles are left.

The physical difference between the three algorithms is the momentum weighting. For the  $k_t$  algorithm, the weighting proportional to  $k_t^2$  implies that jets are reconstructed starting from particles with low transverse momentum. Moreover this algorithm produces jets with irregular borders, thereby complicating the correction for effects such as pile-up. For the CA algorithm there is no transverse momentum weighting, and the particles are merged following just an angular approach, based on the distance  $\Delta_{ij}$ . Also this algorithm leads to jets with irregular borders. Finally, the anti- $k_t$  algorithm uses a weighting proportional to  $1/k_t^2$ , favouring the merging of high transverse momentum particles. In this case the jets grow around the particles with highest transverse momenta and the jets have a circular shape.

Jets reconstructed with different algorithms starting from the same set of simulated particles are shown in Fig. 3.3.

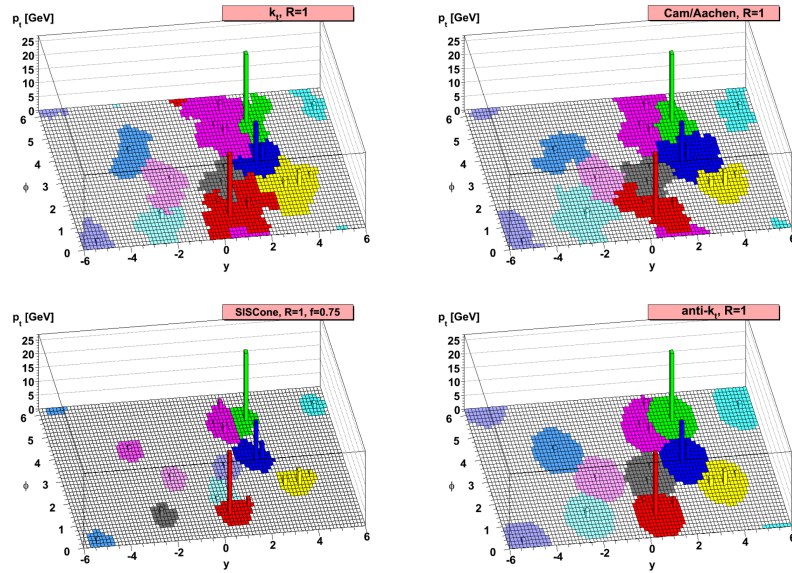


**Figure 3.3:** Jets reconstructed with different algorithms starting from the same set of simulated particles. The jets reconstructed with the sequential recombination algorithms described in the text are shown, as well as with the SIScone algorithm.

### 3.3.2 Jet energy correction

The purpose of jet energy correction is to relate, on average, the jet energy measured in the detector to the true energy of the corresponding final state particle or parton jet. The latter is obtained in simulation by clustering, with the same algorithm used

for jets in the detector, all the stable particles, i.e. with  $c\tau > 1$  cm, produced in the event excluding neutrinos. This mismatch is mainly ascribable to the non uniform and linear response of the CMS calorimeters, to the electronics noise and to pile-up. For this reason, CMS has developed a sequential procedure to calculate and apply the *jet energy corrections* (JEC) [79].

The correction is applied as a multiplicative factor  $\mathcal{C}$  to each component of the raw jet four-momentum  $p_\mu^{\text{raw}}$  (components are indexed by  $\mu$  in the following):

$$p_\mu^{\text{cor}} = \mathcal{C} \cdot p_\mu^{\text{raw}} \quad , \quad (3.8)$$

where  $p_\mu^{\text{cor}}$  is the corrected jet four-momentum. The correction factor is composed of the offset correction  $C_{\text{offset}}$ , the MC calibration factor  $C_{\text{MC}}$ , and the residual calibrations  $C_{\text{rel}}$  and  $C_{\text{abs}}$  for the relative and absolute energy scales, respectively. The offset correction removes the extra energy due to noise and pile-up, and the MC correction removes the bulk of the non-uniformity in  $\eta$  and the non-linearity in  $p_T$ . Finally, the residual corrections account for the small differences between data and simulation. The various components are applied in sequence as described by the equation below:

$$\mathcal{C} = C_{\text{offset}}(p_T^{\text{raw}}) \cdot C_{\text{MC}}(p'_T, \eta) \cdot C_{\text{rel}}(\eta) \cdot C_{\text{abs}}(p''_T) \quad , \quad (3.9)$$

where  $p'_T$  is the jet  $p_T$  after applying the offset correction and  $p''_T$  is the jet  $p_T$  after applying all previous corrections. Each component is briefly described in the following sections.

## Offset correction

The offset correction purpose is to estimate and subtract the average energy contribution that is not associated with the hard scattering in the event. The approach followed for the estimation of the offset correction is known as *Jet Area Method*. For each event, an average  $p_T$ -density per unit area,  $\rho$ , is estimated, characterizing the soft jet activity. This  $p_T$ -density represents the combination of the underlying event, the electronics noise and the pile-up effects. The two latter components contaminate the hard jet energy measurement and need to be corrected for with the offset correction. The key element for this approach is the jet area  $A_j$ . A very large number of infinitely soft four-momentum vectors (soft enough not to change the properties of the true jets) are artificially added in the event and clustered by the jet algorithm together with the true jet components. The extent of the region in the  $\eta$ - $\phi$  space occupied by the soft particles clustered in each jet defines the active jet area. The  $p_T$ -density  $\rho$  is calculated with the  $k_t$  algorithm with a distance parameter  $R = 0.6$ . The quantity  $\rho$  is estimated event by event as the median of the distribution of the variable  $p_{Tj}/A_j$ , where  $j$  runs over all jets in the event, and is not sensitive to the presence of hard jets. At detector level, the measured density  $\rho$  is the convolution of the true particle-level activity (underlying event, pile-up) with the detector response to the various particle

types. Therefore, the event-by-event and jet-by-jet offset correction can be defined as:

$$C_{\text{offset}}(p_{\text{T}}^{\text{raw}}, A_j, \rho) = 1 - \frac{(\rho - \langle \rho_{\text{UE}} \rangle) \cdot A_j}{p_{\text{T}}^{\text{raw}}} . \quad (3.10)$$

In the formula above,  $\langle \rho_{\text{UE}} \rangle$  represents the average  $p_{\text{T}}$ -density component due to the underlying event and electronics noise, and is measured in events with exactly one reconstructed primary vertex, i.e. no pile-up.

An additional pile-up subtraction method that is used in CMS is called *Charged Hadron Subtraction* (CHS). This method makes use of PF jets and exploits the excellent CMS tracking capabilities to identify and remove charged hadrons inside jets that are known to originate from pile-up vertices. This is a particle-by-particle method that is applied to jets before calculating the offset correction.

### MC calibration correction

The MC calibration is based on simulation and corrects the energy of the reconstructed jets such that it is equal on average to the energy of the generated jets. In order to evaluate this correction, simulated QCD events are generated and then processed through the CMS detector simulation, based on the GEANT4 software. The jet reconstruction in simulation is identical to the one applied to the data. Each reconstructed jet is spatially matched, in the  $\eta$ - $\phi$  space, to a generated jet by requiring  $\Delta R < 0.25$ . In each bin of the generated jet transverse momentum  $p_{\text{T}}^{\text{gen}}$ , the response variable  $\mathcal{R} = p_{\text{T}}^{\text{reco}}/p_{\text{T}}^{\text{gen}}$  and the reconstructed jet transverse momentum  $p_{\text{T}}^{\text{reco}}$ , are saved. The average correction in each bin is therefore defined as:

$$C_{\text{MC}}(p_{\text{T}}^{\text{reco}}) = \frac{1}{\langle R \rangle} , \quad (3.11)$$

and is expressed as a function of the average reconstructed jet  $p_{\text{T}}$ ,  $\langle p_{\text{T}}^{\text{reco}} \rangle$ .

### Relative jet energy scale

The goal of the relative jet energy scale correction is to make the jet response flat versus  $\eta$ . This is achieved by employing a Tag and Probe technique, selecting di-jet events in data. The size of this residual correction is of the order of 2–3% in the central  $\eta$  region, while it goes up to about 10% in the forward region.

### Absolute jet energy scale

The goal of the absolute jet energy scale correction is to make the jet response flat versus  $p_{\text{T}}$ . The absolute jet energy response is measured in the reference region  $|\eta| < 1.3$  with the *Missing Transverse Energy Projection Fraction* (MPF) method [80], using  $\gamma + \text{jets}$  and  $Z + \text{jets}$  events. The method is used to estimate the absolute jet energy correction and is based on the fact that  $\gamma + \text{jets}$  and  $Z + \text{jets}$  events have no intrinsic

$E_T^{\text{miss}}$  and that, at parton level, the  $\gamma$  and Z boson are perfectly balanced by the hadronic recoil in the transverse plane.

### Jet energy uncertainties

The uncertainties in the jet energy estimation arise from several sources. Generally these can be categorized as follows:

- physics modelling in MC such as showering, underlying event, etc.;
- MC modelling of true detector response and properties;
- potential biases in the methodologies used to estimate the corrections.

The sources are combined in different groups: absolute scale, relative scale, pile-up, jet flavor and time stability. In Fig. 3.4 the effect of each group of uncertainties is shown together with the total uncertainty obtained summing all sources in quadrature, both as a function of  $\eta$  and  $p_T$ . The pile-up uncertainty dominates for low values of the jet  $p_T$  while the relative and absolute uncertainties are more important in the high  $p_T$  region.

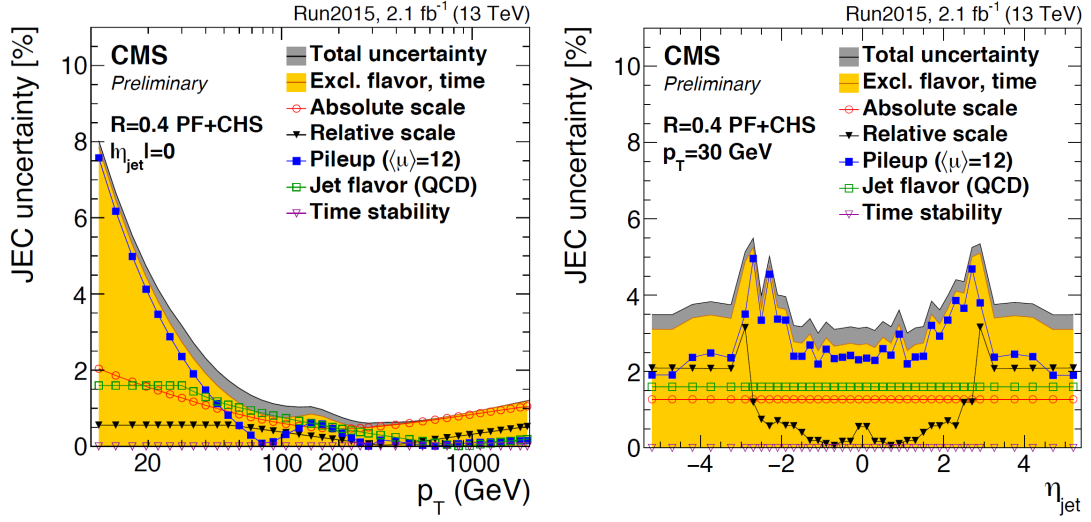


**Figure 3.4:** JEC uncertainties as a function of  $p_T$  (left) for jets reconstructed with  $\eta = 0$  and as a function of  $\eta$  (right) for jets with  $p_T = 30$  GeV. All jets are reconstructed with the PF technique and using the anti- $k_t$  algorithm with  $R = 0.4$ , after applying the CHS correction. Results are based on  $2.1 \text{ fb}^{-1}$  of data collected at 13 TeV.

### Jet energy resolution

Measurements show that the jet energy resolution (JER) in data is worse than in the simulation, therefore the simulated jets need to undergo a smearing procedure in order to have a better description of the data.

Reconstructed jets in simulated events are corrected for the jet energy resolution using a two step procedure. In the first step, the reconstructed jet  $p_T$  is scaled for the observed  $p_T$  difference between reconstructed and generated jets. This method only works for reconstructed jets that are well matched to generated jets, where the matching is based on  $\Delta R$  and  $\Delta p_T$  requirements. For reconstructed jets that do not fulfil the matching requirements, a gaussian smearing of the  $p_T$  distribution is applied in order to obtain the desired resolution.

### 3.3.3 Jet identification

Some basic quality criteria for jets may be required in order to avoid fake jets to be used, which can originate from noisy calorimetric cells or electronics noise. These criteria are collectively called *jet identification* (or Jet ID) and allow the rejection of badly reconstructed or noise jets while maintaining a very large fraction (about 99%) of real jets. Two working points are defined, loose and tight, based on requirements on the hadron and electromagnetic components of the jet. The sets of criteria are illustrated in Table 3.3 for PF jets with  $|\eta| < 3$ . For  $3 < |\eta| < 5$  the neutral electromagnetic fraction is required to be below 0.90 and the neutral multiplicity larger than 10 for both working points.

**Table 3.3:** Jet identification criteria for the loose and tight working points. The requirements are based on PF jets with  $|\eta| < 3$  for the neutral component and  $|\eta| < 2.4$  for the charged component.

Variable	Loose working point	Tight working point
$p_T$	$> 10 \text{ GeV}$	$> 10 \text{ GeV}$
Number of constituents	$> 1$	$> 1$
Charged hadron fraction	$> 0$	$> 0$
Neutral hadron fraction	$< 0.99$	$< 0.90$
Charged multiplicity	$> 0$	$> 0$
Charged electromagnetic fraction	$< 0.99$	$< 0.90$
Neutral electromagnetic fraction	$< 0.99$	$< 0.90$

An additional algorithm may be used to reduce the incidence of jets originating from pile-up. These jets arise mainly from the overlap of multiple low- $p_T$  jets originated from different interaction vertices, which combine forming single high- $p_T$  jets. The pile-up jet identification algorithm makes use of both vertex information, exploiting the charged component of the jet, and jet shape information to identify jets ascribable to pile-up.

### 3.4 Jet b tagging

Jets that arise from bottom quark hadronization (b-jets) are present in many physics processes, such as the decay of top quarks. The ability to accurately identify b-jets is crucial to reduce the otherwise overwhelming background from these processes to channels involving jets from gluons (g) and light-flavour quarks (u, d, s), and from c quarks fragmentation.

Algorithms for b-jets identification (also known as b tagging algorithms) exploit the long life time of b hadrons present in jets originating from the hadronization of b quarks. This long life time results in a decay of the b hadron that is displaced with respect to the primary interaction vertex. This displacement of a few millimetres results in the presence of displaced tracks from which a secondary vertex may be reconstructed. In addition, b hadrons have a probability of around 20% to decay to a muon or electron. Hence, also the presence of these charged leptons can be exploited for b-jets identification techniques and for measuring their performance with the collision data.

A variety of reconstructed physics objects, as tracks, vertices and identified leptons, can be used to build observables that discriminate between b and light-quark jets. Several b tagging algorithms have been developed by CMS, each one based on different input information. A common feature of all the algorithms is that each one yields a single discriminator value for every jet, which measures the likelihood that the jet has been produced by the hadronization of a b quark. The minimum thresholds on these discriminators define loose (“L”), medium (“M”), and tight (“T”) operating points with a misidentification probability for light-parton jets close to 10%, 1%, and 0.1%, respectively, at an average jet  $p_T$  of about 80 GeV. The misidentification probability, also known as mistag rate, is defined as the probability to wrongly identify a light-parton jet as a b-jet.

Some of the algorithms make use of the track impact parameters (IP) with respect to the primary vertex, defined as the distance between the primary vertex and the track at their point of closest approach, to distinguish the decay products of a b hadron from prompt tracks. The impact parameter has the same sign as the scalar product of the vector pointing from the primary vertex to the point of closest approach with the jet direction. Tracks originating from the decay of particles travelling along the jet axis will tend to have positive IP values. In contrast, the impact parameters of prompt tracks can have positive or negative IP values. The impact parameter significance, defined as the ratio of the IP to its estimated uncertainty, is used as an observable.

The *Track Counting* (TC) algorithm sorts tracks inside a jet by decreasing values of the IP significance. Although the ranking tends to bias the values for the first track to high positive IP significances, the probability to have several tracks with high positive values is low for light-parton jets. Therefore two different versions of the algorithm use the IP significance of the second and third ranked track as the discriminator value. These two versions of the algorithm are called *Track Counting High Efficiency* (TCHE) and *Track Counting High Purity* (TCHP), respectively.

A general extension of the TC algorithm, i.e. the *Jet Probability* (JP), combines the IP information of several tracks inside the jet, using an estimate of the likelihood that all tracks associated to the jet come from the primary vertex as a discriminating variable. A variant of the JP algorithm also exists in which the four tracks with the highest impact parameter significance get a higher weight in the jet probability calculation. This algorithm is referred to as *Jet B-Probability* (JBP).

A different approach consists in using the secondary vertices and the related kinematic variables, together with displaced tracks information, to discriminate between b- and non-b-jets. This algorithm is known as *Combined Secondary Vertex* (CSV)<sup>4</sup>. The magnitude and direction of the vector connecting the primary and secondary vertices are used as discriminating variables and quality requirements are imposed to secondary vertex candidates. In addition, the usage of displaced tracks information allows to increase the efficiency for events where no secondary vertex is found. Several variables related to secondary vertices and displaced tracks are used to build likelihood ratios that have a good discriminating power.

Two algorithms for reconstructing secondary vertices are exploited. For the first algorithm, the tracks associated to jets and fulfilling some quality requirements are used in the adaptive vertex reconstruction (AVR) algorithm [81]. The AVR is the algorithm used for CMS analyses during the 8 TeV data taking. In contrast with this method, the Inclusive Vertex Finder (IVF) algorithm is not seeded from tracks associated to reconstructed jets, but instead makes use of all the tracks in the event, with appropriate selections, to reconstruct the secondary vertices. The latter is the default algorithm used to reconstruct secondary vertices for CMS analyses using 13 TeV data.

A new b-jet identification algorithm has been recently developed, combining the discriminators provided by the JP and CSV algorithms with a Boosted Decision Tree (BDT) technique. This combined multivariate algorithm (cMVA) is found to slightly improve the b-jet identification efficiency.

The performance of these algorithms is determined using simulated  $t\bar{t}$  events, selecting events with at least one jet with  $p_T > 30$  GeV. This is shown in Fig. 3.5, where the b-jet identification efficiency versus the misidentification probability is reported for the various algorithms. This figure serves as an illustration as the b tagging performance depend on the  $p_T$  and  $\eta$  distribution of the jets, and need to be checked for each analysis phase space.

## 3.5 Missing transverse energy

In hadron colliders the longitudinal momentum (along the beam axis) carried by the incoming partons is not known, preventing the possibility to measure the total missing energy. Nevertheless, the initial transverse momentum carried by the incoming partons is expected to be zero, thereby, for the conservation of the momentum components, also the net momentum of all the particles in the final state of collisions

---

<sup>4</sup>An improved version of this algorithm, CSVv2, has been developed for Run 2 analyses.

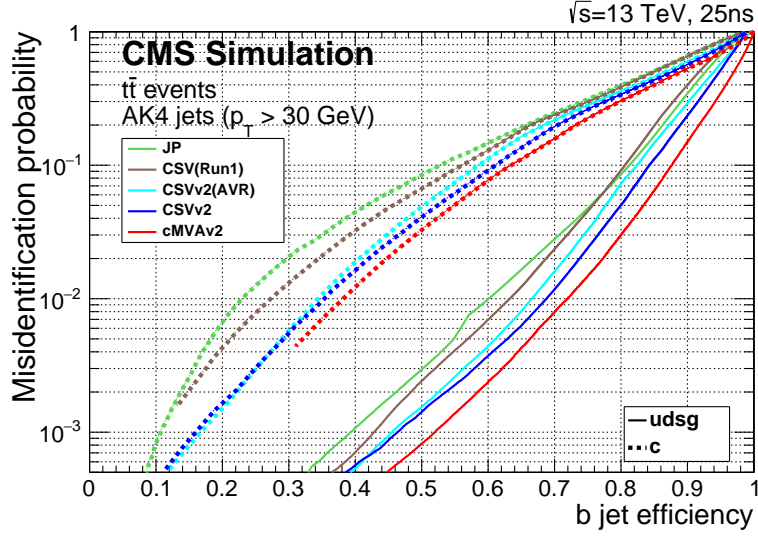


**Figure 3.5:** Performance of the b-jet identification efficiency algorithms demonstrating the probability for non-b-jets to be misidentified as b-jet as a function of the efficiency to correctly identify b-jets. The curves are obtained on simulated  $t\bar{t}$  events using anti- $k_t$  jets clustered with  $R = 0.4$  and requiring  $p_T > 30$  GeV.

must be zero. The missing transverse momentum ( $\vec{p}_T^{\text{miss}}$ ) is the momentum imbalance in the transverse plane of all the visible particles in the event, and its modulus is the missing transverse energy ( $E_T^{\text{miss}}$ ). The  $\vec{p}_T^{\text{miss}}$  vector is defined as the negative vectorial sum of transverse momenta of all reconstructed PF objects, as shown in the following equation:

$$\vec{p}_T^{\text{miss}} = - \sum_{\text{PF obj}} \vec{p}_T^{\text{PF obj}} , \quad (3.12)$$

where the sum extends over all the PF objects. A value of  $E_T^{\text{miss}}$  different from zero is a potential signature of the presence of particles in the event that have not interacted with the detector, such as neutrinos or particles predicted by some BSM models. Nevertheless, the presence of  $E_T^{\text{miss}}$  in the evenet can also be ascribable to detector inefficiencies.

In addition to imperfect resolution of all detectable and reconstructed physics objects, the  $E_T^{\text{miss}}$  measurement is also sensitive to overlapping detector signals from additional pile-up interactions (both in-time and out-of-time pile-up), particle misidentification, as well as detector malfunctions [82, 83]. The bias on the  $E_T^{\text{miss}}$  measurement is reduced by correcting the  $p_T$  of the jets with the jet energy corrections described in Sec. 3.3.2, and propagating the correction to  $E_T^{\text{miss}}$  according to:

$$\vec{p}_T^{\text{miss Type-I}} = \vec{p}_T^{\text{miss}} - \sum_{\text{jets}} (\vec{p}_T^{\text{JEC}} - \vec{p}_T^{\text{jet}}) , \quad (3.13)$$

where the superscript JEC refers to corrected jets. This correction, called “Type-I” correction, uses the JEC for all jets with  $p_T > 15$  GeV that have less than 90% of

their energy deposited in ECAL. Furthermore, if a muon is found inside a jet, its four-momentum is subtracted from the jet four-momentum before the correction and added back to the corrected object.

Anomalous high- $E_T^{\text{miss}}$  events can be ascribable to various phenomena. In the ECAL, spurious deposits may appear due to particles striking the sensors in the ECAL photodetectors, or from real showers with non-collision origins such as those caused by beam halo particles<sup>5</sup>. ECAL dead cells can cause real energy to have been missed, again leading to a spurious imbalance. In the HCAL, spurious energy can arise due to noise in the hybrid photodiode and readout electronics, as well as direct particle interactions with the light guides and photomultiplier tubes of the forward calorimeter. The spurious  $E_T^{\text{miss}}$  produced by these effects is estimated using dedicated algorithms, and a cleaning procedure is applied to data in order to remove the affected events.

### 3.5.1 $E_T^{\text{miss}}$ scale and resolution measurement

The performance (scale and resolution) of  $E_T^{\text{miss}}$  can be studied in events with an identified Z boson or an isolated photon. Momenta of leptons and photons can be reconstructed with good resolutions, around 1–6%, while momenta of jets are reconstructed with less precision, with typical resolutions of 5–15%. As a consequence, the  $E_T^{\text{miss}}$  resolution in Z or  $\gamma$ +jets events is dominated by hadronic activity in the event.

The comparison of the momenta of the vector boson with respect to the hadronic recoil system is used to measure the  $E_T^{\text{miss}}$  performance. In Fig. 3.6 the vector boson momentum in the transverse plane is shown as  $\vec{q}_T$ , and transverse momentum of the hadronic recoil, defined as the vectorial sum of the transverse momenta of all particles except the vector boson (or its decay products, in the case of Z bosons), is shown as  $\vec{u}_T$ . Momentum conservation in the transverse plane dictates that  $\vec{q}_T + \vec{u}_T + \vec{p}_T^{\text{miss}} = 0$ .

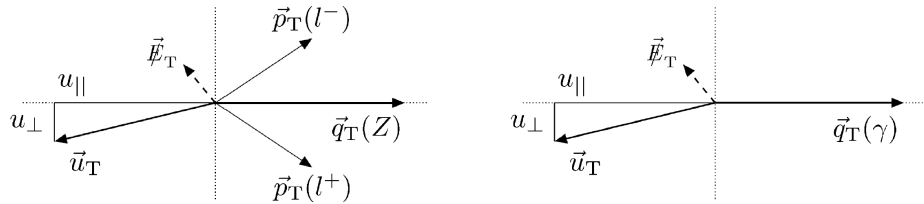


**Figure 3.6:** Illustration of the  $Z \rightarrow \ell^+\ell^-$  (left) and photon (right) event kinematics in the transverse plane.

The  $E_T^{\text{miss}}$  characteristics are evaluated using two components of  $\vec{u}_T$ , one parallel ( $u_{\parallel}$ ) and one perpendicular ( $u_{\perp}$ ) to the axis defined by  $\vec{q}_T$ . The distributions of these variables are parametrized using a convolution of a Breit-Wigner and a Gaussian

<sup>5</sup>This background, also known as *Machine-Induced Background*, originates mainly from interactions of the beam protons with the final set of collimators before the CMS experiment and from proton gas interactions.

distribution, i.e. a Voigtian distribution, which is found to provide a good description of the observables and is used to measure the resolution in  $u_{\parallel}$  and  $u_{\perp}$ ,  $\sigma(u_{\parallel})$  and  $\sigma(u_{\perp})$ , respectively. These resolutions are closely related to the  $E_T^{\text{miss}}$  resolution. The resolutions  $\sigma(u_{\parallel})$  and  $\sigma(u_{\perp})$  obtained using recent 13 TeV data are shown in Fig. 3.7.

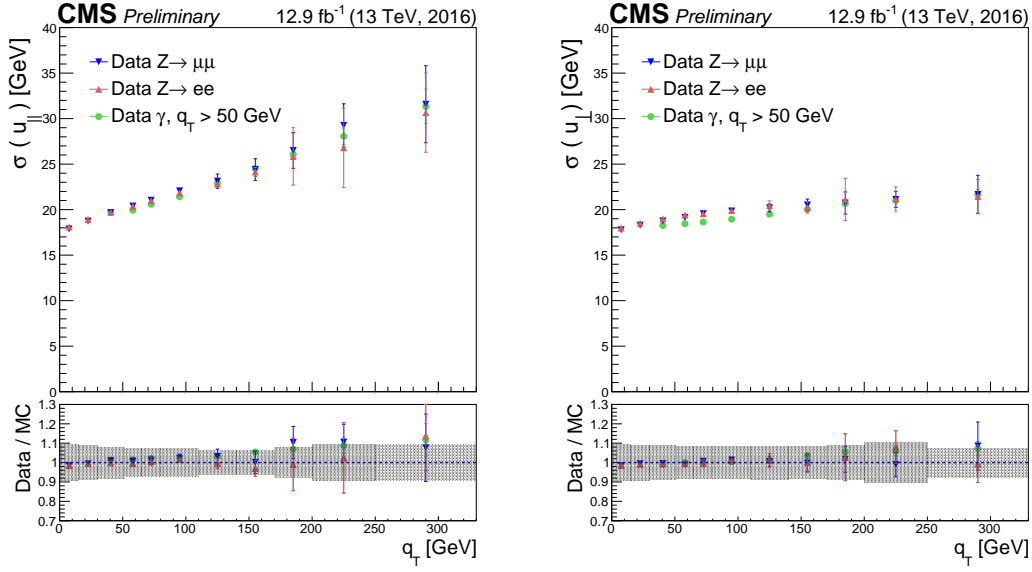


**Figure 3.7:** Resolutions  $\sigma(u_{\parallel})$  (left) and  $\sigma(u_{\perp})$  (right) for  $Z \rightarrow \mu^+\mu^-$ ,  $Z \rightarrow e^+e^-$  and  $\gamma$  events as a function of the vector boson  $p_T$ . The upper panels show the resolution measured in data and the bottom panels the data to simulation ratio.

## Chapter 4

# Measurement of the Higgs boson transverse momentum spectrum at 8 TeV using $H \rightarrow WW \rightarrow 2\ell 2\nu$ decays

Measurements of the fiducial cross sections and of several differential distributions, using the  $\sqrt{s} = 8$  TeV LHC data, have been reported by ATLAS [84–86] and CMS [87, 88] for the  $H \rightarrow ZZ \rightarrow 4\ell$  ( $\ell = e, \mu$ ) and  $H \rightarrow \gamma\gamma$  decay channels. In this chapter a measurement of the fiducial cross section times branching fraction ( $\sigma \times \mathcal{B}$ ) and  $p_T$  spectrum for Higgs boson production in  $H \rightarrow WW \rightarrow e^\pm \mu^\mp \nu\nu$  decays, based on  $\sqrt{s} = 8$  TeV LHC data, is reported [89].

Although the  $H \rightarrow WW \rightarrow 2\ell 2\nu$  channel has lower resolution in the  $p_T^H$  measurement compared to the  $H \rightarrow \gamma\gamma$  and  $H \rightarrow ZZ \rightarrow 4\ell$  channels due to neutrinos in the final state, the channel has a significantly larger  $\sigma \times \mathcal{B}$ , exceeding those for  $H \rightarrow \gamma\gamma$  by a factor of 10 and  $H \rightarrow ZZ \rightarrow 4\ell$  by a factor of 85 for a Higgs boson mass of 125 GeV [46], and is characterized by good signal sensitivity. Such sensitivity allowed the observation of a Higgs boson at the level of 4.3 (5.8 expected) standard deviations for a mass hypothesis of 125.6 GeV using the full LHC data set at 7 and 8 TeV [90].

The measurement is performed in a fiducial phase space defined by kinematic requirements on the leptons that closely match the experimental event selection.

The effect of the limited detector resolution, as well as the selection efficiency with respect to the fiducial phase space are corrected to particle level with an unfolding procedure [91], as explained in Sec. 4.7.

According to the “blinding” policy of the CMS Collaboration, the strategy of the analysis has been scrutinized and approved by a selected committee of internal reviewers before looking at the data in the signal region. This approach prevents the analysts from being biased by the data in the developing phase of the analysis. In this chapter the results after having looked at the data are shown. The same procedure also applies for the analyses described in Chapters 5 and 6.

## 4.1 Data sets and triggers

The data set used for this analysis corresponds to  $19.4 \text{ fb}^{-1}$  of proton-proton collisions at  $\sqrt{s} = 8 \text{ TeV}$ , collected by the CMS detector during 2012. Only data corresponding to good data taking quality are considered.

Events are required to fire one of the unprescaled single-electron, single-muon or muon-electron triggers. Due to the rather high LHC instantaneous luminosity the single-lepton triggers must have high HLT  $p_T$  thresholds, otherwise the rate of these triggers would be too large to be sustained. The double-lepton triggers allow to lower down the  $p_T$  thresholds while keeping a sustainable trigger rate, thus maintaining a good sensitivity to the Higgs boson signal, for which the lepton  $p_T$  can be rather small. A brief overview of the HLT  $p_T$  criteria on the leptons is given in Table 4.1. While the HLT lepton  $p_T$  thresholds of 17 and 8 GeV for the double lepton triggers accommodate the offline lepton  $p_T$  selection of 20 and 10 GeV, the higher  $p_T$  thresholds in the single lepton triggers help partially recovering double lepton trigger inefficiencies as a high  $p_T$  lepton is on average expected due to the kinematic of the Higgs decay.

**Table 4.1:** Transverse momentum thresholds applied in the lepton triggers at the HLT level. Double set of thresholds indicates the thresholds for each leg of the double lepton triggers.

Trigger path	Threshold
Single electron	$p_T > 27 \text{ GeV}$
Single muon	$p_T > 24 \text{ GeV}$
Muon-Electron	$p_T > 17 \text{ and } 8 \text{ GeV}$
Electron-Muon	$p_T > 17 \text{ and } 8 \text{ GeV}$

The trigger is not simulated in MC samples but the combined trigger efficiency is estimated from data and applied as a weight to all simulated events, as described in Sec. 3.2.8.

## 4.2 Monte Carlo samples

Several Monte Carlo event generators are used to simulate the signal and background processes:

- the first version of the POWHEG program (POWHEG V1) provides event samples for the  $H \rightarrow WW$  signal for the ggH and VBF production mechanisms, as well as  $t\bar{t}$  and  $tW$  processes [92], with NLO accuracy;
- the VH process is simulated using PYTHIA 6.426 [41];

- the  $\text{qq} \rightarrow W^+W^-$ , Drell-Yan, ZZ, WZ,  $W\gamma$ ,  $W\gamma^*$ , tri-bosons and  $W+\text{jets}$  processes are generated using the MADGRAPH 5.1.3 event generator;
- the  $\text{gg} \rightarrow W^+W^-$  process is generated using the GG2WW 3.1 generator [93] and its cross section is scaled to the approximate NLO prediction [94, 95].

For samples generated at leading-order (LO) accuracy in perturbative QCD, the CTEQ6L [96] set of parton distribution functions (PDF) is used, while CT10 [97] is used for next-to-leading order (NLO) ones. Cross section calculations at next-to-next-to-leading order (NNLO) are used for the  $H \rightarrow WW$  process [98]. The  $H \rightarrow WW$  process simulation is reweighted so that the  $p_T^H$  spectrum and inclusive production cross section closely match the SM calculations that have NNLO+NNLL QCD accuracy in the description of the Higgs boson inclusive production, in accordance with the LHC Higgs Cross Section Working Group recommendations [46]. The reweighting of the  $p_T^H$  spectrum is achieved by tuning the POWHEG generator, as described in detail in Ref. [99]. Cross sections computed with NLO QCD accuracy are used for the background processes [46]. The contribution of the  $t\bar{t}H$  production mechanism is checked to be negligible (below 1%) in the whole  $p_T^H$  spectrum and is not included in the analysis. In Fig. 4.1 the relative fraction of the four production mechanisms is shown for each  $p_T^H$  bin.

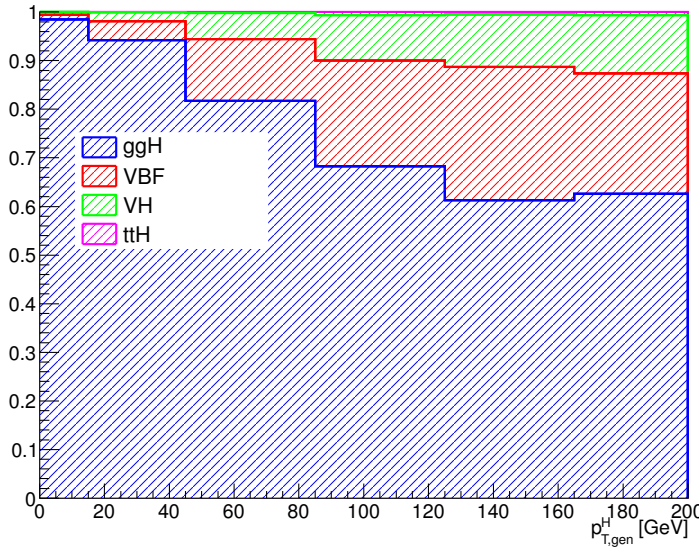


**Figure 4.1:** Relative fraction of ggH, VBF, VH and  $t\bar{t}H$  in each bin of the Higgs boson transverse momentum.

For all processes, the detector response is simulated using a detailed description of the CMS detector, based on the GEANT4 package [100].

Minimum bias events are superimposed on the simulated events to emulate the additional proton-proton interactions per bunch crossing. The pile-up multiplicity in

simulated events has been generated poissonianly sampling from a distribution similar to the one expected from data. The simulated events are reweighted to correct for observed differences between data and simulation in the number of pile-up events, as shown in Fig. 4.2.

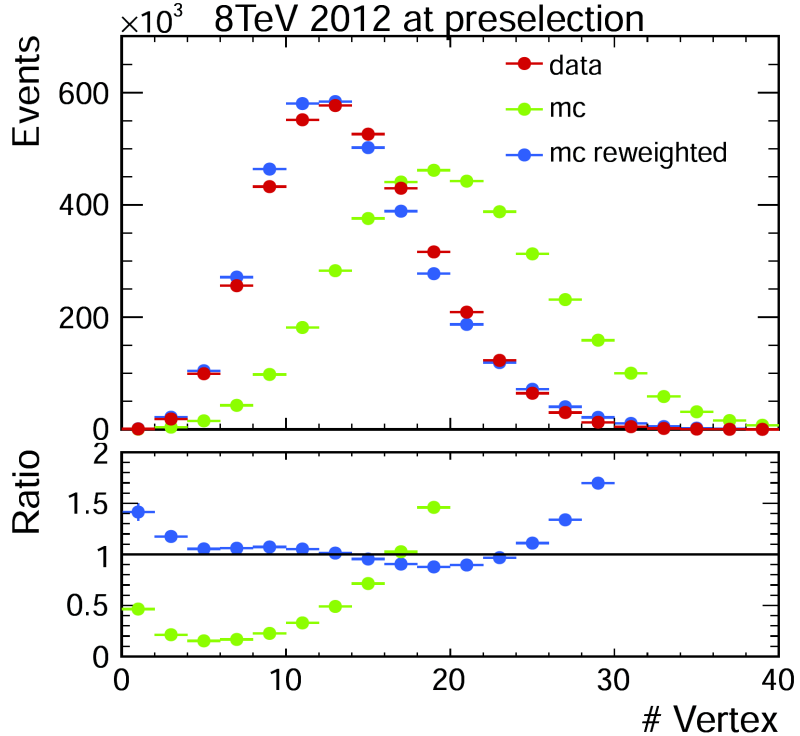


**Figure 4.2:** Distribution of the number of vertices in data and simulation, before and after applying the pile-up reweighting.

For the comparison of the measured unfolded spectrum with the theoretical predictions, two additional MC generators are used for simulating the SM Higgs boson production in the ggH process: HRES 2.3 [28, 29] and the second version of the POWHEG generator (POWHEG V2) [101]. HRES is a partonic level MC generator that computes the SM Higgs boson cross section at NNLO accuracy in QCD and performs the NNLL resummation of soft-gluon effects at small  $p_T$ . The central predictions of HRES are obtained including the top and bottom quark mass contribution to the gluon fusion loop, fixing the renormalization and factorization scale central values at a Higgs boson mass of 125 GeV. The cross section normalization is scaled, to take into account electroweak corrections (by a factor of 1.05) and effects of threshold resummation (by a factor of 1.06) [102, 103]. The upper and lower bounds of the uncertainties are obtained by scaling up and down both the renormalization and the factorization scales by a factor of two. The POWHEG V2 generator is a matrix element based generator that provides a NLO description of the ggH process in association with zero jets, taking into account the finite mass of the bottom and top

quarks. The POWHEG prediction is tuned using the POWHEG damping factor *hdump* of 104.17 GeV, in order to match the  $p_T^H$  spectrum predicted by HRES in the full phase space. This factor reduces the emission of additional jets in the high  $p_T$  regime, and enhances the contribution from the Sudakov form factor in the limit of low  $p_T$ . The POWHEG generator is interfaced to the JHUGEN generator version 5.2.5 [104–106] for the decay of the Higgs boson to a W boson pair and interfaced with PYTHIA 8 [42] for the simulation of parton shower and hadronization effects.

## 4.3 Analysis Strategy

The analysis presented here is based on that used in the previously published  $H \rightarrow WW \rightarrow 2\ell 2\nu$  measurements by CMS [90], modified to be inclusive in the number of jets. This modification significantly reduces the uncertainties related to the modelling of the number of jets produced in association with the Higgs boson.

The signal contribution is extracted performing a template binned likelihood fit, using the two-dimensional ( $m_{\ell\ell}, m_T$ ) shape for each background and signal process, as described in Sec. 4.6.

The  $m_{\ell\ell}$  variable represents the invariant mass of the two leptons in the event while  $m_T$  is the invariant transverse mass of the final state objects, and is defined as follows:

$$m_T = \sqrt{2p_T^{\ell\ell}E_T^{\text{miss}}(1 - \cos \Delta\phi(\vec{p}_T^{\ell\ell}, \vec{p}_T^{\text{miss}}))} , \quad (4.1)$$

where  $\vec{p}_T^{\ell\ell}$  is the dilepton transverse momentum vector and  $\Delta\phi(\vec{p}_T^{\ell\ell}, \vec{p}_T^{\text{miss}})$  the azimuthal angle between  $\vec{p}_T^{\ell\ell}$  and  $\vec{p}_T^{\text{miss}}$ .

### 4.3.1 Event reconstruction and selections

Electrons and muons used in the analysis are reconstructed using the PF technique as described in Sec. 3.2. In particular, muon candidates are required to be identified both as Tracker Muons and Global Muons.

Jets are reconstructed using the standard PF algorithm and using the anti- $k_t$  clustering algorithm with  $R = 0.5$ , as described in Sec. 3.3. If not specified otherwise, jets considered for jet counting are the ones with  $p_T > 30$  GeV.

In addition to the standard CMS PF  $E_T^{\text{miss}}$  a *projected*  $E_T^{\text{miss}}$  variable is also used. The *projected*  $E_T^{\text{miss}}$  is defined as the component of  $\vec{p}_T^{\text{miss}}$  transverse to the nearest lepton if the lepton is situated within the azimuthal angular window of  $\pm\pi/2$  from the  $\vec{p}_T^{\text{miss}}$  direction, or the  $E_T^{\text{miss}}$  itself otherwise. Since the  $E_T^{\text{miss}}$  resolution is degraded by pile-up, the minimum of two projected  $E_T^{\text{miss}}$  variables is used: one constructed from all identified particles (full projected  $E_T^{\text{miss}}$ ), and another constructed from the charged particles only (track projected  $E_T^{\text{miss}}$ ).

Background events from  $t\bar{t}$  and  $tW$  production are rejected applying soft-muon veto and b tagging veto. The soft-muon algorithm is designed to identify muons from b quark decays requiring loose muon identification selections, as described in

Sec. 3.2.1, and low relative isolation (greater than 0.1 for muons with  $p_T > 20$  GeV). Events containing at least one muon satisfying these requirements are rejected by the soft-muon veto.

The b tagging veto rejects events that contain jets identified as b-jets using two different algorithms for high and low  $p_T$  jets (see Sec. 3.4). For jets with  $p_T$  between 10 and 30 GeV, the TCHE algorithm is used. Low- $p_T$  jets passing the TCHE discriminant threshold of 2.1 are tagged as b-jets. For jets with  $p_T > 30$  GeV, a better performing algorithm, JP, is used. Jets are identified as b-jets by the JP algorithm if the discriminating variable has a value above 1.4. In the following, a b-tagged jet is defined as a jet, within  $|\eta| < 2.4$  (b tagging requires the tracker information), and with a value of the discriminating variable above the mentioned thresholds for the two algorithms.

The event selection consists of several steps. The first step is to select WW-like events applying a selection that consists of the following set of cuts:

- **Lepton preselection:**
  - two opposite charge and different flavour ( $e\mu$ ) isolated leptons reconstructed in the event;
  - $|\eta| < 2.5$  for electrons and  $|\eta| < 2.4$  for muons;
  - $p_T > 20$  GeV for the leading lepton. For the trailing lepton, the transverse momentum is required to be larger than 10 GeV.
- **Extra lepton veto:** the event is required to have two and only two leptons with opposite charge passing the lepton selection.
- **$E_T^{\text{miss}}$  preselection:** particle flow  $E_T^{\text{miss}}$  is required to be greater than 20 GeV.
- **projected  $E_T^{\text{miss}}$  selection:** minimum projected  $E_T^{\text{miss}}$  required to be larger than 20 GeV.
- **Di-lepton mass cut:**  $m_{\ell\ell} > 12$  GeV in order to reject low mass resonances and QCD backgrounds.
- **Di-lepton  $p_T$  cut:**  $p_T^{\ell\ell} > 30$  GeV to reduce the contribution of W+jets and DY to  $\tau\tau$  backgrounds.
- **Transverse mass:**  $m_T > 60$  GeV to reject DY to  $\tau\tau$  events.

The requirement of different flavour leptons in the final state is important in order to suppress the sizeable contribution of backgrounds containing a same flavour lepton pair originating from Z boson decay.

Events surviving these requirements are dominantly those where a top quark-antiquark pair is produced and both W bosons, which are part of the top quark decay chain, decay leptonically (dileptonic  $t\bar{t}$ ). Two different selections are used depending

on the number of jets in the event. This is done to suppress the top quark background both in the low  $p_T^H$  region, where 0-jets events have the largest contribution, and for higher  $p_T^H$  values where also larger jet multiplicity events are important. The selection for 0-jets events relies on the soft-muon veto and on a soft jet (with  $p_T < 30 \text{ GeV}$ ) b tagging veto. The latter requirement exploits the TCHE algorithm to reject soft jets that are likely to come from b quarks hadronization.

For events with a jet multiplicity greater or equal than one, a different selection is applied. In this case we exploit the good b tagging performances of the JP tagger to reject all the jets with  $p_T > 30 \text{ GeV}$  that are likely to come from b quarks hadronization. The analysis selection requires to have no events containing b-tagged jets with  $p_T > 30 \text{ GeV}$ .

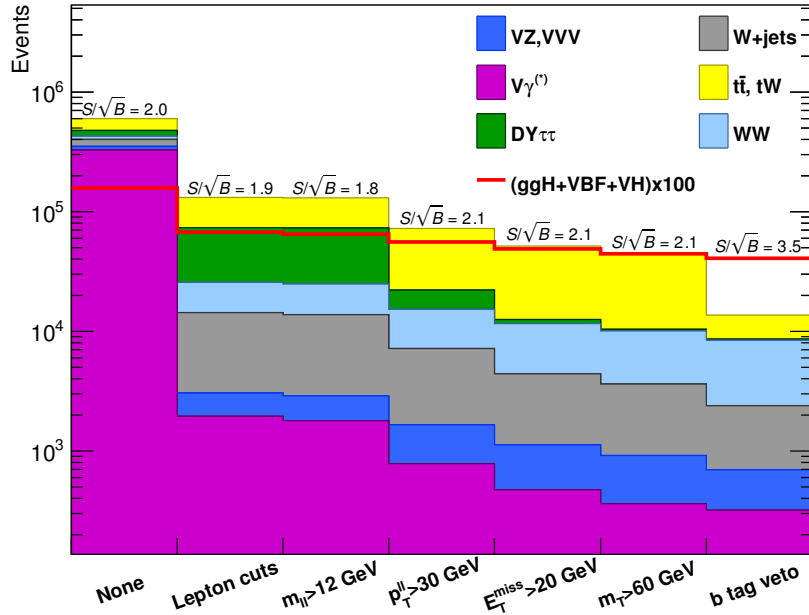


**Figure 4.3:** Effect of selection cuts on simulated samples. The signal (red line) is multiplied by 100 and superimposed on stacked backgrounds. In each bin, corresponding to a different selection, is reported the expected number of events in MC at a luminosity of  $19.46 \text{ fb}^{-1}$ .

A cut-flow plot is shown in Fig. 4.3, illustrating the effect of each selection using signal and background simulations. In the first bin, labelled as “No cut”, only a very loose selection is applied and the bin content corresponds to the total expected number of events with a luminosity of  $19.4 \text{ fb}^{-1}$ . All the events in this bin have at least two leptons with a loose transverse momentum cut of  $8 \text{ GeV}$ . In the following bin the lepton cuts are applied, including the requirement to have two opposite sign and different flavour leptons and the extra lepton veto. Then all the other selections are progressively reported, showing the effect of each cut on the background and signal yields. For each selection the expected significance ( $S/\sqrt{B}$ ) is also shown, which, after

the full selection requirements, reaches a maximum value of about 3.5. The expected significance is computed neglecting all sources of uncertainties.

### 4.3.2 Simulation efficiencies and scale factors

The efficiencies for the identification and isolation of the electrons and muons are measured in data and simulation selecting a pure sample of leptons coming from the  $Z \rightarrow \ell\ell$  decay, and using the Tag and Probe technique described in Sec. 3.2.7. The efficiencies for data and simulation are used as scale factors to correct the simulated events to precisely model the data.

The trigger efficiency is measured in data and applied to simulation as explained in Sec. 3.2.8.

The efficiency of b tagging algorithms is not well simulated by MC generators and discrepancies may occur with respect to the data. For this reason is important to measure the b tagging efficiency and the misidentification probability for the given algorithms both in data and simulation, and to correct the simulated events using scale factors. This affects not only the top quark background estimation, but also the other backgrounds and the signal. As an example, if a light-parton jet in a signal event was misidentified as a b-jet, this event would be rejected by the b-jet veto.

In this analysis, the b tagging efficiency and the misidentification probability are measured both in data and simulation, selecting a control sample enriched in b-jets, and using a Tag and Probe technique similar to the one described in Sec. 3.2.7. The method used to estimate the efficiency of the JP b tagging algorithm is described below, but this method is extendible to any other algorithm.

The control sample is defined selecting the events that pass the selections listed in Sec. 4.3.1, and have at least two jets with  $p_T$  greater than 30 GeV. If the leading jet has a JP discriminator value above the threshold of 0.5, it is considered a *tag*, and the sub-leading jet is the *probe*. In order to avoid any bias that could arise from the probe being always the sub-leading jet, the pair is tested also in reverse order, i.e. sub-leading jet is tested against the *tag* selection, and in case it passes, the leading jet is used as *probe* forming an independent *tag-probe* pair. If the *probe* jet has a discriminator value above the threshold used in the analysis, i.e.  $> 1.4$ , then the *tag-probe* pair is called a *tag-pass-probe* pair. Otherwise it is identified as a *tag-fail-probe* pair.

If the *tag* selection was sufficient to suppress any non top quark event, one could estimate the efficiency by dividing the number of *tag-probe* pairs in which the *probe* passes the analysis JP requirement by the total number of *tag-probe* pairs. However this is not the case, since the contamination due to other background sources is not negligible. In order to estimate the efficiency in the presence of background, a variable that discriminates between true b-jets and other jets in a  $t\bar{t}$  sample is needed. This variable is the  $p_T$  of the *probe* jet. For real b-jets this variable has a peak around 60 GeV, while it has a broad distribution for other types of jets.

The efficiencies are estimated performing a  $\chi^2$  simultaneous fit of the *probe*  $p_T$

spectrum in two different categories: one containing events with a *tag-pass-probe* pair and the other containing events with a *tag-fail-probe* pair. The normalisations in the two categories are linked by the following formulas:

$$\begin{aligned} N_{\text{TPP}} &= N_s \varepsilon_s + N_b \varepsilon_b \\ N_{\text{TFP}} &= N_s (1 - \varepsilon_s) + N_b (1 - \varepsilon_b) \quad , \end{aligned} \quad (4.2)$$

where:

- $N_{\text{TPP}}$  is the number of *tag-pass-probe* pairs;
- $N_{\text{TFP}}$  is the number of *tag-fail-probe* pairs;
- $N_s$  is the number of *tag-probe* pairs in which the *probe* is a b-jet;
- $N_b$  is the number of *tag-probe* pairs in which the *probe* is not a b-jet;
- $\varepsilon_s$  is the efficiency to identify a b-jet, i.e. the b tagging efficiency;
- $\varepsilon_b$  is the probability to misidentify a non b-jet as a b-jet, i.e. the misidentification probability<sup>1</sup>.

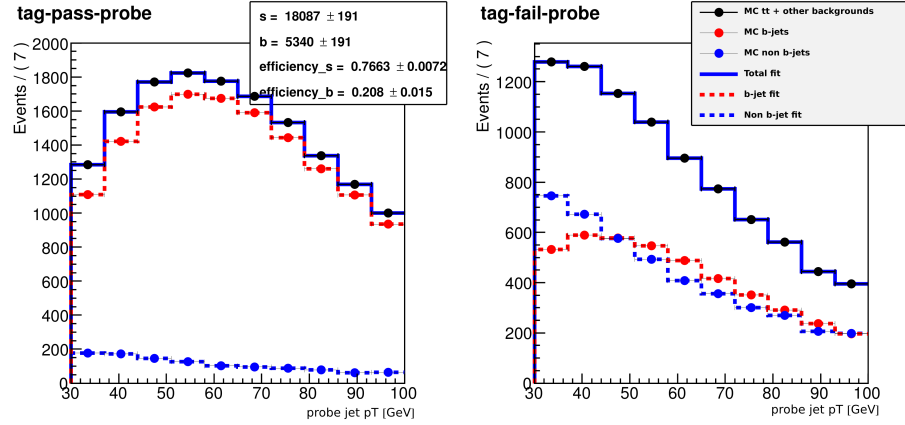


**Figure 4.4:** Results of the simultaneous fit of the *tag-pass-probe* and *tag-fail-probe* pairs in the MC simulation.

The  $p_T$  shapes of the *probe* jet used in the fit are taken from simulation, where the real flavour of the jet is known, both for the *tag-pass-probe* and *tag-fail-probe* categories. To check the consistency of the fitting procedure, a closure test fitting the

<sup>1</sup>In these naming convention, the subscript “s” stays for “signal”, since the b-jets represent the signal in this method. Similarly, the “b” subscript stays for “background”, identifying the cases where the *probe* is not a b-jet

simulation itself has been performed. The result of the fit on MC simulation is shown in Fig. 4.4. The relevant efficiencies are:

$$\begin{aligned}\varepsilon_s^{\text{MC}} &= 0.766 \pm 0.007 \\ \varepsilon_b^{\text{MC}} &= 0.208 \pm 0.015 .\end{aligned}\quad (4.3)$$

These values are consistent with the true value of the b tagging efficiency in simulation. The true value is computed by selecting jets that are matched within a cone of  $\Delta R < 0.5$  with a generator level b quark, and counting the fraction of those that have a JP discriminator above the threshold of 1.4. This check also assures that the *tag-probe* method does not introduce any bias within the simulation statistic accuracy.

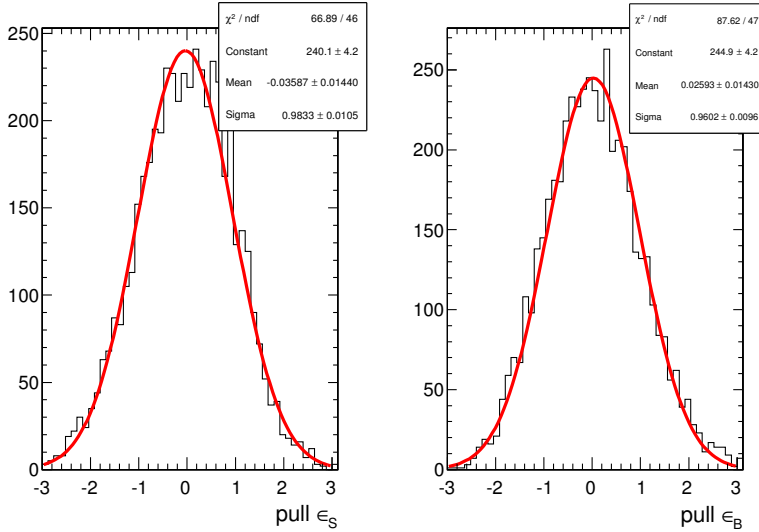


**Figure 4.5:** Pulls distribution for the  $\varepsilon_s$  and  $\varepsilon_b$  efficiencies obtained with MC toy simulations.

In order to assess the robustness of the fit, 5000 toy simulated samples have been generated with a statistics equivalent to the one expected in data and the same fit is performed for each of them. All the 5000 fit succeeded, and the pull distributions for  $\varepsilon_s$  and  $\varepsilon_b$  parameters are shown in Fig. 4.5. The distributions represent the *pull* of the efficiencies measured in the fit, where the pull variable for each toy  $i$  is defined as:

$$\text{pull}(\varepsilon_{s(b)}) = \frac{\varepsilon_{s(b)}^{\text{true}} - \varepsilon_{s(b)}^i}{\sigma(\varepsilon_{s(b)}^i)} , \quad (4.4)$$

where  $\sigma(\varepsilon_{s(b)}^i)$  is the uncertainty on the efficiency extracted from the fit. The pull distributions are centred on zero and have  $\sigma$  close to one, as expected.

Before running the fit on data, the shapes used in the fit have been validated. To do so, a very pure phase space enriched in b jets has been defined by selecting events containing exactly two jets with a JP discriminator greater than 1.5 and no additional

b-tagged jet, rejecting also events containing jets with  $p_T$  smaller than 30 GeV. On this very pure sample, data have been compared against the shape used to fit the true b-jets in the *tag-pass-probe* distribution. The result is shown in Fig. 4.6 and shows good agreement within uncertainties.

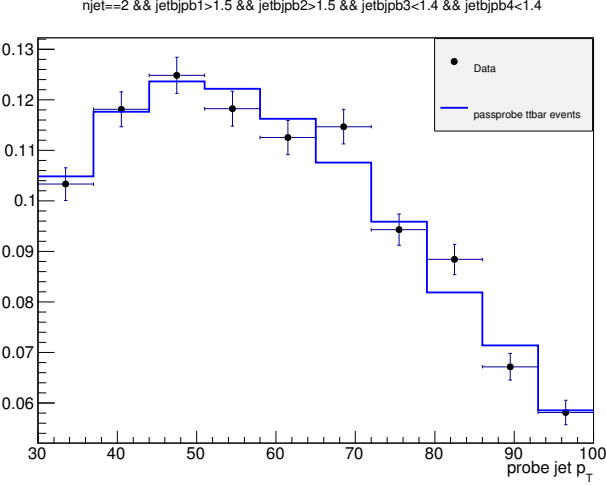


**Figure 4.6:** Shape comparison for the  $p_T$  spectrum of the *probe* jet in data and simulation in a very pure phase space enriched in b-jets.

Finally the fit has been performed on data, as shown in Fig. 4.7, providing the following efficiencies:

$$\begin{aligned}\varepsilon_s^{\text{Data}} &= 0.77 \pm 0.02 \\ \varepsilon_b^{\text{Data}} &= 0.12 \pm 0.05\end{aligned}\quad (4.5)$$

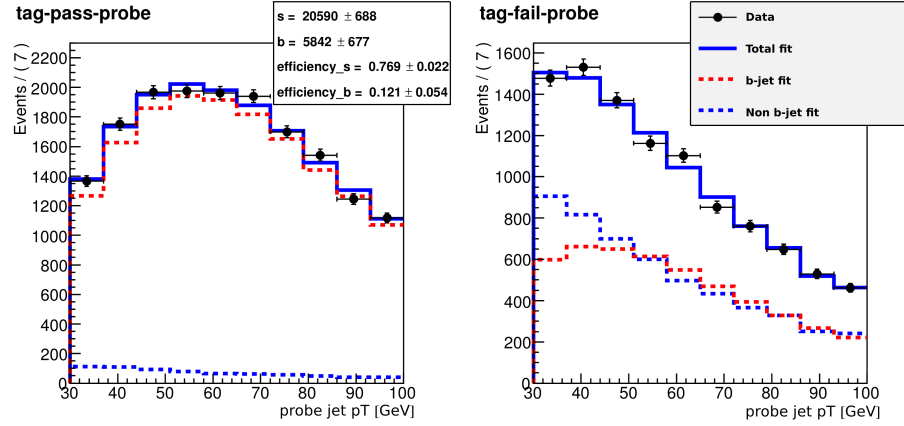


**Figure 4.7:** Results of the simultaneous fit of the *tag-pass-probe* and *tag-fail-probe* pairs in the data.

Further studies have been performed to assess the effect of the relative uncertainty on the  $t\bar{t}$  and  $tW$  event fractions. The procedure described above has been applied to different simulation templates obtained varying the  $t\bar{t}$  and  $tW$  fractions within theoretical uncertainties, and the effect on the parameters extracted with the fit procedure is found to be well below the fit uncertainties.

The ratio of the efficiency measured in data and simulation represents a per-jet scale factor that can be used to reweight the simulated events. The weights to be applied event-by-event depend on the particular jet configuration in the events themselves. For the signal region ( $SR$ ), in which a b tagging veto is required, the event weight to be applied is given by:

$$w_{SR} = \prod_{N_{b\text{-jets}}} \left( \frac{1 - \varepsilon_s^{\text{Data}}}{1 - \varepsilon_s^{\text{MC}}} \right) \prod_{N_{\text{non}-b\text{-jets}}} \left( \frac{1 - \varepsilon_b^{\text{Data}}}{1 - \varepsilon_b^{\text{MC}}} \right) , \quad (4.6)$$

where  $N_{b\text{-jets}}$  and  $N_{\text{non}-b\text{-jets}}$  are the number of true b-jets and the number of non-b-jets in the simulated event, respectively. This weight is valid if the a b tagging veto is applied. If instead the b tagging veto is reverted, also the event weight has to be modified. This is done, for example, when one wants to define a  $t\bar{t}$  enriched control region ( $CR_{t\bar{t}}$ ) for the purpose of measuring the contribution of this background in a phase space orthogonal to the signal region. One simple way to define this control region is to require the leading jet in the event to be b-tagged. Therefore, the simulated events falling in this category must be reweighted using the following weight:

$$w_{CR_{t\bar{t}}} = \begin{cases} \varepsilon_s^{\text{Data}} / \varepsilon_s^{\text{MC}}, & \text{if the leading jet is a b-jet} \\ \varepsilon_b^{\text{Data}} / \varepsilon_b^{\text{MC}}, & \text{if the leading jet is not a b-jet} \end{cases} \quad (4.7)$$

### 4.3.3 Fiducial phase space

The Higgs boson transverse momentum is measured in a particle level fiducial phase space, whose definition is chosen in order to minimize the dependence of the measurements on the underlying model of the Higgs boson production and decay properties.

The exact requirements are determined by considering the two following correlated quantities: the reconstruction efficiency for signal events originating from within the fiducial phase space (fiducial signal efficiency  $\varepsilon_{\text{fid}}$ ), and the ratio of the number of reconstructed signal events that are from outside the fiducial phase space (“out-of-fiducial” signal events) to the number from within the fiducial phase space. The requirement of having a small fraction of out-of-fiducial signal events, while at the same time preserving a high value of the fiducial signal efficiency  $\varepsilon_{\text{fid}}$ , leads to fiducial requirements at the generator level on the low-resolution variables,  $E_T^{\text{miss}}$  and  $m_T$ , that are looser with respect to those applied in the reconstructed event selection.

The fiducial phase space used for the cross section measurements is defined at the particle level by the requirements given in Table 4.2. The leptons are defined as Born-level leptons, i.e. before the emission of final-state radiation (FSR), and are

required not to originate from leptonic  $\tau$  decays. The effect of including FSR is found to modify  $\epsilon_{\text{fid}}$  at most of about 5%. For the VH signal process, the two leptons are required to originate from the  $H \rightarrow WW \rightarrow 2\ell 2\nu$  decays in order to avoid including leptons coming from the associated W or Z boson.

**Table 4.2:** Summary of requirements used in the definition of the fiducial phase space.

Physics quantity	Requirement
Leading lepton $p_T$	$p_T > 20 \text{ GeV}$
Subleading lepton $p_T$	$p_T > 10 \text{ GeV}$
Pseudorapidity of electrons and muons	$ \eta  < 2.5$
Invariant mass of the two charged leptons	$m_{\ell\ell} > 12 \text{ GeV}$
Charged lepton pair $p_T$	$p_T^{\ell\ell} > 30 \text{ GeV}$
Invariant mass of the leptonic system in the transverse plane	$m_T^{\ell\ell\nu\nu} > 50 \text{ GeV}$
$E_T^{\text{miss}}$	$E_T^{\text{miss}} > 0$

A detailed description of the fiducial region definition and its optimization is given in appendix A.

#### 4.3.4 Binning of the $p_T^H$ distribution

Experimentally, the Higgs boson transverse momentum is reconstructed as the vector sum of the lepton momenta in the transverse plane and  $E_T^{\text{miss}}$ .

$$\vec{p}_T^H = \vec{p}_T^{\ell\ell} + \vec{p}_T^{\text{miss}} \quad (4.8)$$

Compared to other differential analyses of the Higgs cross section, such as those in the ZZ and  $\gamma\gamma$  decay channels, this analysis has to cope with the limited resolution due to the  $E_T^{\text{miss}}$  entering the transverse momentum measurement. The effect of the limited  $E_T^{\text{miss}}$  resolution has two main implications on the analysis strategy: the first one is that the choice of the binning of the  $p_T^H$  spectrum needs to take into account the detector resolution; the second implication is that migrations of events across bins are significant and an unfolding procedure needs to be applied to correct for selection efficiencies and bin migration effects.

Given these aspects, the criterion that is used to define the  $p_T^H$  bin size is devised to keep under control the bin migrations due to the finite resolution. For any given bin  $i$ , the purity  $P_i$  of the signal sample is defined as the number of events that are generated and also reconstructed in that bin,  $N_i^{\text{GEN}|\text{RECO}}$ , divided by the number of events reconstructed in the same bin,  $N_i^{\text{RECO}}$ :

$$P_i = \frac{N_i^{\text{GEN}|\text{RECO}}}{N_i^{\text{RECO}}} \quad . \quad (4.9)$$

The bin width is chosen in such a way as to make the smallest bins able to ensure a purity of about 60%, based on a ggH simulated sample. Following this prescription, the whole  $p_T^H$  range is divided in the following six bins: [0–15] GeV, [15–45] GeV, [45–85] GeV, [85–125] GeV, [125–165] GeV, [165– $\infty$ ] GeV.

The fiducial signal efficiency  $\varepsilon_{\text{fid}}$  and the fraction of out-of-fiducial signal events,  $f_{\text{out-of-fid}}$ , are different in each  $p_T^H$  bin and depend on the definition of the fiducial phase space. In Fig. 4.8 the  $\varepsilon_{\text{fid}}$  and  $f_{\text{out-of-fid}}$  parameters are shown in each  $p_T^H$  bin for different definitions of the fiducial phase space. In particular, they have been evaluated adding the requirements reported in Table 4.2 in sequence, starting from a fiducial phase space defined just by the lepton  $p_T$  and  $\eta$  selections, together with the different flavour requirement, and adding each time an additional selection until the full fiducial phase space is obtained. In this way, the effect of every single selection (or group of selections) on  $\varepsilon_{\text{fid}}$  and  $f_{\text{out-of-fid}}$  can be assessed. Since the variables related to leptons are measured with good resolution, the effect of including the lepton selections in the fiducial phase space is to increase  $\varepsilon_{\text{fid}}$  keeping  $f_{\text{out-of-fid}}$  constant. Instead, the effect of including low-resolution variables, such as  $m_T$ , is to increase both  $\varepsilon_{\text{fid}}$  and  $f_{\text{out-of-fid}}$ . Nevertheless, the  $f_{\text{out-of-fid}}$  parameter is different from zero even if only lepton cuts are taken into account. This is ascribable to two different aspects: the first one is that in the fiducial definition electrons and muons are required not to originate from  $\tau$  decays; the second one is instead related to the VH production mechanism, i.e. to the fact that leptons coming from the associated boson are not included.

The overall values integrating over  $p_T^H$  are  $\varepsilon_{\text{fid}} = 0.362 \pm 0.005$  and  $f_{\text{out-of-fid}} = 0.126 \pm 0.004$  respectively, where only statistical uncertainties are taken into account.

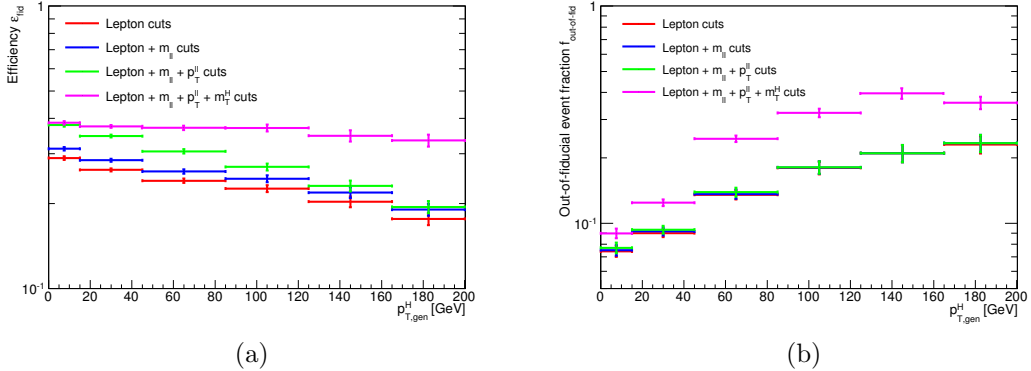


**Figure 4.8:** Fiducial signal efficiency  $\varepsilon_{\text{fid}}$  and fraction of out-of-fiducial signal events  $f_{\text{out-of-fid}}$  in each bin of the generator level  $p_T^H$ .

If a wider acceptance is defined, only requiring that the Higgs boson decays to WW and then to  $2\ell 2\nu$ , the efficiency becomes  $\epsilon = 0.0396 \pm 0.0003$  and the fraction of out-of-fiducial signal events is zero.

## 4.4 Background estimation

The signal extraction procedure requires the determination of the normalization and the  $(m_{\ell\ell}, m_T)$  shape for each background source. In this section, the methods used to estimate these quantities are described.

### 4.4.1 Top quark background

In this analysis the top quark background is divided into two different categories depending on the number of jets in the event. Different selections are applied in the two categories, especially concerning the b tagging requirements, as explained in Sec. 4.3.1. A top quark enriched control region,  $CR_{t\bar{t}}$ , is defined for each of the two categories in order to estimate the process cross section directly from data. For the category with 0 counted jets, the control region is defined selecting events containing at least one soft jet, i.e. with  $p_T < 30 \text{ GeV}$ , that is identified as a b-jet by the TCHE and soft-muon algorithms. In the category with more than 0 counted jets, a similar control region is defined requiring events to contain at least one jet with  $p_T > 30 \text{ GeV}$  identified by the JP algorithm. The control regions defined in this way are very pure and can be used to normalize the simulation prediction to the data (data-driven method).

Since the  $CR_{t\bar{t}}$  control region and the signal region ( $SR$ ) are orthogonal, a factor  $\alpha$  connecting the number of events in the two has to be evaluated using simulation:

$$\alpha = \frac{N_{\text{MC}}^{SR}}{N_{\text{MC}}^{CR_{t\bar{t}}}} , \quad (4.10)$$

where  $N_{\text{MC}}^{SR}$  and  $N_{\text{MC}}^{CR_{t\bar{t}}}$  are the number of  $t\bar{t}$  events obtained from simulation in the  $SR$  and  $CR_{t\bar{t}}$  regions, respectively. The number of  $t\bar{t}$  events in data in the  $CR_{t\bar{t}}$  region,  $N_{\text{Data}}^{CR_{t\bar{t}}}$ , can be estimated subtracting the expected number of non  $t\bar{t}$  events. Finally, the number of expected events in the  $SR$  region  $N_{\text{Data}}^{SR}$ , can be obtained using the following formula:

$$N_{\text{Data}}^{SR} = \alpha N_{\text{Data}}^{CR_{t\bar{t}}} . \quad (4.11)$$

Before applying this procedure, the simulated events have been reweighted using the b tagging efficiency scale factors described in Sec. 4.3.2.

In the 0 jets category the residual top quark background is very small, and its normalization is estimated inclusively in  $p_T^H$ . For the other category, the aforementioned procedure is applied independently in each  $p_T^H$  bin, rather than inclusively, because an overall normalization factor would not be able to cover the discrepancies between data and simulation from bin to bin. This can be understood looking at the  $p_T^H$  distribution in the  $CR_{t\bar{t}}$  region, shown in Fig. 4.9, where data and simulation are compared. The results of the method discussed before are listed in Tab. 4.3 for each bin of  $p_T^H$ .

A comparison of the  $m_{\ell\ell}$  distributions in the  $CR_{t\bar{t}}$  region for data and simulation is shown in Fig. 4.10, separately for each  $p_T^H$  bin and after the application of the data-

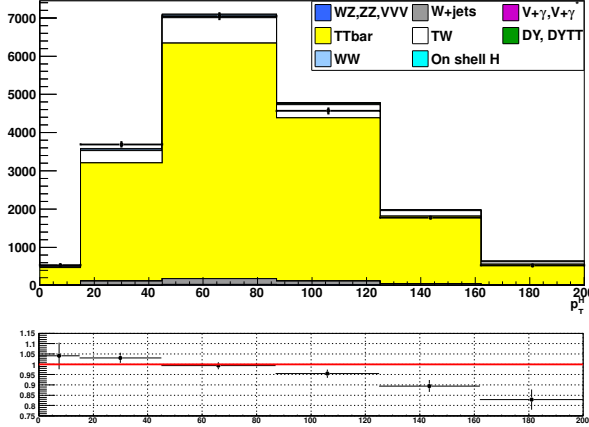


**Figure 4.9:** Distribution of  $p_T^H$  in the  $CR_{t\bar{t}}$  region, comparing data and simulation.

**Table 4.3:** Data driven scale factors related to the top quark background estimation.

$p_T^H$ [ GeV ]	$N_{\text{Data}}^{CR_{t\bar{t}}}$	$N_{\text{MC}}^{CR_{t\bar{t}}}$	$N_{\text{MC}}^{SR}$	$\alpha$	$\Delta\alpha$
[0–15]	406.7	358.8	117.8	0.33	0.08
[15–45]	2930.1	2703.4	859.1	0.32	0.07
[45–85]	5481.0	5207.5	1506.1	0.29	0.07
[85–125]	4126.4	4032.6	861.2	0.21	0.05
[125–165]	1612.6	1654.3	304.7	0.18	0.06
[165– $\infty$ ]	647.5	760.4	201.7	0.27	0.15

driven factors. The agreement between data and simulation is found to be satisfactory within uncertainties.

#### 4.4.2 WW background

First of all, the  $m_{\ell\ell}$  and  $m_T$  shapes of the  $qq \rightarrow W^+W^-$  background process have been compared to the data in a signal free phase space, as shown in Fig. 4.11. The signal-free region is defined requiring the preselections described in Sec. 4.3.1 with the additional cut  $m_{\ell\ell} > 70$  GeV. The comparison, which is performed inclusively in  $p_T^H$  in the 0 and 1 jet categories, shows a good data to simulation agreement within uncertainties.

In this analysis the  $qq \rightarrow W^+W^-$  background normalization is left free to float in each of the six  $p_T^H$  bins to match the data during the fitting procedure. This choice helps mitigating the  $p_T^H$  shape difference between data and simulation. This difference is due to missing higher order QCD corrections in the adopted simulation, obtained using the MADGRAPH generator. In fact, as shown in Fig. 4.12, the theoretical calculations for this process performed at NLO QCD accuracy and including soft-gluon

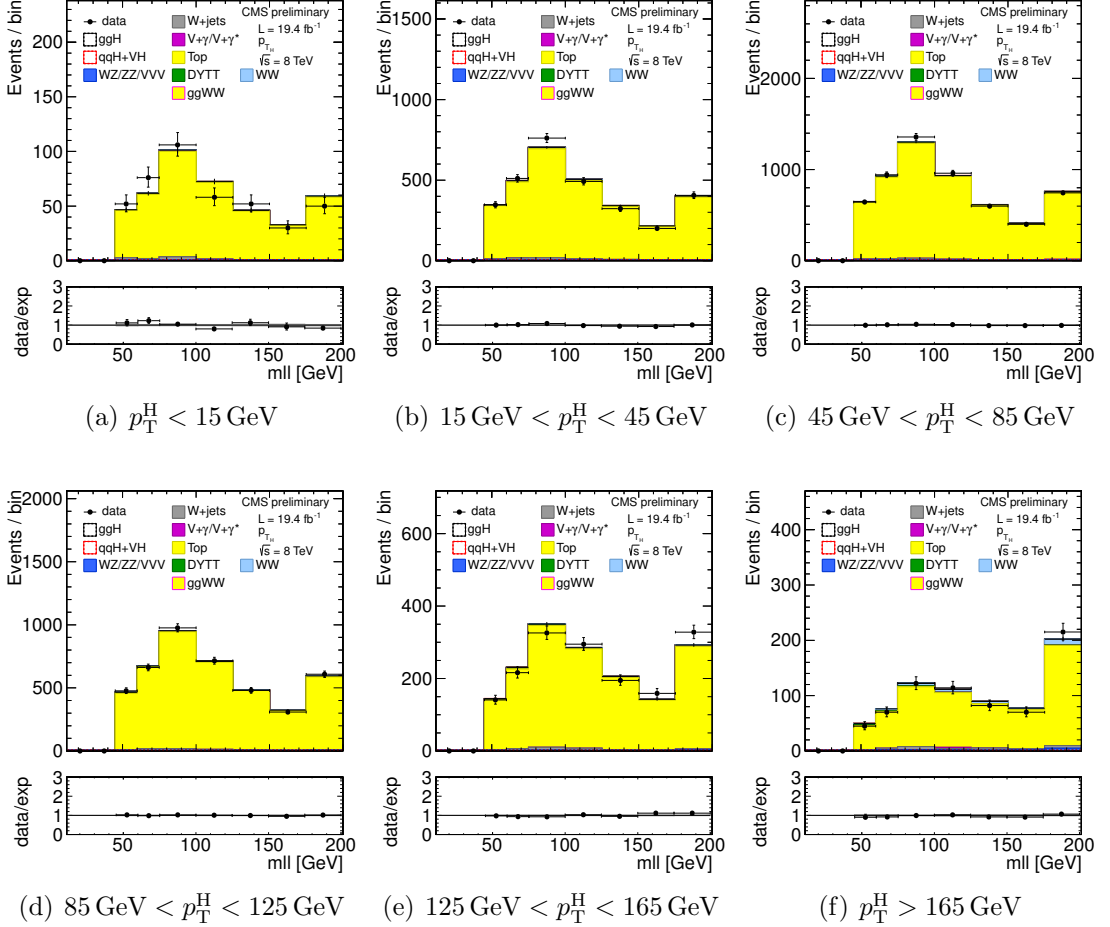


**Figure 4.10:** Comparison of the  $m_{\ell\ell}$  distributions in the  $CR_{t\bar{t}}$  region for data and simulation in each  $p_T^H$  bin, after the application of the data-driven factors.

resummation effects, i.e. NLO+NNLL accuracy, predict a rather different  $p_T^H$  spectrum.

To check the residual dependence of the  $m_{\ell\ell}$  and  $m_T$  shapes on the generator used for simulating the  $q\bar{q} \rightarrow W^+W^-$  process, the shapes obtained using different generators have been compared in each  $p_T^H$  bin, as shown in Figs. 4.13 and 4.14. The usage of different generators only mildly affect the  $m_{\ell\ell}$  and  $m_T$  shapes. Nevertheless the observed differences are taken as shape uncertainties and propagated through the fit.

The gluon-induced WW process, i.e.  $gg \rightarrow W^+W^-$ , has a sub-dominant contribution with respect to the quark-induced process, being the cross section ratio between the two of about 5%. The  $m_{\ell\ell}$  and  $m_T$  shapes for this background are taken from simulation while the cross section is scaled to the approximate NLO calculation [94, 95].

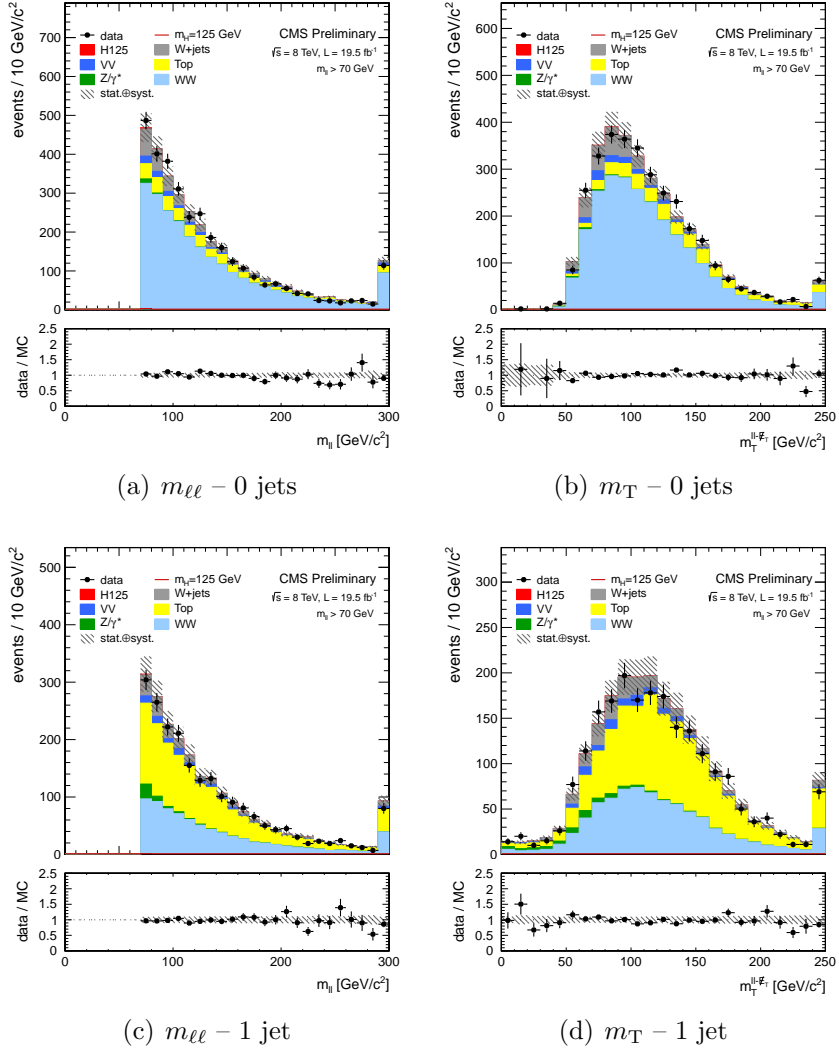


**Figure 4.11:** Comparison of the  $m_{\ell\ell}$  and  $m_T$  shapes in data and simulation for events with 0 and 1 jets, inclusive in  $p_T^H$ . The events are required to pass the analysis requirements and, in order to define a signal-free control region, to have  $m_{\ell\ell} > 70$  GeV.

#### 4.4.3 W+jets background

The non-prompt lepton background, originating from leptonic decays of heavy quarks, hadrons misidentified as leptons, and electrons from photon conversions in W+jets and QCD multijet production, is suppressed by the identification and isolation requirements on electrons and muons, as described in Sec. 3.2. The remaining contribution from the non-prompt lepton background is estimated directly from data and is ascribable especially to W+jets production. A control sample is defined by selecting events with one lepton that passes the standard lepton selection criteria and another lepton candidate that fails the criteria, but passes a looser selection, resulting in a sample of

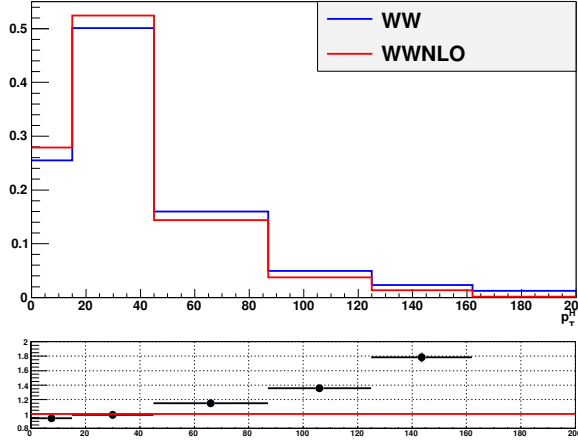


**Figure 4.12:** Comparison between the  $p_T^{\text{WW}}$  distributions obtained with two different MC generators: the blue line corresponds to the MADGRAPH generator and the red line refers to the same sample in which a reweighting has been applied in order to match the theoretical prediction at NLO+NNLL precision.

“pass-fail” lepton pairs.

The efficiency  $\varepsilon_{\text{pass}}$  for a jet that satisfies the loose lepton requirements to pass the standard selection is determined using an independent sample dominated by events with non-prompt leptons from QCD multijet processes. However, this sample is not a pure sample containing only non-prompt leptons, but may still contain prompt leptons coming from the W and Z boson decays. To reject muons from the W decay, the events are required to have  $E_T^{\text{miss}} < 20$  GeV and a W transverse mass below 20 GeV as well. Muons from the Z decay are instead removed requiring  $m_{\mu\mu} \notin [76, 106]$  GeV. For electrons the Z mass peak veto is enlarged to  $m_{ee} \notin [60, 120]$  GeV. Finally, prompt electrons and muons are required to be isolated from the leading jet in the event, i.e.  $\Delta\phi(\ell, j) > 1$ . The residual prompt lepton contamination from EW processes such as W/Z+jets production, which can bias the fake rate measurement, is estimated using simulation and subtracted. This contribution is negligible for small values of the lepton  $p_T$  and increases at larger values.

The  $\varepsilon_{\text{pass}}$  efficiency, parametrized as a function of  $p_T$  and  $\eta$  of the lepton, is then used to weight the events in the pass-fail sample by  $\varepsilon_{\text{pass}}/(1 - \varepsilon_{\text{pass}})$ , to obtain the estimated contribution from the non-prompt lepton background in the signal region. The systematic uncertainties from the determination of  $\varepsilon_{\text{pass}}$  dominate the overall uncertainty of this method.

A validation of the estimate of this background is performed in a control sample obtained selecting events with two leptons with same charge, which is enriched in W+jets events. The results of this closure test show good agreement between data and the estimated background.

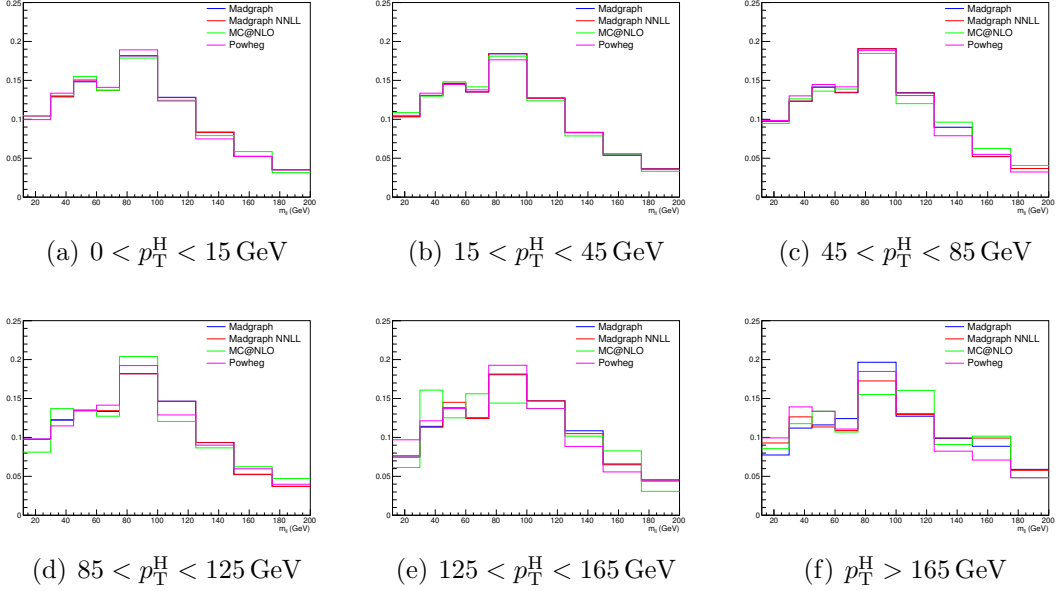


**Figure 4.13:** Comparison between the  $m_{\ell\ell}$  shape obtained with the default  $qq \rightarrow W^+W^-$  background simulation (MADGRAPH) and other theoretical models in every  $p_T^H$  bin.

#### 4.4.4 $Z/\gamma^* \rightarrow \tau^+\tau^-$ background

The low  $E_T^{\text{miss}}$  threshold in the  $e\mu$  final state requires the consideration of the contribution from  $Z/\gamma^* \rightarrow \tau^+\tau^-$ , that is estimated from data. This is accomplished by selecting  $Z/\gamma^* \rightarrow \mu^+\mu^-$  events in data and replacing both muons with a simulated  $\tau \rightarrow \ell\nu_\tau\bar{\nu}_\ell$  decay [90], thus obtaining a “hybrid” event. The Z boson four-momentum is reconstructed in data from the four-momenta of the daughter muons. Then a simulation step allows the replacement of the muon objects with  $\tau$  leptons, in such a way to preserve the Z boson momentum direction in its rest frame. The  $Z/\gamma^* \rightarrow \tau^+\tau^-$  decay is simulated with the TAUOLA package [107] to correctly describe the  $\tau$ -polarization effects.

After replacing muons from  $Z/\gamma^* \rightarrow \mu^+\mu^-$  decays with simulated  $\tau$  decays, the set of pseudo- $Z/\gamma^* \rightarrow \tau^+\tau^-$  events undergoes the reconstruction step. Good agreement in kinematic distributions for this sample and a simulated  $Z/\gamma^* \rightarrow \tau^+\tau^-$  sample is found. The global normalization of pseudo- $Z/\gamma^* \rightarrow \tau^+\tau^-$  events is checked in the low  $m_T$  spectrum, where a rather pure sample enriched in  $Z/\gamma^* \rightarrow \tau^+\tau^-$  events is expected.

This method allows to avoid the simulation of very large MC samples that would be needed for an accurate description of this process, given its large cross section.

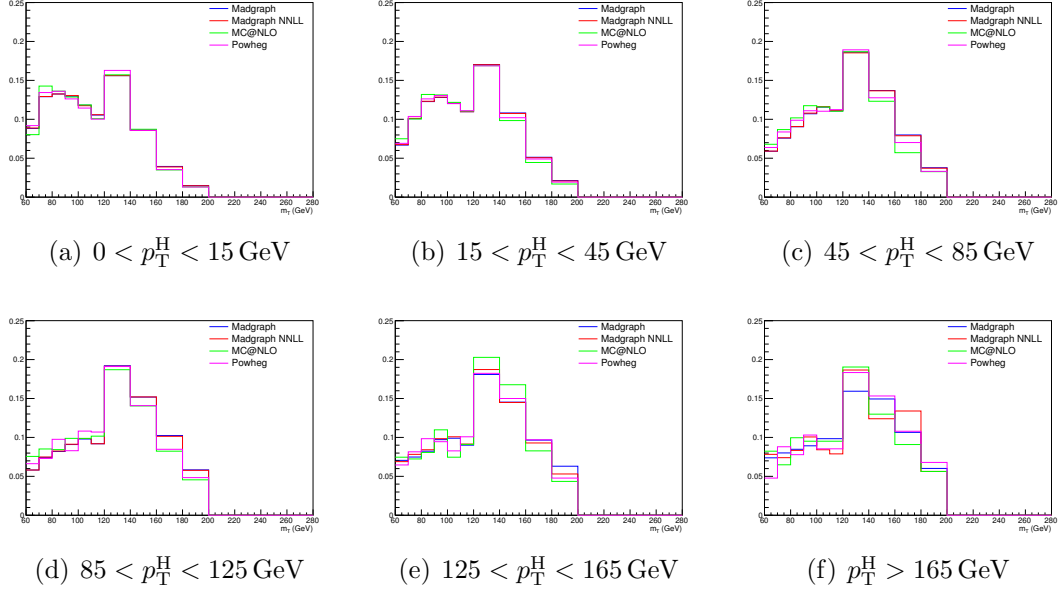


**Figure 4.14:** Comparison between the  $m_T$  shape obtained with the default  $qq \rightarrow W^+W^-$  background simulation (MADGRAPH) and other theoretical models in every  $p_T^H$  bin.

#### 4.4.5 Diboson backgrounds

The WZ and ZZ background events are largely rejected by requiring exactly two high  $p_T$  isolated leptons with opposite charge and different flavour in the event.

The  $W\gamma^*$  electroweak process is included in standard CMS simulations as a part of the WZ process using the MADGRAPH generator. Nevertheless, the low  $m_{\ell\ell}$  region is not properly covered since the standard simulations have a generator-level requirement of  $m_{\gamma^*} > 12$  GeV and there could be a significant rate of events below that threshold passing the selection criteria of the analysis. Therefore the low  $m_{\ell\ell}$  spectrum of the  $W\gamma^*$  process has been produced using a dedicated simulation with MADGRAPH, requiring two leptons with  $p_T > 5$  GeV and no restrictions on the third lepton. However, in order to have a reliable prediction of the background cross section, the simulation needs to be validated using data in a control region.

A high purity  $W\gamma^*$  phase space is defined selecting events with three muons, where the two muons with lowest invariant mass, which is required to be less than 12 GeV, are assumed to originate from the  $\gamma^*$  decay. The top quark background contribution is suppressed using a b tagging veto. The W+jets and multijet contributions are rejected requiring the minimum transverse mass of each lepton and  $E_T^{\text{miss}}$  to be larger than 25 GeV, and the transverse mass of the lepton associated with the W boson and  $E_T^{\text{miss}}$  to be larger than 45 GeV. Moreover, the  $J/\Psi$  meson decay are rejected by requiring  $|m_{\mu^\pm\mu^\mp} - m_{J/\Psi}| > 0.1$  GeV. The measured data/simulation scale factor in this control region is found to be  $1.5 \pm 0.5$ .

The  $W\gamma$  background can also contribute to the signal phase space, because the

photon can interact with the tracker material converting to an  $e^+e^-$  pair. Its normalization is taken from simulation while the  $m_{\ell\ell}$  and  $m_T$  shapes are checked selecting a data sample with one lepton and one photon, finding a good agreement within uncertainties.

## 4.5 Systematic uncertainties

Systematic uncertainties play an important role in this analysis where no strong mass peak is expected due to the presence of undetected neutrinos in the final state. They arise from three sources: background predictions, experimental measurements, and theoretical uncertainties. One of the most important sources is the normalization of the backgrounds that are estimated on data control samples whenever is possible.

The systematic uncertainties can affect the measured signal strengths in different ways. The uncertainties on the background predictions can be divided in those affecting the background cross section, the ( $m_{\ell\ell}$ ,  $m_T$ ) shape or both. As an example, systematic uncertainties changing the background cross section are the ones related to the background data-driven estimation, while the b tagging uncertainties only have an effect on the ( $m_{\ell\ell}$ ,  $m_T$ ) shape. Uncertainties such as lepton energy scale can instead affect both normalization and shape. Also, uncertainties affecting the signal ( $m_{\ell\ell}$ ,  $m_T$ ) shape reflect on an uncertainty on the measured signal strength.

A summary of the main sources of systematic uncertainty and the corresponding estimate is reported in Table 4.4. A brief description of each source of systematic uncertainty is discussed in the following sections.

The uncertainties related to the unfolding procedure are treated separately and are discussed in Sec. 4.7.1.

### 4.5.1 Uncertainties on background predictions

The signal extraction is performed fitting the estimated background contributions and subtracting them to the event counts in data. Therefore, the uncertainties on the background predictions indirectly reflect as uncertainties on the signal measurements. A list of the most important background uncertainties is given below.

- **$t\bar{t}$  and  $tW$  backgrounds:** the shapes of these backgrounds are corrected for different b tagging efficiency in data and simulation, and the normalization is taken from data in a top quark enriched control region independently for each  $p_T^H$  bin, as explained in Sec. 4.4.1. The uncertainties related to this procedure arise from the data sample size in the control regions for each  $p_T^H$  bin, and are embedded in the  $\alpha$  factors used to extrapolate the top quark background normalization from the control region to the signal region. They vary from 20% to 50% depending on the  $p_T^H$  bin.

The simulated samples include both  $t\bar{t}$  and  $tW$  processes, and a systematic uncertainty related to the  $tW/t\bar{t}$  fraction has been included. In fact, a relative

**Table 4.4:** Main sources of systematic uncertainties and their estimate. The first category reports the uncertainties on the normalization of background contributions. The experimental and theoretical uncertainties refer to the effect on signal yields. A range is specified if the uncertainty varies across the  $p_T^H$  bins.

<b>Uncertainties in backgrounds contributions</b>	
Source	Uncertainty
t <bar>t&gt;, tW</bar>	20–50%
W+jets	40%
WZ, ZZ	4%
W $\gamma^*$ , W $\gamma$	30%

<b>Effect of the experimental uncertainties on the signal and background yields</b>	
Source	Uncertainty
Integrated luminosity	2.6%
Trigger efficiency	1–2%
Lepton reconstruction and identification	3–4%
Lepton energy scale	2–4%
$E_T^{\text{miss}}$ modelling	2%
Jet energy scale	10%
Pileup multiplicity	2%
b mistag modelling	3%

<b>Effect of the theoretical uncertainties on signal yield</b>	
Source	Uncertainty
b jet veto scale factor	1–2%
PDF	1%
WW background shape	1%

variation of the contribution of these two processes could modify the shape of the simulated sample, and is thus included as a shape uncertainty affecting the ( $m_{\ell\ell}$ ,  $m_T$ ) shape in each  $p_T^H$  bin in a correlated way.

- **WW background:** due to the fact that the WW background ( $m_{\ell\ell}$ ,  $m_T$ ) shape is entirely taken from simulation, the analysis is relying on theoretical models and can thus be affected by their uncertainties. Especially, higher order QCD radiative effects have an influence on the generated WW shape. To study this impact the shapes of the distributions produced with the MADGRAPH generator are compared to the ones produced with MC@NLO and other generators (see

Sec. 4.4.2). The comparison is performed separately in each bin of  $p_T^H$  and the uncertainty includes shape differences originating from the renormalization and factorization scale choice. The effect on the signal strengths is found to be of the order of 1%.

- **W+jets background:** the systematic uncertainties on W+jets background arise from the estimation method explained in Sec. 4.4.3. This uncertainty has two sources: the dependence of  $\varepsilon_{\text{pass}}$  on the sample composition, and the method. The first source is estimated by modifying the jet  $p_T$  threshold in the QCD multijet sample, which modifies the jet sample composition. The uncertainty in the method is obtained from a closure test, where  $\varepsilon_{\text{pass}}$  is derived from simulated QCD multijet events and applied to simulated samples to predict the number of background events. The total uncertainty in  $\varepsilon_{\text{pass}}$ , including the statistical precision of the control sample, is of the order of 40%.
- **Diboson backgrounds:** these backgrounds are expected to give a small contribution in the signal phase space. Uncertainties on the cross sections reported in [108, 109] are 4% for WZ and 2.5% for ZZ. A 30% uncertainty is assigned to the  $W\gamma$  [110] yield and another 30% on  $W\gamma^*$  contribution according to the uncertainty on the normalization study (see Sec. 4.4.5).

### 4.5.2 Experimental uncertainties

The following experimental systematic sources have been taken into account:

- **Luminosity:** using the CMS online luminosity monitoring system, the uncertainty on the integrated luminosity ( $19.4 \text{ fb}^{-1}$ ) collected during the 2012 data taking period is found to be of 2.6%.
- **Trigger efficiency:** the uncertainties for both electrons and muons, estimated as described in Sec. 3.2.8, are at 1-2% level.
- **Lepton reconstruction and identification efficiency:** this uncertainty is estimated with the Tag and Probe technique described in Sec. 3.2, resulting in a 4% uncertainty for electrons and 3% for muons.
- **Muon momentum and electron energy scale:** the momentum scale of leptons has relatively large uncertainties due to different detector effects, as explained in Sec. 3.2. For electrons a scale uncertainty of 2% for the barrel, and 4% for the endcaps respectively, is assigned. For muons, a momentum scale uncertainty of 1.5%, independent on the muon pseudorapidity, is assigned.
- **$E_T^{\text{miss}}$  modelling:** the  $E_T^{\text{miss}}$  measurement is affected by the possible mismeasurement of individual particles addressed above, as well as the additional contributions from the pile-up interactions, as described in Sec. 3.5. The effect

of the missing transverse momentum resolution on the event selection is studied by applying a Gaussian smearing of 10% on the  $x$  and  $y$  components of the missing transverse momentum. All correlated variables, like the transverse mass, are recalculated. The effect on the signal yield is found to be around 2%.

- **Jet energy scale (JES) uncertainties:** JES uncertainties affect both the jet multiplicity and the jet kinematic variables, reflecting also on the ( $m_{\ell\ell}$ ,  $m_T$ ) shape. This uncertainty is estimated varying the kinematics of the reconstructed jets within the uncertainties on the JES (which depend on  $\eta$  and  $p_T$  of the jet) described in Sec. 3.3, and recomputing all the correlated variables, like  $m_{\ell\ell}$  and  $m_T$ .
- **b-jets misidentification modelling:** a fraction of signal events is rejected because erroneously identified as b-jets by the b tagging algorithms. The misidentification probability, as measured with the Tag and Probe technique described in Sec. 4.3.2, has an uncertainty related to different b tagging performance in data and simulation. This affects both signal and background.
- **Pileup multiplicity:** some of the variables used in the analysis are affected by the average number of pile-up interactions. The simulated events have been reweighted according to the instantaneous luminosity measured on data. The error on the average number of pile-up interactions measured in data and the simulation of the modelling and physics aspects of the pile-up simulation provide an uncertainty of at most 5% on the distribution used in the reweighting procedure. This uncertainty is propagated through all the analysis, and the estimated uncertainty on the signal strengths is found to not exceed 2%.

### 4.5.3 Theoretical uncertainties

Theoretical uncertainties generally arise from missing higher-order QCD corrections and PDF uncertainties. These uncertainties can affect both the cross section and the ( $m_{\ell\ell}$ ,  $m_T$ ) shape of the background predictions, as well as the shape of the signal model.

- **QCD scale uncertainties:** the uncertainties on the total cross sections due to the choice of the renormalization and factorization scales are assigned to simulation-driven backgrounds. For the signal processes these uncertainties are separated in two categories: those affecting the selection efficiency and those affecting the jet bin fractions. The effect of renormalization and factorization scale on the selection efficiency is of the order of 2% for all processes. Although this analysis is inclusive in number of jets, the effect of the QCD scales variation on the jet bin migrations has to be taken into account because of the b tagging veto efficiency. Indeed, the b tagging veto efficiency is not flat as a function of jet multiplicity nor  $p_T^H$ , as shown in Fig. 4.15, therefore introducing a dependence of the selection efficiency on the number of jets in the event. In order to

take into account this effect, an uncertainty on the ggH production mode has been included according to the Stewart-Tackman method, following the recipe proposed in Refs. [46, 111]. The effect on the signal strengths is found to be of the order of 1–2%.

- **PDFs uncertainties:** the utilization of different PDF sets can affect the ( $m_{\ell\ell}$ ,  $m_T$ ) shapes of the signal contributions, as well as the normalization and shape of the background predictions. The uncertainty related to the choice of PDF set is considered following the PDF4LHC [112, 113] prescription, using CT10, NNPDF2.1 [114] and MSTW2008 [115] PDF sets. The effect on the signal strengths is found to be of at most 1%.

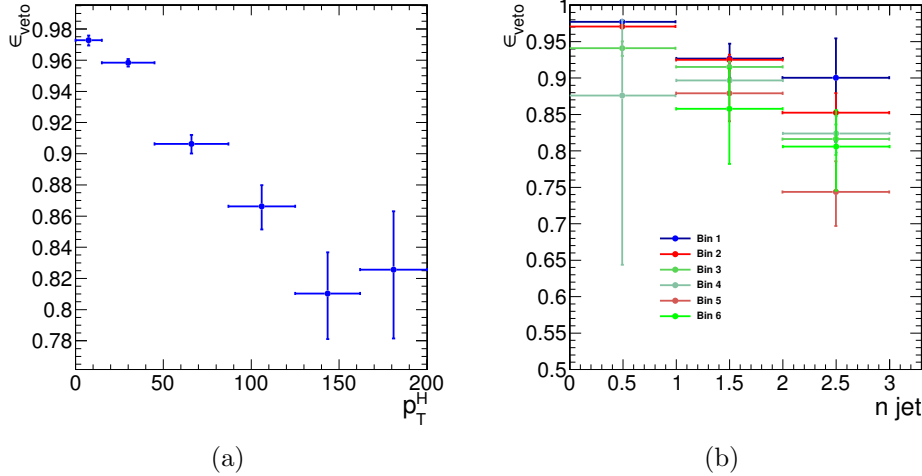


**Figure 4.15:** (a) Efficiency of the b tagging veto in different bins of  $p_T^H$ . (b) Efficiency of the b tagging veto in different bins of  $p_T^H$ , as a function of number of jets.

#### 4.5.4 Statistics uncertainty of the simulated samples

Due to the large range of weights used to correct the simulated distributions in order to match those in data, the effective size of the simulated samples are sometimes smaller than the actual number of events in the sample. The uncertainties due to the finite statistics of the simulated samples are taken into account and propagated through the final result. Their effect on the signal strengths is found to be negligible.

#### 4.5.5 Treatment of systematic uncertainties in the analysis

As explained before, one can distinguish between normalization uncertainties, where a systematic effect is changing the normalization of a given process assuming the ( $m_{\ell\ell}$ ,  $m_T$ ) shape is not affected, and shape uncertainties where the actual change in the ( $m_{\ell\ell}$ ,

$m_T$ ) shape of the process is taken into account. The normalization uncertainties enter the analysis as constant normalization factors, whereas for shape uncertainties the nominal and the  $+1\sigma$  and  $-1\sigma$  shapes enter the analysis in form of three histograms with the same normalization.

Effects of experimental uncertainties are studied by applying a scaling and smearing of certain variables related to physics objects, followed by a subsequent recalculation of all the correlated variables. This is done in simulation to account for possible systematic mis-measurements of the data. All experimental sources from Section 4.5.2 but luminosity are treated both as normalization and shape uncertainties. For background with a data-driven normalization estimation, only the shape uncertainty is considered.

## 4.6 Signal extraction

The fitting procedure as well as the measured signal and background yields are described in this section.

### 4.6.1 Fitting procedure

The signal, including ggH, VBF, and VH production mechanisms, is extracted in each bin of  $p_T^H$  by performing a binned maximum likelihood fit simultaneously in all  $p_T^H$  bins to a two-dimensional template for signal and background in the  $m_{\ell\ell}$ – $m_T$  plane. The variables used for the two-dimensional template are chosen for their power to discriminate signal and background contributions. This is shown in Fig. 4.16, where the two-dimensional simulated distributions are shown for the signal and background processes in the 0-jets category. As can be observed, the signal contribution in the 0-jets category is mostly distributed in the low- $m_{\ell\ell}$  region and for  $m_T$  values around 90–110 GeV. The background contribution, which is mainly owed to the WW, W+jets and  $Z/\gamma^* \rightarrow \tau^+\tau^-$  production, is instead distributed in the high- $m_{\ell\ell}$  region and for intermediate values of  $m_T$  (below 100 GeV).

Six different signal strength parameters are extracted from the fit, one for each  $p_T^H$  bin. The relative contributions of the different Higgs production mechanisms in the signal template are taken to be the same as in the SM. The sources of systematic uncertainty are considered as nuisance parameters in the fit.

The binning of the  $m_{\ell\ell}$  and  $m_T$  templates is chosen to be:

- $m_{\ell\ell}$ : [12, 30, 45, 60, 75, 100, 125, 150, 175, 200]
- $m_T$ : [60, 70, 80, 90, 100, 110, 120, 140, 160, 180, 200, 220, 240, 280]

To avoid a dependence of the results on the variables used for the template fit,  $m_{\ell\ell}$  and  $m_T$  need to be uncorrelated with respect to  $p_T^H$ . This has been verified and the correlation between the discriminating variables and  $p_T^H$  is shown in Fig. 4.17 and Fig. 4.18 for ggH and VBF production modes, respectively.

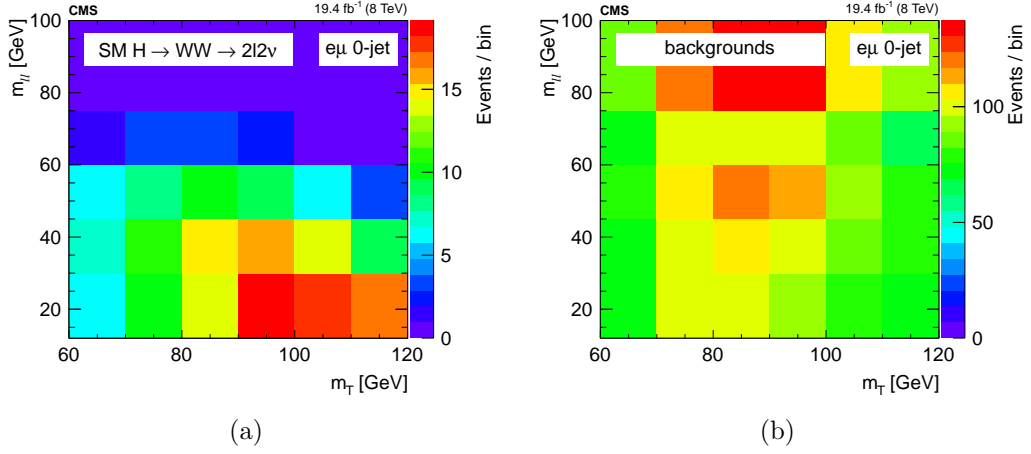


**Figure 4.16:** Two-dimensional  $m_{\ell\ell}$ - $m_T$  distribution for signal (a) and background (b) processes in the 0-jets category.

The signal strength  $\mu$  in each bin, defined as the ratio between the measured cross section and the SM one,  $\mu = \sigma/\sigma_{\text{SM}}$ , is allowed to float between -10 and +10, thus allowing negative values. This is mainly intended to allow future combinations with similar measurements without introducing any bias.

Because of detector resolution effects, some of the reconstructed  $H \rightarrow WW$  signal events might originate from outside the fiducial phase space. These out-of-fiducial signal events cannot be precisely handled by the unfolding procedure and must be subtracted from the reconstructed spectrum. The  $p_T^H$  distribution of the out-of-fiducial signal events is taken from simulation, and each bin is multiplied by the corresponding measured signal strength before performing the subtraction.

At the end, the number of events in each bin  $i$  of the measured spectrum is:

$$N_i = \mu_i(s_i - f_i) \quad , \quad (4.12)$$

where  $\mu_i$  is the measured signal strength,  $s_i$  and  $f_i$  are respectively the total number of reconstructed signal events and the number of reconstructed out-of-fiducial signal events expected from simulation.

The fit makes use of the binned maximum likelihood approach. The likelihood function,  $\mathcal{L}$ , restricted to the  $p_T^H$  bin  $j$ , can be written as:

$$\mathcal{L}(\mu_j, \theta) = \prod_{i=0}^{N_{\text{bins}}} \frac{(\mu_j s_i(\theta) + b_i(\theta))^{n_i}}{n_i!} e^{-\mu_j s_i(\theta) - b_i(\theta)} \cdot p(\tilde{\theta}|\theta) \quad , \quad (4.13)$$

where  $\mu_j$  is the signal strength in the bin  $j$ , i.e. the parameter of interest of the fit, which multiplies the signal yield. The index  $i$  runs over the bins of the  $m_{\ell\ell}$ - $m_T$  two-dimensional histogram corresponding to the  $p_T^H$  bin  $j$ ,  $s_i$  and  $b_i$  are the expected number of signal and background events respectively in bin  $i$ , and  $n_i$  is the total number of observed events in bin  $i$ . The set of parameters  $\theta$  represents the full suite of

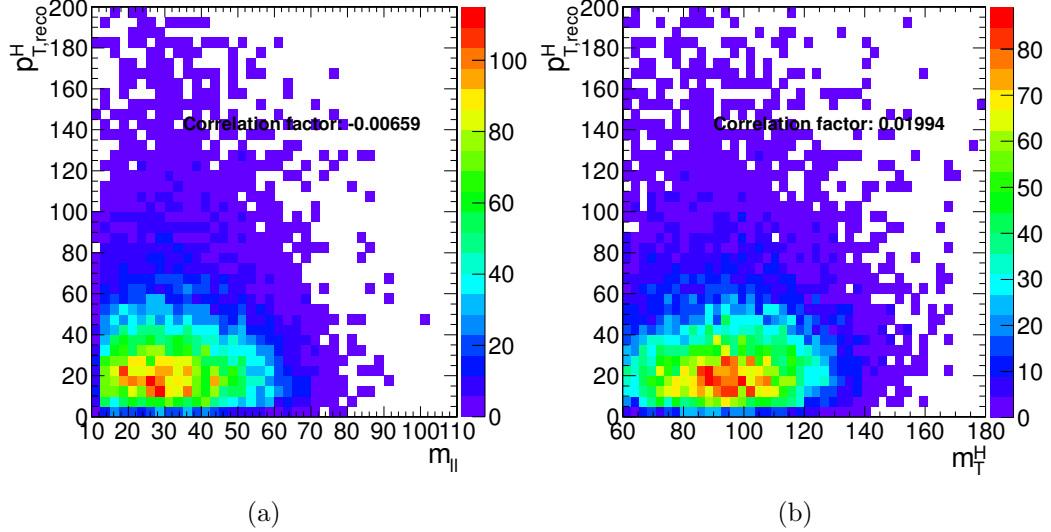


**Figure 4.17:** Correlation between  $p_T^H$  and  $m_{\ell\ell}$  (a) and between  $p_T^H$  and  $m_T$  (b) after the full selection for the ggH production mode.

nuisance parameters used to incorporate the systematic uncertainties. Each nuisance parameter is constrained in the fit including the prior distributions functions  $p(\tilde{\theta}|\theta)$  in the likelihood, where  $\tilde{\theta}$  is the set of default values for the  $\theta$  parameters [116]. For the major part of the nuisance parameters a log-normal prior distribution is used, with a standard deviation corresponding to the given systematic uncertainty. This is the optimal choice to describe uncertainties on definite positive observables, like cross sections, efficiencies, luminosity, etc. The usage of a gaussian distribution, under certain circumstances, would indeed allow the observable value to fluctuate below zero. For some nuisance parameters, as the ones related to the statistical uncertainty coming from the background measurement in data control regions, a Gamma distribution is instead recommended. A log-uniform distribution is used for the uncertainties related to the normalization of background contributions that are left unconstrained in the fit, such as for the WW background process. Finally, some of the experimental uncertainties related to the shape of signal and background processes are modelled by means of additional histograms as explained in Sec. 4.5.5. The correlations of nuisance parameters across different  $p_T^H$  bins are taken into account. Moreover the nuisance parameters can also be correlated (or anti-correlated) between signal and different background processes. As an example, the uncertainty related to the integrated luminosity measurement is fully correlated for all the signal and background processes.

Before running the fit on the data, the same procedure has been applied to the so called *Asimov data set*<sup>2</sup>, which provides a simple method to estimate the signal

<sup>2</sup>In a parallel reality imagined by the science fiction writer I. Asimov, politics was run in a peculiar way: instead of mobilizing millions of people to cast their vote to deliberate on something,

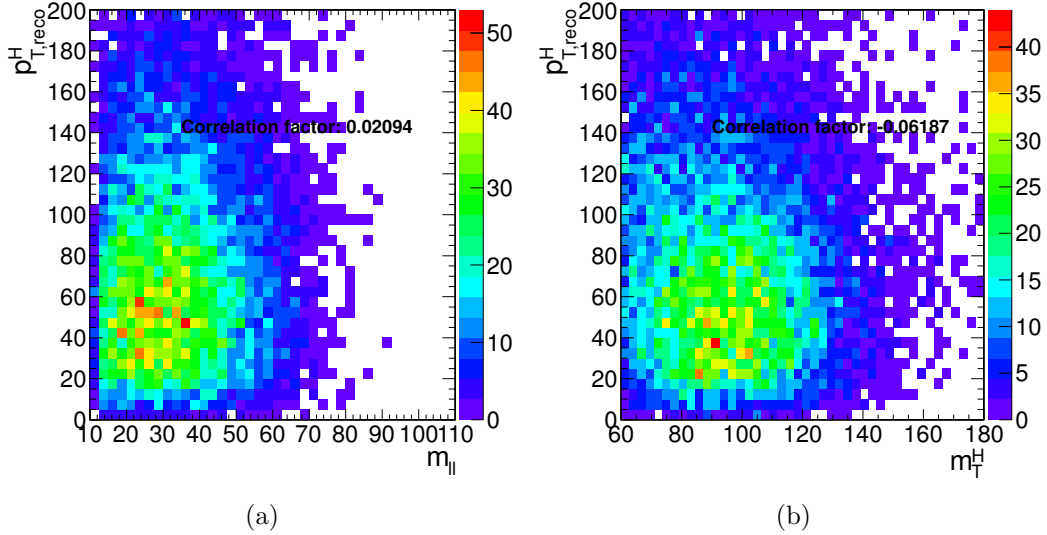


**Figure 4.18:** Correlation between  $p_T^H$  and  $m_{\ell\ell}$  (a) and between  $p_T^H$  and  $m_T$  (b) after the full selection for the VBF production mode.

sensitivity before looking at the data [117].

#### 4.6.2 Signal and background yields

A comparison of data and background predictions is shown in Fig. 4.19, where the  $m_{\ell\ell}$  distribution is shown for the six  $p_T^H$  bins. Distributions are shown in the  $m_T$  window of [60, 110] GeV, in order to emphasize the signal contribution. The  $m_T$  distributions are shown in Fig. 4.20 and correspond to the  $m_{\ell\ell}$  window of [12, 75] GeV.

The signal and background yields after the analysis selection are reported in Table 4.5.

The signal strengths obtained performing the fit are shown in Table ???. In order to assess the robustness of the fit, several toy MC samples have been generated with a mean value for each bin corresponding to the sum of the expected background plus signal events and a statistical accuracy comparable to the one expected in data. Each toy sample is fitted with the same procedure described before. The distribution of the signal strengths extracted in each bin using the toy MC samples and found to be consistent with 1, implying that no bias is introduced by the fit procedure.

The reconstructed spectrum is obtained starting from the signal yield  $N_i$  in each  $p_T^H$  bin  $i$ , obtained subtracting the out-of-fiducial events as shown in Eq. (4.12), and dividing it by the bin width  $w_i$  and integrated luminosity  $\mathcal{L}$ , i.e.:

$$\frac{d\sigma_i}{dp_{T,\text{reco}}^H} = \frac{N_i}{w_i \mathcal{L}} . \quad (4.14)$$

---

an algorithm was used to select an individual “average” person, and then this person was asked to take the decision on that matter.

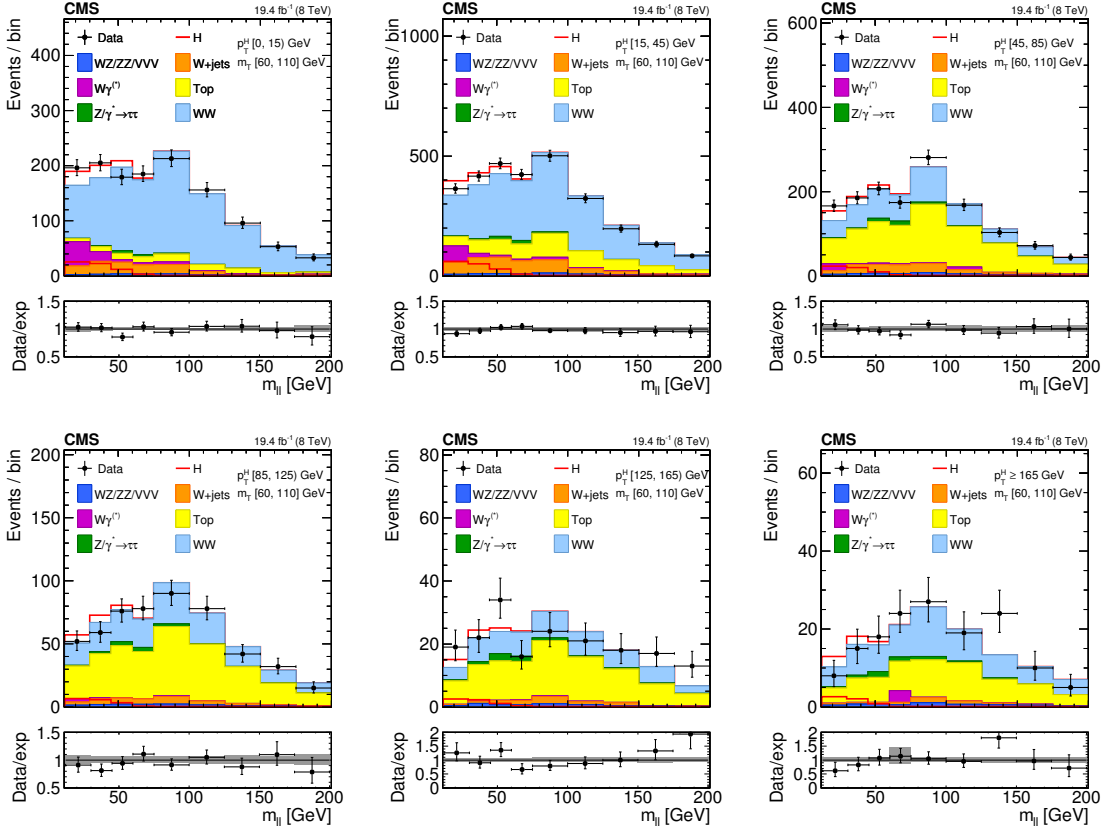


**Figure 4.19:** Distributions of the  $m_{\ell\ell}$  variable in each of the six  $p_T^H$  bins. Background normalizations correspond to the values obtained from the fit. Signal normalization is fixed to the SM expectation. The distributions are shown in an  $m_T$  window of  $[60, 110]$  GeV in order to emphasize the Higgs boson (H) signal. The signal contribution is shown both stacked on top of the background and superimposed on it. Ratios of the expected and observed event yields in individual bins are shown in the panels below the plots. The uncertainty band shown in the ratio plot corresponds to the envelope of systematic uncertainties after performing the fit to the data.

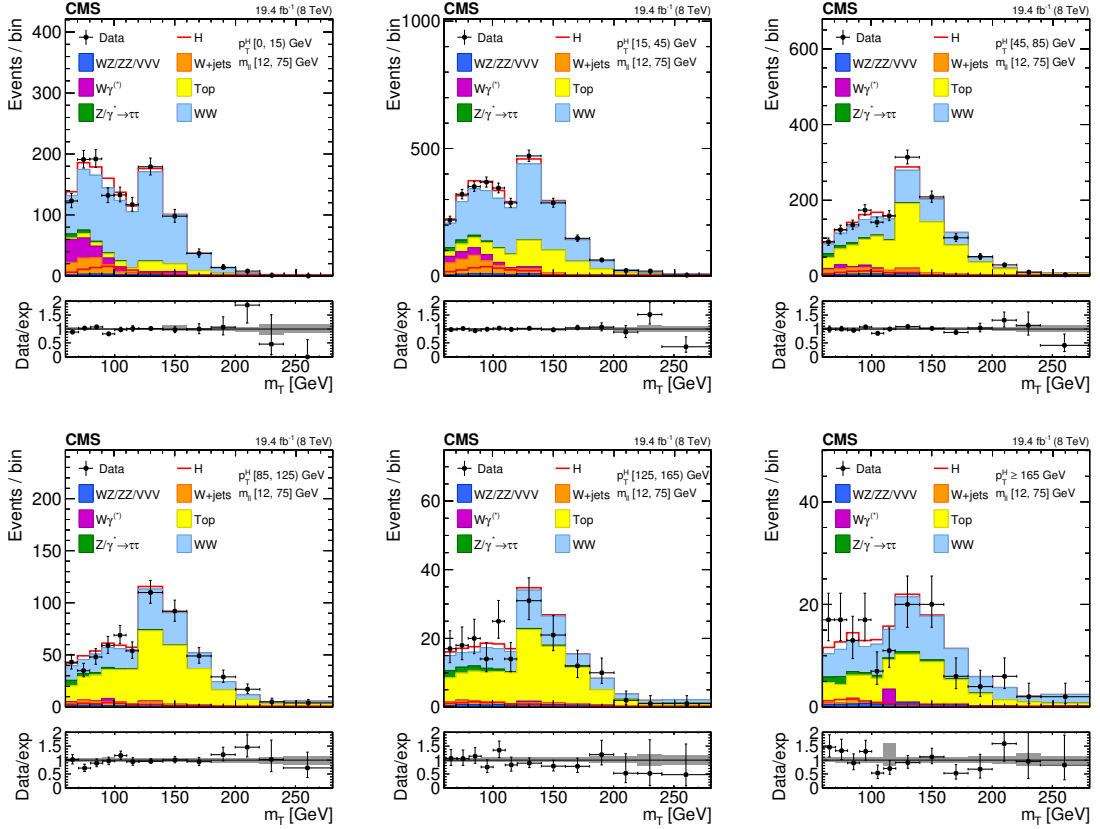


**Figure 4.20:** Distributions of the  $m_T$  variable in each of the six  $p_T^H$  bins. Background normalizations correspond to the values obtained from the fit. Signal normalization is fixed to the SM expectation. The distributions are shown in an  $m_{\ell\ell}$  window of  $[12, 75]$  GeV in order to emphasize the Higgs boson (H) signal. The signal contribution is shown both stacked on top of the background and superimposed on it. Ratios of the expected and observed event yields in individual bins are shown in the panels below the plots. The uncertainty band shown in the ratio plot corresponds to the envelope of systematic uncertainties after performing the fit to the data.

**Table 4.5:** Signal prediction, background estimates and observed number of events in data are shown in each  $p_T^H$  bin after applying the analysis selection requirements. The total uncertainty on the number of events is reported. For signal processes, the yield related to the ggH are shown, separated with respect to the contribution of the other production mechanisms (XH=VBF+VH). The WW process includes both quark and gluon induced contribution, while the Top process takes into account both  $t\bar{t}$  and tW.

Process	$p_T^H$ [GeV]					
	0–15	15–45	45–85	85–125	125–165	165–∞
ggH	$73 \pm 3$	$175 \pm 5$	$59 \pm 3$	$15 \pm 2$	$5.1 \pm 1.5$	$4.9 \pm 1.4$
XH=VBF+VH	$4 \pm 2$	$15 \pm 4$	$16 \pm 4$	$8 \pm 2$	$3.8 \pm 1.1$	$3.0 \pm 0.8$
Out-of-fiducial	$9.2 \pm 0.5$	$19.9 \pm 0.7$	$11.4 \pm 0.6$	$4.4 \pm 0.3$	$1.6 \pm 0.2$	$2.4 \pm 0.2$
Data	2182	5305	3042	1263	431	343
Total background	$2124 \pm 128$	$5170 \pm 321$	$2947 \pm 293$	$1266 \pm 175$	$420 \pm 80$	$336 \pm 74$
WW	$1616 \pm 107$	$3172 \pm 249$	$865 \pm 217$	$421 \pm 120$	$125 \pm 60$	$161 \pm 54$
Top	$184 \pm 38$	$1199 \pm 165$	$1741 \pm 192$	$735 \pm 125$	$243 \pm 51$	$139 \pm 49$
W+jets	$134 \pm 5$	$455 \pm 10$	$174 \pm 6$	$48 \pm 4$	$14 \pm 3$	$9 \pm 3$
WZ+ZZ+VVV	$34 \pm 4$	$107 \pm 10$	$71 \pm 7$	$29 \pm 5$	$14 \pm 3$	$13 \pm 4$
$Z/\gamma^* \rightarrow \tau^+\tau^-$	$23 \pm 3$	$67 \pm 5$	$47 \pm 4$	$22 \pm 3$	$12 \pm 2$	$10 \pm 2$
$W\gamma^{(*)}$	$132 \pm 49$	$170 \pm 58$	$48 \pm 30$	$12 \pm 9$	$3 \pm 3$	$5 \pm 10$

The spectrum shown in Fig. 4.21 is obtained after having performed the fit and after the subtraction of the out-of-fiducial signal events, but before undergoing the unfolding procedure. The theoretical distribution after the detector simulation and event reconstruction is also shown for comparison. Also, the expected distribution of the sub-dominant VBF and VH production mechanisms is shown.

In order to measure the inclusive cross section times branching fraction in the fiducial phase space, the reconstructed differential spectrum of Fig. 4.21 is integrated over  $p_T^H$ . The contribution of the uncertainty in each bin is propagated to the inclusive measurement taking into account the correlations of the signal strengths, i.e. using the covariance matrix. For the extrapolation of this result to the fiducial phase space the unfolding procedure is not needed and the inclusive measurement has only to be corrected for the fiducial phase space selection efficiency  $\epsilon_{fid}$ . Dividing the measured number of events by the integrated luminosity and correcting for the overall selection efficiency, which is estimated in simulation to be  $\epsilon_{fid} = 36.2\%$ , the inclusive fiducial cross section times branching fraction  $\sigma_{fid}$ , is computed to be:

$$\sigma_{fid} = 39 \pm 8 \text{ (stat)} \pm 9 \text{ (syst)} \text{ fb} , \quad (4.15)$$

in agreement within uncertainties with the theoretical estimate of  $48 \pm 8$  fb, computed integrating the simulated spectrum obtained with the POWHEG V2 generator for the ggH process and including the XH contribution.

**Table 4.6:** Signal strengths measured in data for each  $p_T^H$  bin with 68% CL uncertainties.

$p_T^H$ [GeV]	$\mu$	Uncertainty (68% CL)
0–15	+0.753	-0.424/+0.437
15–45	+0.716	-0.300/+0.308
45–85	+1.309	-0.445/+0.465
85–125	+0.165	-0.890/+0.898
125–165	+1.715	-1.103/+1.217
165– $\infty$	+0.796	-0.913/+1.059

## 4.7 Unfolding

To facilitate comparisons with theoretical predictions or other experimental results, the signal extracted performing the fit has to be corrected for detector resolution and efficiency effects and for the efficiency of the selection defined in the analysis. An unfolding procedure is used relying on the ROOUNFOLD package [118], which provides the tools to run various unfolding algorithms.

The basic principle behind the unfolding procedure in this analysis is to use MC signal samples to make the “true” distribution of the variable of interest, which is obtained using simulated events before particle interaction with the detector, and the same distribution obtained using events reconstructed after the full GEANT4 simulation of the CMS detector and event reconstruction.

These two distributions are used to calculate the detector response matrix  $M$ :

$$R_i^{\text{MC}} = \sum_{j=1}^n M_{ij} T_j^{\text{MC}} , \quad (4.16)$$

where  $T^{\text{MC}}$  and  $R^{\text{MC}}$  are two  $n$ -dimensional vectors representing the distribution before and after event processing through CMS simulation and reconstruction. The dimension  $n$  of the two vectors corresponds to the number of bins in the distributions, equal to six in this analysis. The response matrix  $M$  includes all the effects related to the detector and analysis selection that affect the  $R^{\text{MC}}$  distribution. The goal of the unfolding procedure is to obtain the  $T^{\text{truth}}$  distribution starting from the measured  $R^{\text{observed}}$  distribution by inverting the matrix  $M$ .

Given the finite data statistical accuracy, a simple inversion could lead to large fluctuations between bins in the unfolded result. In particular, if the off-diagonal elements of the response matrix are sizeable, the unfolded distribution has large variance and strong negative correlations between the neighbouring bins [91]. Several unfolding methods with regularization are available in literature, such as a method based on the Bayes’ theorem, which overcomes the unfolding instability using an iterative

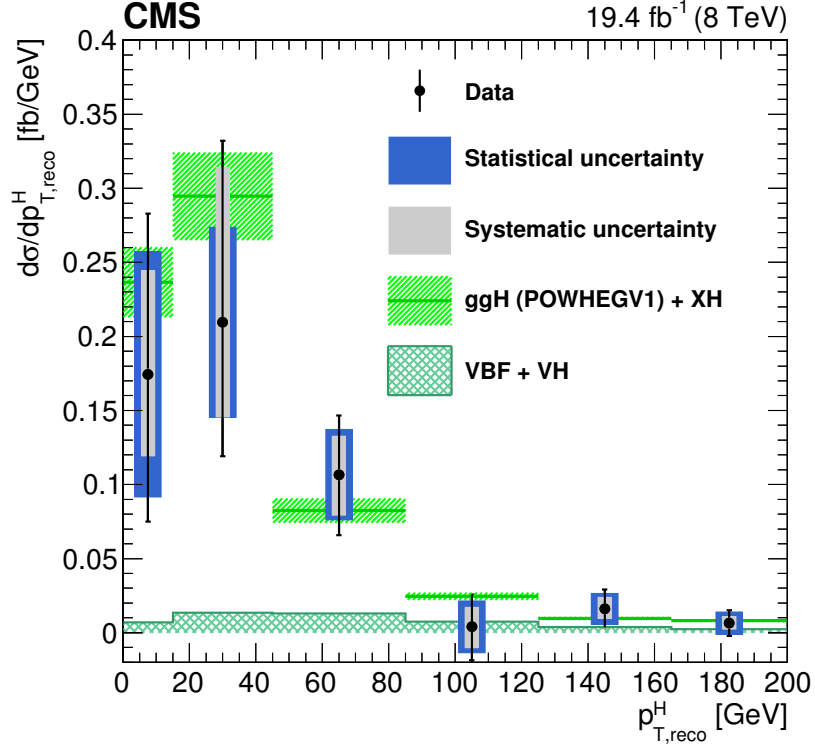


**Figure 4.21:** Differential Higgs boson production cross section as a function of the reconstructed  $p_T^H$ , before applying the unfolding procedure. Data values after the background subtraction are shown together with the statistical and the systematic uncertainties, determined propagating the sources of uncertainty through the fit procedure. The line and dashed area represent the SM theoretical estimates in which the acceptance of the dominant ggH contribution is modelled by POWHEG V1. The sub-dominant component of the signal is denoted as XH=VBF+VH, and is shown with the cross filled area separately.

procedure [119].

The unfolding procedure in this analysis relies on the Singular Value Decomposition (SVD) [120] method based on the Tikhonov regularization function. Such method introduces a regularization function that controls the smoothness of the distribution and depends generally on one regularization parameter, which can be controlled to achieve the desired degree of smoothness. The choice of the regularization parameter is particularly critical, and it should represent an optimal trade-off between taming the fluctuations in the unfolded result, and biasing the unfolded distribution. The main feature of this method is the use of the singular value decomposition of the response matrix, including an additional term to suppress the oscillatory component of the solution, i.e. the regularization term, which represents some *a priori* knowledge of the final solution. The regularization parameter  $k_{\text{reg}}$  is chosen to obtain results that are robust against numerical instabilities and statistical fluctuations, following the prescription described in Ref. [120]. This prescription consists in the diagonalization

of the response matrix using the SVD approach and in the subsequent calculation of the vector  $\vec{d}$ , whose values  $d_i$  represent the measured distribution expressed in a specific base defined by the SVD decomposition. Plotting  $\log |d_i|$  as a function of  $i$ , where  $i$  is related to the amount of regularization, one should obtain a curve that flattens out at some value of  $i$ . The regularization parameter corresponding to that value represents the optimal  $k_{\text{reg}}$  choice. The parameter obtained using this prescription is  $k_{\text{reg}} = 3$ .

The detector response matrix is built as a two-dimensional histogram, with the generator-level  $p_T^H$  on the  $y$  axis and the same variable after the reconstruction on the  $x$  axis, using the same binning for both distributions.

The resulting matrix, including all signal sources and normalized by row, is shown in Fig. 4.22(a). The diagonal bins correspond to the purity  $P$ , defined in Eq.(4.9). The same matrix, normalized by column, is shown in Fig. 4.22(b). In this case the diagonal bins correspond to the stability  $S$ , defined as the ratio of the number of events generated and reconstructed in a given bin, and the number of events reconstructed in that bin. The  $S$  and  $P$  parameters provide an estimate of the  $p_T^H$  resolution and migration effects, the main source being the limited resolution in the measurement of  $E_T^{\text{miss}}$ .

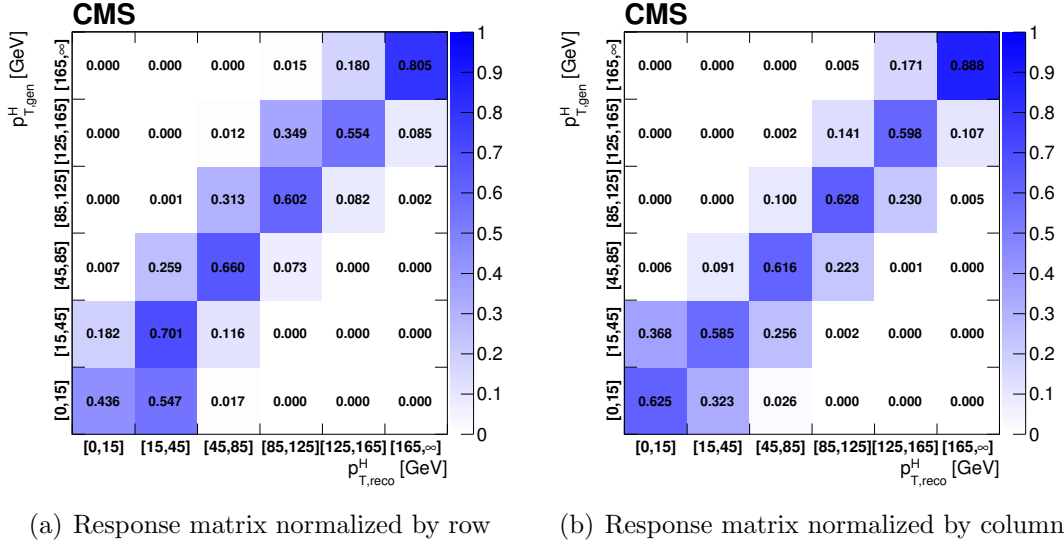


**Figure 4.22:** Response matrix normalized by row (a) and by column (b) including all signal processes. The matrices are normalized either by row or by column in order to show the purity or stability in diagonal bins.

Several tests are performed in order to validate the unfolding procedure. To estimate the uncertainty in the unfolding procedure due to the particular model adopted for building the response matrix, two independent ggH samples are used, corresponding to two different generators: POWHEG V1 and JHUGEN generators, both interfaced to PYTHIA 6.4. The JHUGEN generator sample is used to build the response

matrix while the Powheg V1 sample is used to build the  $p_T^H$  spectra at generator and reconstructed level. The reconstructed spectrum obtained using Powheg V1 is then unfolded using the response matrix built with JHUGEN, and the unfolded spectrum is compared to the Powheg V1 spectrum at generator level. The result of this test shows good agreement between the two distributions.

In order to further prove the choice of the regularization parameter, a large number of simulated pseudo-experiments has been generated to verify that the coverage of the unfolded uncertainties obtained with this procedure is as expected. From each pseudo-experiment the reconstructed  $p_T^H$  spectrum is obtained and then unfolded using the procedure described above, including only the statistical uncertainties. The coverage is calculated for each  $p_T^H$  bin, counting the number of pseudo-experiments for which the statistical uncertainty covers the true value. The results are shown in Table 4.7 for different values of the regularization parameter: starting from  $k_{\text{reg}} = 2$  (stronger regularization) up to  $k_{\text{reg}} = 5$  (weaker regularization). The criterion for choosing the best  $k_{\text{reg}}$  value is to increase the regularization as much as possible without introducing a bias, i.e. until a 68% coverage is fulfilled. This criterion leads to the same result as the prescription described before, strengthening the choice of  $k_{\text{reg}} = 3$ .

**Table 4.7:** Coverage interval for each bin and for different values of the regularization parameter, obtained using pseudo-experiments.

$p_T^H$ bin [GeV]	Coverage			
	$k_{\text{reg}} = 2$	$k_{\text{reg}} = 3$	$k_{\text{reg}} = 4$	$k_{\text{reg}} = 5$
0–15	$0.654 \pm 0.016$	$0.704 \pm 0.015$	$0.727 \pm 0.015$	$0.755 \pm 0.014$
15–45	$0.701 \pm 0.015$	$0.665 \pm 0.016$	$0.683 \pm 0.015$	$0.733 \pm 0.015$
45–85	$0.717 \pm 0.015$	$0.706 \pm 0.015$	$0.709 \pm 0.015$	$0.716 \pm 0.015$
85–125	$0.634 \pm 0.016$	$0.681 \pm 0.015$	$0.714 \pm 0.015$	$0.739 \pm 0.015$
125–165	$0.599 \pm 0.016$	$0.650 \pm 0.016$	$0.700 \pm 0.015$	$0.751 \pm 0.014$
165– $\infty$	$0.632 \pm 0.016$	$0.674 \pm 0.015$	$0.701 \pm 0.015$	$0.722 \pm 0.015$

### 4.7.1 Treatment of systematic uncertainties in the unfolding

An important aspect of this analysis is the treatment of systematic uncertainties and their propagation through the unfolding procedure. The sources of uncertainty are divided into three categories, depending on whether the uncertainty affects only the signal yield (type A), both the signal yield and the response matrix (type B), or only the response matrix (type C). These three classes propagate differently through the unfolding procedure.

Type A uncertainties are extracted directly from the fit in the form of a covariance matrix, which is passed to the unfolding tool as the covariance matrix of the measured distribution. The nuisance parameters belonging to this category are the background

shape and normalization uncertainties. To extract the effect of type A uncertainties a dedicated fit is performed fixing to constant all the nuisance parameters in the model but type A ones. The correlation matrix among the six signal strengths corresponding to the six  $p_T^H$  bins, including all type A uncertainties, is shown in Fig. 4.23. The correlation  $\text{cor}(i,j)$  of bins  $i$  and  $j$  is defined as:

$$\text{cor}(i,j) = \frac{\text{cov}(i,j)}{s_i s_j} , \quad (4.17)$$

where  $\text{cov}(i,j)$  is the covariance of bins  $i$  and  $j$ , and  $s_i, s_j$  are the standard deviations of bins  $i$  and  $j$ , respectively.

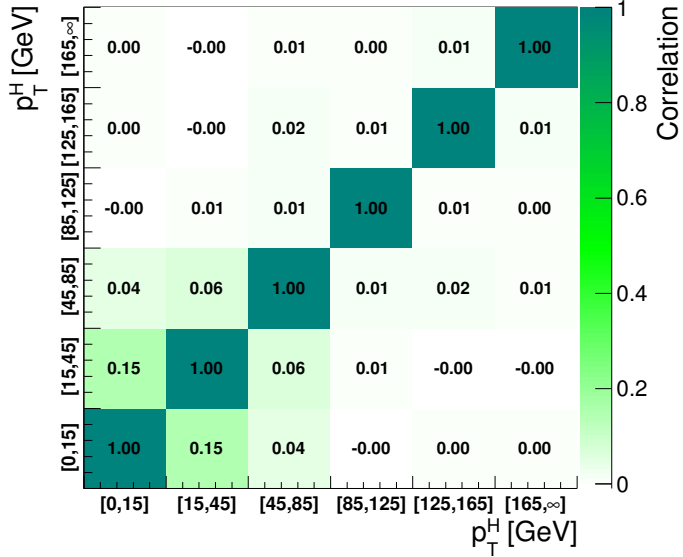


**Figure 4.23:** Correlations among the signal strengths corresponding to the six  $p_T^H$  bins including all type A uncertainties.

The nuisance parameters belonging to the Type B class are the ones related to:

- b veto scale factor: it affects the signal and background templates by varying the number of events with jets that enter the selection. It also affects the response matrix because the reconstructed spectrum is harder or softer depending on the number of jets, which in turn depends on the veto;
- lepton efficiency scale factor: it affects the signal and background template shape and normalization. It affects the response matrix by varying the reconstructed spectrum;
- $E_T^{\text{miss}}$  scale and resolution: the effect is similar to the above;
- lepton scale and resolution: the effect is similar to the above;

- jet energy scale: it affects the signal and background template shape and normalization. It also affects the response matrix because, by varying the fraction of events with jets, the b veto can reject more or fewer events, thus making the reconstructed spectrum harder or softer.

The effect of each type B uncertainty is evaluated separately, since each one changes the response matrix in a different way. In order to evaluate their effect on the signal strengths parameters, two additional fits are performed, each time fixing the nuisance parameter value to  $\pm 1$  standard deviation with respect to its nominal value. The results of the fits are then compared to the results of the full fit obtained by floating all the nuisance parameters, thus determining the relative uncertainty on the signal strengths due to each nuisance parameter, as shown in Tab. 4.8. Using these uncertainties, the measured spectra for each type B source are built. The effects are propagated through the unfolding by building the corresponding variations of the response matrix and unfolding the measured spectra with the appropriate matrix.

Type C uncertainties are related to the underlying assumption on the Higgs boson production mechanism used to extract the fiducial cross sections. These are evaluated using alternative response matrices that are obtained by varying the relative fraction of VBF and ggH components within the experimental uncertainty, as given by the CMS combined measurement [45]. Three different response matrices are built, corresponding to the nominal, scaled up, and scaled down VBF/ggH ratio. The nominal matrix assumes the SM VBF/ggH ratio, while up- and down-scaled matrices are constructed by varying the SM signal strengths within the experimental constraints for VBF and ggH in such a way as to obtain the maximal variation of the VBF/ggH ratio allowed by the experimental constraints. These three matrices are used to unfold the reconstructed spectrum with the nominal VBF/ggH fraction, and obtain an uncertainty on the unfolded spectrum.

**Table 4.8:** Effect of all the Type B uncertainties on the signal strengths of each bin. In the table are reported the signal strength variations corresponding to an up or down scaling of each nuisance parameter. Uncertainties related to  $E_T^{\text{miss}}$  and lepton resolution are single-sided, i.e. only an up variation is implemented.

Type B uncertainty	Effect on signal strength ( $+1\sigma / -1\sigma$ [%])					
	[0–15]	[15–45]	[45–85]	[85–125]	[125–165]	[165– $\infty$ ]
b veto	-10.1/-8.8	7.3/12.2	-6.3/3.1	-14.4/-4.8	-5.4/14.5	-7.9/17.8
lepton efficiency	-14.7/-3.9	4.5/15.1	-5.7/2.5	-13.2/-5.3	-0.2/7.6	-0.1/6.8
$E_T^{\text{miss}}$ resolution	-12.5/0.0	15.4/-0.0	-12.8/-0.0	8.7/0.0	-20.9/-0.0	10.5/0.0
$E_T^{\text{miss}}$ scale	-14.4/-6.8	-0.0/17.7	-6.1/-7.1	9.6/-20.9	2.3/32.4	2.5/2.6
lepton resolution	-12.5/-0.0	11.2/0.0	-2.4/0.0	-13.4/-0.0	9.9/0.0	-4.6/-0.0
e momentum scale	-2.7/-13.1	15.9/9.9	10.8/-16.8	16.2/-33.1	30.9/-14.4	12.6/-10.9
$\mu$ momentum scale	-7.0/-10.7	11.8/8.9	1.1/-8.7	-0.7/-14.4	14.5/-4.6	8.0/-1.6
jet energy scale	-10.9/-10.1	9.0/9.0	-3.0/-2.9	-10.3/-8.9	0.3/3.4	5.2/3.1

## 4.8 Results

In order to unfold the measured spectrum, the procedure described in section 4.7 has been pursued. The statistical plus type A systematic uncertainties are propagated by the unfolding procedure into the final spectrum, taking into account the signal strengths covariance matrix. The type B systematic uncertainty has been propagated using the following procedure: for each  $p_T^H$  bin the upper bound of the systematic band is computed by calculating the square sum of all the signal strength variations that deviate in the up direction with respect to the bin central value, whether or not this variation corresponds to the up or down shift of the systematic uncertainty. A similar procedure is used for the lower bound of the systematic band. If both the up and down shifts of a given nuisance parameter lead to a same direction variation of the signal strength, only the larger variation is considered.

The unfolded  $p_T^H$  spectrum is shown in Fig. 4.24. Statistical, systematic, and model dependence uncertainties are shown as separate error bands in the plot. The model dependence uncertainty corresponds to the effect of Type C errors described before.

The unfolded spectrum is compared with the SM-based theoretical predictions where the ggH contribution is modelled using the HRES and POWHEG V2 programs. The comparison shows good agreement between data and theoretical predictions within uncertainties. The measured values for the differential cross section in each bin of  $p_T^H$  are reported together with the total uncertainty in Table 4.9.

**Table 4.9:** Differential cross section in each  $p_T^H$  bin, together with the total uncertainty and the separate components of the various sources of uncertainty.

$p_T^H$ [GeV]	$d\sigma/dp_T^H$ [fb/GeV]	Total uncertainty [fb/GeV]	Statistical uncertainty [fb/GeV]	Type A uncertainty [fb/GeV]	Type B uncertainty [fb/GeV]	Type C uncertainty [fb/GeV]
0–15	0.615	+0.370/-0.307	$\pm 0.246$	$\pm 0.179$	+0.211/-0.038	+0.0782/-0.0608
15–45	0.561	+0.210/-0.157	$\pm 0.120$	$\pm 0.093$	+0.146/-0.041	+0.0395/-0.0327
45–85	0.215	+0.084/-0.078	$\pm 0.059$	$\pm 0.037$	+0.047/-0.034	+0.0089/-0.0084
85–125	0.071	+0.038/-0.038	$\pm 0.029$	$\pm 0.017$	+0.018/-0.017	+0.0018/-0.0022
125–165	0.027	+0.020/-0.019	$\pm 0.016$	$\pm 0.009$	+0.007/-0.007	+0.0003/-0.0006
165– $\infty$	0.028	+0.027/-0.027	$\pm 0.023$	$\pm 0.012$	+0.008/-0.007	+0.0002/-0.0006

Figure 4.25 shows the correlation matrix for the six bins of the differential spectrum, where the correlation is defined as in Eq. (4.17). The correlation among unfolded bins is mostly of statistical nature, arising from the unfolding procedure.

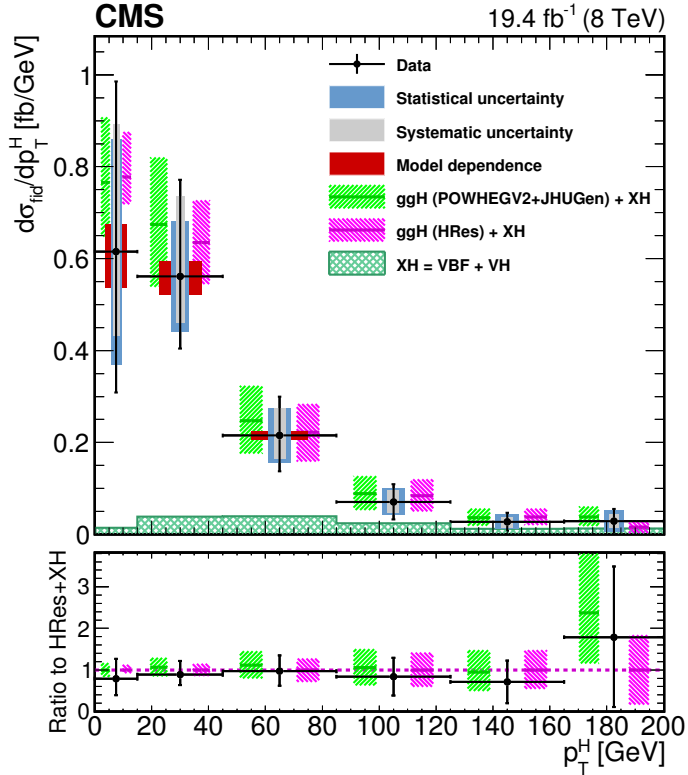


**Figure 4.24:** Higgs boson production cross section as a function of  $p_T^H$ , after applying the unfolding procedure. Data points are shown, together with statistical and systematic uncertainties. The vertical bars on the data points correspond to the sum in quadrature of the statistical and systematic uncertainties. The model dependence uncertainty is also shown. The pink (and back-sashed filling) and green (and slashed filling) lines and areas represent the SM theoretical estimates in which the acceptance of the dominant  $\text{ggH}$  contribution is modeled by HRES and POWHEG V2, respectively. The sub-dominant component of the signal is denoted as  $\text{XH}=\text{VBF}+\text{VH}$  and it is shown with the cross filled area separately. The bottom panel shows the ratio of data and  $\text{HRes+XH}$  theoretical estimate to the HRES theoretical prediction.

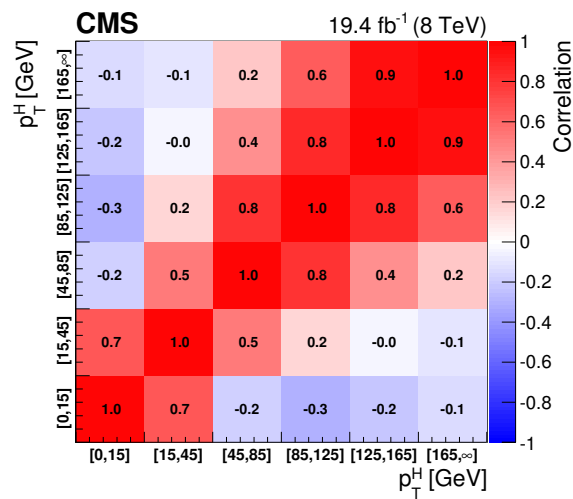


**Figure 4.25:** Correlation matrix among the  $p_T^H$  bins of the differential spectrum.

# Chapter 5

## Measurement of Higgs boson production using $H \rightarrow WW$ decays with first 13 TeV data

In this chapter, the first measurement of the 125 GeV Higgs boson cross section times branching ratio to a W boson pair at 13 TeV is presented, using a total integrated luminosity of  $2.3 \text{ fb}^{-1}$ , collected during the 2015 proton-proton data taking period of the LHC. The analysis strategy follows the one described in Chapter 4, with some differences described in the following.

With respect to the centre-of-mass energy of 8 TeV, the ggH production cross section at 13 TeV is expected to increase of a factor of 2, thus raising the number of expected signal events. In addition, the cross section for the background processes increases as well: the WW production cross section of a factor of 1.8 and the  $t\bar{t}$  cross section of a factor of 3.5.

### 5.1 Data and simulated samples

This analysis makes use of data recorded in proton-proton collisions at 13 TeV during 2015, corresponding to a total integrated luminosity of  $2.3 \text{ fb}^{-1}$ . Events are selected according to single and double lepton triggers, similarly to the 8 TeV analysis. The HLT trigger  $p_T$  thresholds used in this analysis are listed in Table 5.1. Trigger efficiencies are measured in data and applied to simulated events as described in Sec. 3.2.8.

Concerning the simulated samples, several different MC generators are used. Higgs boson signal samples are simulated using POWHEG v2 [36, 99, 121], designed to generate these processes with NLO QCD accuracy. In particular, for Higgs boson produced via ggH [38] and VBF [39], the decay into two W bosons and subsequently into leptons is done using JHUGEN v5.2.5. For associated production with a vector boson ( $W^+H$ ,  $W^-H$ ,  $ZH$ ) [122], including gluon fusion produced  $ZH$  (ggZH), the Higgs boson decay is instead simulated using PYTHIA 8.1 [42]. All the signal samples are

**Table 5.1:** Transverse momentum thresholds required for lepton triggers at HLT level. Double set of thresholds indicates the thresholds for each leg of the double lepton triggers.

Trigger path	Threshold
Single electron	$p_T > 23$ GeV
Single muon	$p_T > 20$ GeV
Muon-Electron	$p_T > 17$ and $12$ GeV
Electron-Muon	$p_T > 17$ and $8$ GeV

generated assuming a Higgs boson mass of 125 GeV.

The POWHEG v2 [123] is also used for simulating the  $q\bar{q}$  induced  $WW$  production in different decay channels. The simulated events are reweighted to reproduce the  $p_T^{WW}$  distribution obtained from  $p_T$ -resummed calculations [125, 126]. Gluon fusion produced  $WW$  is generated at LO QCD accuracy using MCFM v7.0 [127].

The  $t\bar{t}$  process with dilepton final state is also generated using POWHEG v2. The simulated processes for the  $WW$  and  $t\bar{t}$  production are illustrated in Table 5.2, together with the associated cross sections. Other minor background samples are also generated, a list of the most relevant ones is presented in Table 5.3.

**Table 5.2:** Simulated processes for  $t\bar{t}$  and  $WW$  production.

Process	$\sigma \times \mathcal{B}$ [pb]
$t\bar{t} \rightarrow WW b\bar{b} \rightarrow 2\ell 2\nu b\bar{b}$	87.31
$q\bar{q} \rightarrow WW \rightarrow 2\ell 2\nu$	12.178
$gg \rightarrow WW \rightarrow 2\ell 2\nu$	0.5905

All processes are generated using NNPDF2.3 [19, 128] for NLO generators. The LO version of the same PDF set is used for LO generators. All the event generators are interfaced to PYTHIA 8.1 [42] for the showering of partons and hadronization, as well as for including a simulation of underlying event (UE) and multiple parton interaction (MPI) based on the CUET8PM1 tune [129].

To estimate the systematic uncertainties related to the choice of UE and MPI tunes, the signal processes and the  $WW$  background are generated with two alternative tunes which are representative of the errors on the tuning parameters. The showering and hadronization systematic uncertainty is estimated by interfacing the same MC samples with the HERWIG++ 2.7 parton shower [130, 131] instead of PYTHIA 8.

Drell-Yan (DY) production of  $Z/\gamma^*$  is generated using AMC@NLO [40]. Other multiboson processes, such as  $WZ$ ,  $ZZ$ , and  $VVV$  ( $V=W/Z$ ), are generated with

**Table 5.3:** Simulated samples for other minor background processes used in the analysis. Single top quark production includes the dominant tW process, as well as the sub-dominant production in the s- and t-channels.

Process	$\sigma \times \mathcal{B}$ [pb]
Drell-Yan ( $10 \text{ GeV} < m_{\ell\ell} < 50 \text{ GeV}$ )	20471.0
Drell-Yan ( $m_{\ell\ell} > 50 \text{ GeV}$ )	6025.26
Single top	71.7
$WZ \rightarrow 2\ell 2q$	5.5950
$ZZ \rightarrow 2\ell 2q$	3.2210
$WWZ$	0.1651
$WZZ$	0.05565
$ZZZ$	0.01398

AMC@NLO and normalized to the cross section calculated at NLO accuracy.

The simulated samples are generated with distributions for the number of pile-up interactions that are meant to roughly cover, though not exactly match, the conditions expected for the different data taking periods. In order to factorize these effects, the number of true pile-up interactions from the simulation truth is reweighted to match the data. In Fig. 5.1, the effect of this reweighting on a sample enriched in Drell-Yan events is shown. The average number of pile-up is approximately 11.5.

For Higgs boson signal, the inclusive cross sections used are the ones reported by the LHC Higgs Cross Section Working Group [132]. The ggH cross section is computed at NNLO+NNLL QCD and NLO EW accuracy, while NNLO QCD and NLO EW accuracy is used for the other production modes. The branching fractions are the ones reported in Ref. [46].

The cross section used for the  $q\bar{q}$  induced WW processes is computed at NNLO QCD accuracy [124]. The normalization of this background is eventually directly taken from a fit to data and the NNLO cross section is used as initial guess. The LO cross section for the gluon induced WW process is obtained directly from MCFM, and a  $k$ -factor of 1.4 is applied to correct for the difference between the LO and NLO theoretical calculation [133]. The contribution of the interference between the  $gg \rightarrow WW$  and  $gg \rightarrow H \rightarrow WW$  processes is evaluated using MCFM and is found to be negligible compared to the signal contribution.

The cross sections of the different single top processes are estimated by the LHC Top Working group [134] with NLO accuracy. The  $t\bar{t}$  cross section is also provided by the LHC Top Working group [135], and it is computed at NNLO QCD accuracy and NNLL accuracy for soft gluon resummation effects.

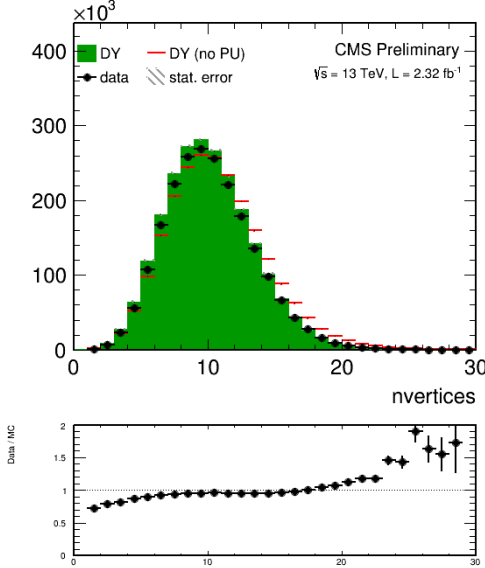


**Figure 5.1:** Distribution of the number of vertices in a Drell-Yan enriched phase space in data, together with the simulation before (red) and after (solid green) the pile-up reweighting.

## 5.2 Analysis strategy

### 5.2.1 Event reconstruction

Regarding electrons, muons, jets and  $E_T^{\text{miss}}$  definition and reconstruction, the standard CMS recommendations described in Chapter 2 are used. The specific selections used in this analysis are briefly summarised below.

Muons are identified according to the definition described in Sec. 3.2.1, with some specific modifications regarding the impact parameters of the tracks ( $d_{xy}$  and  $d_z$ ) with respect to the primary vertex. In particular the requirements are lowered with respect to the *tight muon selection* illustrated in Table 3.1.

The PF relative isolation described in Eq.(3.1) is used for muon isolation, corresponding to a requirement on the isolation variable of  $I_{\Delta\beta}^{\text{rel}} < 0.15$ . In addition a tracker relative isolation is also applied.

The tight working point described by the requirements in Table 3.2 is used for the electron identification. Some additional requirements to make the selection “trigger-safe” are included. This is done because the electron triggers already include some identification and isolation requirements that are based on the raw detector information, while the offline selections make use of particle flow requirements. The “trigger-safe” selections are defined to make the offline identification and isolation requirements tighter with respect to the online triggers.

The simulated events are corrected for the lepton trigger, identification and isolation efficiencies measured in data using the same techniques described in Sec. 4.3.1.

Jets are obtained clustering the particle flow objects using the anti- $k_t$  algorithm with a distance parameter of 0.4. The CHS pile-up mitigation technique is used and the jet energy corrections are applied, as described in Sec. 3.3.2. To reject jets arising from calorimeter or readout electronics noise, the loose working point for PF jet identification is used (see Sec. 3.3.3). The jet counting used in the event selection is based on jets with  $p_T > 30 \text{ GeV}$ .

### 5.2.2 B tagging performance

B tagging algorithms are used to identify jets that are likely arising from b quarks hadronization. A b-jets veto is then applied to suppress the top quark background, rejecting events that contain at least one b-tagged jet. The b tagging algorithm is chosen comparing the performance of different algorithms using simulations for signal and background contributions in the phase space defined by the analysis kinematic requirements. More precisely, two simulated samples are used: one corresponding to the  $H \rightarrow WW \rightarrow 2\ell 2\nu$  signal produced via the ggH mechanism and the other to the  $t\bar{t}$  background process. The first sample is enriched in light jets, i.e. originating by the hadronization of light quarks or gluons, while the second sample is enriched in b-jets, coming from the top quark decay. The b-veto efficiency,  $\epsilon_{b \text{ veto}}$ , is computed separately for the two samples and for various b tagging algorithms. To compare the b tagging performance  $\epsilon_{b \text{ veto}}$  is computed for different working points, i.e. different selections on the specific b tagging discriminator, and the results are reported in the form of a ROC curve. In general, ROC curves are built reporting the signal efficiency on the  $x$  axis and the background rejection on the  $y$  axis. In this case the  $x$  axis shows the b-jets veto efficiency for signal,  $\epsilon_{b \text{ veto}}^{\text{ggH}}$ , and the  $y$  axis the  $t\bar{t}$  background rejection,  $1 - \epsilon_{b \text{ veto}}^{t\bar{t}}$ . The best algorithm is the one that provides the highest background rejection for a given signal efficiency.

The ROC curves corresponding to events with 0, 1 and  $\geq 2$  jets are shown in Fig. 5.2. Events considered for this study are the ones passing a WW baseline selection. Here 0 jets means that events do not contain any jet with  $p_T$  above 30 GeV. In this category the b veto rejects the event if at least one jet with  $20 \text{ GeV} < p_T < 30 \text{ GeV}$  is identified by the b tagging algorithm. Events containing exactly one jet with  $p_T > 30 \text{ GeV}$  are rejected if that jet is b-tagged, while events with 2 or more jets are rejected if at least one jet is identified.

The ROC curves show that the cMVAv2 algorithm has the best performance for the analysis phase space among the algorithms taken into account. For both the CSVv2 and cMVAv2 algorithms<sup>1</sup>, three working points are defined corresponding to the mistag rates (see Sec. 3.4) of 10% (loose), 1% (medium) and 0.1% (tight). These mistag rates correspond roughly to  $1 - \epsilon_{b \text{ veto}}^{\text{ggH}}$  in events with 1 jet. The distribution of the cMVAv2 discriminator associated to the leading jet for both the ggH and  $t\bar{t}$  samples is shown in Fig. 5.3. The events falling on the left side of the vertical lines,

---

<sup>1</sup>The CSVv2 and cMVAv2 algorithms are improved versions of the CSV and cMVA described in Sec. 3.4, developed by CMS for the 13 TeV data taking period.

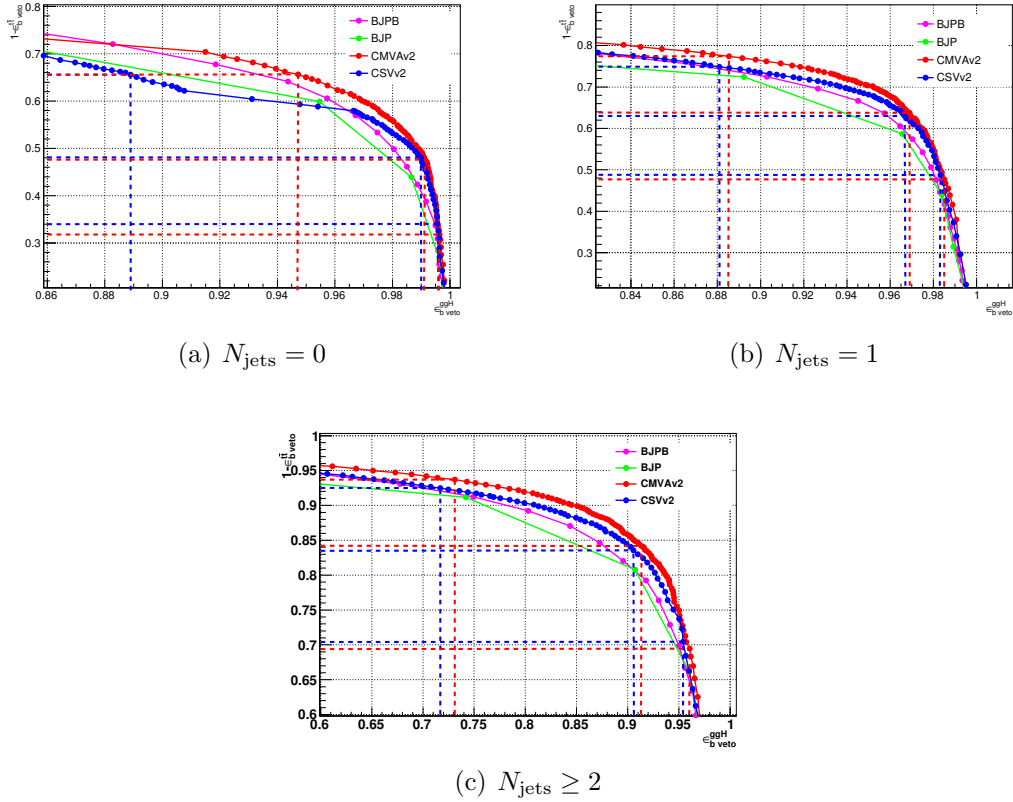


**Figure 5.2:** ROC curve for the b veto efficiency on signal and background events. The blue and red lines point out the signal efficiency and the background rejection corresponding to the three working points considered for the CSVv2 and the cMVAv2 algorithms respectively.

which corresponds to the three working points of the cMVAv2 algorithm, are those that pass the b veto requirement.

In order to determine the best working point for this analysis a signal significance assessment is performed, in which only statistical uncertainties are taken into account. The expected signal significance is calculated applying the event selections and using the statistical procedure described in the next sections, testing the effect of the b veto for the three working points.

The signal significance is computed for the two jet categories separately and eventually for the combination of the two. This leads to the values listed in Table 5.4 for the three working points.

The loose working point is found to be the one for which the best signal significance is achieved in the combined  $0 + 1$  jets category, and is thus chosen for the definition of the b veto requirement.

To correct for a possible different b tagging efficiency in data and simulation, the simulated events are reweighted using scale factors computed in bins of the jet  $\eta$  and  $p_T$ . The scale factors related to the b tagging efficiency and mistag rate, together

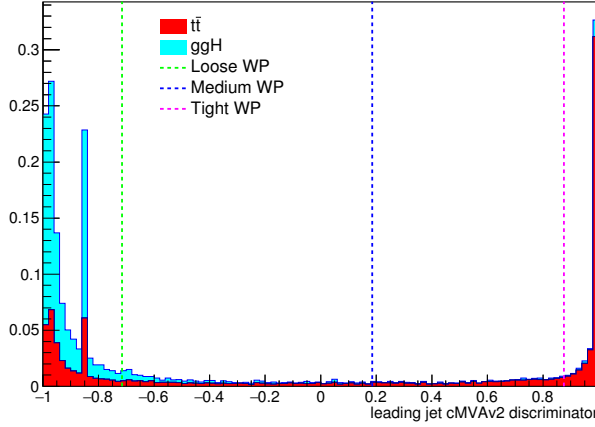


**Figure 5.3:** cMVAv2 discriminator associated to the leading jet (with  $p_T > 30 \text{ GeV}$ ) for both the ggH and the  $t\bar{t}$  processes. The two processes are normalized to unity and stacked. The vertical dashed lines show the discriminator value corresponding to the three working points.

**Table 5.4:** Signal significance corresponding to the three working points and for different jet categories.

Jet category	Loose WP (-0.715)	Medium WP (0.185)	Tight WP (0.875)
0 jets	2.022	2.043	2.036
1 jet	1.439	1.404	1.305
0 + 1 jets	2.481	2.479	2.420

with the corresponding uncertainties, are estimated in data and simulation adopting a Tag & Probe technique similar to the one described in Sec. 4.3.2.

In simulation the efficiency has to be computed for different jet flavours, i.e. b, c and light (u,d,s), using jet matching information<sup>2</sup>. The efficiencies for tagging b-, c- and light-jets estimated using  $t\bar{t}$  simulated events are shown in Fig. 5.4 in  $\eta$  and  $p_T$  bins. The uncertainties associated to the efficiencies are representative of the statistics of the simulated  $t\bar{t}$  sample, and are computed according to a binomial distribution.

The effect of the event reweighting is to correct the shape of the b tagging discriminator in simulation, moving events from the b tag region (discriminator greater than  $> -0.715$ ) to the b veto region (discriminator  $< -0.715$ ) and viceversa. A data/simulation comparison of the b tagging discriminator for the leading and sub-

<sup>2</sup>There are a couple of techniques developed by the CMS Collaboration to assess the flavour of a reconstructed jet in simulation. The technique used here makes use of the flavour of the hadrons clustered into a jet.

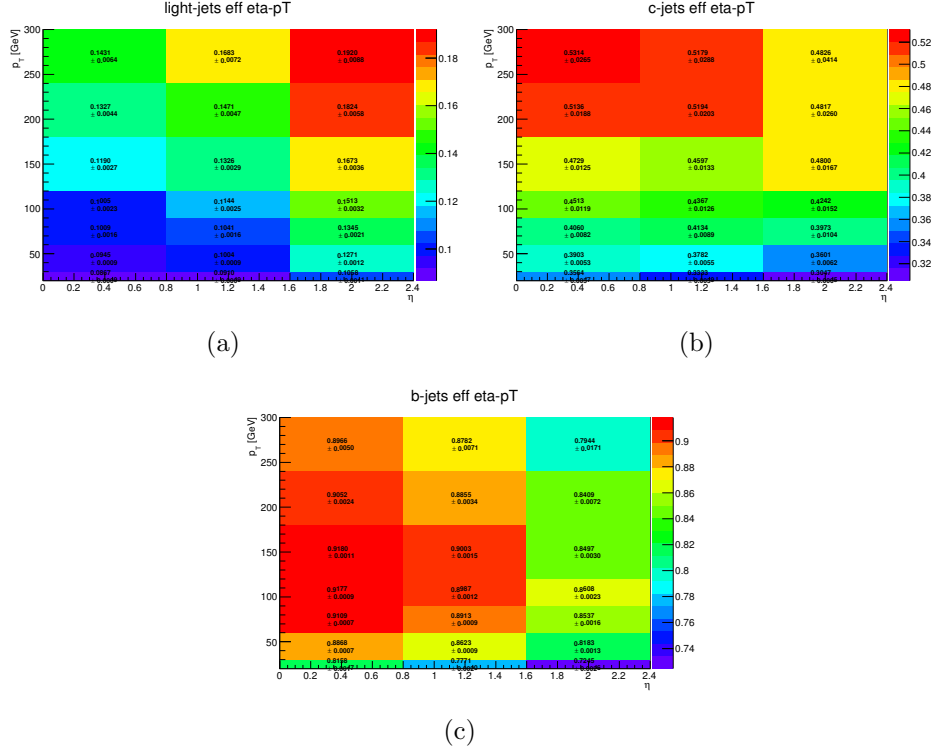


**Figure 5.4:** B tagging efficiencies for light jets (a), c-jets (b) and b jets (c), as a function of  $\eta$  and  $p_T$ .

leading jets is performed to check the agreement after the application of the event weights. In order to evaluate the data/simulation agreement for b-jets, the data and simulation are compared to each other in a top quark enriched control region, defined by the following requirements:

- two leptons, an electron and a muon with opposite charge, with leading lepton  $p_T$  greater than 20 GeV and sub-leading lepton  $p_T$  greater than 15 GeV;
- no other electron or muon with  $p_T$  greater than 10 GeV;
- $m_{\ell\ell}$  greater than 50 GeV;
- at least two jets with  $p_T$  greater than 30 GeV;
- at least one of the two leading jets with cMVAv2 btagging score greater than -0.715 (loose working point).

In order to evaluate the agreement for light jets, a second control region is defined, populated by Z+light jet events, defined as follows:

- two electrons or two muons with opposite charge, with leading lepton  $p_T$  greater than 20 GeV and sub-leading lepton  $p_T$  greater than 15 GeV;

- no other electron or muon with  $p_T$  greater than 10 GeV;
- $m_{\ell\ell}$  between 80 GeV and 110 GeV;
- at least two jets with  $p_T$  greater than 30 GeV;
- no jets above 20 GeV with a TCHE score above 2.1.

Although a Z+jets sample is dominated by light flavor jets, a b-veto on an alternative algorithm (TCHE) is applied to reduce the contamination from b-jets, especially above the cMVAv2 cut. This helps mitigating possible data/simulation discrepancies in the modelling of the heavy/light flavour ratio. The comparison of the discriminator shape in data and simulation after the event reweighting is shown in Figs. 5.5 and 5.6 for the b-jets and light jets enriched control regions, respectively. The discriminator distribution is displayed in two bins and the edge represents the discriminator cut, in this case the one corresponding to the loose working point. Therefore, the entries falling in the left (right) bin correspond to events in which the leading or subleading jet fails (passes) the b tagging selection.

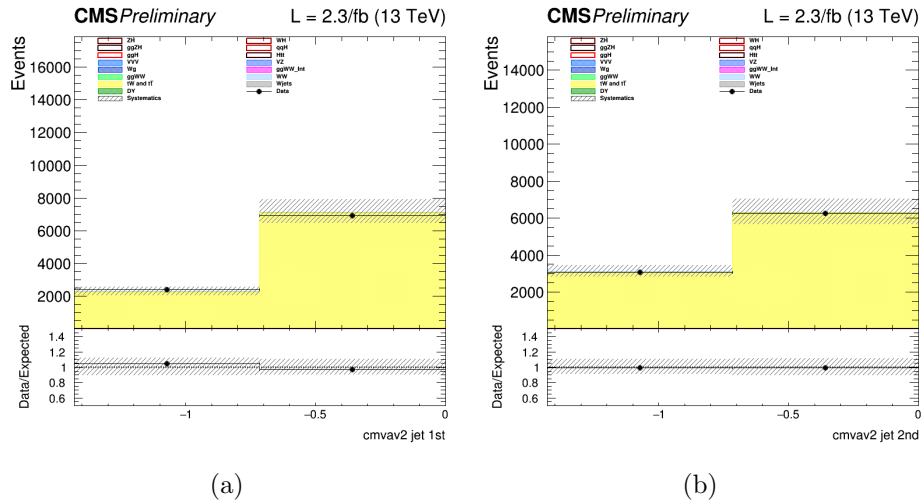


**Figure 5.5:** cMVAv2 discriminator for the leading (a) and the subleading (b) jet in the b-jets enriched control region.

### 5.2.3 Event selection and background rejection

Since the ggH production mechanism, which is the main production mode for a Higgs boson mass of 125 GeV, is characterized by the emission of few jets arising from initial state radiation, this analysis is limited to events with no jets or one jet. Due to the large Drell-Yan background in di-electrons and di-muons events, only the  $e\mu$  final state is studied in this early Run 2 data analysis, including the indirect contribution from  $\tau$  leptons decaying to electron or muons. Exactly one electron and one muon

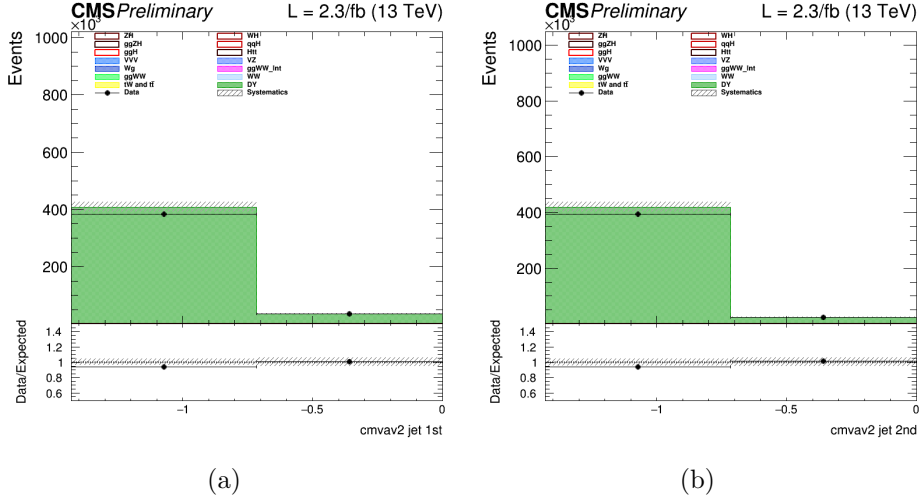


**Figure 5.6:** cMVAv2 discriminator for the leading (a) and the subleading (b) jet in the light jets enriched control region.

with opposite charge and a minimum  $p_T$  of 10 (13) GeV for the muon (electron) are required to be reconstructed in the event. One of the two leptons should also have a  $p_T$  larger than 20 GeV and both leptons are required to be well identified and isolated to reject fake leptons and leptons coming from hadron decays. To suppress background processes with three or more leptons in the final state, such as ZZ, WZ, Z $\gamma$ , W $\gamma$ , or triboson production, no additional identified and isolated lepton with  $p_T > 10$  GeV should be reconstructed. The low  $m_{\ell\ell}$  region dominated by hadron decays of leptons is not considered in the analysis and  $m_{\ell\ell}$  is requested to be larger than 12 GeV. To suppress the background arising from Drell-Yan events decaying to a  $\tau$  lepton pair which subsequently decays to an  $e\mu$  final state ( $Z/\gamma^* \rightarrow \tau^+\tau^-$ ) and suppress processes without genuine  $E_T^{\text{miss}}$ , a minimal  $E_T^{\text{miss}}$  of 20 GeV is required. The  $Z/\gamma^* \rightarrow \tau^+\tau^-$  background is further reduced by requesting  $p_T^{\ell\ell} > 30$  GeV. Finally the contribution from leptonic decays of single top quark and  $t\bar{t}$  production is reduced by requesting the b-jet veto.

The requirements described above define the WW baseline selection. After those requirements the data sample is dominated by events arising from the non-resonant WW production and  $t\bar{t}$  production. To further reduce the effect of these backgrounds on the signal sensitivity, the events are categorized depending on the jet multiplicity, counting jets with  $p_T > 30$  GeV. Events with zero associated jets mainly arise from WW production, while  $t\bar{t}$  production has a larger contribution in the category with one jet. The b-jet veto acts differently in the two categories as explained in the previous section: in the 0 jet category it rejects events containing at least one b-tagged jet with  $20 \text{ GeV} < p_T < 30 \text{ GeV}$ , while in the category with exactly one jet, the event is rejected if that same jet is identified by the b tagging algorithm. Higher jet multiplicity categories that are sensitive to other Higgs boson production

mechanisms, such as VBF, are not included given the very low expected yield for the analysed integrated luminosity.

Distributions of some variables of interest for the 0 and 1 jet categories separately are shown in Figs. 5.7, 5.8 and 5.9 after applying the WW baseline selections, with the addition of a cut on  $m_{\ell\ell}$  to remove the Higgs signal contribution ( $m_{\ell\ell} > 80 \text{ GeV}$ ), and a cut on  $m_T$  to be orthogonal to the  $Z/\gamma^* \rightarrow \tau^+\tau^-$  background control region ( $m_T > 60 \text{ GeV}$ ).

An additional categorization is applied in order to increase the signal sensitivity. The 0 ad 1 jets categories are further split according to the lepton flavour to  $e\mu$  and  $\mu e$ , where the first lepton refers to the leading one. In this way an improvement of about 10% in terms of the signal significance can be achieved, exploiting the different W+jets background contribution in the two categories. In fact this background is characterized by the presence of one jet misidentified as a lepton, and the probability for a jet to be misidentified as a muon is larger than as an electron.

#### 5.2.4 Signal extraction

To extract the Higgs boson signal contribution in the four previously mentioned categories, a similar approach to the one used in the Run 1 analysis [90] is pursued. The analysis is based on two-dimensional templates of  $m_{\ell\ell}$  versus  $m_T$  to discriminate signal and background contributions. The  $m_{\ell\ell}$  template is defined using 5 bins from  $m_{\ell\ell} = 10 \text{ GeV}$  up to  $m_{\ell\ell} = 110 \text{ GeV}$ , while for the  $m_T$  template 7 bins are defined in the range  $60 \text{ GeV} < m_T < 200 \text{ GeV}$ . The phase space with  $m_T < 60 \text{ GeV}$  is used as an orthogonal control region to extract the normalization of the  $Z/\gamma^* \rightarrow \tau^+\tau^-$  background. A binned maximum likelihood fit to the signal and background two-dimensional templates is performed to extract the signal strength in the four categories.

The statistical methodology used to interpret the data and combine the results from the independent 0 and 1 jet categories in the  $e\mu$  and  $\mu e$  final states has been developed by the ATLAS and CMS collaborations in the context of the LHC Higgs Combination Group [45, 116]. The number of events in each category and in each bin of the two-dimensional template is modelled as a Poisson random variable, with a mean value given by the sum of the contributions from all the processes under consideration. Systematic uncertainties are represented by individual nuisance parameters with log-normal distributions. The uncertainties affect the overall normalization of the signal and backgrounds, as well as their ( $m_{\ell\ell}$ ,  $m_T$ ) shape. Correlation between systematic uncertainties in different categories are taken into account.

### 5.3 Background estimation

The main background processes affecting the analysis signature, non-resonant WW production and top quark processes, are estimated using data. Backgrounds arising from an experimental misidentification of the objects, such as W+jets (also called

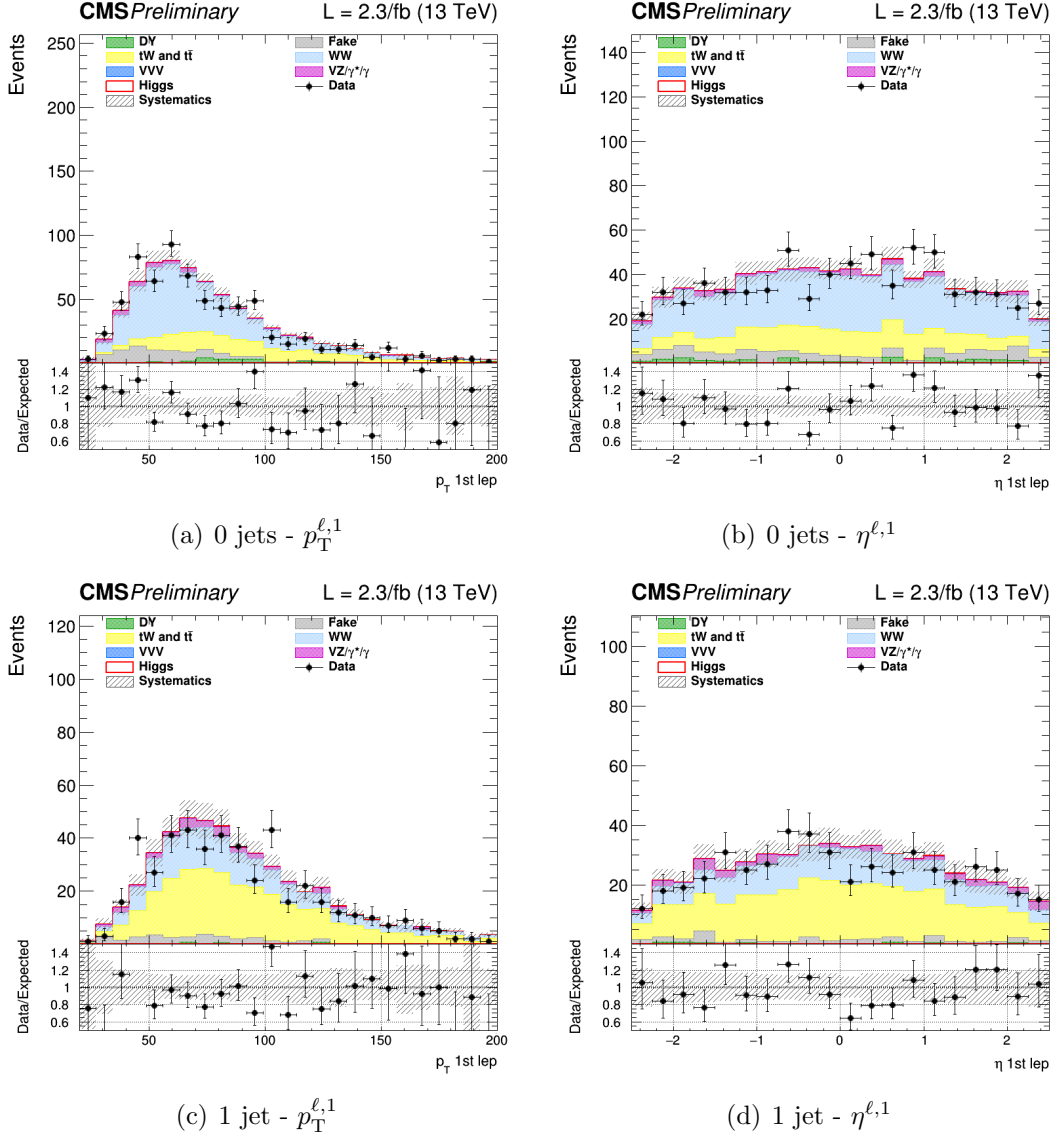


**Figure 5.7:** Distributions of  $p_T$  (left) and  $\eta$  (right) of the leading lepton for events with 0 jet (upper row) and 1 jet (lower row), for the main backgrounds (stacked histograms), and for a SM Higgs boson signal with  $m_H = 125$  GeV (superimposed and stacked red histogram) at the WW selection level. The last bin of the histograms includes overflows.

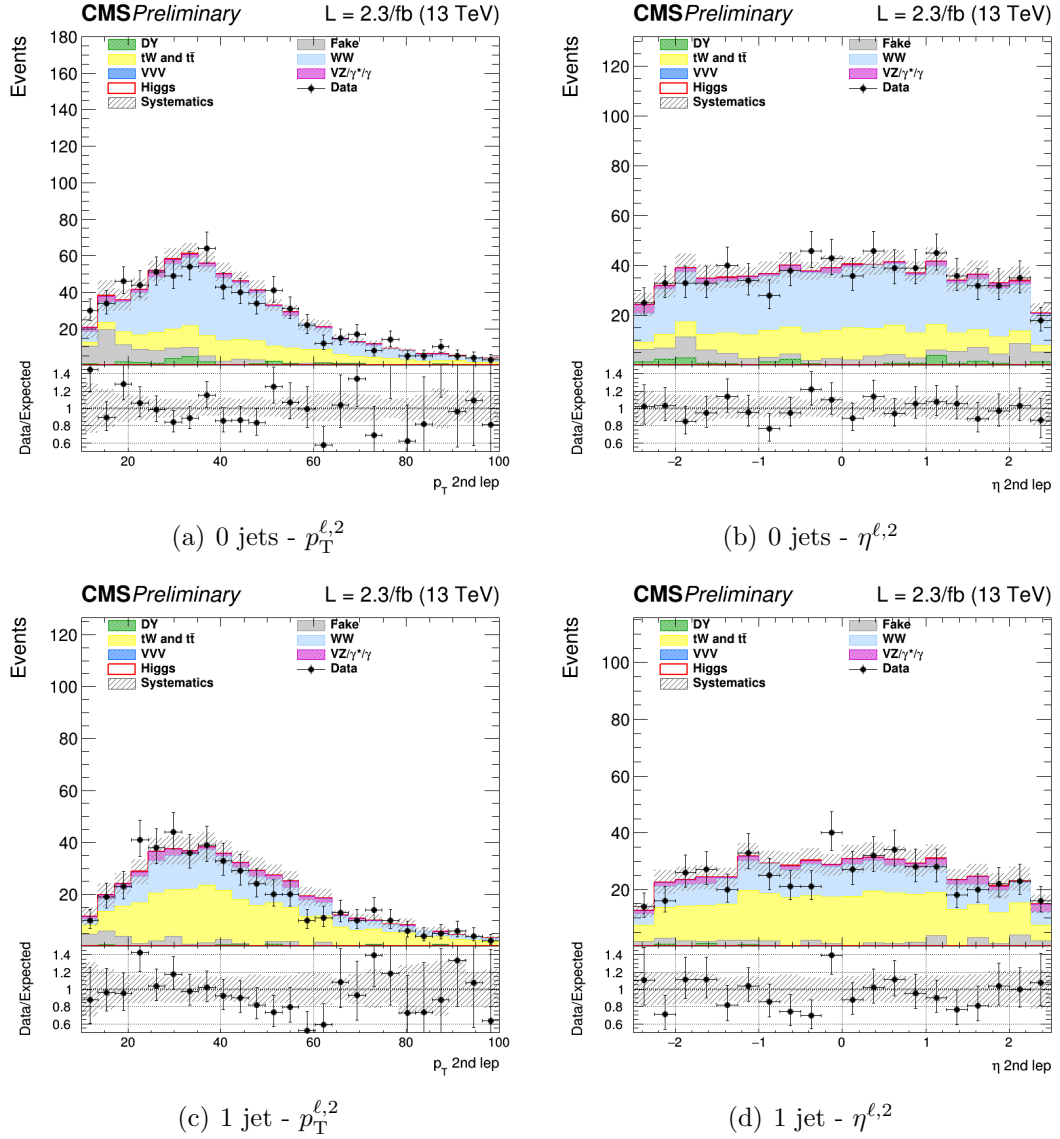


**Figure 5.8:** Distributions of  $p_T$  (left) and  $\eta$  (right) of the subleading lepton for events with 0 jets (upper row) and 1 jet (lower row), for the main backgrounds (stacked histograms), and for a SM Higgs boson signal with  $m_H = 125$  GeV (superimposed and stacked red histogram) at the WW selection level. The last bin of the histograms includes overflows.

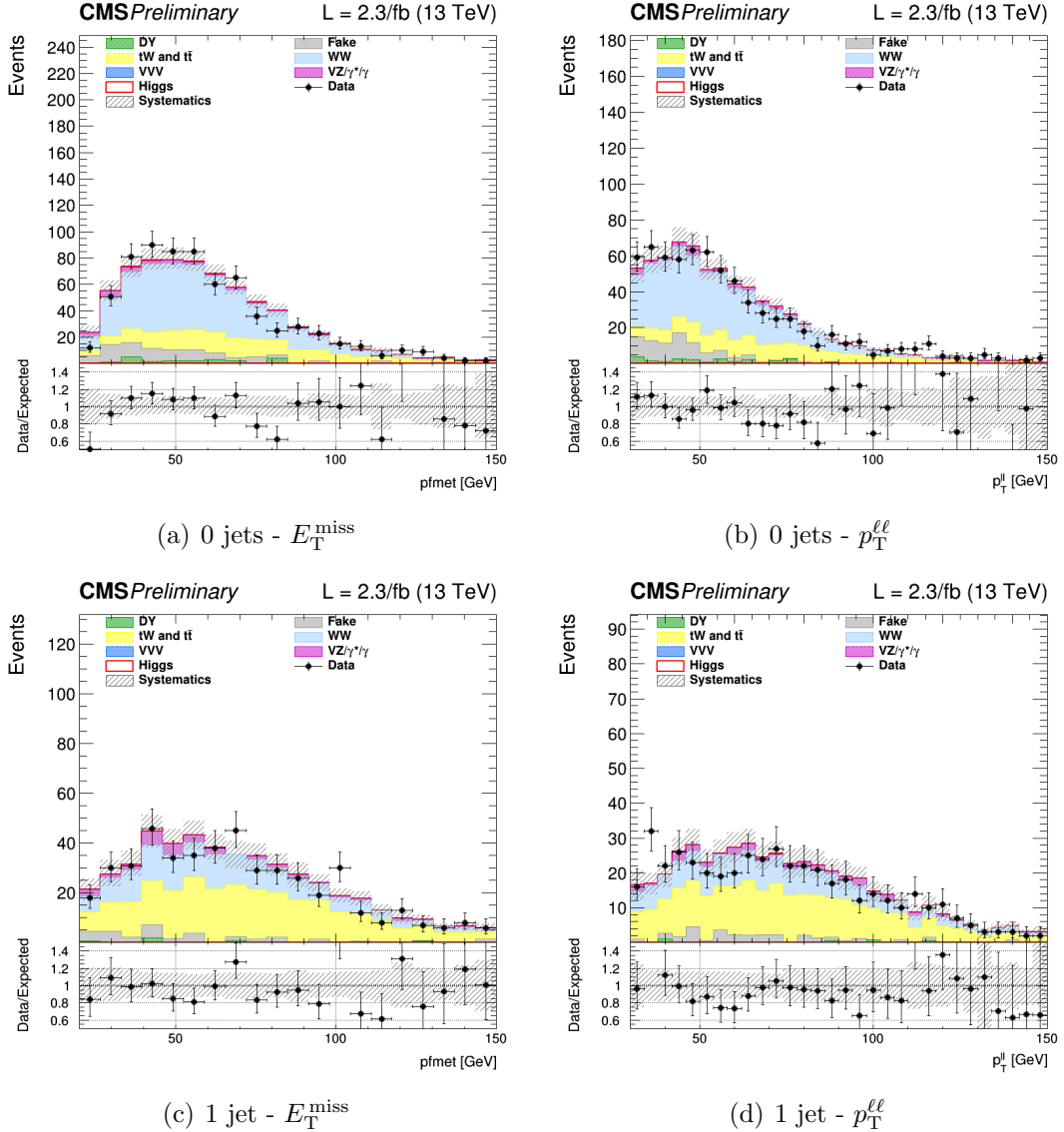


**Figure 5.9:** Distributions of  $E_T^{\text{miss}}$  (left) and  $p_T^{\ell\ell}$  (right) for events with 0 jets (upper row) and 1 jet (lower row), for the main backgrounds (stacked histograms), and for a SM Higgs boson signal with  $m_H = 125$  GeV (superimposed and stacked red histogram) at the  $WW$  selection level. The last bin of the histograms includes overflows.

“fake” or “jet-induced”), are estimated using data as well. The other minor backgrounds are generally estimated directly from simulation as described in the following sections.

### 5.3.1 WW background

The quark-induced WW background is simulated with NLO accuracy in perturbative QCD, and the transverse momentum of the diboson system is reweighted to match the NNLO+NNLL accuracy from theoretical calculations [125, 126]. However, given the large uncertainties on the jet multiplicity distribution associated to this process, the normalization of this background is measured from data separately for the 0 and 1 jet categories. The normalization  $k$ -factors are extracted directly from the fit, leaving the WW normalization free to float separately in the two jet multiplicity categories. An orthogonal control region for the WW background normalization estimation is not needed in this case, owing to the different ( $m_{\ell\ell}$ ,  $m_T$ ) shape for signal and background.

The gluon-induced WW production is sub-dominant with respect to the quark-induced production, and its shape and normalization are taken from simulation, scaling the cross section to the theoretical NLO accuracy prediction [133].

### 5.3.2 Top quark background

As explained in Sec. 5.2, the production of top quark pairs represents one of the dominant backgrounds in this analysis given its large cross section and a final state similar to signal. A b-jet veto, based on the cMVAv2 b tagging algorithm, is used to suppress this background and a reweighting procedure is applied to the simulated events to correct for different b tagging efficiency in data and simulation.

The top quark background normalization is measured using data, defining a b-jets enriched control region by inverting the b-jet veto. More precisely, the b-jets enriched control region for the 0 jets category is defined with the same WW baseline selection but requiring at least one jet with  $20 < p_T < 30 \text{ GeV}$  to be identified as a b jet and no other jets with  $p_T > 30 \text{ GeV}$ . For the 1 jet category, the b-jets enriched region is defined requiring exactly one jet with  $p_T > 30 \text{ GeV}$  identified as a b-jet. To reduce other backgrounds in these two regions, the dilepton mass has to be greater than 50 GeV. Distributions of the  $m_{\ell\ell}$  and  $m_T$  variables in the b-jets enriched control regions after applying the data driven estimation are shown in Figure 5.10 for the 0 and 1 jet categories separately.

The top quark background normalization is constrained during the fit procedure separately in the two jet categories, by means of the control regions defined above, which are treated in the fit as two additional categories.

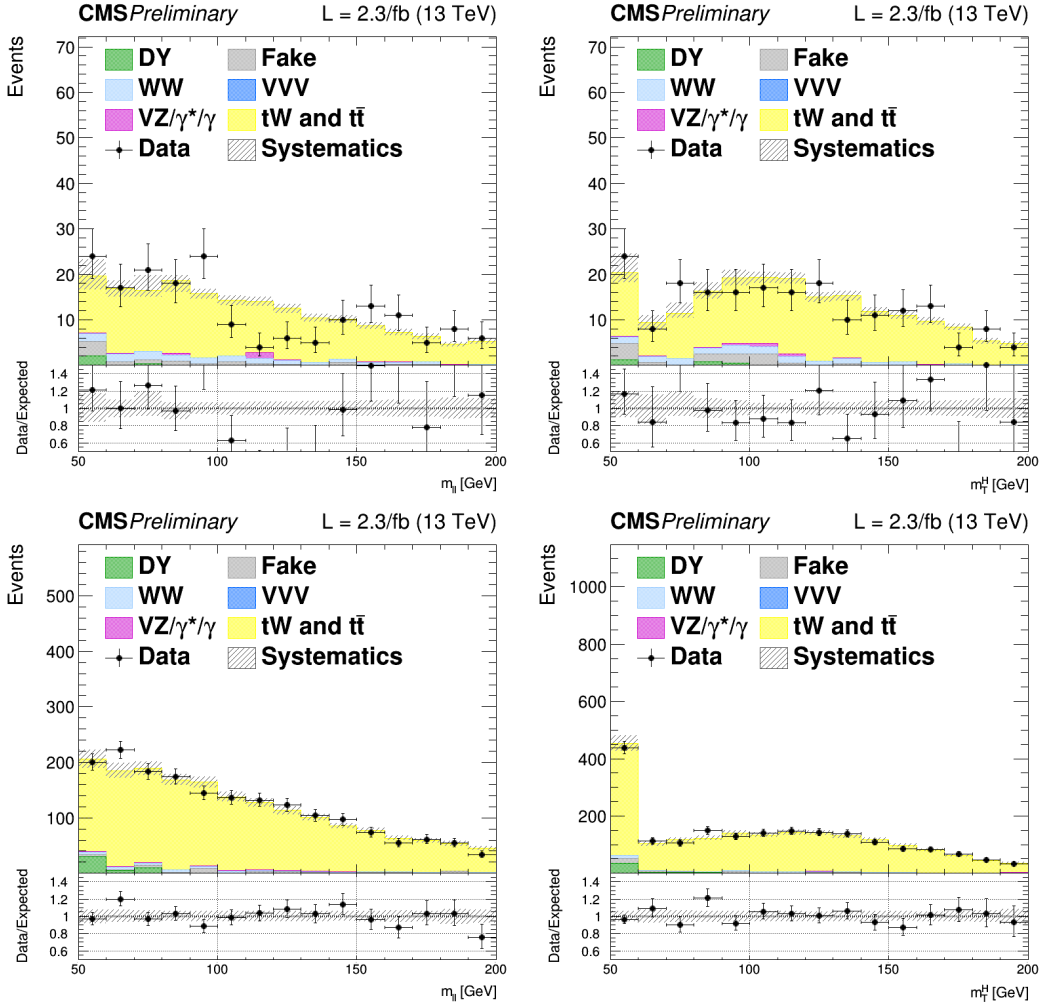


**Figure 5.10:** Distributions of  $m_{\ell\ell}$  (left) and  $m_T$  (right) for events with 0 jets (top) and 1 jet (bottom) in top enriched phase space. Scale factors estimated from data are applied. The first (last) bin includes underflows (overflows).

### 5.3.3 W+jets background

One of the primary source belonging to this category arises from the misidentification of leptons in W+jets (also known as “Fake”) processes in the 0 jets category. Also, semileptonic  $t\bar{t}$  decays contribute especially for higher jet multiplicities. Multijet production and hadronic  $t\bar{t}$  decays are also taken into account, despite their smaller contribution.

This background is fully estimated using data, with the technique described in Sec. 4.4.3. To check the agreement of the background estimated in this way with data, a control sample enriched in Fake events is defined. The events in the control sample are selected applying the WW baseline requirements but requesting an  $e\mu$  pair with same charge, significantly suppressing the WW and  $t\bar{t}$  processes. The  $m_{\ell\ell}$

distributions in this control region for the 0 and 1 jet categories are shown in Fig. 5.11. From this cross-check a global normalization factor of 0.8 is derived in both categories and applied to the Fake background.

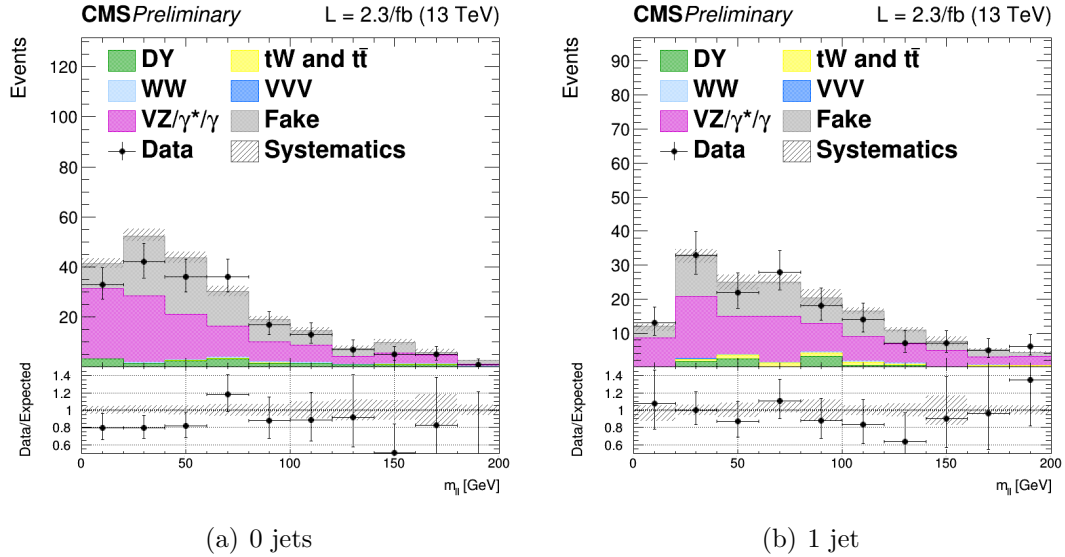


**Figure 5.11:** Control plots for  $m_{\ell\ell}$  in a Fake enriched phase space for events with 0 and 1 jet with  $p_T > 30 \text{ GeV}$ , in  $e\mu$  final state.

### 5.3.4 $Z/\gamma^* \rightarrow \tau^+\tau^-$ background

This background contributes to the analysis phase space because of the  $Z/\gamma^*$  decays to a pair of  $\tau$  leptons, which consequently decays to an  $e\mu$  pair. This background process is predominant in the low  $m_T$  region, which is used as an orthogonal control region to determine the background normalization in the 0 and 1 jet categories separately. In particular this control region is defined by selecting events with  $m_T < 60 \text{ GeV}$  and  $30 \text{ GeV} < m_{\ell\ell} < 80 \text{ GeV}$ . The  $m_{\ell\ell}$  distributions in these control regions for the 0 and 1 jet categories are shown in Fig. 5.12.

As for the top quark background, the normalization of this background in the 0 and 1 jet categories, is constrained directly in the fit by means of control regions, which are treated as two additional categories.

The kinematics of this background is taken from simulation, after reweighting the  $Z$  boson  $p_T$  spectrum to match the observed distribution measured in data. In fact, this variable is not well reproduced by the MC generator used for simulating this process, especially in the bulk of the distribution. The discrepancy is ascribed to the missing contribution from resummed calculations.

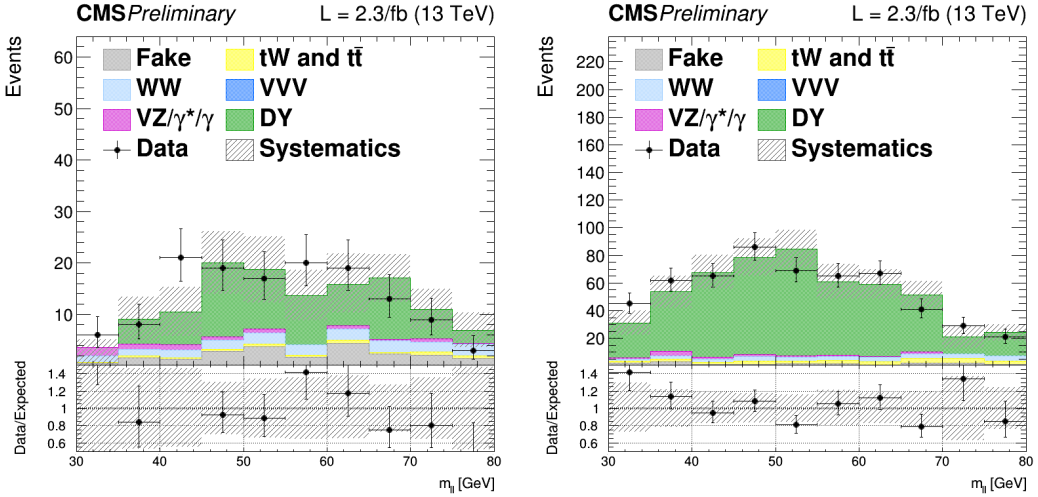


**Figure 5.12:** Distributions of  $m_{\ell\ell}$  for events with 0 jets (left) and 1 jet (right) in the  $Z/\gamma^* \rightarrow \tau^+\tau^-$  enriched control region. Scale factors estimated from data are applied.

### 5.3.5 Other backgrounds

The  $W\gamma^*$  and the  $WZ$  electroweak processes can be gathered in the same physical process, although the final state kinematics is rather different. In particular, the invariant mass of the leptons arising from the  $\gamma^*$  decays is generally below 4 GeV, while the leptons from the  $Z$  boson decay are characterized by a larger invariant mass. Another background which can be experimentally identical to those is the  $W\gamma$  production, where a real photon is produced in association with a  $W$  boson and undergoes a photon conversion to leptons due to the interaction with the material of the silicon tracker.

All these backgrounds may contribute to the signal phase space whenever one of the three leptons escape from the detector acceptance or is not identified. The shape and cross section of these backgrounds are taken from simulation. The only exception is the normalization of the  $W\gamma^*$  background, being this process dominant in the low  $m_{\ell\ell}$  region, which is scaled to data defining a proper control region. The control region is defined selecting events with three isolated muons, with  $p_T > 10$ , 5 and 3 GeV for the first three leading muons respectively. The selection is further defined by requiring  $E_T^{\text{miss}} < 25$  GeV. The pair of muons with the smallest invariant mass is taken as coming from the  $\gamma^*$  decay. The  $k$ -factor measured in data for this background is  $1.98 \pm 0.54$ .

All remaining backgrounds from diboson and triboson production, which are of minor importance in the analysis phase space, are normalized according to their expected theoretical cross sections.

## 5.4 Systematic uncertainties

The systematic uncertainties affecting this measurement can be divided into three categories: the uncertainties on the background estimation, experimental uncertainties and theoretical uncertainties.

The first category includes the uncertainties related to the background normalization and  $(m_{\ell\ell}, m_T)$  shape. For the non-resonant WW production the  $(m_{\ell\ell}, m_T)$  shape is taken from simulation. The input normalization to the fit is set to the expected value from simulation (scaled to match the NNLO cross section), and an unconstrained nuisance parameter with a flat prior distribution is associated to it, in order to freely float the normalization in the fit. This is done separately for the two jet categories.

The top quark background shape is taken from simulation after applying b tagging scale factors. The uncertainties on the normalization are treated similarly to the WW background case, but constraining the corresponding nuisance parameters by means of two control regions orthogonal to the signal phase space. A similar procedure is used for estimating the normalization of the  $Z/\gamma^* \rightarrow \tau^+\tau^-$  background process.

Effects due to experimental uncertainties are studied by applying a scaling and smearing of variables related to the physics objects, e.g. the  $p_T$  of the leptons, followed by a subsequent recalculation of all the correlated variables. This is done for simulation to account for possible systematic mismodelling.

All experimental sources of uncertainty, except for the one related to luminosity, are treated both as normalization and shape uncertainties, and are correlated among the signal and background processes in all categories. The following experimental uncertainties are considered:

- the uncertainty determined by the CMS online luminosity monitoring, 2.7% for the first data collected at  $\sqrt{s} = 13$  TeV;
- the acceptance uncertainty associated with the combination of single and double lepton triggers, which is 2%;
- the lepton reconstruction and identification efficiency uncertainties, that are in the range 0.5–5% for electrons and 1–7% for muons depending on  $p_T$  and  $\eta$ ;
- the muon momentum and electron energy scale and resolution uncertainties, that amount to 0.01–0.5% for electrons and 0.5–1.5% for muons depending on  $p_T$  and  $\eta$ ;
- the jet energy scale uncertainties, that vary between 1–11% depending on the  $p_T$  and  $\eta$  of the jet;
- the  $E_T^{\text{miss}}$  resolution uncertainty, that is taken into account by propagating the corresponding uncertainties on the leptons and jets;

- the uncertainty on b tagging and mistag scale factors. These systematic uncertainties are anticorrelated between the top quark enriched control region and the other ones.

The uncertainties in the signal and background production rates due to theoretical uncertainties include several components, which are assumed to be independent: the PDFs and  $\alpha_s$ , the underlying event and parton shower model, and the effect of missing higher-order corrections.

The effects of the variation of PDFs,  $\alpha_s$  and renormalization/factorization QCD scales, mainly affect the signal processes, since the most important backgrounds are estimated using data driven techniques. However, the uncertainties on minor backgrounds that are estimated from simulation are taken into account. These uncertainties are split into uncertainties on cross section, which are computed by the LHC cross section working group [136], and selection efficiency [137]. The PDFs and  $\alpha_s$  signal cross section uncertainties are about 6–7% for ggH and 1–3% for VBF production mechanism. The PDFs and  $\alpha_s$  acceptance uncertainties are less than 1% for all gluon- and quark-induced processes. The effect of varying the renormalization and factorization scales on the selection efficiency is around 1–3% depending on the specific process.

In addition, the categorization of events based on jet multiplicity introduces additional uncertainties on the ggH production mode related to missing higher order corrections. These uncertainties are evaluated following the prescription described in Refs. [46, 111] and are found to be of 5.6% for the 0 jets and 13% for the 1 jet category.

The underlying event uncertainty on the signal contribution is estimated by comparing two different PYTHIA 8 tunes, while parton shower modelling uncertainty is estimated by comparing samples interfaced with PYTHIA 8 and HERWIG++ programs. The effect on the ggH (VBF) expected yield is about 5% (5%) for the PYTHIA 8 tune variation and about 7% (10%) for the parton shower description.

Other specific theoretical uncertainties are associated to some backgrounds. An uncertainty on the ratio of the  $t\bar{t}$  and  $tW$  cross sections is included. Indeed, these two processes are characterized by a different number of b-jets in the final state (2 b-jets for  $t\bar{t}$  and 1 for  $tW$ ) and the b veto acts differently for the two. A variation of the relative ratio of the cross sections can thus cause a migration of events from the 0 to the 1 jet categories and viceversa. The uncertainty on the  $t\bar{t}/tW$  cross section ratio is 8%, according to the theoretical cross section calculations [134, 135].

For what the  $qq \rightarrow WW$  background shape is concerned, an uncertainty related to the diboson  $p_T$  reweighting is evaluated varying the renormalization, factorization and resummation QCD scales.

Finally, the uncertainties due to the limited statistical accuracy of the MC simulations are also taken into account, including an independent uncertainty for each bin of the two-dimensional ( $m_{\ell\ell}, m_T$ ) distribution, and for each category. The uncertainty for a certain bin and process is given by the standard deviation of the Poisson distribution with mean corresponding to the number of simulated events in that bin.

## 5.5 Results

Distributions of the  $m_{\ell\ell}$  and  $m_T$  variables after the full analysis selection are shown in Fig. 5.13 for the 0 and 1 jet categories separately, but merging the  $e\mu$  and  $\mu e$  final states together.

**Table 5.5:** Observed and expected significance and signal strength for the SM Higgs boson with a mass of 125 GeV in the 0 and 1 jet,  $\mu e$  and  $e\mu$ , categories.

Category	Expected significance	Observed significance	$\sigma/\sigma_{SM}$
0 jet $\mu e$	1.1	1.3	$1.13^{+0.9}_{-0.9}$
0 jet $e\mu$	1.3	0.4	$0.33^{+0.7}_{-0.7}$
1 jet $\mu e$	0.8	0	$-0.11^{+0.5}_{-1.7}$
1 jet $e\mu$	0.9	0	$-0.54^{+1.4}_{-1.4}$
0 jet	1.6	1.3	$0.71^{+0.6}_{-0.5}$
1 jet	1.2	0	$-0.56^{+1.0}_{-1.0}$
Combination	2.0	0.7	$0.33^{+0.5}_{-0.5}$

The expected and observed signal significance are shown in Table 5.5 for all the categories separately. Also, the observed signal strengths and the corresponding uncertainties are shown. The best fit signal strength obtained combining all the categories together is found to be  $0.3^{+0.5}_{-0.5}$ , corresponding to an observed significance of  $0.7\sigma$ , to be compared with the expected significance of  $2.0\sigma$  for a Higgs boson mass of 125 GeV.

The measurement is dominated by the statistical uncertainties on data. The main systematic contributions affecting the uncertainty on the signal strength arise from the Fake background estimation, lepton identification and isolation, luminosity, b tagging scale factors, WW and  $t\bar{t}$  background normalization and other minor backgrounds. The uncertainty on the data driven backgrounds mainly arise from the limited data statistics in the control regions used for measuring the normalization. A summary of the most important systematic uncertainties and their effect on the signal strength uncertainty is illustrated in Table 5.6.

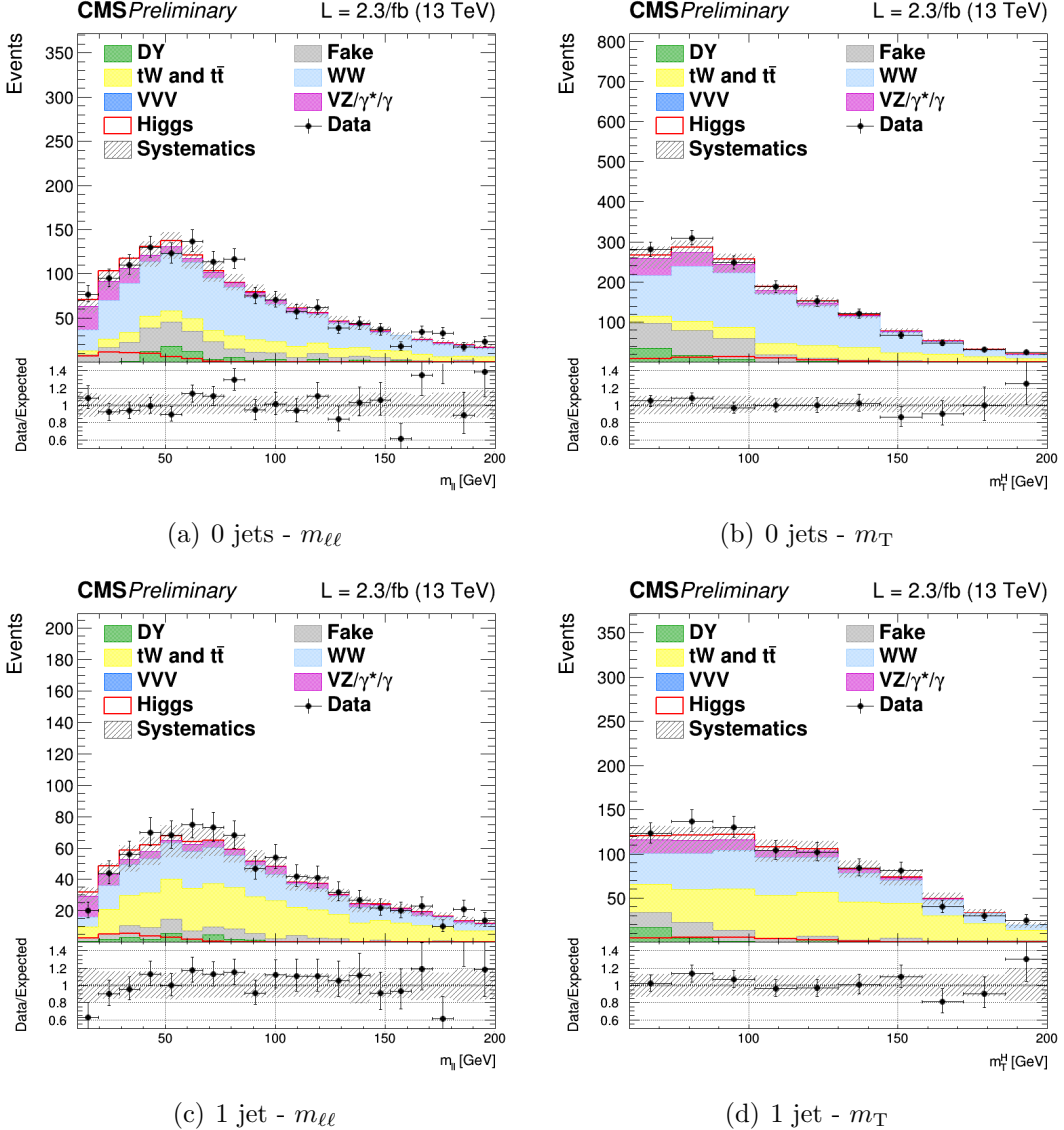


**Figure 5.13:** Distributions of  $m_{\ell\ell}$  (left) and  $m_T$  (right) for events with 0 jets (upper row) and 1 jet (lower row), for the main backgrounds (stacked histograms), and for a SM Higgs boson signal with  $m_H = 125 \text{ GeV}$  (superimposed and stacked red histogram) at the  $WW$  selection level. The last bin of the histograms includes overflows. The simulation of the  $WW$  background is normalized to data.

**Table 5.6:** Main systematic sources and their contribution to the signal strength uncertainty ( $\Delta\mu/\mu$ ).

Systematic uncertainty	$\Delta\mu/\mu$
Fake background estimation	25%
Lepton identification and isolation	20%
$W\gamma^*$ background cross section	12%
$WW$ and $t\bar{t}$ data driven normalization	10%
Luminosity	8%
b tagging scale factors	6%
Lepton scale and resolution	3%



# Chapter 6

## Search for high mass resonances decaying to a W boson pair with first 13 TeV data

In this chapter, a search for a high mass spin-0 particle (from now on denoted as X) in the  $X \rightarrow WW \rightarrow \ell\nu\ell'\nu'$  decay channel is presented, where  $\ell$  and  $\ell'$  refer to different flavour lepton pairs, i.e.  $e\mu$ . The search is based upon the same proton-proton collision data samples considered in the previous chapter, corresponding to an integrated luminosity of  $2.3 \text{ fb}^{-1}$  at  $\sqrt{s} = 13 \text{ TeV}$ . This analysis represents a general extension of the SM Higgs boson search presented in 5 and is performed in a range of heavy scalar masses from  $M_X = 200 \text{ GeV}$  up to  $1 \text{ TeV}$ , extending the range studied in a similar analysis performed using Run 1 LHC data [138], which provided upper limits on the production cross section of new scalar resonances up to  $600 \text{ GeV}$ .

This analysis reports a generic search for a scalar particle with different resonance decay hypotheses, produced via the ggH and VBF production mechanisms. The results can then be interpreted in terms of different theoretical models as discussed in Sec. 1.2. This analysis is based on the SM Higgs measurement described in Chapter 5 in terms of physics objects, selections and background estimations. The differences are discussed in the following sections.

### 6.1 Data and simulated samples

The data sets, triggers, pile-up reweighting, lepton identification and isolation used in this analysis are the same as the  $125 \text{ GeV}$  mass Higgs boson measurement and are described in Sec. 5.1.

Also, the same MC simulations are used for the background processes, the only exception being the Drell-Yan background. Given that this analysis aims to probe regions of phase space where the Drell-Yan contribution is very small, like in the high transverse mass region, the usage of a simulation of the inclusive Drell-Yan process

leads to large uncertainties due to the limited simulation statistics in the sample. To partially overcome this issue the MADGRAPH5\_AMC@NLO generator is used with LO QCD accuracy, matching together events with up to four jets in addition to the vector boson with the MLM [142] matching scheme, in order to generate different Drell-Yan samples in restricted portions of the phase space defined by the  $H_T$  variable, i.e. the scalar sum of all the partons  $p_T$  in the event. The samples are merged using the parton level information, and a smooth transition between different  $H_T$  regions is achieved, as shown in Fig. 6.1. The Drell-Yan LO cross section obtained from the simulation is scaled using a LO to NNLO  $k$ -factor of 1.23.

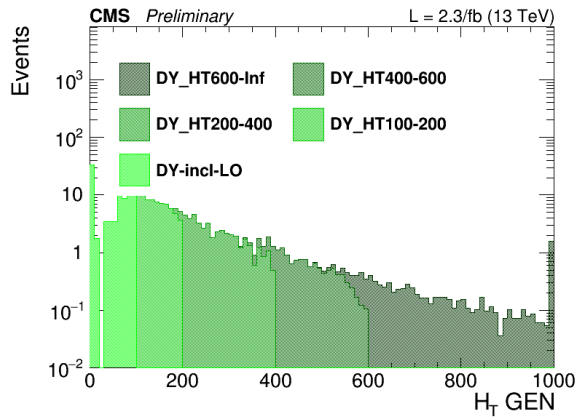


**Figure 6.1:** Generator level  $H_T$  distribution for the merged Drell-Yan (DY in the legend) sample.

In order to perform the resonance search in a large part of the mass spectrum, several signal samples for the ggH<sup>1</sup> and VBF mechanisms have been generated corresponding to different resonance masses in the range between 200 GeV and 1 TeV. The signal width for each mass point corresponds to the one expected for a SM Higgs boson at that mass (see Fig. 1.8). The samples are produced with a mass step of 50 GeV from 250 to 800 GeV and of 100 GeV from 800 to 1000 GeV. A finer stepping is used between 200 and 250 GeV. All the signal samples are generated with the POWHEG V2 generator, interfaced with the JHUGEN v6.2.8 generator, which handles the decay of the scalar resonance to  $W^+W^- \rightarrow 2\ell 2\nu$ .

The interference effects among  $gg \rightarrow X \rightarrow WW$ ,  $gg \rightarrow WW$  and  $gg \rightarrow H \rightarrow WW$  are evaluated using the MCFM and JHUGEN generators, as implemented in the MELA (Matrix Element Likelihood Approach) framework [43]. Details about the interference effects are given in Sec. 6.2.

---

<sup>1</sup>The ggH notation is used for the gluon-gluon fusion production mode, even in the cases where a non-SM Higgs boson is created through this mechanism.

## 6.2 Analysis strategy

The analysis strategy for the first results on the high mass search in the  $W^+W^- \rightarrow 2\ell 2\nu$  decay channel closely follows the strategy presented in the 13 TeV Higgs boson measurement described in the previous chapter. In addition a category dedicated to the VBF production mechanism is added, given the importance of this production mode in the high mass region. Indeed, assuming a SM Higgs boson, the ratio of cross sections  $\sigma_{\text{VBF}}/\sigma_{\text{ggH}}$  increases with the Higgs boson mass, making the VBF production mechanism more and more important as the mass of the resonance approaches to large values.

This analysis is essentially affected by the same background processes as the 125 GeV mass Higgs boson measurement, with the difference that in this case the Higgs boson contribution is treated as background.

In addition to selecting events that pass the single or double lepton triggers, exactly one electron and one muon with opposite charges are required to be reconstructed in the event with a minimum  $p_T$  of 20 GeV for both the muon and electron. Both leptons are required to be well identified and isolated to reject fake leptons and leptons coming from in flight decays. To suppress background processes with three or more leptons in the final state, such as diboson or triboson production, events with any additional identified and isolated lepton with  $p_T > 10$  GeV are rejected. To suppress the contribution of the production of the Higgs boson at 125 GeV,  $m_{\ell\ell}$  is requested to be higher than 50 GeV. The other event requirements are identical to the 125 GeV Higgs boson measurement and are described in Sec. 5.2.3.

In addition to the 0 and 1 jet categories, a specific category sensitive to the VBF production mode is defined exploiting the characteristic signature of this process, where two energetic jets are emitted in the forward region of the detector and have large  $\Delta\eta$  gap. Events belonging to the VBF-enriched category are selected by requiring at least two jets with  $p_T > 30$  GeV, an invariant mass  $m_{jj} > 500$  GeV and a pseudorapidity gap of  $\Delta\eta_{jj} > 3.5$ .

Beyond the transverse mass  $m_T$ , which is used in the analysis selection to define the  $Z/\gamma^* \rightarrow \tau^+\tau^-$  background control region, an additional variable is defined, that from now on will be labelled as “improved transverse mass”  $m_T^i$ . This variable is defined as the invariant mass of the four momentum resulting from the sum of the two leptons four momenta ( $p_{\ell\ell}, \vec{p}_{\ell\ell}$ ) and four momentum  $\mathbf{E}_T^{\text{miss}} = (E_T^{\text{miss}}, \vec{p}_T^{\text{miss}})$ , i.e.:

$$m_T^i = \sqrt{(p_{\ell\ell} + E_T^{\text{miss}})^2 - (\vec{p}_{\ell\ell} + \vec{p}_T^{\text{miss}})^2} . \quad (6.1)$$

This variable allows a better sensitivity to different resonance mass hypotheses as illustrated in Fig. 6.2, where the shape of the  $m_T^i$  variable is shown for different SM Higgs mass hypotheses and is compared to the standard  $m_T$  variable. The usage of this variable also provide a good discriminating power between signal and background.

The signal extraction is based on a binned maximum likelihood fit using the  $m_T^i$  distribution for signal and background contributions as template. The  $m_T^i$  template is defined using the following bin boundaries:

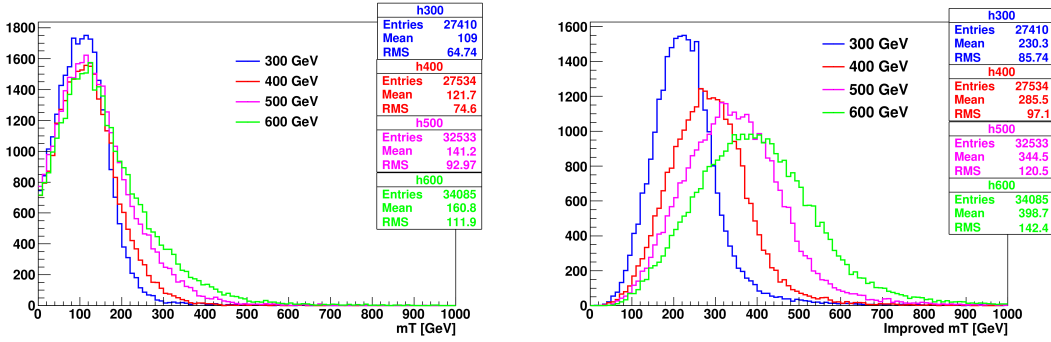


**Figure 6.2:** Distributions of the  $m_T$  and  $m_T^i$  variables at generator level for different resonance mass hypothesis.

- 0/1 jet: [100,150,200,250,300,350,400,450,500,600,700,1000] ,
- VBF: [100,150,200,250,300,350,400,500,700,1000] ,

where the first number represents the lower edge of the first bin while the other numbers represent the upper edges. The last bin is an overflow bin.

In order to test different resonance decay widths hypotheses, the signal samples, which are generated with a decay width corresponding to the expected value for a SM Higgs boson at that mass ( $\Gamma_{SM}$ ), are reweighted to obtain the desired width value ( $\Gamma'$ ). In particular the following values are used:  $\Gamma' = \Gamma_{SM}$ ,  $\Gamma' = 0.49 \times \Gamma_{SM}$ ,  $\Gamma' = 0.25 \times \Gamma_{SM}$  and  $\Gamma' = 0.09 \times \Gamma_{SM}$ . The reweighting is performed at generator level by computing the ratio of two relativistic Breit Wigner distributions with different decay widths,  $f(E, \Gamma', M_X)/f(E, \Gamma_{SM}, M_X)$ , where:

$$f(E) \propto \frac{1}{(E^2 - M^2)^2 + M^2 \Gamma^2} . \quad (6.2)$$

Here,  $f(E, \Gamma_{SM}, M_X)$  represents the distribution used for simulating the signal at a mass  $M_X$ , and  $f(E, \Gamma', M_X)$  the distribution with the new decay width. Each event is multiplied by this ratio (which depends on the energy  $E$  of the event) to obtain the reweighted distribution.

When a resonance with a non negligible width is considered, it is important to take into account the interference effects both with the  $gg \rightarrow WW$  background and the off-shell tail of the 125 GeV Higgs boson. A study of the interference effects for a resonance  $X$  produced through the gluon fusion mechanism is performed within the MCFM+JHUGEN framework, including NNLO cross section corrections using the HNNLO program [143]. The matrix element package MELA supports all these processes and allows fast MC re-weighting and optimal discriminant calculation. The basic idea of this approach is to compute the matrix elements of the processes under study with the MCFM and JHUGEN generators, including the interference terms, and using these matrix elements to compute an event weight used to reweight the simulated

samples. Using this approach the simulated events can be reweighted according to different scenarios, for instance including some or all the interference terms, allowing a detailed study of the interference contribution. The effect of the various interference terms for the  $M_X$  variable at generator level is shown in Fig. 6.3, after having applied the WW baseline selections. As can be observed, the contribution of the interference of the scalar resonance with the  $gg \rightarrow WW$  background and SM Higgs boson have opposite sign and partially cancel out. This cancellation effect is different for different resonance masses and depends on the event selection. In particular the interference term with the SM Higgs off-shell tail is positive for values below  $M_X$  while it turns negative above  $M_X$ . The contribution of the interference with the  $gg \rightarrow WW$  background is instead characterized by an opposite sign lineshape, thus leading to a partial cancellation when considering the total interference.

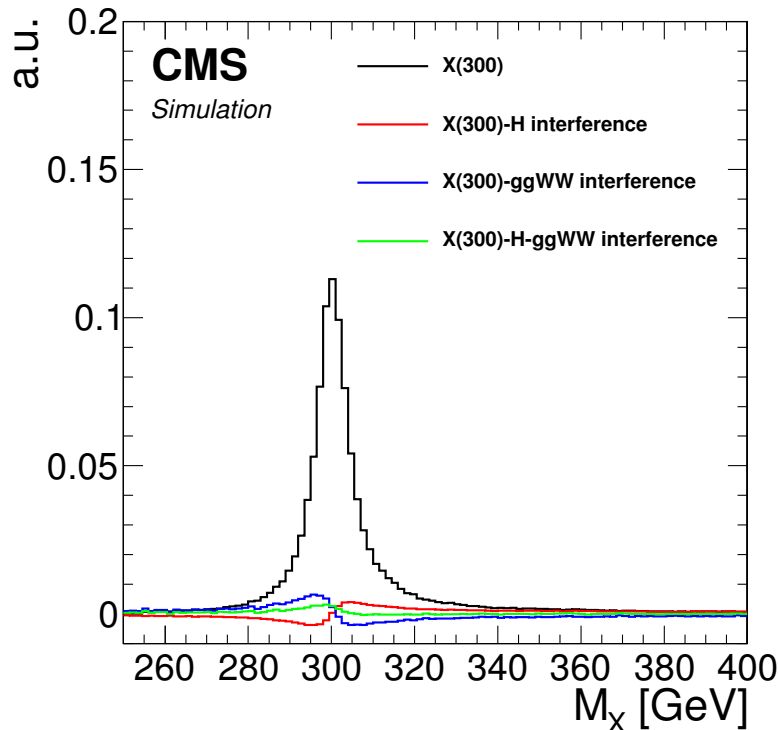


**Figure 6.3:** Distribution of the  $M_X$  variable for a resonance mass of 300 GeV, showing the various interference terms after the WW baseline selections.

The effect of the resulting interference contribution including all the different terms is shown in Fig. 6.4 for the  $m_T^i$  signal templates, in the three categories separately and for different  $M_X$  hypotheses.

The interference contribution is thus not negligible, especially for large values of  $M_X$ , and is included in the analysis as part of the signal contribution. More specifically, during the fit procedure the signal yield is scaled by the signal strength parameter  $\mu$  (which is the parameter of interest of the fit), while the interference yield is scaled by

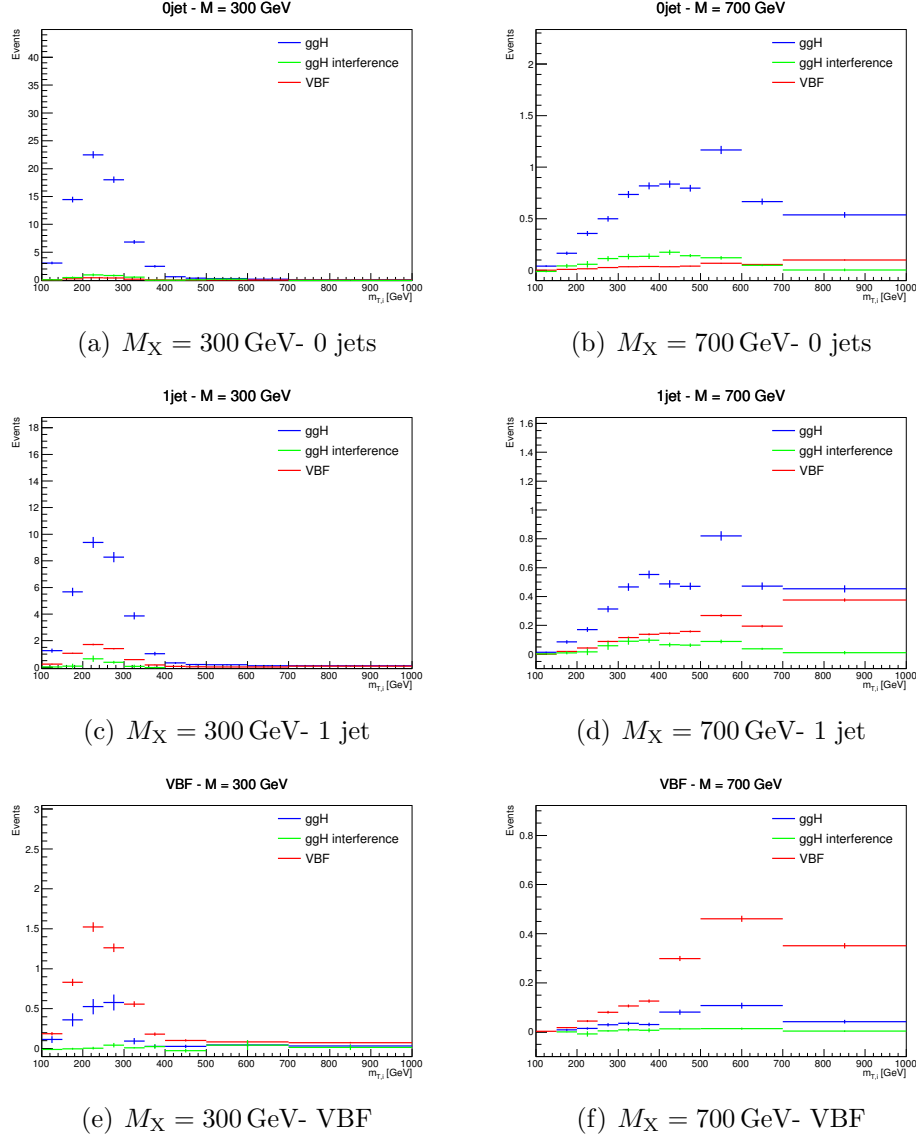


**Figure 6.4:** Distributions of the  $m_T^i$  variable for  $M_X = 300$  and 700 GeV, showing the signal (both the ggH and VBF mechanisms) and the interference contributions in the three jet categories.

$$\sqrt{\mu}.$$

### 6.3 Background estimation

The background processes affecting the analysis phase space are the same as the ones contributing to the SM Higgs measurement described in Sec. 5.3. The techniques used for the background estimation are the same as well.

The most relevant difference is the addition of the 2 jets category. The WW, top quark and  $Z/\gamma^* \rightarrow \tau^+\tau^-$  background normalizations are estimated in this category using data driven techniques, similarly to the other jet bins.

Given the slightly different WW baseline selection with respect to the SM Higgs search, also the control regions for the top quark and DY backgrounds estimation change, while the WW background normalization is estimated from data in the three signal regions separately, owing to the different  $m_T^i$  shapes for signal and background.

For the estimation of the top quark background, three control regions enriched in b-jets are defined by selecting events that pass the WW baseline selections and applying a b tagging requirement which depends on the jet category as follows:

- 0 jets category: at least one b-tagged jet with  $20 < p_T < 30$  GeV is required;
- 1 jet category: exactly one b-tagged jet with  $p_T$  above 30 GeV is required;
- 2 jets category: at least one b-tagged jet with  $p_T$  above 30 GeV is required.

Distributions of the  $m_T^i$  variable in the 0 jets, 1 jet and 2 jets top quark enriched control regions after applying the data driven estimation are shown in Fig. 6.5.

The jet induced background, here labelled as “non-prompt” background so as to highlight that these events do not contain prompt leptons, is estimated using the method described in 4.4.3. A cross-check is performed selecting events passing the WW baseline selection but with an  $e\mu$  pair with same charge. The  $m_T^i$  distributions for this phase space are shown in Fig. 6.6 for the three jet categories separately, showing agreement between data and simulation within uncertainties.

Due to the selections on the leptons  $p_T$  and on  $m_{\ell\ell}$  in the WW baseline requirements, the contribution of the  $Z/\gamma^* \rightarrow \tau^+\tau^-$  background is very small in the signal regions, especially in the VBF phase space. The normalization of this background is estimated from a control region in data, defined in the same way as explained in 5.3.4, for the 0 and 1 jet categories. In the VBF category the normalization of this background is taken from simulation.

Other minor background processes are estimated as described in 5.3.5.

## 6.4 Systematic uncertainties

The systematic uncertainties affecting this analysis are the same discussed in Sec. 5.4. The differences with respect to the Higgs boson cross section measurement presented in Chapter 5 are described below.

The PDF and  $\alpha_s$  uncertainties on the signal cross sections are taken from the computations performed by the LHC cross section working group [136], and are included for all the mass points. The value of these uncertainties depends on the resonance mass and vary from 3 and 5% for ggH and from 2 and 3% for VBF production modes. The PDFs and  $\alpha_s$  uncertainties on the signal selection are evaluated for every resonance mass and are found to be less than 1% for both ggH and VBF.

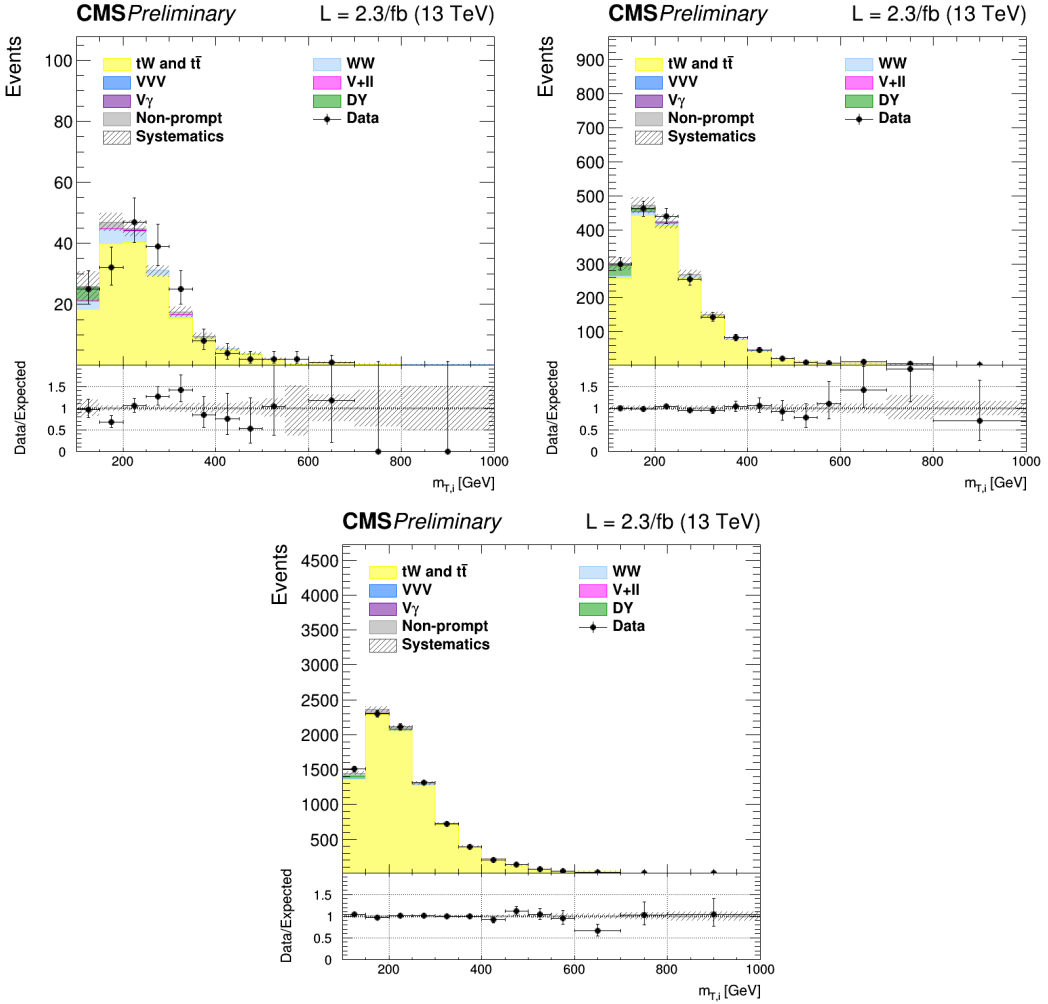


**Figure 6.5:** Distributions of  $m_{T,i}^i$  for events with 0 jets (top left), 1 jet (top right) and 2 jets (bottom) in top quark enriched control region. Scale factors estimated from data are not applied in the plots.

The theoretical uncertainties in the signal yields due to the jet categorization are evaluated for all the ggH signals following the prescription described in Refs. [46, 111].

An additional uncertainty on the modelling of the  $t\bar{t}$  background is derived from the observed discrepancy between data and POWHEG V2 plus PYTHIA 8.1 simulation on the top quark  $p_T$  spectrum [144], which is particularly important in the tail of the  $m_{T,i}^i$  distribution. Another uncertainty affecting the  $m_{T,i}^i$  tail for the top quark background is the parton shower uncertainty. This is evaluated comparing the generator level  $m_{T,i}^i$  distributions corresponding to two different simulations of the  $t\bar{t}$  process: one obtained using PYTHIA 8.1 for the showering and hadronization of the simulated events, and the other using HERWIG++. The difference between the two is used to extract a shape uncertainty, which is less than 1% for low  $m_{T,i}^i$  values and reaches about 6% in the  $m_{T,i}^i$  tail.

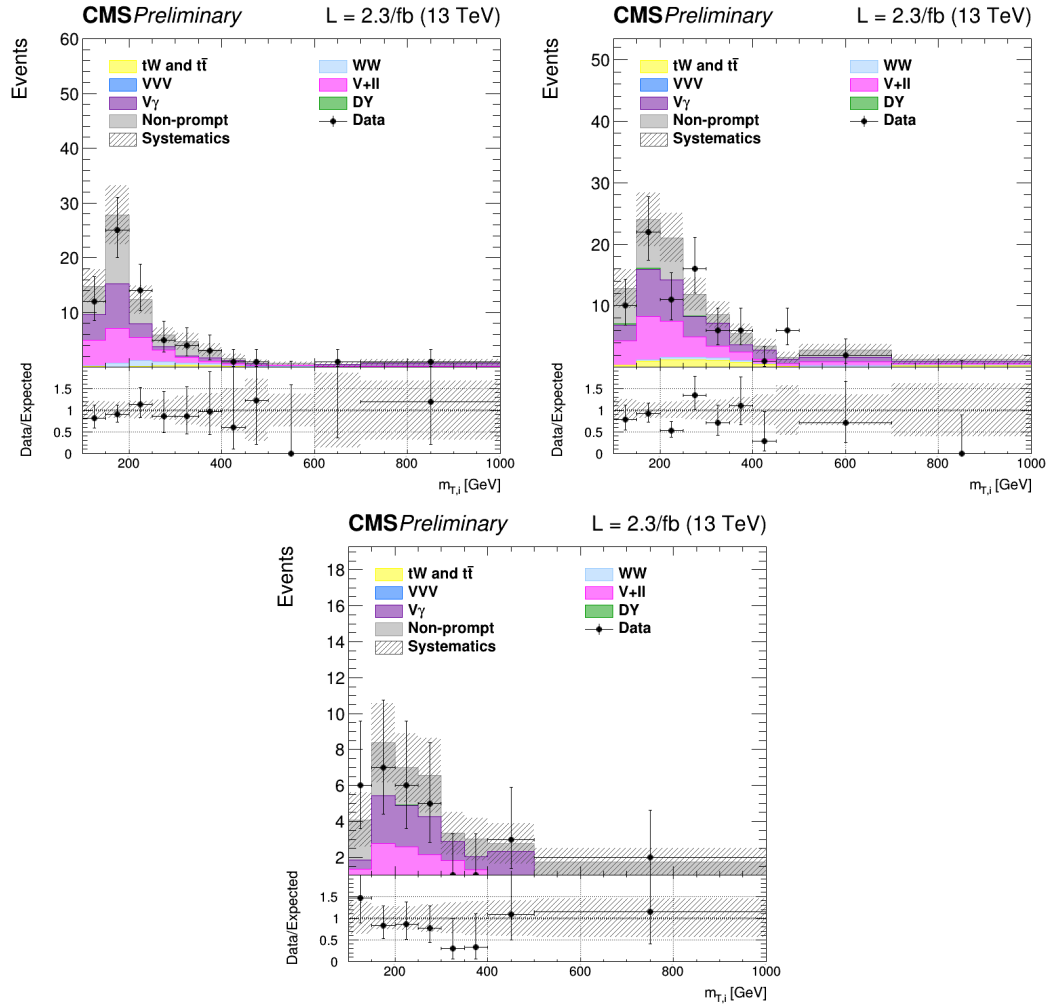


**Figure 6.6:** Distributions of  $m_{T,i}^i$  for events with 0 jets (top left), 1 jet (top right) and 2 jets (bottom) in the same-charge dilepton control region. The last bin of the histograms includes overflows.

## 6.5 Signal extraction and limit setting

The signal yield, including both ggH and VBF production modes, is extracted performing a combined fit of the three categories to the  $m_{T,i}^i$  simulation templates for backgrounds and signal, and is repeated for each resonance mass hypothesis. Moreover, fixed the mass of the resonance, the fit is performed again for the various hypotheses of the resonance decay width. A single signal strength  $\mu$  is extracted from each fit, which multiplies both the ggH and VBF contributions. In other words it is assumed that the ratio of the two production mechanism stays the same as the one predicted by the SM<sup>2</sup>.

<sup>2</sup>This is an approximation that limits the amount of models that can be tested with the provided results. A future development of this analysis, with larger integrated luminosity, might also include

The background yields expected from simulation corresponding to the three jet categories and after the analysis event selection are shown in Table 6.1. The signal yields corresponding to a selection of mass points and assuming  $\Gamma' = \Gamma_{\text{SM}}$  are shown in Table 6.2.

**Table 6.1:** Expected yields estimated from simulation (except for the non-prompt contribution which is estimated using data) for each background process in the three analysis categories, after the analysis event selection. The uncertainties are shown for the processes estimated from simulation.

Background process	0 jets	1 jet	VBF
qq $\rightarrow$ WW	$501.93 \pm 0.00$ (0%)	$198.72 \pm 0.00$ (0%)	$4.54 \pm 0.00$ (0%)
gg $\rightarrow$ WW	$37.28 \pm 5.77$ (15%)	$19.63 \pm 3.04$ (15%)	$1.05 \pm 0.16$ (15%)
Top quark	$188.75 \pm 0.00$ (0%)	$330.05 \pm 0.00$ (0%)	$25.06 \pm 0.00$ (0%)
DY	$33.24 \pm 0.00$ (0%)	$12.99 \pm 0.00$ (0%)	$0.28 \pm 0.00$ (0%)
Non-prompt	$64.21 \pm 19.26$ (30%)	$31.69 \pm 9.51$ (30%)	$2.10 \pm 0.63$ (30%)
$V\gamma$	$26.62 \pm 0.72$ (3%)	$14.18 \pm 0.38$ (3%)	$0.64 \pm 0.02$ (3%)
$V\gamma^*$	$4.44 \pm 1.12$ (25%)	$3.39 \pm 0.85$ (25%)	$0.14 \pm 0.04$ (25%)
$VZ$	$13.51 \pm 0.76$ (6%)	$11.67 \pm 0.66$ (6%)	$0.28 \pm 0.02$ (6%)
VVV	$0.01 \pm 0.00$ (3%)	$0.02 \pm 0.00$ (3%)	$0.00 \pm 0.00$ (3%)
SM H $\rightarrow$ WW	$6.04 \pm 0.40$ (7%)	$3.10 \pm 0.11$ (5%)	$0.34 \pm 0.02$ (7%)
SM H $\rightarrow$ $\tau\tau$	$0.50 \pm 0.05$ (9%)	$0.43 \pm 0.04$ (9%)	$0.04 \pm 0.00$ (9%)
Total background	876.5	625.9	34.5

The strategy for computing the exclusion limits is based on the modified frequentist approach, also referred to as  $\text{CL}_s$ , as described in [116]. The first step is to construct the likelihood function  $\mathcal{L}(\mu, \theta)$ :

$$\mathcal{L}(\mu, \theta) = \text{Poisson}(data|\mu \cdot s(\theta) + b(\theta)) \cdot p(\tilde{\theta}|\theta) , \quad (6.3)$$

where  $data$  represents the experimental observation,  $s$  and  $b$  are the expected signal and background yields respectively and  $\theta$  is the full set of true values for the nuisance parameters constrained by the prior distribution functions  $p(\tilde{\theta}|\theta)$ . The default values assigned to the nuisance parameters are labelled as  $\tilde{\theta}$ .

For a binned shape analysis,  $\text{Poisson}(data|\mu \cdot s + b)$  is the product of the Poisson probabilities to observe  $n_i$  events in bin i:

$$\prod_i \frac{(\mu \cdot s_i + b_i)^{n_i}}{n_i!} e^{-\mu \cdot s_i - b_i} . \quad (6.4)$$

---

the cases for which different ggH and VBF relative contributions are expected.

**Table 6.2:** Expected signal yields for the ggH and VBF production modes estimated from simulation after the analysis event selection for different mass hypothesis assuming  $\Gamma' = \Gamma_{\text{SM}}$  in the three analysis categories. The errors correspond to the theoretical uncertainties in the signal estimation.

Mass [GeV]	0 jets	1 jet	VBF
ggH signal yields			
200	$90.21 \pm 6.67$ (7%)	$37.47 \pm 1.81$ (5%)	$1.25 \pm 0.26$ (21%)
400	$66.35 \pm 4.90$ (7%)	$32.65 \pm 1.57$ (5%)	$2.04 \pm 0.42$ (21%)
600	$13.86 \pm 1.05$ (8%)	$8.56 \pm 0.44$ (5%)	$0.68 \pm 0.14$ (21%)
800	$3.20 \pm 0.25$ (8%)	$2.32 \pm 0.13$ (6%)	$0.22 \pm 0.05$ (21%)
1000	$0.88 \pm 0.07$ (8%)	$0.70 \pm 0.04$ (6%)	$0.07 \pm 0.02$ (21%)
VBF signal yields			
200	$1.54 \pm 0.06$ (4%)	$6.18 \pm 0.25$ (4%)	$5.05 \pm 0.20$ (4%)
400	$0.91 \pm 0.04$ (4%)	$3.42 \pm 0.14$ (4%)	$3.19 \pm 0.13$ (4%)
600	$0.50 \pm 0.02$ (4%)	$1.95 \pm 0.08$ (4%)	$1.88 \pm 0.08$ (4%)
800	$0.33 \pm 0.01$ (4%)	$1.21 \pm 0.05$ (4%)	$1.16 \pm 0.05$ (4%)
1000	$0.22 \pm 0.01$ (4%)	$0.79 \pm 0.03$ (4%)	$0.69 \pm 0.03$ (4%)

In order to test the compatibility of the data with the signal plus background (or the background only) hypothesis, the test statistic  $\tilde{q}_\mu$  is constructed based on the profile likelihood ratio:

$$\tilde{q}_\mu = -2 \ln \frac{\mathcal{L}(\text{data}|\mu, \hat{\theta}_\mu)}{\mathcal{L}(\text{data}|\hat{\mu}, \hat{\theta})} \quad \text{with } 0 \leq \hat{\mu} \leq \mu , \quad (6.5)$$

where  $\hat{\theta}_\mu$  refers to the conditional maximum likelihood estimators of  $\theta$ , given the signal strength  $\mu$ . The parameter estimators  $\hat{\mu}$  and  $\hat{\theta}$  correspond to the global maximum of the likelihood. The  $0 \leq \hat{\mu}$  constraint is imposed to have a positive signal yield, e.g. background underfluctuations are forbidden, while  $\hat{\mu} \leq \mu$  is imposed to have a one-sided confidence interval. The observed test statistic for the signal strength  $\mu$  under test is referred to as  $\tilde{q}_\mu^{\text{obs}}$ . The values of the nuisance parameters obtained maximising the likelihood function are labelled as  $\hat{\theta}_0^{\text{obs}}$  and  $\hat{\theta}_\mu^{\text{obs}}$  for the background only and signal plus background hypotheses, respectively. The pdf of the test statistic is constructed by generating toy MC pseudo-data for both the background only and signal plus background hypotheses, i.e.  $f(\tilde{q}_\mu|\mu, \hat{\theta}_\mu^{\text{obs}})$  and  $f(\tilde{q}_\mu|0, \hat{\theta}_0^{\text{obs}})$ . These distributions can be used to define two p-values corresponding to the two hypotheses,  $p_\mu$  and  $p_b$ :

$$p_\mu = P(\tilde{q}_\mu \geq \tilde{q}_\mu^{\text{obs}} | \text{signal + background}) = \int_{\tilde{q}_\mu^{\text{obs}}}^{\infty} f(\tilde{q}_\mu|\mu, \hat{\theta}_\mu^{\text{obs}}) d\tilde{q}_\mu , \quad (6.6)$$

$$1 - p_b = (\tilde{q}_\mu \geq \tilde{q}_\mu^{\text{obs}} | \text{background only}) = \int_{\tilde{q}_0^{\text{obs}}}^{\infty} f(\tilde{q}_\mu | 0, \hat{\theta}_0^{\text{obs}}) d\tilde{q}_\mu \quad . \quad (6.7)$$

According to these definitions,  $p_\mu$  and  $p_b$  can be identified with  $\text{CL}_{s+b}$  and  $1 - \text{CL}_b$ , respectively. The  $\text{CL}_s(\mu)$  is calculated using the following ratio:

$$\text{CL}_s(\mu) = \frac{\text{CL}_{s+b}}{\text{CL}_b} = \frac{p_\mu}{1 - p_b} \quad . \quad (6.8)$$

If, for a given signal strength  $\mu$ ,  $\text{CL}_s \leq \alpha$ , then the hypothesis is excluded with a  $(1 - \alpha)$  confidence level (CL). For instance, if one wants to quote the upper limit on  $\mu$  with a 95% CL, the signal strength has to be adjusted until  $\text{CL}_s = 0.05$ .

The expected median upper limit, as well as the  $\pm 1\sigma$  (68% CL) and  $\pm 2\sigma$  (95% CL) bands, are determined generating a large amount of pseudo-data in the background only hypothesis and calculating  $\text{CL}_s$  and the 95% CL upper limit for each of them, as if they were real data. Then the cumulative distribution of the 95% CL upper limits is built and the median expected value is identified as the value at which the cumulative distribution crosses the 50% quantile. The  $\pm 1\sigma$  ( $\pm 2\sigma$ ) band is defined by the values at which the cumulative distribution crosses the 16% (2.5%) and 84% (97.5%) quantiles.

In order to assess the sensitivity of the analysis, the expected upper exclusion limits at 95% CL on the signal strength are shown in Fig. 6.7 for the three jet categories separately. For a given mass of the resonance, the limits are derived assuming a signal decay width  $\Gamma' = \Gamma_{\text{SM}}$  and a cross section equal to the one expected from a SM Higgs boson at that mass. The other decay width hypotheses have been tested as well, showing a very similar expected exclusion limit, suggesting that this analysis is not strongly sensitive to variations of the resonance decay width. In fact, the width of the  $m_T^i$  distribution is driven by the experimental resolution and the choice of different decay widths has a mild effect on this variable.

The 0 jets category is the most sensitive especially in the low mass region, while for very large masses of the resonance the 1 jet and VBF categories start being important. This is explained mainly by the fact that the VBF contribution increases, with respect to ggH, as the mass increases. The expected exclusion limit on the signal strength after the combination of the three categories is shown in Fig. 6.8. Comparing the limits in the single categories with the combination of the three it is evident how the higher jet multiplicity categories help in improving the results for large values of  $M_x$ . For the analysed luminosity the expected exclusion mass range for the production of a resonance with the SM Higgs boson cross section extends roughly from 350 to 450 GeV.

## 6.6 Results

The  $m_T^i$  distributions for the signal region after the full analysis selection are shown in Fig. 6.9 for the three jet categories. Two different signal hypotheses corresponding

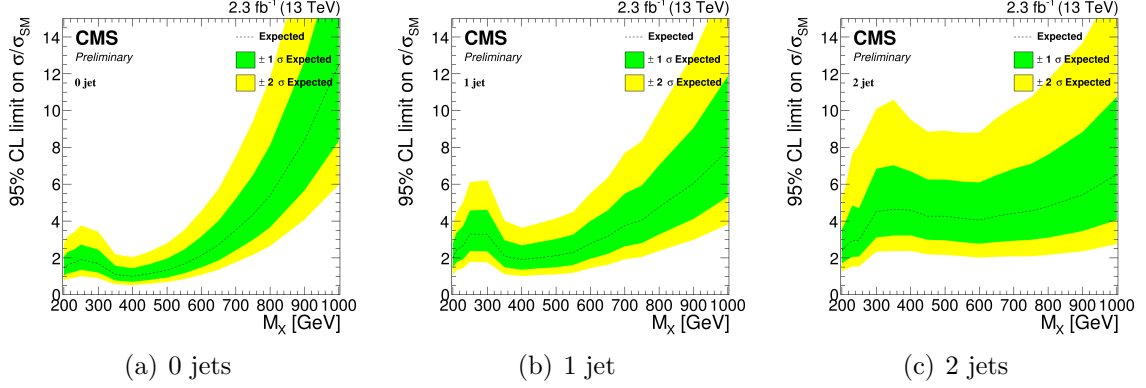


**Figure 6.7:** Expected exclusion upper limits at 95% CL on the signal strength in the three categories, as a function of the resonance mass. The dashed line corresponds to median upper limit, while the green and yellow regions represent the  $\pm 1\sigma$  and  $\pm 2\sigma$  uncertainty bands, respectively. Limits are derived assuming the SM Higgs boson cross section and decay width for each mass point.

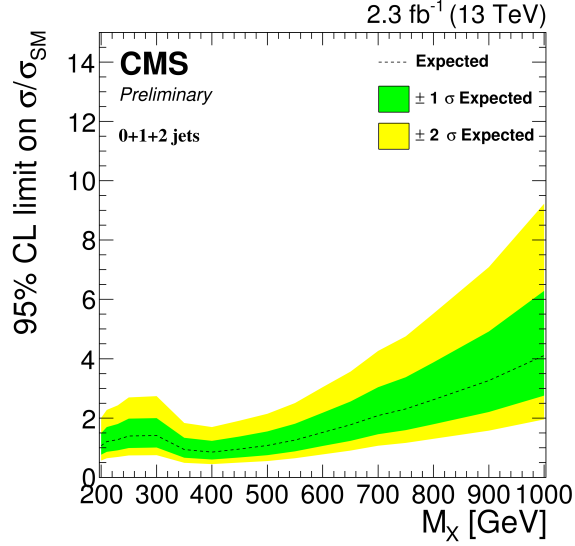


**Figure 6.8:** Expected exclusion upper limit at 95% CL on the signal strength for the combination of the three categories, as a function of the resonance mass. The dashed line corresponds to median upper limit, while the green and yellow regions represent the  $\pm 1\sigma$  and  $\pm 2\sigma$  uncertainty bands, respectively. The limit is derived assuming the SM Higgs boson cross section and decay width for each mass point.

to  $M_X = 400$  GeV and  $M_X = 800$  GeV are shown superimposed on the background for comparison.

For every mass point from 200 GeV up to 1 TeV the observed p-value and the 95% CL upper exclusion limit are calculated for four hypotheses of the signal decay width. The observed p-value as a function of the resonance mass for the combination of the

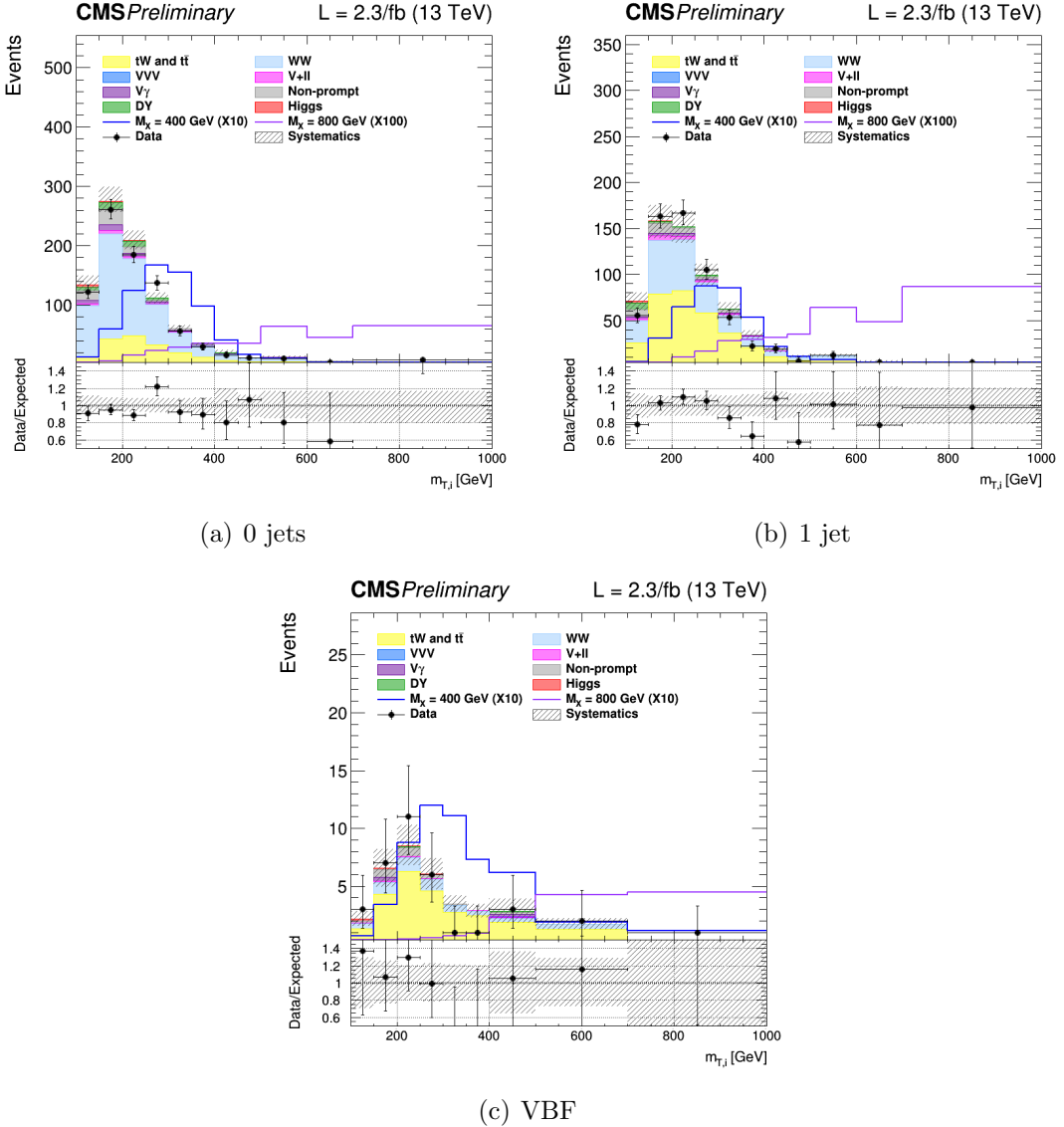


**Figure 6.9:** Distributions of  $m_T^i$  in the signal region for the 0 jets, 1 jet and VBF categories. Background normalisations correspond to the pre-fit value. Signal contributions for two mass hypotheses,  $M_X = 400$  GeV and  $M_X = 800$  GeV, are shown superimposed on the background and scaled to facilitate the comparison.

three jet categories is shown in Table 6.3.

In order to be independent on the particular model assumed for the signal cross section, the results are interpreted as exclusion limits on  $\sigma \times \mathcal{B}$ , where  $\sigma$  stands for the sum of the ggH and VBF cross sections, and  $\mathcal{B}$  represents the  $X \rightarrow WW \rightarrow 2\ell 2\nu$  branching ratio including all lepton flavours. The expected and observed upper exclusion limits on  $\sigma \times \mathcal{B}$  for  $\Gamma' = \Gamma_{\text{SM}}$  are shown in Fig. 6.10.

A mild excess is observed in the 0 jets category and, more evident, in the 1 jet

**Table 6.3:** Observed p-value and corresponding significance (set to 0 in case of underfluctuations of the observed number of events) for the combination of the three jet categories for different resonance masses. Different values of the signal width are shown.

Mass [GeV]	$\Gamma = 0.09 \times \Gamma_{SM}$ p-value (signif.)	$\Gamma = 0.25 \times \Gamma_{SM}$ p-value (signif.)	$\Gamma = 0.49 \times \Gamma_{SM}$ p-value (signif.)	$\Gamma = \Gamma_{SM}$ p-value (signif.)
200	0.50 (0)	0.50 (0)	0.50 (0)	0.56 (0)
210	0.58 (0)	0.45 (0.1)	0.35 (0.4)	0.24 (0.7)
230	0.21 (0.8)	0.22 (0.8)	0.23 (0.7)	0.26 (0.6)
250	0.29 (0.5)	0.20 (0.8)	0.15 (1.0)	0.12 (1.2)
300	0.014 (2.2)	0.015 (2.2)	0.016 (2.1)	0.018 (2.1)
350	0.16 (1.0)	0.17 (1.0)	0.18 (0.9)	0.23 (0.7)
400	0.50 (0)	0.49 (0)	0.49 (0)	0.57 (0)
450	0.51 (0)	0.50 (0)	0.50 (0)	0.52 (0)
500	0.50 (0)	0.51 (0)	0.50 (0)	0.52 (0)
550	0.50 (0)	0.51 (0)	0.51 (0)	0.51 (0)
600	0.50 (0)	0.50 (0)	0.51 (0)	0.51 (0)
650	0.50 (0)	0.50 (0)	0.54 (0)	0.50 (0)
700	0.50 (0)	0.50 (0)	0.50 (0)	0.50 (0)
750	0.50 (0)	0.54 (0)	0.50 (0)	0.40 (0.3)
800	0.50 (0)	0.55 (0)	0.39 (0.3)	0.29 (0.6)
900	0.29 (0.6)	0.27 (0.6)	0.24 (0.7)	0.22 (0.8)
1000	0.18 (0.9)	0.18 (0.9)	0.18 (0.9)	0.18 (0.9)

category around 250–300 GeV. A deficit is instead observed in the VBF category around 250 GeV, which is mainly due to an underfluctuation of the background. This effect can be understood looking at the VBF shape in Fig. 6.9, where two adjacent data points, corresponding to the fifth and sixth bins of the  $m_T^j$  distribution, clearly underfluctuate with respect to the background prediction, causing the dip in the observed limit.

The exclusion limit resulting from the combination of the three categories is shown in Fig. 6.11, for the four  $\Gamma'$  hypotheses discussed before. From the combined exclusion limits no significant evidence of a deviation from the background only hypothesis is observed. In the case the new resonance has the same decay width as the SM Higgs boson, i.e.  $\Gamma' = \Gamma_{SM}$ , the expected cross section times branching ratio is also displayed, excluding this hypothesis in the mass range from 350 to 550 GeV.

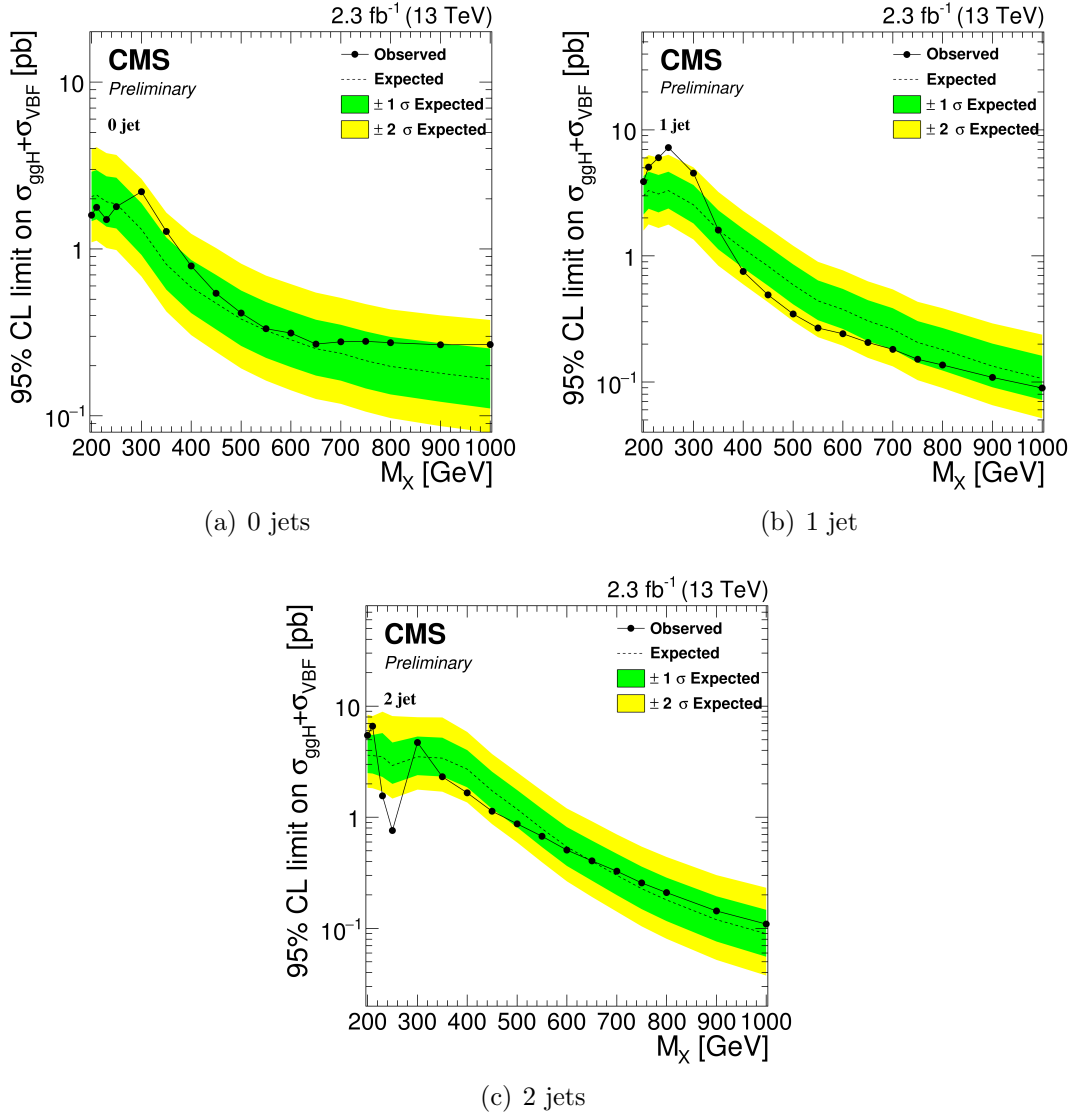


**Figure 6.10:** Expected and observed exclusion upper limits at 95% CL on  $\sigma \times \mathcal{B}$  in the three categories, as a function of the resonance mass. The dashed line corresponds to median upper limit, while the green and yellow regions represent the  $\pm 1\sigma$  and  $\pm 2\sigma$  uncertainty bands, respectively. The dotted line represents the observed limit. Limits are derived assuming  $\Gamma' = \Gamma_{SM}$  for each mass point.

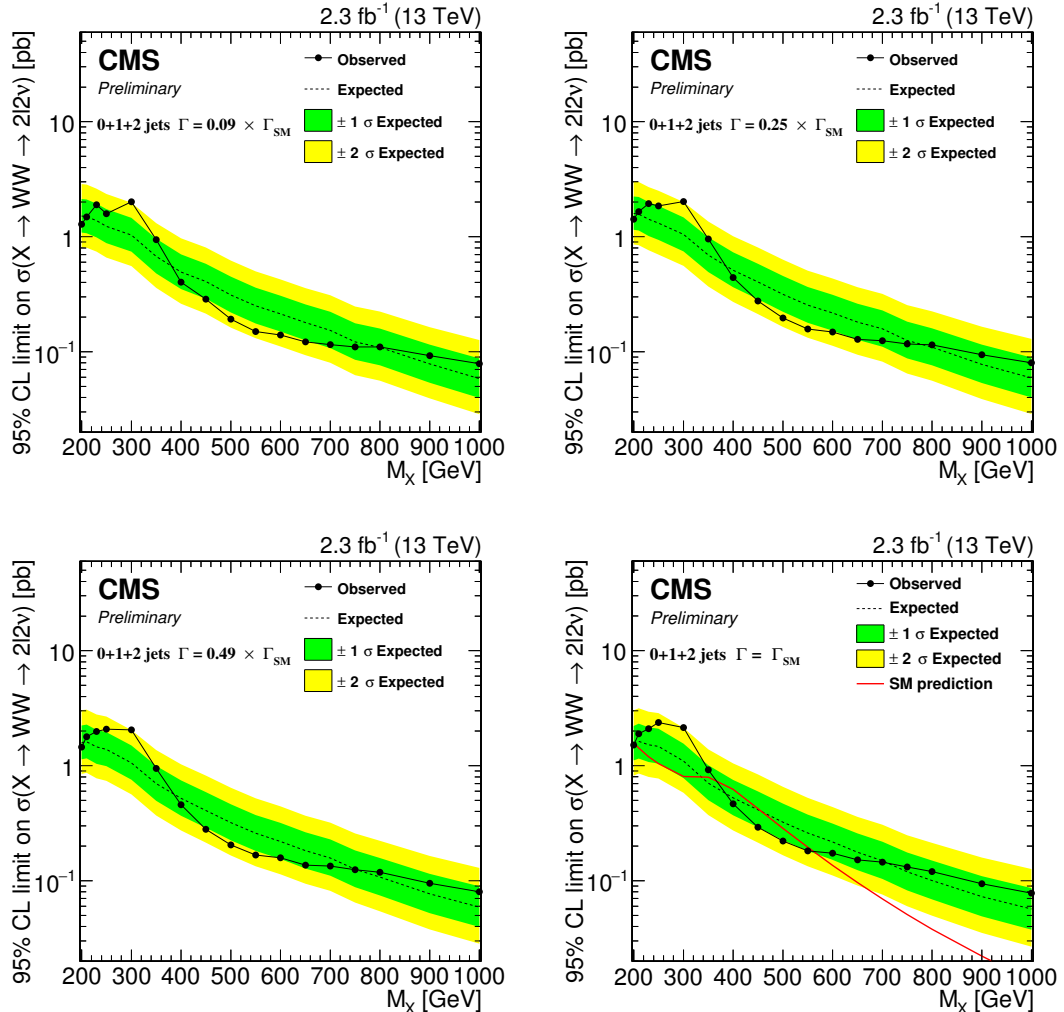


**Figure 6.11:** Expected and observed exclusion limits at 95% CL on  $\sigma \times \mathcal{B}$  for the combination of the three jet categories as a function of the resonance mass. The black dotted line corresponds to the observed value while the yellow and green bands represent the  $\pm 1\sigma$  and  $\pm 2\sigma$  uncertainties respectively. Limits are displayed for four decay width hypotheses.



# Summary

This thesis work has been organized according to a twofold purpose, reporting firstly a precision measurement of the Higgs boson transverse momentum spectrum using proton-proton collision data collected at a centre-of-mass energy of 8 TeV and thereafter focusing on the first data collected by the CMS experiment at the unprecedented centre-of-mass energy of 13 TeV.

The transverse momentum spectrum and the inclusive cross section times branching fraction for the Higgs boson production have been reported using  $H \rightarrow W^+W^- \rightarrow e^\pm\mu^\mp\nu\nu$  decays. Measurements have been performed using data from proton-proton collisions at a centre-of-mass energy of 8 TeV collected by the CMS experiment at the LHC and corresponding to an integrated luminosity of  $19.4\text{ fb}^{-1}$ . The Higgs boson transverse momentum has been reconstructed using the lepton pair transverse momentum and missing transverse momentum. A two-dimensional template fit based on dilepton invariant mass and transverse mass has been used to extract the signal contribution. The differential cross section times branching fraction has been measured as a function of the Higgs boson transverse momentum in a fiducial phase space defined to match the experimental acceptance in terms of lepton kinematics and event topology. An unfolding procedure has been used to extrapolate the measured results to the fiducial phase space and to correct for detector effects. The measurements have been compared to SM theoretical estimations provided by the **HRES** and **POWHEG V2** generators, showing good agreement within experimental uncertainties. The inclusive cross section times branching fraction in the fiducial phase space has been measured to be  $39 \pm 8\text{ (stat)} \pm 9\text{ (syst)}\text{ fb}$ , consistent with the SM expectation.

The first 13 TeV proton-proton collision data collected during 2015, corresponding to an integrated luminosity of  $2.3\text{ fb}^{-1}$ , have been used to perform a re-discovery analysis of the Higgs boson in the  $H \rightarrow W^+W^- \rightarrow e^\pm\mu^\mp\nu\nu$  decay channel. The signal strength has been measured performing a two-dimensional template fit using the dilepton invariant mass and transverse mass to separate signal and background contributions. The observed signal strength, which is driven by the low data statistics, has been found to be  $0.3 \pm 0.5$ , corresponding to an observed significance of  $0.7\sigma$ , to be compared with the expected value of  $2.0\sigma$  for a Higgs boson mass of 125 GeV.

The same 13 TeV data have been used to search for new resonances decaying to  $W^+W^- \rightarrow e^\pm\mu^\mp\nu\nu$  in the mass range between 200 GeV and 1 TeV. The analysis relied on a maximum likelihood template fit using a transverse mass variable that is able to discriminate between signal and background contributions. No significant excess

with respect to the background only expectation has been observed, and exclusion limits on the production cross section times branching fraction of the new resonance have been reported over the whole analysed mass spectrum, studying also different hypotheses of the resonance decay width.

# Appendix A

## Fiducial region definition and optimization

The generator level fiducial phase space definition must be chosen in order to closely match the selections applied in the analysis at the reconstructed level, in order to reduce the model dependence in the extrapolation step. This means that, for optimizing the fiducial phase space definition, the efficiency  $\epsilon_{\text{fid}}$  (see 4.3.3) has to be maximized. Another parameter playing an important role is the number of out-of-fiducial signal events (also called fakes),  $f_{\text{out-of-fid}}$ , in other words the number of reconstructed events which do not belong to the fiducial phase space. This parameter should instead be as small as possible. A simplistic way to improve the fiducial phase space definition is to maximize the ratio between the overall efficiency and out-of-fiducial rate.

Several different fiducial region definitions have been tested and the results show that:

- **Lepton flavour:** the fiducial phase space definition must include only the opposite flavour combination including one electron and one muon. If the combinations involving  $\tau$  leptons are included the efficiency falls down;
- **Lepton selections:** given the good resolution on lepton transverse momentum, there is no need to loosen the cuts related to these variables, i.e. the same cuts defined in the analysis selection can be kept also at generator level;
- **Neutrino pair  $p_T$  cut:** since the resolution on the measurement of the missing transverse energy is poor, the neutrino pair cut should not be included in the definition of the fiducial region, because it would increase the fake rate without increasing the efficiency, thus resulting in a lower ratio between overall efficiency and out-of-fiducial rate;
- **$m_T$  cut:** also, the  $m_T$  cut in the analysis selection, i.e.  $m_T > 60 \text{ GeV}$ , should be loosened or removed because it involves neutrinos, therefore increasing the out-of-fiducial rate. This cut has been loosened to 50 GeV at generator level.

The efficiency and fraction of fake events have been measured also as a function of the  $E_T^{\text{miss}}$  and  $m_T$  cuts in the fiducial phase space. Since these two variables are correlated, the results are reported as two-dimensional histograms. In Fig. A.1 the efficiency and fraction of out-of-fiducial events for these two variables are reported.

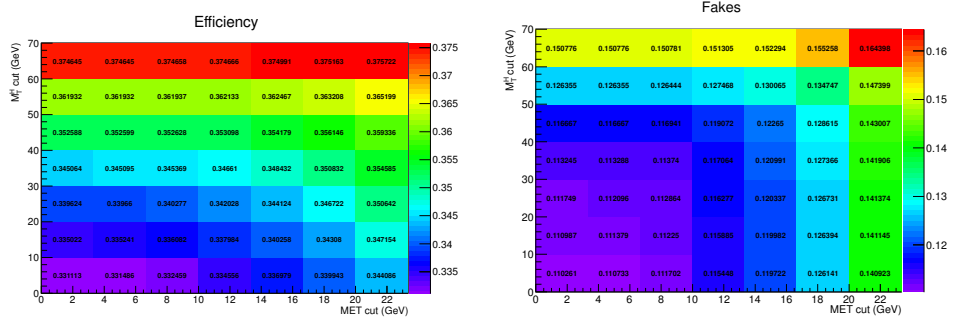


**Figure A.1:** Efficiency and out-of-fiducial rate as a function of  $E_T^{\text{miss}}$  and  $m_T$  cuts in the fiducial phase space.

The criterion adopted to define the fiducial phase space is a trade-off between having a large efficiency and a small fraction of fake events. Especially when looking at the low resolution variables, such as  $E_T^{\text{miss}}$  and  $m_T$ , a suitable figure of merit has to be chosen for the estimation of the best cuts. Several different figures of merit have been checked, such as  $\varepsilon_{\text{fid}}/f_{\text{out-of-fid}}$ ,  $\varepsilon_{\text{fid}} - f_{\text{out-of-fid}}$  and  $(1 - f_{\text{out-of-fid}})/\varepsilon_{\text{fid}}$ . The results for these three different figures of merit are shown in Fig. A.2 as a function of the  $E_T^{\text{miss}}$  and  $m_T$  cuts in the fiducial region. These three figures of merit have been used to establish the selections in the generator level fiducial phase space for the low resolution variables.

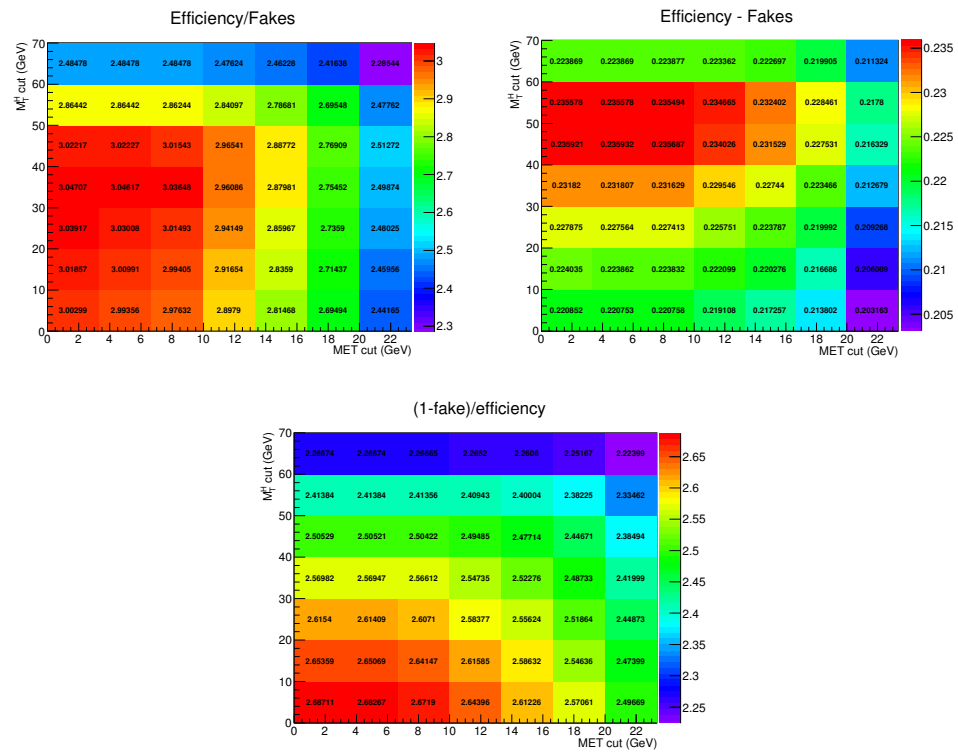


**Figure A.2:** Different figures of merit as a function of  $E_T^{\text{miss}}$  and  $m_T$  cuts in the fiducial phase space.



# Bibliography

- [1] F. Halzen and A. D. Martin. *QUARKS AND LEPTONS: An Introductory Course In Modern Particle Physics*. 1984. ISBN: 0471887412, 9780471887416.
- [2] S. L. Glashow. “Partial Symmetries of Weak Interactions”. In: *Nucl. Phys.* 22 (1961), p. 579. DOI: 10.1016/0029-5582(61)90469-2.
- [3] S. Weinberg. “A Model of Leptons”. In: *Phys. Rev. Lett.* 19 (1967), p. 1264. DOI: 10.1103/PhysRevLett.19.1264.
- [4] C. S. Wu et al. “Experimental Test of Parity Conservation in Beta Decay”. In: *Phys. Rev.* 105 (1957), p. 1413. DOI: 10.1103/PhysRev.105.1413.
- [5] R. L. Garwin, L. M. Lederman, and M. Weinrich. “Observations of the Failure of Conservation of Parity and Charge Conjugation in Meson Decays: The Magnetic Moment of the Free Muon”. In: *Phys. Rev.* 105 (1957), p. 1415. DOI: 10.1103/PhysRev.105.1415.
- [6] S. L. Glashow, J. Iliopoulos, and L. Maiani. “Weak Interactions with Lepton-Hadron Symmetry”. In: *Phys. Rev. D2* (1970), pp. 1285–1292. DOI: 10.1103/PhysRevD.2.1285.
- [7] R. Wolf. *The Higgs Boson Discovery at the Large Hadron Collider*. Vol. 264. Springer, 2015. ISBN: 978-3-319-18512-5, 978-3-319-18511-8. DOI: 10.1007/978-3-319-18512-5.
- [8] R. K. Ellis, W. J. Stirling, and B. R. Webber. “QCD and collider physics”. In: *Camb. Monogr. Part. Phys. Nucl. Phys. Cosmol.* 8 (1996), pp. 1–435.
- [9] P. Langacker. *The standard model and beyond*. 2010. ISBN: 9781420079067.
- [10] T. Robens and T. Stefaniak. “Status of the Higgs singlet extension of the standard model after LHC run 1”. In: *Eur. Phys. J. C* 75 (2015), p. 105. DOI: 10.1140/epjc/s10052-015-3323-y. arXiv: 1501.02234 [hep-ph].
- [11] G. C. Branco et al. “Theory and phenomenology of two-Higgs-doublet models”. In: *Phys. Rept.* 516 (2012), p. 1. DOI: 10.1016/j.physrep.2012.02.002. arXiv: 1106.0034 [hep-ph].
- [12] N. Craig, J. Galloway, and S. Thomas. “Searching for Signs of the Second Higgs Doublet”. In: (2013). arXiv: 1305.2424 [hep-ph].

- [13] G. Altarelli. “Collider Physics within the Standard Model: a Primer”. In: (2013). arXiv: 1303.2842 [hep-ph].
- [14] J. C. Collins, D. E. Soper, and G. F. Sterman. “Factorization of Hard Processes in QCD”. In: *Adv. Ser. Direct. High Energy Phys.* 5 (1989), p. 1. DOI: 10.1142/9789814503266\_0001. arXiv: hep-ph/0409313 [hep-ph].
- [15] J. M. Butterworth, G. Dissertori, and G. P. Salam. “Hard Processes in Proton-Proton Collisions at the Large Hadron Collider”. In: *Ann. Rev. Nucl. Part. Sci.* 62 (2012), p. 387. DOI: 10.1146/annurev-nucl-102711-094913. arXiv: 1202.0583 [hep-ex].
- [16] G. Altarelli and G. Parisi. “Asymptotic Freedom in Parton Language”. In: *Nucl. Phys. B* 126 (1977), p. 298. DOI: 10.1016/0550-3213(77)90384-4.
- [17] P. M. Nadolsky et al. “Implications of CTEQ global analysis for collider observables”. In: *Phys. Rev. D* 78 (2008), p. 013004. DOI: 10.1103/PhysRevD.78.013004. arXiv: 0802.0007 [hep-ph].
- [18] G. Watt. “Parton distribution function dependence of benchmark Standard Model total cross sections at the 7 TeV LHC”. In: *JHEP* 09 (2011), p. 069. DOI: 10.1007/JHEP09(2011)069. arXiv: 1106.5788 [hep-ph].
- [19] NNPDF Collaboration. “Parton distributions with QED corrections”. In: *Nucl. Phys. B* 877 (2013), p. 290. DOI: 10.1016/j.nuclphysb.2013.10.010. arXiv: 1308.0598 [hep-ph].
- [20] J. Ellis and D. S. Hwang. “Does the ‘Higgs’ have Spin Zero?” In: *JHEP* 09 (2012), p. 071. DOI: 10.1007/JHEP09(2012)071. arXiv: 1202.6660 [hep-ph].
- [21] M. Spira et al. “Higgs boson production at the LHC”. In: *Nucl. Phys. B* 453 (1995), p. 17. DOI: 10.1016/0550-3213(95)00379-7. arXiv: hep-ph/9504378 [hep-ph].
- [22] R. Harlander and P. Kant. “Higgs production and decay: Analytic results at next-to-leading order QCD”. In: *JHEP* 12 (2005), p. 015. DOI: 10.1088/1126-6708/2005/12/015. arXiv: hep-ph/0509189 [hep-ph].
- [23] V. Ravindran, J. Smith, and W. L. van Neerven. “NNLO corrections to the total cross-section for Higgs boson production in hadron hadron collisions”. In: *Nucl. Phys. B* 665 (2003), p. 325. DOI: 10.1016/S0550-3213(03)00457-7. arXiv: hep-ph/0302135 [hep-ph].
- [24] S. Catani and M. Grazzini. “An NNLO subtraction formalism in hadron collisions and its application to Higgs boson production at the LHC”. In: *Phys. Rev. Lett.* 98 (2007), p. 222002. DOI: 10.1103/PhysRevLett.98.222002. arXiv: hep-ph/0703012 [hep-ph].
- [25] C. Anastasiou et al. “Higgs Boson Gluon-Fusion Production in QCD at Three Loops”. In: *Phys. Rev. Lett.* 114 (2015), p. 212001. DOI: 10.1103/PhysRevLett.114.212001. arXiv: 1503.06056 [hep-ph].

- [26] X. Chen et al. “NNLO QCD corrections to Higgs boson production at large transverse momentum”. In: (2016). arXiv: 1607.08817 [hep-ph].
- [27] G. Bozzi et al. “Transverse-momentum resummation and the spectrum of the Higgs boson at the LHC”. In: *Nucl. Phys. B* 737 (2006), p. 73. DOI: 10.1016/j.nuclphysb.2005.12.022. arXiv: hep-ph/0508068 [hep-ph].
- [28] D. de Florian et al. “Higgs boson production at the LHC: transverse momentum resummation effects in the  $H \rightarrow 2\gamma$ ,  $H \rightarrow WW \rightarrow l\nu l\nu$  and  $H \rightarrow ZZ \rightarrow 4l$  decay modes”. In: *JHEP* 06 (2012), p. 132. DOI: 10.1007/JHEP06(2012)132. arXiv: 1203.6321 [hep-ph].
- [29] M. Grazzini and H. Sargsyan. “Heavy-quark mass effects in Higgs boson production at the LHC”. In: *JHEP* 09 (2013), p. 129. DOI: 10.1007/JHEP09(2013)129. arXiv: 1306.4581 [hep-ph].
- [30] A. Azatov and A. Paul. “Probing Higgs couplings with high  $p_T$  Higgs production”. In: *JHEP* 01 (2014), p. 014. DOI: 10.1007/JHEP01(2014)014. arXiv: 1309.5273 [hep-ph].
- [31] R. V. Harlander and T. Neumann. “Probing the nature of the Higgs-gluon coupling”. In: *Phys. Rev. D* 88 (2013), p. 074015. DOI: 10.1103/PhysRevD.88.074015. arXiv: 1308.2225 [hep-ph].
- [32] D. Marzocca, M. Serone, and J. Shu. “General Composite Higgs Models”. In: *JHEP* 08 (2012), p. 013. DOI: 10.1007/JHEP08(2012)013. arXiv: 1205.0770 [hep-ph].
- [33] A. Banfi, A. Martin, and V. Sanz. “Probing top-partners in Higgs+jets”. In: *JHEP* 08 (2014), p. 053. DOI: 10.1007/JHEP08(2014)053. arXiv: 1308.4771 [hep-ph].
- [34] S. Hoeche et al. “Matching parton showers and matrix elements”. In: *HERA and the LHC: A Workshop on the implications of HERA for LHC physics: Proceedings Part A*. 2006. arXiv: hep-ph/0602031 [hep-ph]. URL: [https://inspirehep.net/record/709818/files/arXiv:hep-ph\\_0602031.pdf](https://inspirehep.net/record/709818/files/arXiv:hep-ph_0602031.pdf).
- [35] M. Krämer, S. Mrenna, and D. E. Soper. “Next-to-leading order QCD jet production with parton showers and hadronization”. In: *Phys. Rev. D* 73 (2006), p. 014022. DOI: 10.1103/PhysRevD.73.014022. arXiv: hep-ph/0509127 [hep-ph].
- [36] S. Frixione, P. Nason, and C. Oleari. “Matching NLO QCD computations with Parton Shower simulations: the POWHEG method”. In: *JHEP* 11 (2007), p. 070. DOI: 10.1088/1126-6708/2007/11/070. arXiv: 0709.2092 [hep-ph].
- [37] N. Lavesson and L. Lonnblad. “Extending CKKW-merging to one-loop matrix elements”. In: *JHEP* 12 (2008), p. 070. DOI: 10.1088/1126-6708/2008/12/070. arXiv: 0811.2912 [hep-ph].

- [38] S. Alioli et al. “NLO Higgs boson production via gluon fusion matched with shower in POWHEG”. In: *JHEP* 04 (2009), p. 002. DOI: 10.1088/1126-6708/2009/04/002. arXiv: 0812.0578 [hep-ph].
- [39] P. Nason and C. Oleari. “NLO Higgs boson production via vector-boson fusion matched with shower in POWHEG”. In: *JHEP* 02 (2010), p. 037. DOI: 10.1007/JHEP02(2010)037. arXiv: 0911.5299 [hep-ph].
- [40] J. Alwall et al. “The automated computation of tree-level and next-to-leading order differential cross sections, and their matching to parton shower simulations”. In: *JHEP* 07 (2014), p. 079. DOI: 10.1007/JHEP07(2014)079. arXiv: 1405.0301 [hep-ph].
- [41] T. Sjöstrand, S. Mrenna, and P. Skands. “PYTHIA 6.4 physics and manual”. In: *JHEP* 05 (2006), p. 026. DOI: 10.1088/1126-6708/2006/05/026. arXiv: hep-ph/0603175 [hep-ph].
- [42] T. Sjöstrand, S. Mrenna, and P. Z. Skands. “A Brief Introduction to PYTHIA 8.1”. In: *Comput. Phys. Commun.* 178 (2008), p. 852. DOI: 10.1016/j.cpc.2008.01.036. arXiv: 0710.3820 [hep-ph].
- [43] Bolognesi, S. and Gao, Y. and Gritsan, A. V. and others. “JHUGen”. In: (2011). URL: <http://www.pha.jhu.edu/spin/>.
- [44] ATLAS and CMS Collaborations. “Combined measurement of the Higgs boson mass in  $pp$  collisions at  $\sqrt{s} = 7$  and 8 TeV with the ATLAS and CMS experiments”. In: *Phys. Rev. Lett.* 114 (2015), p. 191803. DOI: 10.1103/PhysRevLett.114.191803. arXiv: 1503.07589 [hep-ex].
- [45] CMS Collaboration. “Precise determination of the mass of the Higgs boson and tests of compatibility of its couplings with the standard model predictions using proton collisions at 7 and 8 TeV”. In: *Eur. Phys. J. C* 75 (2015), p. 212. DOI: 10.1140/epjc/s10052-015-3351-7. arXiv: 1412.8662 [hep-ex].
- [46] LHC Higgs Cross Section Working Group. *Handbook of LHC Higgs cross sections: 3. Higgs properties*. CERN Report CERN-2013-004. 2013. DOI: 10.5170/CERN-2013-004. arXiv: 1307.1347 [hep-ph].
- [47] ATLAS, CMS. “Measurements of the Higgs boson production and decay rates and constraints on its couplings from a combined ATLAS and CMS analysis of the LHC pp collision data at  $\sqrt{s} = 7$  and 8 TeV”. In: *JHEP* 08 (2016), p. 045. DOI: 10.1007/JHEP08(2016)045. arXiv: 1606.02266 [hep-ex].
- [48] F. Caola and K. Melnikov. “Constraining the Higgs boson width with ZZ production at the LHC”. In: *Phys. Rev. D* 88 (2013), p. 054024. DOI: 10.1103/PhysRevD.88.054024. arXiv: 1307.4935 [hep-ph].
- [49] CMS Collaboration. “Search for Higgs boson off-shell production in proton-proton collisions at 7 and 8 TeV and derivation of constraints on its total decay width”. In: *JHEP* 09 (2016), p. 051. DOI: 10.1007/JHEP09(2016)051. arXiv: 1605.02329 [hep-ex].

- [50] LHC Study Group. *The Large Hadron Collider: conceptual design*. Tech. rep. CERN-AC-95-05-LHC. Oct. 1995. URL: <http://cds.cern.ch/record/291782>.
- [51] O. S. Brüning et al. *LHC Design Report*. Geneva: CERN, 2004. URL: <http://cds.cern.ch/record/782076>.
- [52] O. S. Brüning et al. *LHC Design Report*. Geneva: CERN, 2004. URL: <http://cds.cern.ch/record/815187>.
- [53] M. Benedikt et al. *LHC Design Report*. Geneva: CERN, 2004. URL: <http://cds.cern.ch/record/823808>.
- [54] *LEP design report*. By the LEP Injector Study Group. Geneva: CERN, 1983. URL: <http://cds.cern.ch/record/98881>.
- [55] *LEP design report*. Copies shelved as reports in LEP, PS and SPS libraries. Geneva: CERN, 1984. URL: <http://cds.cern.ch/record/102083>.
- [56] C. Wyss. *LEP design report, v.3: LEP2*. Vol. 1-2 publ. in 1983-84. Geneva: CERN, 1996. URL: <http://cds.cern.ch/record/314187>.
- [57] CMS Collaboration. “The CMS experiment at the CERN LHC”. In: *JINST* 3 (2008), S08004. DOI: [10.1088/1748-0221/3/08/S08004](https://doi.org/10.1088/1748-0221/3/08/S08004).
- [58] ATLAS Collaboration. “The ATLAS Experiment at the CERN Large Hadron Collider”. In: *JINST* 3 (2008), S08003. DOI: [10.1088/1748-0221/3/08/S08003](https://doi.org/10.1088/1748-0221/3/08/S08003).
- [59] LHCb Collaboration. “The LHCb Detector at the LHC”. In: *JINST* 3 (2008), S08005. DOI: [10.1088/1748-0221/3/08/S08005](https://doi.org/10.1088/1748-0221/3/08/S08005).
- [60] ALICE Collaboration. “The ALICE experiment at the CERN LHC”. In: *JINST* 3 (2008), S08002. DOI: [10.1088/1748-0221/3/08/S08002](https://doi.org/10.1088/1748-0221/3/08/S08002).
- [61] TOTEM Collaboration. “The TOTEM experiment at the CERN Large Hadron Collider”. In: *JINST* 3 (2008), S08007. DOI: [10.1088/1748-0221/3/08/S08007](https://doi.org/10.1088/1748-0221/3/08/S08007).
- [62] LHCf Collaboration. “The LHCf detector at the CERN Large Hadron Collider”. In: *JINST* 3 (2008), S08006. DOI: [10.1088/1748-0221/3/08/S08006](https://doi.org/10.1088/1748-0221/3/08/S08006).
- [63] CMS Collaboration. *The CMS magnet project: Technical Design Report*. Technical Design Report CMS. Geneva: CERN, 1997. URL: <http://cds.cern.ch/record/331056>.
- [64] CMS Collaboration. *The CMS electromagnetic calorimeter project: Technical Design Report*. Technical Design Report CMS. Geneva: CERN, 1997. URL: <http://cds.cern.ch/record/349375>.
- [65] CMS Collaboration. *Changes to CMS ECAL electronics: addendum to the Technical Design Report*. Technical Design Report CMS. Geneva: CERN, 2002. URL: <http://cds.cern.ch/record/581342>.

- [66] CMS Collaboration. *The CMS hadron calorimeter project: Technical Design Report*. Technical Design Report CMS. Geneva: CERN, 1997. URL: <http://cds.cern.ch/record/357153>.
- [67] CMS Collaboration. *The CMS muon project: Technical Design Report*. Technical Design Report CMS. Geneva: CERN, 1997. URL: <http://cds.cern.ch/record/343814>.
- [68] CMS Collaboration. “CMS. The TriDAS project. Technical design report, vol. 1: The trigger systems”. In: (2000).
- [69] CMS Collaboration. *CMS The TriDAS Project: Technical Design Report, Volume 2: Data Acquisition and High-Level Trigger. CMS trigger and data-acquisition project*. Technical Design Report CMS. Geneva: CERN, 2002. URL: <http://cds.cern.ch/record/578006>.
- [70] CMS Collaboration. *Particle-Flow Event Reconstruction in CMS and Performance for Jets, Taus, and  $E_T^{\text{miss}}$* . CMS Physics Analysis Summary CMS-PAS-PFT-09-001. 2009. URL: <http://cdsweb.cern.ch/record/1194487>.
- [71] CMS Collaboration. “Description and performance of track and primary-vertex reconstruction with the CMS tracker”. In: *JINST* 9.10 (2014), P10009. DOI: 10.1088/1748-0221/9/10/P10009. arXiv: 1405.6569 [physics.ins-det].
- [72] P. Billoir and S. Qian. “Simultaneous pattern recognition and track fitting by the Kalman filtering method”. In: *Nucl. Instrum. Meth. A* 294 (1990), p. 219. DOI: 10.1016/0168-9002(90)91835-Y.
- [73] W. Adam et al. *Reconstruction of Electrons with the Gaussian-Sum Filter in the CMS Tracker at the LHC*. Tech. rep. CMS-NOTE-2005-001. Geneva: CERN, Jan. 2005. URL: <https://cds.cern.ch/record/815410>.
- [74] CMS Collaboration. “Performance of CMS muon reconstruction in  $pp$  collision events at  $\sqrt{s} = 7$  TeV”. In: *JINST* 7 (2012), P10002. DOI: 10.1088/1748-0221/7/10/P10002. arXiv: 1206.4071 [physics.ins-det].
- [75] CMS Collaboration. *Electron reconstruction and identification at  $\sqrt{s} = 7$  TeV*. Tech. rep. CMS-PAS-EGM-10-004. Geneva: CERN, 2010. URL: <http://cds.cern.ch/record/1299116>.
- [76] CMS Collaboration. “Performance of Electron Reconstruction and Selection with the CMS Detector in Proton-Proton Collisions at  $\sqrt{s} = 8$  TeV”. In: *JINST* 10.06 (2015), P06005. DOI: 10.1088/1748-0221/10/06/P06005. arXiv: 1502.02701 [physics.ins-det].
- [77] G. P. Salam. “Towards Jetography”. In: *Eur. Phys. J.* C67 (2010), pp. 637–686. DOI: 10.1140/epjc/s10052-010-1314-6. arXiv: 0906.1833 [hep-ph].
- [78] G. C. Blazey et al. “Run II jet physics”. In: *QCD and weak boson physics in Run II. Proceedings, Batavia, USA, March 4-6, June 3-4, November 4-6, 1999*. 2000, pp. 47–77. arXiv: hep-ex/0005012 [hep-ex]. URL: [http://lss.fnal.gov/cgi-bin/find\\_paper.pl?conf-00-092](http://lss.fnal.gov/cgi-bin/find_paper.pl?conf-00-092).

- [79] CMS Collaboration. “Determination of jet energy calibration and transverse momentum resolution in CMS”. In: *JINST* 6 (2011), P11002. doi: 10.1088/1748-0221/6/11/P11002. arXiv: 1107.4277 [physics.ins-det].
- [80] D0 Collaboration. “Determination of the absolute jet energy scale in the D0 calorimeters”. In: *Nucl. Instrum. Meth. A* 424 (1999), p. 352. doi: 10.1016/S0168-9002(98)01368-0. arXiv: hep-ex/9805009 [hep-ex].
- [81] W. Waltenberger. *Adaptive Vertex Reconstruction*. Tech. rep. CMS-NOTE-2008-033. Geneva: CERN, July 2008. URL: <https://cds.cern.ch/record/1166320>.
- [82] CMS Collaboration. *MET performance in 8 TeV data*. Tech. rep. CMS-PAS-JME-12-002. Geneva: CERN, 2013. URL: <http://cds.cern.ch/record/1543527>.
- [83] CMS Collaboration. *Performance of missing energy reconstruction in 13 TeV pp collision data using the CMS detector*. Tech. rep. CMS-PAS-JME-16-004. Geneva: CERN, 2016. URL: <http://cds.cern.ch/record/2205284>.
- [84] ATLAS Collaboration. “Fiducial and differential cross sections of Higgs boson production measured in the four-lepton decay channel in  $pp$  collisions at  $\sqrt{s} = 8$  TeV with the ATLAS detector”. In: *Phys. Lett. B* 738 (2014), p. 234. doi: 10.1016/j.physletb.2014.09.054. arXiv: 1408.3226 [hep-ex].
- [85] ATLAS Collaboration. “Measurements of fiducial and differential cross sections for Higgs boson production in the diphoton decay channel at  $\sqrt{s} = 8$  TeV with ATLAS”. In: *JHEP* 09 (2014), p. 112. doi: 10.1007/JHEP09(2014)112. arXiv: 1407.4222 [hep-ex].
- [86] ATLAS Collaboration. “Measurements of the Total and Differential Higgs Boson Production Cross Sections Combining the  $H \rightarrow \gamma\gamma$  and  $H \rightarrow ZZ^* \rightarrow 4\ell$  Decay Channels at  $\sqrt{s} = 8$  TeV with the ATLAS Detector”. In: *Phys. Rev. Lett.* 115 (2015), p. 091801. doi: 10.1103/PhysRevLett.115.091801. arXiv: 1504.05833 [hep-ex].
- [87] CMS Collaboration. “Measurement of differential cross sections for Higgs boson production in the diphoton decay channel in  $pp$  collisions at  $\sqrt{s} = 8$  TeV”. In: *Eur. Phys. J. C* 76 (2016), p. 13. doi: 10.1140/epjc/s10052-015-3853-3. arXiv: 1508.07819 [hep-ex].
- [88] CMS Collaboration. “Measurement of differential and integrated fiducial cross sections for Higgs boson production in the four-lepton decay channel in  $pp$  collisions at  $\sqrt{s} = 7$  and 8 TeV”. In: *JHEP* 04 (2016), p. 005. doi: 10.1007/JHEP04(2016)005. arXiv: 1512.08377 [hep-ex].
- [89] CMS Collaboration. “Measurement of the transverse momentum spectrum of the Higgs boson produced in  $pp$  collisions at  $\sqrt{s} = 8$  TeV using  $H \rightarrow WW$  decays”. In: *Submitted to: JHEP* (2016). arXiv: 1606.01522 [hep-ex].

- [90] CMS Collaboration. “Measurement of Higgs boson production and properties in the WW decay channel with leptonic final states”. In: *JHEP* 01 (2014), p. 096. DOI: 10.1007/JHEP01(2014)096. arXiv: 1312.1129 [hep-ex].
- [91] G. Cowan. “A survey of unfolding methods for particle physics”. In: *Conf. Proc.* C0203181 (2002), p. 248.
- [92] S. Alioli, S. Moch, and P. Uwer. “Hadronic top-quark pair-production with one jet and parton showering”. In: *JHEP* 01 (2012), p. 137. DOI: 10.1007/JHEP01(2012)137. arXiv: 1110.5251 [hep-ph].
- [93] T. Binoth et al. “Gluon-induced  $W$ -boson pair production at the LHC”. In: *JHEP* 12 (2006), p. 046. DOI: 10.1088/1126-6708/2006/12/046. arXiv: hep-ph/0611170 [hep-ph].
- [94] M. Bonvini et al. “Signal-background interference effects for  $gg \rightarrow H \rightarrow W^+W^-$  beyond leading order”. In: *Phys. Rev. D* 88 (2013), p. 034032. DOI: 10.1103/PhysRevD.88.034032. arXiv: 1304.3053 [hep-ph].
- [95] G. Passarino. “Higgs CAT”. In: *Eur. Phys. J. C* 74 (2014), p. 2866. DOI: 10.1140/epjc/s10052-014-2866-7. arXiv: 1312.2397 [hep-ph].
- [96] H. Lai et al. “Uncertainty induced by QCD coupling in the CTEQ global analysis of parton distributions”. In: *Phys. Rev. D* 82 (2010), p. 054021. DOI: 10.1103/PhysRevD.82.054021. arXiv: 1004.4624 [hep-ph].
- [97] H. Lai et al. “New parton distributions for collider physics”. In: *Phys. Rev. D* 82 (2010), p. 074024. DOI: 10.1103/PhysRevD.82.074024. arXiv: 1007.2241 [hep-ph].
- [98] LHC Higgs Cross Section Working Group. “Handbook of LHC Higgs Cross Sections: 1. Inclusive Observables”. In: (2011). DOI: 10.5170/CERN-2011-002. arXiv: 1101.0593 [hep-ph].
- [99] S. Alioli et al. “A general framework for implementing NLO calculations in shower Monte Carlo programs: the POWHEG BOX”. In: *JHEP* 06 (2010), p. 043. DOI: 10.1007/JHEP06(2010)043. arXiv: 1002.2581 [hep-ph].
- [100] GEANT4. “GEANT4: A simulation toolkit”. In: *Nucl. Instrum. Meth. A* 506 (2003), p. 250. DOI: 10.1016/S0168-9002(03)01368-8.
- [101] E. Bagnaschi et al. “Higgs production via gluon fusion in the POWHEG approach in the SM and in the MSSM”. In: *JHEP* 02 (2012), p. 088. DOI: 10.1007/JHEP02(2012)088. arXiv: 1111.2854 [hep-ph].
- [102] S. Actis et al. “NLO Electroweak Corrections to Higgs Boson Production at Hadron Colliders”. In: *Phys. Lett. B* 670 (2008), p. 12. DOI: 10.1016/j.physletb.2008.10.018. arXiv: 0809.1301 [hep-ph].
- [103] S. Catani et al. “Soft gluon resummation for Higgs boson production at hadron colliders”. In: *JHEP* 07 (2003), p. 028. DOI: 10.1088/1126-6708/2003/07/028. arXiv: hep-ph/0306211 [hep-ph].

- [104] Y. Gao et al. “Spin determination of single-produced resonances at hadron colliders”. In: *Phys. Rev. D* 81 (2010), p. 075022. DOI: 10.1103/PhysRevD.81.075022. arXiv: 1001.3396 [hep-ph].
- [105] S. Bolognesi et al. “Spin and parity of a single-produced resonance at the LHC”. In: *Phys. Rev. D* 86 (2012), p. 095031. DOI: 10.1103/PhysRevD.86.095031. arXiv: 1208.4018 [hep-ph].
- [106] I. Anderson et al. “Constraining anomalous  $HVV$  interactions at proton and lepton colliders”. In: *Phys. Rev. D* 89 (2014), p. 035007. DOI: 10.1103/PhysRevD.89.035007. arXiv: 1309.4819 [hep-ph].
- [107] S. Jadach, J. H. Kuhn, and Z. Was. “TAUOLA: A Library of Monte Carlo programs to simulate decays of polarized tau leptons”. In: *Comput. Phys. Commun.* 64 (1990), p. 275. DOI: 10.1016/0010-4655(91)90038-M.
- [108] CMS Collaboration. “Standard Model Cross Sections for CMS at 7 TeV”. In: *CMS Generator Group Twiki* (2010).
- [109] J. M. Campbell, R. K. Ellis, and C. Williams. “Vector boson pair production at the LHC”. In: *JHEP* 07 (2011), p. 018. DOI: 10.1007/JHEP07(2011)018. arXiv: 1105.0020 [hep-ph].
- [110] J. Ohnemus. “Order alpha-s calculations of hadronic W+- gamma and Z gamma production”. In: *Phys. Rev. D* 47 (1993), pp. 940–955. DOI: 10.1103/PhysRevD.47.940.
- [111] I. W. Stewart and F. J. Tackmann. “Theory uncertainties for Higgs and other searches using jet bins”. In: *Phys. Rev. D* 85 (2012), p. 034011. DOI: 10.1103/PhysRevD.85.034011. arXiv: 1107.2117 [hep-ph].
- [112] S. Alekhin et al. “The PDF4LHC Working Group Interim Report”. In: (2011). arXiv: 1101.0536 [hep-ph].
- [113] Michiel Botje et al. “The PDF4LHC Working Group Interim Recommendations”. In: (2011). arXiv: 1101.0538 [hep-ph].
- [114] R. D. Ball et al. “Impact of Heavy Quark Masses on Parton Distributions and LHC Phenomenology”. In: *Nucl. Phys. B* 849 (2011), p. 296. DOI: 10.1016/j.nuclphysb.2011.03.021. arXiv: 1101.1300 [hep-ph].
- [115] A. D. Martin et al. “Parton distributions for the LHC”. In: *Eur. Phys. J. C* 63 (2009), p. 189. DOI: 10.1140/epjc/s10052-009-1072-5. arXiv: 0901.0002 [hep-ph].
- [116] ATLAS and CMS Collaborations. *Procedure for the LHC Higgs boson search combination in Summer 2011*. Tech. rep. CMS-NOTE-2011-005. ATL-PHYS-PUB-2011-11. Geneva: CERN, Aug. 2011.

- [117] G. Cowan et al. “Asymptotic formulae for likelihood-based tests of new physics”. In: *Eur. Phys. J.* C71 (2011). [Erratum: Eur. Phys. J.C73,2501(2013)], p. 1554. DOI: 10.1140/epjc/s10052-011-1554-0, 10.1140/epjc/s10052-013-2501-z. arXiv: 1007.1727 [physics.data-an].
- [118] T. Adye. “Unfolding algorithms and tests using RooUnfold”. In: (2011), p. 313. arXiv: 1105.1160 [physics.data-an].
- [119] G. D’Agostini. “A Multidimensional unfolding method based on Bayes’ theorem”. In: *Nucl. Instrum. Meth. A* 362 (1995), pp. 487–498. DOI: 10.1016/0168-9002(95)00274-X.
- [120] A. Hocker and V. Kartvelishvili. “SVD approach to data unfolding”. In: *Nucl. Instrum. Meth. A* 372 (1996), p. 469. DOI: 10.1016/0168-9002(95)01478-0. arXiv: hep-ph/9509307 [hep-ph].
- [121] P. Nason. “A New method for combining NLO QCD with shower Monte Carlo algorithms”. In: *JHEP* 11 (2004), p. 040. DOI: 10.1088/1126-6708/2004/11/040. arXiv: hep-ph/0409146 [hep-ph].
- [122] G. Luisoni et al. “ $HW^\pm/HZ + 0$  and 1 jet at NLO with the POWHEG BOX interfaced to GoSam and their merging within MiNLO”. In: *JHEP* 10 (2013), p. 083. DOI: 10.1007/JHEP10(2013)083. arXiv: 1306.2542 [hep-ph].
- [123] T. Melia et al. “W+W-, WZ and ZZ production in the POWHEG BOX”. In: *JHEP* 11 (2011), p. 078. DOI: 10.1007/JHEP11(2011)078. arXiv: 1107.5051 [hep-ph].
- [124] T. Gehrmann et al. “ $W^+W^-$  Production at Hadron Colliders in Next to Next to Leading Order QCD”. In: *Phys. Rev. Lett.* 113.21 (2014), p. 212001. DOI: 10.1103/PhysRevLett.113.212001. arXiv: 1408.5243 [hep-ph].
- [125] P. Meade, H. Ramani, and M. Zeng. “Transverse momentum resummation effects in  $W^+W^-$  measurements”. In: *Phys. Rev. D* 90.11 (2014), p. 114006. DOI: 10.1103/PhysRevD.90.114006. arXiv: 1407.4481 [hep-ph].
- [126] P. Jaiswal and T. Okui. “Explanation of the  $WW$  excess at the LHC by jet-veto resummation”. In: *Phys. Rev. D* 90.7 (2014), p. 073009. DOI: 10.1103/PhysRevD.90.073009. arXiv: 1407.4537 [hep-ph].
- [127] J. M. Campbell, R. K. Ellis, and C. Williams. “Bounding the Higgs width at the LHC: Complementary results from  $H \rightarrow WW$ ”. In: *Phys. Rev.* D89.5 (2014), p. 053011. DOI: 10.1103/PhysRevD.89.053011. arXiv: 1312.1628 [hep-ph].
- [128] NNPDF Collaboration. “Unbiased global determination of parton distributions and their uncertainties at NNLO and at LO”. In: *Nucl. Phys. B* 855 (2012), p. 153. DOI: 10.1016/j.nuclphysb.2011.09.024. arXiv: 1107.2652 [hep-ph].

- [129] CMS Collaboration. “Event generator tunes obtained from underlying event and multiparton scattering measurements”. In: (2015). arXiv: 1512 . 00815 [hep-ex].
- [130] P. Richardson and A. Wilcock. “Monte Carlo Simulation of Hard Radiation in Decays in Beyond the Standard Model Physics in Herwig++”. In: *Eur. Phys. J.* C74 (2014), p. 2713. DOI: 10 . 1140 / epjc / s10052 - 014 - 2713 - x. arXiv: 1303 . 4563 [hep-ph].
- [131] J. Bellm et al. “Herwig++ 2.7 Release Note”. In: (2013). arXiv: 1310 . 6877 [hep-ph].
- [132] *SM Higgs production cross sections at  $\sqrt{s} = 13\text{-}14 \text{ TeV}$* . <https://twiki.cern.ch/twiki/bin/view/LHCPhysics/CERNYellowReportPageAt1314TeV>.
- [133] F. Caola et al. “QCD corrections to  $W^+W^-$  production through gluon fusion”. In: *Phys. Lett. B* 754 (2016), p. 275. DOI: 10 . 1016 / j . physletb . 2016 . 01 . 046. arXiv: 1511 . 08617 [hep-ph].
- [134] *NLO single-top channel cross sections*. <https://twiki.cern.ch/twiki/bin/view/LHCPhysics/SingleTopRefXsec>.
- [135] *NNLO+NNLL top-quark-pair cross sections*. <https://twiki.cern.ch/twiki/bin/view/LHCPhysics/TtbarNNLO>.
- [136] *LHC Higgs Cross Section Working Group*. <https://twiki.cern.ch/twiki/bin/view/LHCPhysics/LHCHXSWG>.
- [137] J. Butterworth et al. “PDF4LHC recommendations for LHC Run II”. In: *J. Phys.* G43 (2016), p. 023001. DOI: 10 . 1088 / 0954 - 3899 / 43 / 2 / 023001. arXiv: 1510 . 03865 [hep-ph].
- [138] CMS Collaboration. “Search for a Higgs Boson in the Mass Range from 145 to 1000 GeV Decaying to a Pair of W or Z Bosons”. In: *JHEP* 10 (2015), p. 144. DOI: 10 . 1007 / JHEP10 (2015) 144. arXiv: 1504 . 00936 [hep-ex].
- [139] N. Craig and T. Scott. “Exclusive signals of an extended Higgs sector”. In: *JHEP* 11 (2012), p. 083. DOI: 10 . 1007 / JHEP11 (2012) 083. arXiv: 1207 . 4835 [hep-ph].
- [140] H. Haber and O. Stal. “New LHC benchmarks for the CP-conserving two-Higgs-doublet model”. In: *Eur. Phys. J. C* 75 (2015), p. 491. DOI: 10 . 1140 / epjc / s10052 - 015 - 3697 - x. arXiv: 1507 . 04281 [hep-ph].
- [141] S. Choi, S. Jung, and P. Ko. “Implications of LHC data on 125 GeV Higgs-like boson for the Standard Model and its various extensions”. In: *JHEP* 1310 (2013), p. 225. DOI: 10 . 1007 / JHEP10 (2013) 225. arXiv: 1307 . 3948.
- [142] J. Alwall et al. “Comparative study of various algorithms for the merging of parton showers and matrix elements in hadronic collisions”. In: *Eur. Phys. J. C* 53 (2008), pp. 473–500. DOI: 10 . 1140 / epjc / s10052 - 007 - 0490 - 5. arXiv: 0706 . 2569 [hep-ph].

- [143] M. Grazzini. “NNLO predictions for the Higgs boson signal in the  $H \rightarrow WW \rightarrow \ell\nu\ell\nu$  and  $H \rightarrow ZZ \rightarrow 4\ell$  decay channels”. In: *JHEP* 02 (2008), p. 043. DOI: 10.1088/1126-6708/2008/02/043. arXiv: 0801.3232 [hep-ph].
- [144] CMS Collaboration. “Measurement of the differential cross section for top quark pair production in pp collisions at  $\sqrt{s} = 8$  TeV”. In: *Eur. Phys. J. C* 75.11 (2015), p. 542. DOI: 10.1140/epjc/s10052-015-3709-x. arXiv: 1505.04480 [hep-ex].